

A Study of Structures and the Binding in Cationized Host-Guest Complexes in the Gas Phase

by

© Yanyang Chen

A Thesis submitted to the
School of Graduate Studies

In partial fulfillment of the requirements of the degree of

Doctor of Philosophy

Department of Chemistry

Memorial University of Newfoundland

May, 2025

St. John's

Newfoundland and Labrador

Abstract

Studying host-guest complexes in the gas phase provides a way to understand the intrinsic properties of the non-covalent interactions between hosts and guests. Two hosts were studied in the current thesis. One is 1,1,n,n-tetramethyl[n](2,11)teropyrenophane (TMnTP, n=7, 8, 9), synthesized by Dr. Bodwell's group, in which the non-planar teropyrene of TMnTP molecules allow alkali metal cations and protonated glycine to associate. The other types of hosts are ethers, including ortho-, meta-, para- and bridge-tetra anisole (TA) substituted anthraquinodimethane (AQ), namely o-TAAQ, m-TAAQ, p-TAAQ and b-TAAQ, synthesized by Dr. Zhao's group. The oxygen atoms, as well as the π electrons enable complexation with alkali metal cations. These cationized host-guest complexes were electrosprayed and isolated in the Fourier-transform ion cyclotron resonance (FT-ICR) cell, which allowed tandem mass spectrometry to be performed in order to explore the structures and unimolecular dissociation chemistries of host-guest complexes. Along with experiments, computational methods were also used to obtain proposed structures and energy information to compare with experimental results.

Fragments of the host-guest complexes under sustained off-resonance irradiation collision induced dissociation (SORI-CID) were analyzed. The fragments of $M^+(\text{TMnTP})$ ($M = \text{K, Rb, Cs}$) complexes are alkali metal cations and TMnTP, whereas the fragments of protonated glycine (GlyH^+)/TMnTP complexes were Gly and protonated TMnTP. Energy resolved SORI-CID provided relative gaseous stabilities of the host-guest complexes. Two species (*endo*- and *exo*- guests/hosts) were observed in both the $M^+(\text{TMnTP})$ and GlyH^+ /TMnTP by the means of blackbody infrared radiative dissociation (BIRD).

Structures with guests associating the host at different sites were proposed and computed using density functional theory (DFT). In this research, only $M^+(\text{TMnTP})$ dissociated under infrared multiphoton dissociation (IRMPD) in the range of 3150 cm^{-1} to 2700 cm^{-1} . The experimental IRMPD spectra of $M^+(\text{TMnTP})$ agreed well with the computed infrared (IR) spectra of *endo*- $M^+(\text{TMnTP})$. Additionally, the non-covalent interactions between GlyH^+ and TMnTP were a little more complicated thus they were visualized using the independent gradient model based on Hirshfeld partition (IGMH), and the nature of these non-covalent interactions were analyzed by natural energy decomposition analysis (NEDA). It showed a strong ion-induced dipole interaction within *endo*-protonated glycine TMnTP complexes.

As for $M^+(\text{TAAQ})$ complexes ($M = \text{Na}, \text{K}, \text{Rb}, \text{and Cs}$), they decompose to M^+ and TAAQ under SORI-CID experiments except lithiated TAAQ and sodiated *o*-TAAQ. The relative gas phase stabilities of $M^+(\text{TAAQ})$ were determined both experimentally resulting in the following series $\text{Na}^+(\text{TAAQ}) > \text{K}^+(\text{TAAQ}) > \text{Rb}^+(\text{TAAQ}) > \text{Cs}^+(\text{TAAQ})$. This agreed with the results of NEDA analysis that the interactions between alkali metal cations and TAAQ are electrostatic. The structures of $M^+(\text{TAAQ})$ complexes were explored using DFT method.

Acknowledgements

There are many people whom I would like to appreciate for their support in finishing this dissertation. First and foremost, I want to thank my supervisor Dr. Travis D. Fridgen. I will never forget when I first entered his office, his smile really eased my nervousness. He talked to me gently, slowly and clearly to help me quickly adapt to the English environment. I also greatly appreciate Travis giving me this opportunity to work on this exciting research project. His patient supervision really helped me enjoy my research life and complete this thesis. He also provided a free environment for us to conduct research and encouraged us to boldly express our own opinions. Because of his training, I have learned not only various proficient research skills, but also to think independently, and to learn teamwork, communication skills and the ability to troubleshoot. He was generous with his time meeting with me and patiently helped me to identify and solve problems.

I also would like to thank my committee members, Dr. Francesca M. Kerton and Dr. Christopher Flinn. They inspired me to develop new ideas for the research. I would also like to thank Dr. Graham J. Bodwell and Dr. Yuming Zhao for providing interesting host molecules for me to study.

I would also like to thank the China Scholarship Council, which contributed to the successful completion of my research program.

I am also thankful to the members of our Group, Bryan Linford who helped me in the lab at the very beginning of my PhD program; and Yasaman Jami Alahmadi who helped me with the experiments of my first project. I also would like to thank Mohammad Azargun,

Maryam Moghaddam, Barry Power, Ruodi Cheng, Mahsa Sharifi, Sam Atkinson and Kelsey Menard for their generously sharing their knowledge and friendship. I appreciate their help and encouragements before my every academic talk. We really had a good time together.

Special thanks go to my husband Kaijie Ni and my daughter Chloe Joy Ni. Without their love and understanding, this thesis work would not have been completed. Also, I want to thank my parents Dewei Chen and Yuying Li for their support, love and encouragement. Especially my mom who always supports and motivates me in every possible way that you can imagine when I face difficulties. I also want to thank Liangbaikai's music. Every night when I felt tired, frustrated and wanted to give up, his gentle voice and the encouraging melody of his songs gave me a big hug and saved me from a pessimistic mood. I also want to thank myself for insisting on doing my own research no matter what difficulties I met in my life. Thank you all.

TABLE OF CONTENTS

| | |
|---|----|
| Chapter 1 – Introduction | 1 |
| 1.1 General Introduction of Supramolecular Chemistry | 1 |
| 1.2 Hosts and Guests | 6 |
| 1.2.1 Host 1: Cyclophanes | 6 |
| 1.2.2 Host 2: Ethers..... | 11 |
| 1.2.3 Guests..... | 13 |
| 1.3 Experimental Methods | 15 |
| 1.3.1 Electrospray Ionization (ESI)..... | 16 |
| 1.3.2 Fourier Transform Ion Cyclotron Resonance Mass Spectrometry (FT-ICR MS) | 19 |
| 1.3.3 MS/MS | 24 |
| 1.3.3.1 Sustained Off-Resonance Irradiation Collision Induced Dissociation (SORI-CID)..... | 25 |
| 1.3.3.2 Instruments and Principles of Infrared Multiphoton Dissociation (IRMPD) Spectroscopy | 26 |
| 1.3.4 Blackbody Infrared Radiative Dissociation (BIRD) | 29 |
| 1.4 Computational Methods | 33 |
| 1.4.1 Density Functional Theory (DFT)..... | 34 |
| 1.4.2 Basis Set..... | 35 |
| 1.4.3 Collecting and Processing Data | 36 |
| 1.4.4 Master Equation Modeling (MEM) | 37 |
| 1.4.5 Natural Energy Decomposition Analysis (NEDA) | 39 |
| 1.4.6 Independent Gradient Model Based on Hirshfeld partition (IGMH)..... | 41 |
| 1.5 References..... | 43 |
| Chapter 2: Endo or Exo? Structures of Gas Phase Alkali Metal Cation/Aromatic Half-Belt Complexes | 56 |

| | |
|---|-----------|
| 2.1. Introduction..... | 57 |
| 2.2 Methods..... | 60 |
| 2.2.1 Experimental | 60 |
| 2.2.2 Computational..... | 61 |
| 2.2.3 Master Equation Modelling | 62 |
| 2.3 Results and Discussion..... | 63 |
| 2.4 Conclusions..... | 74 |
| 2.5 Acknowledgements..... | 74 |
| 2.6 References..... | 75 |
| Chapter 3: Glycine in a Basket: Protonated 1,1,n,n-tetramethyl[n](2,11)teropyrenophane (n=7, 8, 9) Complexes With Glycine in the Gas-Phase | 83 |
| 3.1 Introduction..... | 85 |
| 3.2 Methods..... | 90 |
| 3.2.1 Experimental | 90 |
| 3.2.1.1 Energy-Resolved SORI-CID..... | 91 |
| 3.2.1.2 BIRD Measurements..... | 92 |
| 3.2.2 Computational..... | 93 |
| 3.2.2.1 Independent Gradient Model Based on Hirshfeld partition | 93 |
| 3.2.2.2 Natural Energy Decomposition Analysis | 94 |
| 3.2.3 Master Equation Modeling..... | 95 |
| 3.3 Results and Discussions | 97 |
| 3.3.1 SORI-CID and Computed Proton Affinities..... | 97 |
| 3.3.2 BIRD Experiments..... | 99 |
| 3.3.3 Energy Resolved SORI-CID | 105 |
| 3.3.4 Computed Structures and Energies | 107 |
| 3.3.5 Non-covalent Interactions Analysis | 114 |

| | |
|--|------------|
| 3.3.5.1 Independent Gradient Model Based on Hirshfeld Partition Analysis | 114 |
| 3.3.5.2 Natural Energy Decomposition Analysis | 116 |
| 3.4 Conclusions..... | 118 |
| 3.5 Acknowledgements..... | 119 |
| 3.6 References..... | 120 |
| Chapter 4: Complexation of Tetraanisoyl-Anthraquinodimethanes with Alkali Metal Ions: A Combined Mass Spectrometric and Computational Study | 131 |
| 4.1 Introduction..... | 132 |
| 4.2 Methods..... | 136 |
| 4.2.1 Experimental | 136 |
| 4.2.2 Computational..... | 137 |
| 4.3 Results and Discussion..... | 139 |
| 4.3.1 SORI-CID Reactions..... | 139 |
| 4.3.1.1 Fragment Ions of Li ⁺ (o-TAAQ) and Na ⁺ (o-TAAQ) with Similar Structures Containing the Metal Cation. | 144 |
| 4.3.1.2 SORI-CID of Fragment Ions Without a Metal Cation in Li ⁺ (o-TAAQ) and Na ⁺ (o-TAAQ)..... | 147 |
| 4.3.1.3 Fragment Ions only Observed in the SORI-CID Spectra of Li ⁺ (o-TAAQ) | 148 |
| 4.3.1.4 Fragmentation of Li ⁺ (m-TAAQ) | 149 |
| 4.3.1.5 Fragmentation of Li ⁺ (p-TAAQ) | 151 |
| 4.3.1.6 Fragmentation of Li ⁺ (b-TAAQ) | 152 |
| 4.3.2 Energy-resolved SORI-CID | 152 |
| 4.3.3 Computed Structures for the M ⁺ (TAAQ) Complexes..... | 156 |
| 4.3.3.1 Computed structures for M ⁺ (o-TAAQ). | 158 |
| 4.3.3.2 Computed structures for M ⁺ (m-TAAQ). | 159 |
| 4.3.3.3 Computed Structures for M ⁺ (p-TAAQ)..... | 160 |
| 4.3.3.4 Computed Structures for M ⁺ (b-TAAQ)..... | 162 |

| | |
|--|------------|
| 4.3.3.5. Analysis of Computed Binding Energies. | 165 |
| 4.3.4 Natural Energy Decomposition Analysis (NEDA) | 166 |
| 4.4 Conclusions..... | 169 |
| 4.5 Acknowledgments..... | 170 |
| 4.6 References..... | 171 |
| Chapter 5-Conclusions and Future work | 178 |
| 5.1 Summary | 178 |
| 5.2 Future Work..... | 183 |

LIST OF FIGURES

Chapter 1

| | |
|--|----|
| Figure 1.1 Structures of a) α -CD; b) dibenzo-18-crown-6; c) carboxyethyl substituted azacrown ether; d) HP- β -CD ($r=CH_2CHOHCH_3$) and e) cisapride | 2 |
| Figure 1.2 Adsorption of Ag^+ by azacrown ether carboxylic acid derivative which was intercalated into a layered gadolinium hydroxides. Reprinted with permission from <i>Inorg. Chem.</i> 2013, 52, 24, 14010–14017. Copyright (2013) American Chemical Society. ¹⁸ | 3 |
| Figure 1.3 Schematic representation of (a) catenane and (b) rotaxane | 6 |
| Figure 1.4 Structures of [2.2]paracyclophane and [2.2.2]paracyclophane..... | 7 |
| Figure 1.5 Structure of 1,1,n,n-Tetramethyl[n](2,11)teropyrenophane ($x=1, 2, 3, n = 7, 8, 9$) and technical numbering scheme of aromatic carbons. | 9 |
| Figure 1.6 Structures of corannulene, sumanene and Armchair SWCNT. | 9 |
| Figure 1.7 Structures of 12-crown-4 (12c4), 15-crown-5 (15c5), and 18-crown-6 (18c6)..... | 11 |
| Figure 1.8 Structures of o-TAAQ, m-TAAQ, p-TAAQ and b-TAAQ. Schemes of TAAQs at the bottom are generated from 3-dimensional structures..... | 13 |
| Figure 1.9 The structure of protonated glycine..... | 14 |
| Figure 1.10 The OPO laser/Bruker ApexQe 7 FT-ICR mass spectrometer/Apollo II ESI in the laboratory at Memorial university..... | 16 |
| Figure 1.11 Scheme of ESI process. Reprinted with permission from <i>Mass Spec Rev</i> 2001, 20: 362–387. Copyright (2001) John Wiley & Sons, Inc. ⁷⁴ | 17 |
| Figure 1.12 Three models of ESI. Adapted with permission from <i>Anal. Chem.</i> 2013, 85, 1, 2–9. Copyright (2013) American Chemical Society. ⁷⁵ | 18 |
| Figure 1.13 Ion motion in a magnetic field. Reprinted with permission from <i>Mass Spec Rev</i> 17, 1998, 1–35. Copyright (1998) John Wiley & Sons, Inc. ⁸⁷ | 20 |
| Figure 1.14 Schematic diagram of ion path and detection in FT-ICR. | 22 |
| Figure 1.15 Mechanisms of IRMPD process. Adapted with permission from Dr. Travis D. Fridgen (Memorial University)..... | 27 |
| Figure 1.16 Fragmentations of $Cs^+(TM9TP)$ during IRMPD scan. The band near 2978 cm^{-1} corresponds to aliphatic C-H stretching | 28 |

Chapter 2

Figure 2.1 SORI-CID mass spectra of potassium, rubidium, and cesium TM9TP complexes. 63

Figure 2.2 Normalized ion intensity vs time plots for BIRD of $K(TM9TP)^+$, $Rb(TM9TP)^+$, and $Cs(TM9TP)^+$. The ICR cell temperature was 20 °C. The dashed red lines are theoretical BIRD plots computed using the master equation. 65

Figure 2.3 B3LYP/6-31+G(d,p), Def2SVP on Rb, computed 298 K enthalpy diagram for the dissociation of *endo*- $Rb(TM9TP)^+$ 66

Figure 2.4 Comparison of the IRMPD spectra (grey traces) and computed spectra (black traces) for the $Rb(TM9TP)^+$ (left) and $Cs(TM9TP)^+$ (right) complexes in the *exo* (top) and *endo* (bottom) configurations. 70

Figure 2.5 A plot of the computed (grey circles) and observed (black circles) central bridge C-H stretch (see inset structures) positions vs the ionization energy of the metal. 73

Chapter 3

Figure 3.1 SORI-CID mass spectra of $[(TMnTP)(Gly)]H^+$ ($n=7, 8, 9$) decomposing to protonated $TMnTP$ 97

Figure 3.2 BIRD kinetic plots of $[(TMnTP)(Gly)]H^+$ ($n=7, 8, 9$) at 342 K, precursor ions $[(TMnTP)(Gly)]H^+$ are denoted as solid shapes and fragment ions $TMnTPH^+$ are denoted as hollow shapes. Circles, triangles and squares corresponded to the $n=7, 8, 9$ complexes respectively. The solid curved lines are biexponential fits of the experimental data. The data plotted in a) and b) are the same with different scales on the abscissa. 100

Figure 3.3 Arrhenius plots for the BIRD of a) SD- $[(TMnTP)(Gly)]H^+$ and b) FD- $[(TMnTP)(Gly)]H^+$, ($n=7, 8, 9$). The error bars are due to the standard error in fitting the kinetic plots. 104

Figure 3.4 a) Intensity vs. the center-of-mass energy survival yields curves for ER-SORI-CID of SD- $[(TMnTP)(Gly)]H^+$ complexes exposed to Ar gas pulsed with 10 mbar reservoir pressure; b) Relative center-of-mass collisional energies at half dissociation of SD- $[(TMnTP)(Gly)]H^+$ ($n=7, 8, 9$) under 10 and 15 mbar reservoir pressures. 106

Figure 3.5 Global minimum structures of $[(TMnTP)(Gly)]H^+$ $n=7, 8, 9$, first row, respectively; the lowest energy structures of *endo*- $(TMnTPH^+)(Gly)$ $n=7, 8, 9$, second row, respectively; the lowest energy structures of *exo*- $(TMnTPH^+)(Gly)$ $n=7, 8, 9$, third row, respectively; and the lowest energy structures of *exo*- $(TMnTP)(Gly)H^+$ $n=7, 8, 9$, fourth row, respectively. Structures and energies were computed by B3LYP-D3/6-31+g(d,p). Thermochemical values are in kJ mol^{-1} and are 298 K values. Bond lengths are in Å. 109

Figure 3.6 Results of the IGMH analysis of the lowest energy structures of each type of $[(TM9TP)(Gly)]H^+$ complexes. Upper figures are three dimensional isosurfaces (isovalue = 0.005

a.u.), lower figures are IGMH scatter plots. Both are colored according to the BGR scheme over the range of $-0.04 < \text{sign}(\lambda_2)\rho < 0.04$ au, where the blue, green, and red correspond to strong attraction, weak attraction, and steric repulsion respectively. To make a better view of the isosurfaces, structures of *endo*-(TM9TP) (GlyH⁺) and *endo*-(TMnTPH⁺)(Gly) are rotated slightly from the corresponding structures of Figure 3.5; structures of *exo*-(TM9TP)(GlyH⁺) are rotated up almost 90° from the corresponding structure of Figure 3.5; and the structures of *exo*-(TMnTPH⁺)(Gly) are flipped and rotated 90° from the corresponding structure of Figure 3.5... 115

Figure 3.7 Computed NEDA component energies (in kJ mol⁻¹) at the B3LYP-D3/6-31+G(d,p) level for the lowest energy structures of each type of [(TMnTP)(Gly)]H⁺ complex. 117

Chapter 4

Figure 4.1 SORI-CID mass spectra of the complexes of Na⁺ with o-, m-, p- and b-TAAQs, respectively. 139

Figure 4.2 Comparison of the SORI-CID mass spectra for Li⁺(o-TAAQ) and Na⁺(o-TAAQ)... 140

Figure 4.3 Energy-resolved SORI-CID breakdown curves for the Na⁺(TAAQ) complexes under a) 10 mBar and b) 15 mBar Ar reservoir pressure. 153

Figure 4.4 Relative center of mass collision energies at half dissociation for loss of neutral TAAQ from the M⁺(TAAQ) complex ions at 15 mbar (black bars) and 10 mbar (grey bars) of reservoir Ar pressure. Plot a) compares the metal cation binding to each of the TAAQs and plot b) compares the TAAQ binding to each of the metal cations. Also shown are the relative binding energies computed at the B3LYP-D3/6-31+G(d,p) on C, H, O and def2svp on metals level and basis set (black bars). 154

Figure 4.5 B3LYP-D3/6-31+G(d,p)/Def2-SVP computed lowest energy structures of M⁺(o-TAAQ) $\Delta_{\text{bind}}H$ and $\Delta_{\text{bind}}G$ are in unit kJ mol⁻¹ at 298 K, 1 atm. 157

Figure 4.6 Computed lowest energy structures of M⁺(o-TAAQ) by the B3LYP-D3 method with the 6-31+G(d,p) basis set used on C, H and O, and the Def2-SVP basis set on alkali metal atoms. 161

Figure 4.7 Results of the NEDA computations on the lowest energy structures of M⁺(TAAQs) which are M⁺(o-4O-TAAQ), M⁺(m₁-2O-3Ph-TAAQ), M⁺(p-2O-3Ph-TAAQ) (M = Li, Na, K, Rb, Cs) and M⁺(b_{2u}-4O-TAAQ) (M = Li, Na), M⁺(b_{2d}-2O-TAAQ) (M = K, Rb, and Cs). Calculations were done by B3LYP-D3/6-31+G(d,p) on C, H, O and B3LYP-D3/Def2-SVP on alkali metals. 167

Chapter 5

Figure 5.1 SORI-CID spectra of (a) Ag(TMnTP)⁺ and (b) Ag⁺(ACN)(TM9TP) 184

Figure 5.2 SORI-CID spectra of TMnTP⁺ 185

| | |
|--|-----|
| Figure 5.3 IRMPD spectra (gray traces) overlaid by computed IR spectra (black traces) of <i>endo</i> - and <i>exo</i> -Ag(TM9TP) ⁺ | 185 |
| Figure 5.4 SORI-CID spectra of protonated AAs/o-TAAQ. | 186 |
| Figure 5.5 SORI-CID spectra of protonated AAs/o-TAAQ. | 187 |
| Figure 5.6 SORI-CID spectra of protonated AAs/o-TAAQ. | 187 |

LIST OF TABLES

Chapter 2

Table 2.1 Computed potential energy surface for the dissociation of $M(TM9TP)^+$. Values are relative 298 K enthalpies computed using B3LYPD3 (and CAM-B3LYP) with 6-31+G(d,p) basis on C and H, and def2-SVP basis on metal atoms. 68

Chapter 3

Table 3.1 Experimental observed activation energy E_{aobs} , logarithm of pre-exponential factors $\log A_{obs}$, activation entropies ΔS^\ddagger , MEM threshold dissociation energy E_0 and computed binding energies at 298K, 1 atm..... 102

Chapter 4

Table 4.1 Distances (\AA) from alkali metal cations to the oxygens nearby and distances (\AA) from Li^+ to the middle of anthracene computed by B3LYP- D3/6-31+G(d,p) on C, H, O and def2svp on metal..... 159

Table 4.2 Computed binding energies (values in the bracket are computed dissociation Gibbs free energies) of the lowest energy structure of alkali metal cationized o-, m-, p-, b_{2u^-} , b_{1u1d^-} and b_{2d^-} TAAQs. Energies are listed in kJ mol^{-1} and calculated by B3LYP-D3/6-31+G(d,p) on C, H, O and B3LYP-D3/Def2-SVP on metal at 298K, 1atm. Values in bold are computed under the level of M06-2x/6-31+G(d,p) on C, H, O and B3LYP-D3/Def2-SVP on metal at 298K, 1atm..... 162

LIST OF SCHEMES

Chapter 2

Scheme 2.1 Homoditopic hexamino bicyclic cyclophane (1), duplexiphane (2), [7]paracyclophane (3), and TM9TP (4). 58

Chapter 3

Scheme 3.1 1,1,n,n-Tetramethyl(2,11)teropyrenophane (TMnTP) (x=1-3, n = 7-9) 87

Chapter 4

Scheme 4.1 Structures of four tetra-anisole substituted anthraquinodimethane (TAAQ) host molecules, from top left to right corresponding to the ortho-, meta-, para- and bridging- TAAQ respectively. 135

Scheme 4.2 Proposed dissociation pathways for Li⁺(o-TAAQ)..... 142

Scheme 4.3 Proposed dissociation pathways for Na⁺(o-TAAQ)..... 143

LIST OF ABBREVIATIONS AND SYMBOLS

| | |
|------------------------------|---|
| $E_{\text{CM}}^{\text{max}}$ | center of mass energy |
| $\rho(r)$ | sum of charge densities of perturbed monomers |
| $\rho_{\text{A}}(r)$ | charge density of perturbed monomers |
| $\rho_{\text{A}}^0(r)$ | densities of relaxed monomers |
| $\rho_{\text{tot}}(r)$ | total charge densities for the system |
| $\Delta_{\text{bind}}G$ | binding Gibbs free energy |
| $\Delta_{\text{bind}}H$ | binding enthalpy |
| $\Delta_{\text{rel}}G$ | Gibbs free energies relative to the lowest energy structure |
| $\Delta_{\text{rel}}H$ | enthalpies relative to the lowest energy structure |
| ΔS^\ddagger | entropy of activation |
| $\Delta\vartheta$ | frequency offset |
| A | pre-exponential factor |
| AA | amino acid |
| B | strength of a uniform magnetic field |
| B3LYP | Becke-(3 parameter)-Lee-Yang-Parr |
| BE | binding energies |
| BIRD | blackbody infrared radiative dissociation |
| C | Coulomb |
| CD | cyclodextrin |
| CEM | Chain ejection model |

| | |
|-------------|---|
| CRM | charge residue model |
| CT | charge transfer |
| d | diameter of the ICR cell |
| Da | Dalton |
| DEF | deformation |
| Def2SVP | Karlsruhe basis sets split valence polarization |
| DFT | Density functional theory |
| e | elementary charge |
| E_0 | dissociation threshold energy |
| $E_{50\%}$ | half dissociation |
| E_a | activation energy |
| ED | electron density |
| ER-SORI-CID | energy resolved-SORI-CID |
| ES | electrostatic |
| ESI | electrospray ionization |
| f_c | cyclotron frequency |
| FEL | free electron laser |
| FT-ICR-MS | Fourier transform ion cyclotron resonance |
| Gly | glycine |
| h | Planck's constant |
| Hz | Hertz |
| IEM | ion evaporation model |

| | |
|------------------|--|
| IGM | independent gradient model |
| IGMH | Independent gradient model based on Hirshfeld partition |
| IRMPD | infrared multiphoton dissociation |
| IVR | intramolecular vibrational-energy redistribution |
| k_{abs} | photon absorption rate constant |
| k_{B} | Boltzmann constant |
| k_{d} | unimolecular dissociation rate constant |
| k_{em} | photon emission rate constant |
| kg | kilogram |
| k_{uni} | overall rate constant of the overall unimolecular dissociation |
| m | mass |
| m/z | mass to charge ratio |
| MEM | Master Equation Modeling |
| m_{g} | mass of a collisional gas molecule |
| m_{p} | mass of a precursor ion |
| MS | mass spectrometry |
| MS/MS | tandem mass spectrometry |
| N_{A} | Avogadro constant |
| Nd:YAG | neodymium-doped yttrium aluminium garnet |
| NEDA | Natural Energy Decomposition Analysis |
| OPO/OPA | optical parametric oscillation/amplifier |
| PAH | polycyclic aromatic hydrocarbon |

| | |
|------------|--|
| POL | polarization |
| q | charge |
| R | gas constant |
| r | radius of circular motions |
| REX | rapid energy exchange |
| rf | radio frequency |
| SORI-CID | Sustained off-resonance irradiation collision-induced dissociation |
| SWCNTs | Single walled carbon nanotubes |
| T | Tesla |
| t | time |
| TAAQ | tetra anisole anthraquinodimethane |
| TMnTP | 1,1, n,n -Tetramethyl[n](2,11)teropyrenophanes ($n=7, 8, 9$) |
| TS | transition state |
| v | velocity |
| V_{p-p} | peak-to-peak excitation voltage |
| XC | exchange and correlation |
| z | charge number |
| β | geometrical factor of the ICR cell |
| ν | frequency of the electromagnetic radiation |
| ω_c | angular velocity |

LIST OF APPENDICES

| | |
|--|-----|
| Appendix A: Chapter 2 Supplemental Information..... | 189 |
| Appendix B: Chapter 3 Supplemental Information..... | 199 |
| Appendix C: Chapter 4 Supplemental Information..... | 241 |

CO-AUTHORSHIP STATEMENT

The experiments presented in Chapter 2-4 of this dissertation were designed by the principal author and Dr. Travis D. Fridgen. All experiments were conducted by the principal author. In chapter 2, Yasaman Jami Alahmadi collaborated in collecting the IRMPD spectra of $K^+(\text{TM9TP})$. In chapter 3, Maria Demireva assisted in master equation modeling. TMnTP ($n=7-9$) complexes which were used in chapter 2 and 3 were provided by Kiran Sagar Unikela, Parisa Ghods Ghasemabadi and Dr. Graham J. Bodwell. TAAQ complexes which were used in chapter 4 were provided by Maryam F. Abdollahi and Dr. Yuming Zhao.

Chapter 1 – Introduction

1.1 General Introduction of Supramolecular Chemistry

Supramolecular chemistry is a branch of chemistry that focuses on studying the non-covalent interactions between molecules, in which these interactions give rise to forming larger, more complex structures. The inception of supramolecular chemistry dates back to 1891 with the first identification of cyclodextrin (CD) by Villiers. CD was initially known as cellulose and possess a conical configuration containing an internal hollow space (Figure 1.1) that allows CDs to form inclusion complexes with guest molecules, where the guest molecule is partially or completely enclosed within the cyclodextrin cavity.^{1,2} The first studies on cyclodextrins date back to the 1950s when Cramer and Helfferich investigated their complexation properties.³ Since then, there has been extensive exploration of the encapsulation characteristics of cyclodextrins.^{4,5} In the early 20th century, Gilbert Lewis introduced the phenomenon of association of a certain polar substance and the combination of polar substance with other substances which were known as complexes.⁶ In the 1960s, Charles Pedersen pioneered work on synthesizing thirty three crown ethers containing 3-20 oxygen atoms in the cyclic polyethers, such as dibenzo 18-crown-6 (Figure 1.1) that allow the binding of metal cations and ammonium cation.⁷ In 1978, Jean-Marie Lehn first used the term “supramolecular chemistry”^{8,9} which studied the assemblies of two or more species and the intermolecular bonding of the assemblies. According to the substrate selectivity of enzymes, Danald J. Cram designed various hosts with the cyclic ether as a basic unit to selectively encapsulate alkylammonium salts, amino acids and metal cations.¹⁰ In 1987, the Nobel Prize in Chemistry was granted to Charles J.

Pedersen, Jean-Marie Lehn, and Donald J. Cram in recognition of their achievements in creating and utilizing molecules that exhibit highly selective interactions based on specific structures.¹¹

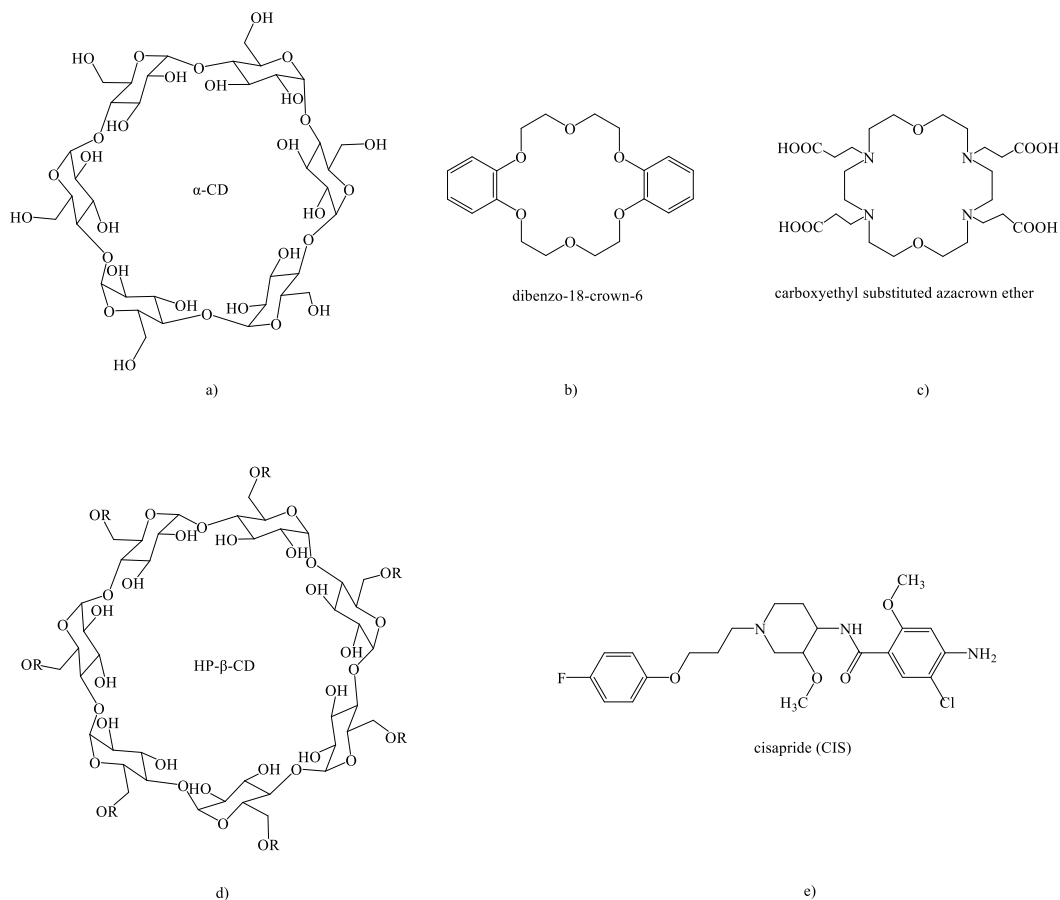


Figure 1.1 Structures of a) α -CD; b) dibenzo-18-crown-6; c) carboxyethyl substituted azacrown ether; d) HP- β -CD (R=CH₂CHOHCH₃) and e) cisapride

Literally, supramolecular chemistry can be defined as “chemistry beyond the molecule”.⁹ It describes the chemistry of systems consisting of two or more molecules held together through intermolecular or non-covalent interactions such as dipole-dipole, hydrogen bonding, cation- π , and van der Waals interactions, etc.¹²⁻¹⁶ Host-guest chemistry,

a subset of supramolecular chemistry, focuses on the formation of complexes where host molecules possess significant cavities or voids, while ionic or neutral guest molecules bind to them through intermolecular interactions, resulting in the creation of distinctive structures.¹⁷

Host-guest chemistry is applied in diverse fields and the design and synthesis of functional supramolecular systems allow for precise control over molecular recognition and assembly processes. Thus, these systems can make possible the encapsulation, safeguarding, or transportation of guest molecules. For example, some host molecules exhibit the capability to capture metal cations.

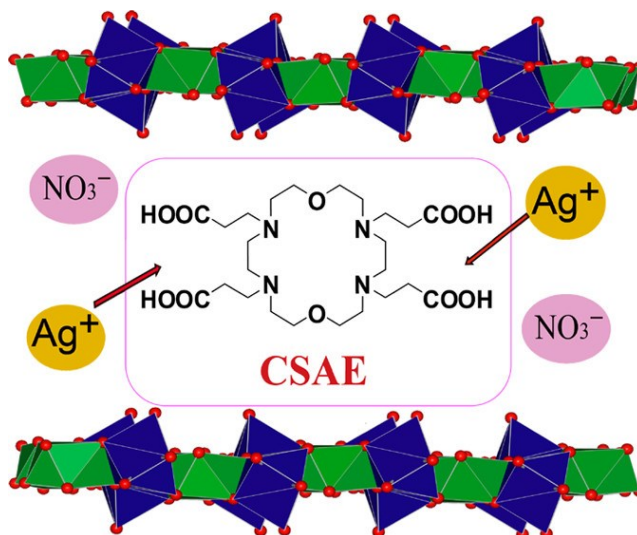


Figure 1.2 Adsorption of Ag⁺ by azacrown ether carboxylic acid derivative which was intercalated into a layered gadolinium hydroxides. Reprinted with permission from *Inorg. Chem.* 2013, 52, 24, 14010–14017. Copyright (2013) American Chemical Society.¹⁸

The intercalated carboxyethyl-substituted azacrown ether acting as a secondary host into a parent host of layered gadolinium hydroxides (Figure 1.2) exhibited an affinity towards transition and heavy metal ions, particularly demonstrating high selectivity for

Cu^{2+} , Ag^+ , and Hg^{2+} . However, the adsorption capability towards alkali metal ions was found to be relatively low.¹⁸ Due to the selectivity of certain hosts towards specific cations, these hosts can serve as ionophores and find application in ion sensors.¹⁹⁻²³ Host-guest systems can also be applied in drug delivery. For example, the hydrophobic cavities of CDs, CD derivatives and CD containing materials enable them to encapsulate hydrophobic active pharmaceutical ingredients (API) through non-covalent interactions such as Van der Waals forces and hydrogen bonding.²⁴ CD containing complexes can increase the aqueous solubility of API, control drug release profiles, conceal odors, and etc.⁵ There are more than thirty pharmaceutical products containing CD or CD derivatives host/guest complexes, such as hydroxypropyl- β -cyclodextrin (HP- β -CD)/cisapride (CIS).²⁴ CIS (Figure 1.1) is a substituted piperidinyll benzamide, which helps bowel movements and reducing duodenogastric reflux.²⁵ HP- β -CD is a hydroxyalkyl derivative of β -CD. The additional hydroxyl groups of HP- β -CD (Figure 1.1) make the aqueous solubility of HP- β -CD higher than β -CD. CIS is encapsulated by HP- β -CD through van der Waals interactions and very little electrostatic interactions.²⁶ When CIS is in a mixture (with a pH of 7) of Ora-Sweet[®] and Ora-Plus[®] (1:1), it is only stable for 60 days at 5 °C and 25 °C.²⁷ Boonleang found out that when CIS oral suspension mixed with HP- β -CD, the CIS suspension can be stored at least 12.5 months at 5 °C and 30 °C.²⁸

Host-guest interactions are crucial for the development of molecular machines. Many activities and metabolic processes are carried out by the machine-like operation of biological macromolecules. After biologists have revealed the workings of nature's molecular machinery, chemists try to mimic these large molecules by designing synthetic

small molecules. In 1983, a mechanically interlocked molecule, catenane, (Figure 1.3) was synthesized by Sauvage and co-workers.²⁹ Two strategies of catenane synthesis were proposed. One used copper (I) cation coordination to bring the two crescent ligands closer and then closed the two rings by adding other groups. Copper (I) cation was used to bring a cyclic ligand and a crescent ligand close to each other in the other strategy. The interlocked molecules can be prepared not only by metal coordination but also by non-covalent interactions. Hunter and coworkers formed the [2]catenane (Figure 1.3) when they prepared a bis-isophthalamide macrocycle by reacting bis amine-containing isophthalamide with isophthaloyl dichloride.³⁰ The driving forces for the formation of this type of interlocked structures are hydrogen bonds and π - π stacking interactions. It's feasible for the internal isophthalamide groups to undergo a rocking movement within the macrocyclic cavity up to 90 degrees in solution.³¹ In 1991, Stoddart synthesized a rotaxane (Figure 1.3), which is a type of mechanically interlocked ring.³² Bulky stoppers prevent the linear molecule that threaded through a macrocyclic ring in a rotaxane from dissociating. The ring molecules are at different recognition sites of the linear molecules, which can be recognized as two different signals (0 and 1), which can be used for molecular switching. Using temperature-variable NMR, Stoddart et al. determined that at 20 °C, the circular molecule can ferry between the two end-like bonds of the linear molecule, and at -50 °C, it stops moving, thus achieving the ferry movement of the moving molecule in solution.

Supramolecular chemistry continues to evolve, and it is worth studying the non-covalent interactions that are often harnessed in the design and construction of molecular assemblies.

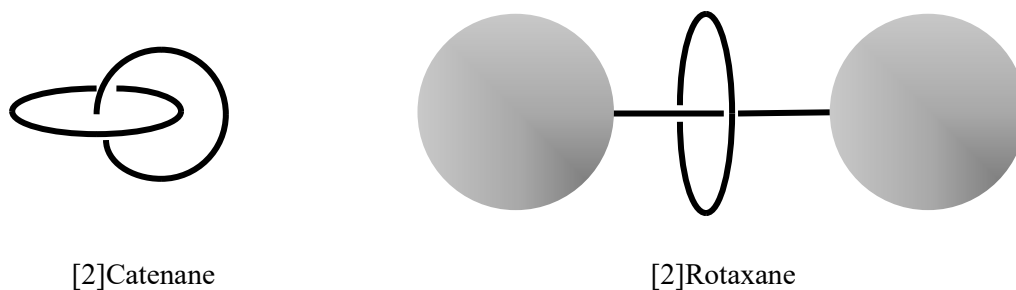


Figure 1.3 Schematic representation of (a) catenane and (b) rotaxane

There is a significant time gap between the initial discovery of cyclodextrin and the extensive investigations into the physical properties of host-guest molecules. One of the reasons is primarily attributed to limitations in the methodology used to study complexes bound by weak interactions and the challenge of eliminating solvent interactions. The development of various soft ionization sources and diverse mass analyzers played a significant role in advancing the fundamental research on complexes that are held together through non-covalent interactions.³³ In this research, electrospray ionization (ESI) coupled with Fourier transform ion cyclotron resonance mass spectrometry (FT-ICR-MS) was employed. The instrumentation will be discussed in section 1.3.

1.2 Hosts and Guests

1.2.1 Host 1: Cyclophanes

Two types of hosts were used in this research. The first are cyclophanes. A cyclophane is a molecule composed of one or more aromatic rings that are fused together to form a cage-like or bridged structure. Cyclophanes can have different sizes and shapes

by manipulating the number of rings, their arrangement, and the bridging units. The unique structures of cyclophanes make them suitable hosts for encapsulating guest molecules within their cavities or outside of the cavity through non-covalent interactions.

In the early 1950s, the term "cyclophane" was first introduced by Donald J. Cram.³⁴ One of the first cyclophanes, [2.2]paracyclophane, was reported by Cram and his team in 1955.³⁵ Two benzene rings are linked by two ethyl bridges, creating a unique cage-like structure as shown in Figure 1.4. When univalent metal cations, such as sodium(I),³⁶ potassium(I),³⁶ silver(I)³⁷ and thallium(I)³⁸ cations interact with [2.2]paracyclophane in the gas phase, the most probable structures are computationally found to be where the metal cations lie outside of the cavity and above one of the benzene rings of [2.2]paracyclophane.

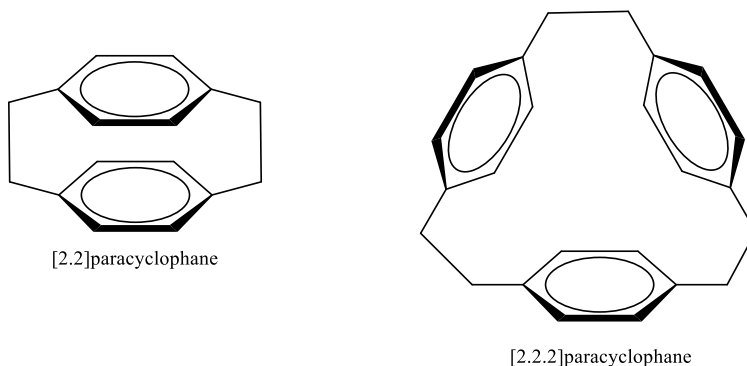


Figure 1.4 Structures of [2.2]paracyclophane and [2.2.2]paracyclophane

This is because the distance between the two benzenes of [2.2]paracyclophane is computed to be 2.99 Å,³⁶ but the ionic diameters of Na⁺, K⁺, Ag⁺ and Tl⁺ are 2.04 Å, 2.76 Å, 2.30 Å and 3.0 Å respectively.³⁹ The diameters of these metal cations are close to or larger than the distance between two benzenes, thus these metal cations do not prefer to occupy the cavity

of [2.2]paracyclophane. However, Li^+ shows preference (by 4.6 kJ mol^{-1}) for binding between the two benzenes of [2.2]paracyclophane compared with sitting outside of one benzene, since the ionic diameter of Li^+ is 1.52 \AA ,³⁹ considerably less than the distance between two benzenes of [2.2]paracyclophane. By changing aliphatic bridges and aromatic systems, different sizes of cavity can be obtained. The structural difference between [3.3]paracyclophane and [2.2]paracyclophane is that two benzene rings are bridged by two propyl groups. In [2.2.2]paracyclophane, three benzene rings are connected by three ethyl bridges (Figure 1.4), the structure of which is more extended than [2.2]paracyclophane owing to the addition of a benzene ring and a ethylene bridge. The distance between two adjacent benzene rings is in the range of 2.98 \AA to 5.77 \AA .⁴⁰ The sizable cavity enables Li^+ ,⁴⁰ Na^{+41} and K^{+42} to occupy the cavity. It is very interesting to investigate the interactions between a diversity of host and guest molecules.

In this research, 1,1,*n,n*-Tetramethyl[*n*](2,11)teropyrenophanes ($n=7, 8, 9$) (TMnTP) are used as hosts and are depicted in Figure 1.5. TMnTP ($n=7, 8, 9$) are cyclophanes that are constructed from a teropyrene and an aliphatic chain with *n* carbons that bridges carbon 2 and 11 of the teropyrene.⁴³ Teropyrene is a bulky non-planar polycyclic aromatic hydrocarbon (PAH) containing 10 fused benzene rings, which can be seen as a segment of armchair Single walled carbon nanotubes (SWCNTs). The differences in the shapes of TMnTP molecules are determined by the length of the bridging aliphatic chain.

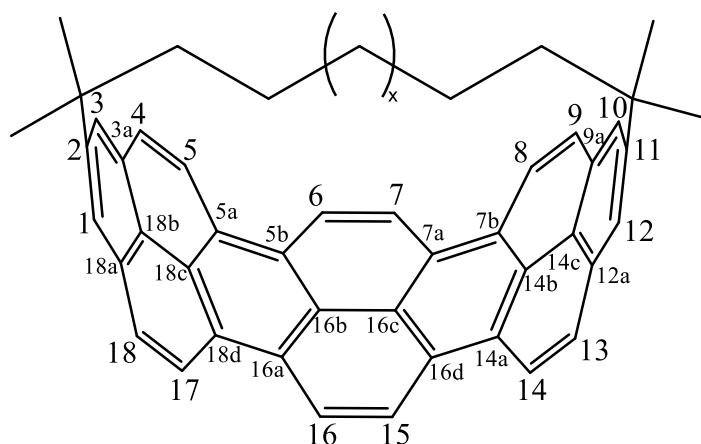


Figure 1.5 Structure of 1,1,n,n-Tetramethyl[n](2,11)teropyrenophane ($x=1, 2, 3, n = 7, 8, 9$) and systematic numbering scheme of aromatic carbons.

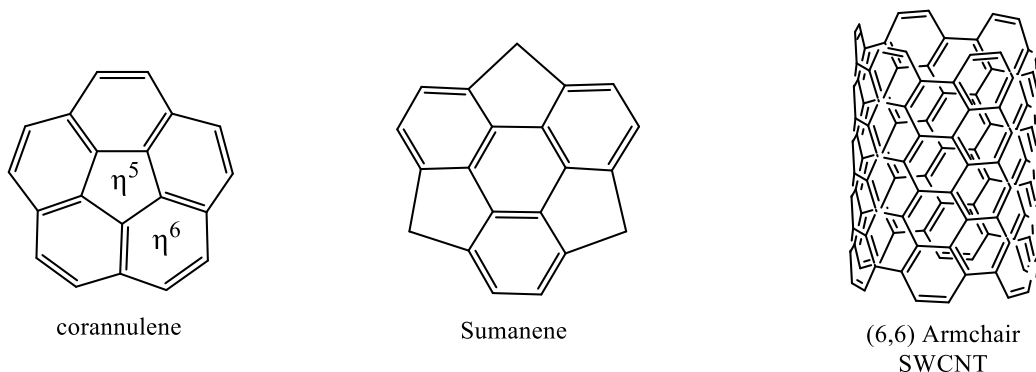


Figure 1.6 Structures of corannulene, sumanene and Armchair SWCNT.

In contrast to planar PAHs, which have a flat, two-dimensional structure, and whose two surfaces are identical, non-planar PAHs or contorted polycyclic aromatics⁴⁴ show unique structures containing different π -faces. Non-planar PAHs, such as bowl-shaped molecules like corannulene or sumanene as displayed in Figure 1.6, can create well-defined three-dimensional cavities or pockets that can serve as host environments for guest

molecules to be encapsulated. Corannulene which consists of a central pentagon and five hexagons has both concave (*endo*) and convex (*exo*) π -surfaces⁴⁵ which allow guests like cations⁴⁶⁻⁴⁹ to bind by cation- π interactions. The nonequivalent concave and convex curved π -surfaces of corannulene impart a dipole moment, and a variety of coordination sites on both sides. Li^+ , Na^+ , and K^+ have a slight preference, of only few kJ mol^{-1} , for the convex surface of corannulene.⁴⁵ Through computational work by Bohme, Li^+ was found to prefer binding in an η^6 site over an η^5 site in corannulene.⁵⁰ However, for Na^+ and K^+ , the η^6 and η^5 site are computed to be equally favored.⁴⁵ Sumanene consists of three benzene rings fused in a triangular arrangement of pentagons. The concave shape of sumanene is deeper than that of corannulene.⁵¹ The mono- alkali metal cationized complexes, coordinated through η^6 bonding on the six-membered rings, exhibit a preference for larger cations such as Na^+ and K^+ to bind on the concave face of the central six-membered ring in sumanene. In contrast, for Li^+ , both faces appear equally probable, albeit with a slight preference for the convex face.⁵²

SWCNTs are cylindrical nanostructures composed entirely of carbon atoms and also contain non-planar π -surfaces.⁵³ SWCNTs are also able to interact with cations through cation- π interactions.⁵⁴ The binding energy between metal cations and carbon nanotubes (CNTs) is influenced by the curvature of the nanotube. Specifically, as the diameter of armchair CNTs increases (resulting in reduced curvature), the computed binding energies of *exo*-alkali metal cations and *exo*-alkaline earth metal cations to the CNTs also increase.⁵⁵ TMnTP, Figure 1.6, can be seen as a segment of armchair SWCNTs.⁴³ Variations in the shapes of TMnTP molecules arise from differences in the length of the connecting aliphatic

chain. It will be very interesting to investigate the structures and non-covalent interactions of alkali metal cationized TMnTP complexes which will be discussed in chapter 2.

1.2.2 Host 2: Ethers

Crown ethers are a family of cyclic polyethers, the structure of which resembles a crown with a cyclic arrangement of ether oxygen atoms forming a ring. The standard formula for crown ethers is $[-(\text{CH}_2)_2-\text{O}-]_m$ ($m = 4-10$), and the ring size is variable. In Figure 1.7 are displayed the structures of three crown ethers: 12-crown-4 (12c4), 15-crown-5 (15c5), and 18-crown-6 (18c6) which have diameters that are 1.2-1.5 Å,⁵⁶ 1.7-2.2 Å,⁵⁷ and 2.6-3.2 Å,⁵⁷ respectively. The circular arrangement of crown ethers enables the creation of thermodynamically stable complexes as they encapsulate metal ions within the ring's cavity. The size of the ring and the number of oxygen atoms of crown ethers make them distinctively capable of selectively forming complexes with metal cations, especially those of alkali and alkaline earth metals.

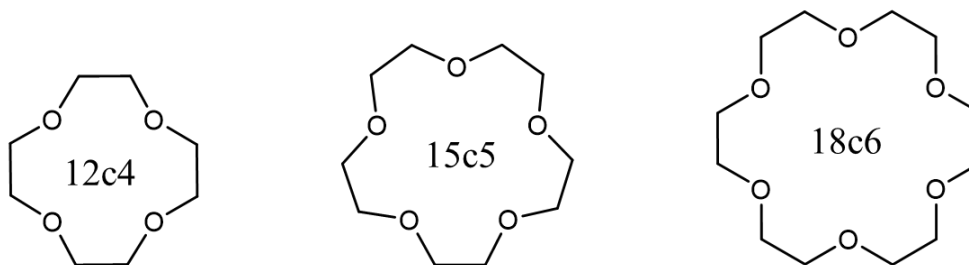


Figure 1.7 Structures of 12-crown-4 (12c4), 15-crown-5 (15c5), and 18-crown-6 (18c6).

One of the most interesting combinations of crown ethers and alkali metal cations is potassiated 18c6, since 18c6 shows a high selectivity towards K^+ in aqueous solution. The experimental selectivity order of 18c6 is $K^+ > Rb^+ > Cs^+ > Na^+ > Li^+$ in aqueous solution.⁵⁸ Brodbelt and coworkers found that the relative experimental stability of gaseous $M^+(18c6)$ follows $Na^+ > K^+ > Li^+ > Cs^+ > Rb^+$ in 1993.⁵⁹ However, in 1999, Armentrout et al. found that the trend of experimental gas-phase stability of 18c6 complexes follows $Na^+ > K^+ > Rb^+ > Cs^+$.⁶⁰ The computed binding ability of 18c6 to alkali metal cations follows the order of $Li^+ > Na^+ > K^+ > Rb^+ > Cs^+$,⁶¹ which is expected for ion-dipole bound complexes. The reason for the difference in the trend of binding between 18c6 and alkali metal cations (M^+) in the gas phase is due to the competition between the solvation of alkali metal cations and the complexation of alkali metal cations/crown ethers.⁶⁰ The larger the difference in the gas phase binding energies between $M^+(18c6)$ ⁶⁰ and $M^+(H_2O)_x$,⁶² the more favorable the $M^+(18c6)$ complex. When $x=1-4$, 18c6 showed selectivity towards Na^+ , followed by K^+ , Rb^+ and Cs^+ , which has the same tendency as the computational and experimental trends in the gas phase. However, when $x=5$, the energy difference of $K^+(18c6)$ and $K^+(H_2O)_5$ is larger than that of $Na^+(18c6)$ and $Na^+(H_2O)_5$, which means K^+ is more favored by 18c6 than Na^+ with the existence of more water molecules. Molecular dynamic simulation studies of $M^+(18c6)$ showed that the selectivity of 18c6 to alkali metal cations follow the trend, $Li^+ \ll Na^+ < K^+ > Rb^+ > Cs^+$.⁶³

An alkali metal cation was both experimentally and computationally found binding with 18c6 the most strongly, followed by 15c5 and 12c4 in the gas phase.^{60,64,65} This is because larger crown ethers have more oxygens to electrostatically interact with the alkali

metal cation, and the larger crown ethers are more flexible so that favorable conformations of alkali metal cationized crown ethers are formed.

The ethers that were used in this study are composed of ortho, meta, or para tetra anisole (TA) substituted anthraquinodimethane (AQ) or o-TAAQ, m-TAAQ and p-TAAQ. Another, b-TAAQ, describes the structure where each of the two ortho-substituted phenoxy groups on the same carbon of anthraquinodimethane are connected by a methylene bridge. The presence of oxygen atoms and aromatic rings in the TAAQs enable them to interact with alkali metal cations (chapter 4) through non-covalent interactions. All four TAAQ are displayed in Figure 1.8.

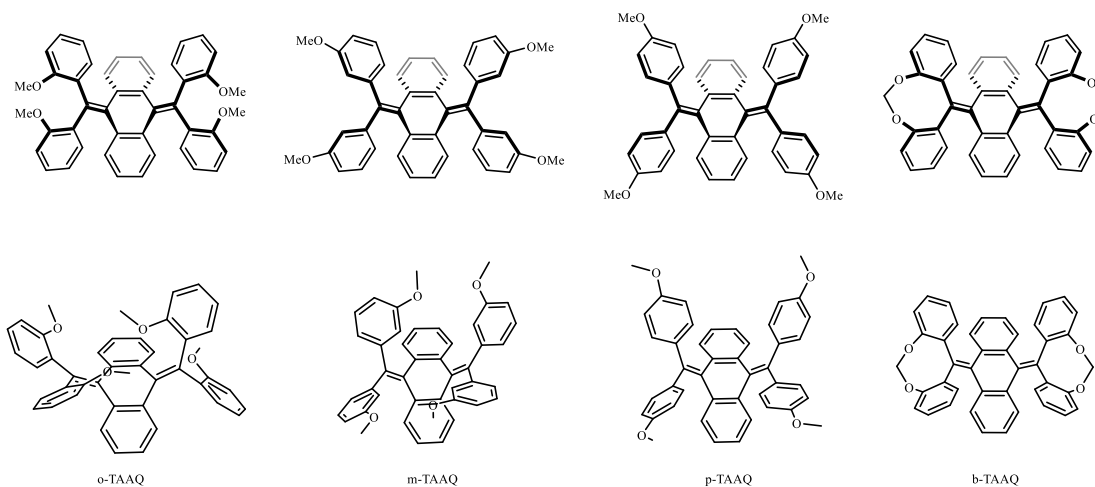


Figure 1.8 Structures of o-TAAQ, m-TAAQ, p-TAAQ and b-TAAQ. Schemes of TAAQs at the bottom are generated from 3-dimensional structures.

1.2.3 Guests

Protonated glycine (GlyH^+) (Figure 1.9) was used as a guest in protonated Gly/TMnTP complexes. Glycine is the simplest of the 20 proteinogenic amino acids. In its

protonated form, glycine binds a proton to the amine group (NH₂) and becomes positively charged. Protonation is an important influencer of chemical properties of biological systems. It can occur in various contexts, including the protonation of amino acids (AAs), proteins, and other biomolecules. Protonation of amino acid residues plays important roles not only on the structures and stabilities of proteins, but also on protein-ligand binding and enzymatic mechanisms.⁶⁶⁻⁶⁸ Protonated glycine, like other protonated molecules, can play a role in supramolecular chemistry through various non-covalent interactions. The interaction strengths of different protonated amino acids with a tri-O-methyl-β-cyclodextrin (TMCD) were explored by Lebrilla and coworkers by recording dissociation temperatures of the protonated AA/TMCD complexes in the gas phase.⁶⁹ The dissociation temperatures of protonated Lys, His, and Arg are relatively larger than other protonated AA/TMCD complexes due to extensive hydrogen bonding between the host and guest. For protonated AAs such as Ile, Val and Leu with large alkyl side chains, the dissociation temperatures of these protonated amino acid/TMCD complexes are small. The destabilization of the host/guest complexes arises from repulsive interactions between the side chain and the inner cavity of TMCD. In this case, the number of hydrogen bonding interactions and TMCD's steric locking ability contributes to the strength of interactions within the host/guest complexes.

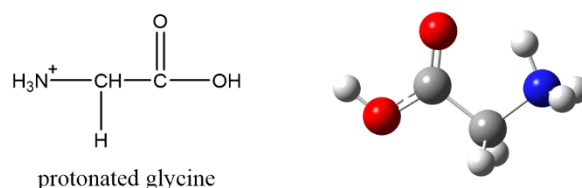


Figure 1.9 The structure of protonated glycine.

Ma and coworkers investigated cucurbit[7]uril (CB7)/ protonated AAs and neutral AA complexes.⁷⁰ They found the inclusion of protonated and neutral amino acids by CB7 yield the most stable structures. The binding strengths of protonated AA/CB7 complexes are larger than the corresponding neutral AA/CB7 complexes, because protonation of the amino acids brings into play stronger ion-dipole and/or ion-induced dipole interactions and stronger ionic hydrogen bonding into the host/guest system. Chapter 3 will discuss the structures and energies of protonated glycine/TMnTP complexes.

1.3 Experimental Methods

Mass spectrometry is a technique that can be used to examine the intrinsic properties of supramolecules held together by non-covalent interactions. The intact complex ions of interest are generated by a soft ionization source and are isolated in the gas phase in a high vacuum reservoir for further tandem mass spectrometry (MS/MS) analysis. In this research, electrospray ionization (ESI) coupled with Fourier transform ion cyclotron resonance mass spectrometer (FT-ICR) as shown in Figure 1.10 is used for experimental studies. With FT-ICR, ions can be trapped for a long period of time to conduct structure-probing experiments. Sustained off-resonance irradiation collision-induced dissociation (SORI-CID), energy resolved-SORI-CID (ER-SORI-CID), blackbody infrared radiative dissociation (BIRD) and infrared multiphoton dissociation (IRMPD) spectroscopy were chosen to study supramolecules in this research. These techniques will be discussed in the following sections.



OPO laser

FT-ICR

ESI

Figure 1.10 The OPO laser/Bruker ApexQe 7 FT-ICR mass spectrometer/Apollo II ESI in the laboratory at Memorial university.

1.3.1 Electrospray Ionization (ESI)

Since many complexes in solution are thermally unstable and not volatile, extraction of these complexes from the liquid phase into the gas phase is necessary. ESI is a soft ionization technique and is a useful method for extracting supramolecules in many cases. The ESI ion source used in this research is shown on the very right in Figure 1.10. Generally, a solution containing the complex precursors is introduced into the ESI ion source in which an electric field is applied to produce a spray of charged liquid droplets, which is then fed into the mass spectrometer. The electrospray process can be divided into three stages: formation of a mist of droplets, droplet shrinkage, and gaseous ion formation. As shown in Figure 1.11 for positive ions, the electrospray ionization capillary maintains a high positive potential with respect to the mass spectrometer entrance, forcing the positive ions to move toward the mass spectrometer entrance. When the electrostatic field is in balance with the surface tension of the solution at the tip of the needle, a Taylor cone is formed,⁷¹ and charged droplets are emitted from the apex of the Taylor cone.⁷² With the aid

of a nebulization gas (i.e. nitrogen), these initial droplets undergo evaporations which lead to their surface area shrinking and the surface charge density increasing. The shrinking of the droplet continues until the repulsive Coulombic forces and the surface tension of the droplet reach the Rayleigh limit,⁷³ and the droplets undergo fission, or a so-called Coulombic explosion.

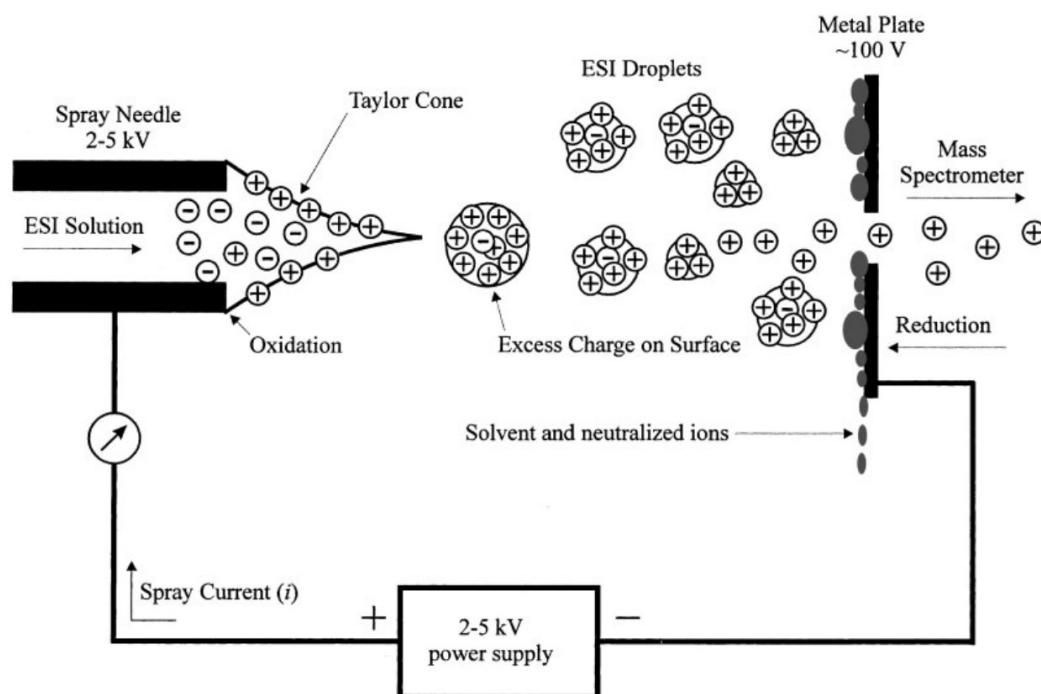


Figure 1.11 Scheme of ESI process. Reprinted with permission from *Mass Spec Rev* 2001, 20: 362–387. Copyright (2001) John Wiley & Sons, Inc.⁷⁴

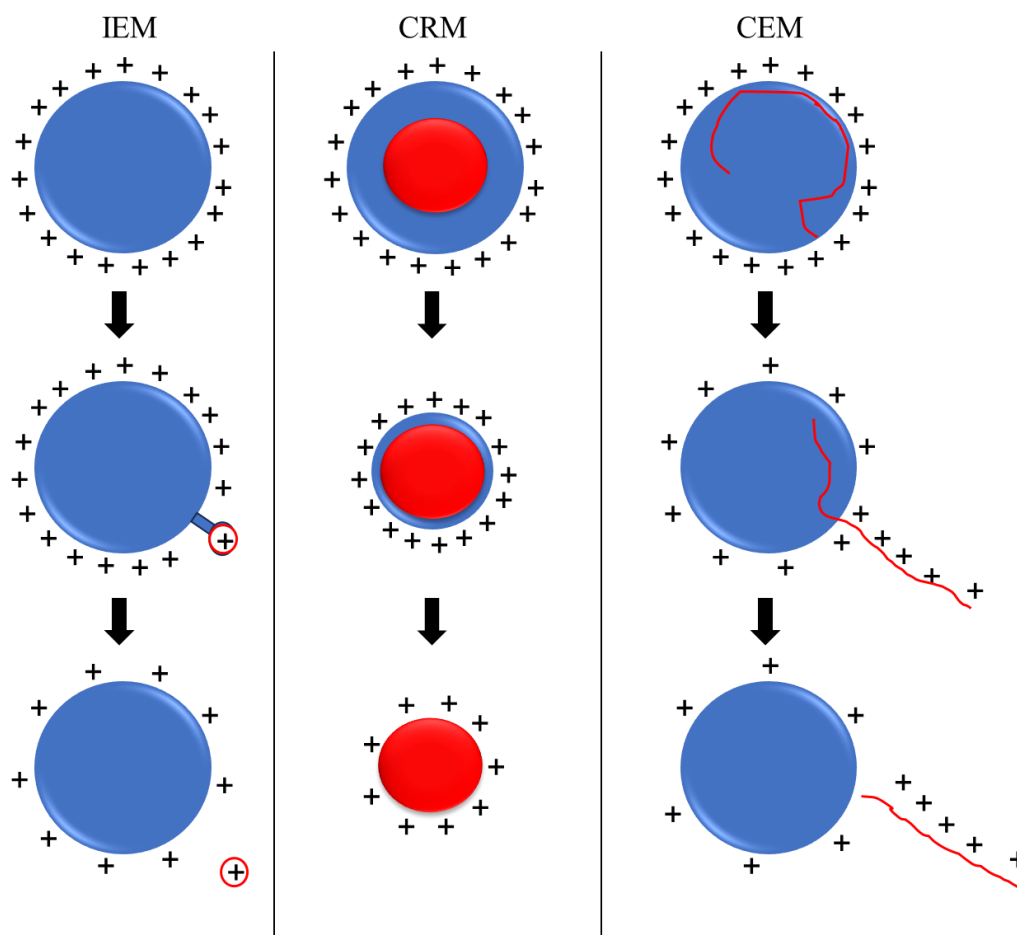


Figure 1.12 Three models of ESI. Adapted with permission from *Anal. Chem.* 2013, 85, 1, 2–9. Copyright (2013) American Chemical Society.⁷⁵

There are three mechanisms (or models) that explain ion formation from the charged droplets as shown in Figure 1.12. In the charge residue model (CRM),⁷⁶ droplets shrink in a process of repeated evaporations until dryness. In the last steps of desolvation, the charge of the solvent shell is transferred to the analyte. The CRM model explains the release of large globular and multi-charged ions into the gas phase. The ion evaporation model (IEM)⁷⁷ is a process by which the charged droplet reaches a size where it cannot support the overall charge and a small singly-charged analyte ion is expelled or evaporated from

the droplet.⁷⁸ The cationized host/guest complexes in my research follow IEM when they undergo ESI. Chain ejection model (CEM) explains the way that unfolded proteins undergo ESI.⁷⁵ In neutral aqueous solution, most proteins are globular folded. By exposing them to acidic environment, these folded proteins are triggered to unfold. The unfolding causes the protein to not be as hydrophilic as it is in aqueous solution. The hydrophobic character make the protein unfavored inside of the Rayleigh-charged nanodroplet. Thus, the unfolded chain of protein migrates to the surface of the droplet and is then expelled, after which stepwise sequential expulsion of protein chains occurs.

ESI is widely used in the mass spectrometric study of proteins^{79,80} and nucleic acids.^{81,82} Although these biopolymers are very large, they can form multiply charged ions which enable further analysis in a mass spectrometer. ESI can also be used to volatilize ionic non-covalent host-guest complexes^{83,84} since it is a soft ionization technique in which very little energy is imparted to the analyte complex.

1.3.2 Fourier Transform Ion Cyclotron Resonance Mass Spectrometry (FT-ICR MS)

The charged ions generated from ESI are transferred into a mass analyzer where ions can be separated based on their mass to charge ratios (m/z). The abundance of the ions is recorded. There are several different types of mass analyzers such as quadrupole mass filter, quadrupole ion trap, time-of-flight analyzer, orbitrap and FT-ICR. FT-ICR offers several advantages over other mass analyzers. FT-ICR MS can provide high mass accuracy (ppm),⁸⁵ which allows confirmation of molecular formulas and identifying unknown compounds. FT-ICR instruments can achieve very high resolving power (above one million), which allows us to distinguish very small differences in the mass of ions. Thus,

FT-ICR can identify isotopic peaks and determine the elemental composition of even very large ions. FT-ICR can handle measurement of ions with a wide m/z range, which allows the identification and structural characterizations of polypeptides, proteins and other biological macromolecules.⁸⁶ Additionally, the high sensitivity of FT-ICR allows detection of ions with low abundance. Most importantly, ions can be trapped in the ICR cell for a long time, allowing further dissociation techniques to be conducted. However, the FT-ICR instrument is very expensive (more than a million dollars), mainly due to the superconducting magnet. The operating costs including liquid helium and nitrogen cryogenics needed by the superconducting magnet are also considerable. The FT-ICR instrument that is used in this research is shown in Figure 1.10.

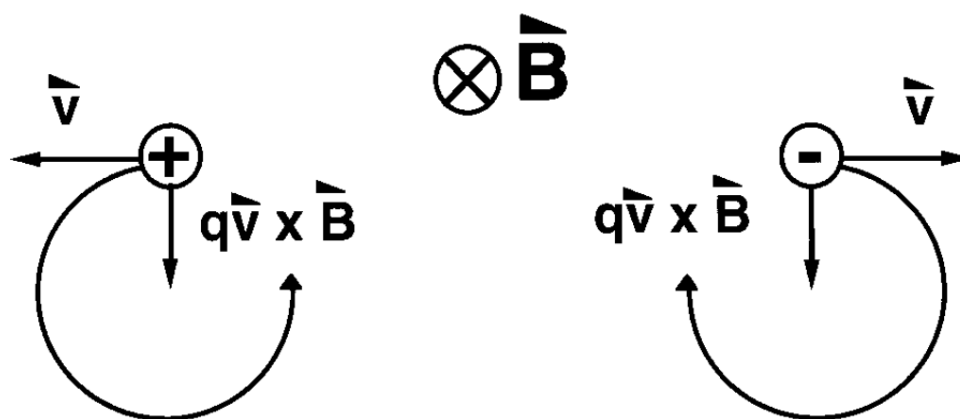


Figure 1.13 Ion motion in a magnetic field. Reprinted with permission from *Mass Spec Rev* 17, 1998, 1–35. Copyright (1998) John Wiley & Sons, Inc.⁸⁷

The application of ICR technology in the field of MS can be traced back to the middle of the 20th century. It was initially mainly applied in the study of ion-molecule

reactions. The principle is based on magnetic field mechanics, in which the mass to charge ratios of different ions are distinguished according to the ICR frequency of ions in the magnetic field.^{88,89} As a result of the Lorentz force, a particle with a charge, q , and mass, m , moving with velocity, v , perpendicular to a uniform magnetic field of strength, B , as shown in Figure 1.13 will undergo circular motion with radius, r , in a plane perpendicular to B . In a stable orbit, the Lorentz magnetic force equals the centrifugal force giving:

$$qvB = m \frac{v^2}{r} \quad \text{Eq 1.1}$$

The relationship between angular velocity (ω_c) and v is given by Eq 1.2. The cyclotron frequency (f_c) of an ion is the frequency of the ion's orbit in the ICR cell, and it is related to ω_c by Eq. 1.3.

$$v = \omega_c r \quad \text{Eq 1.2}$$

$$\omega_c = 2\pi f_c \quad \text{Eq 1.3}$$

Substituting Eq 1.2 and Eq 1.3 into Eq 1.1 and rearranging, the following equation is derived,

$$\frac{m}{q} = \frac{B}{2\pi f_c} = \frac{B}{\omega_c} \quad \text{Eq 1.4}$$

In Eq. 1.4, the unit of cyclotron frequency is Hertz (Hz or s^{-1}), the unit of magnetic field strength is Tesla (T), the unit of mass is kilogram (kg), and the unit of charge is Coulomb (C). A charge q can be expressed as $q=ze$, where z is the charge number and e is elementary charge ($e = 1.6022 \times 10^{-19}$ C). Making this substitution gives Eq. 1.5. To provide a unit of

m/z in g/mol which is numerically equivalent to the Dalton (Da) kg is converted to g by multiplying by 10^3 and then dividing by Avogadro constant $N_A = 6.0221 \times 10^{23} \text{ mol}^{-1}$ the expression of ion m/z in Da is:

$$\frac{m}{z} = \frac{N_A e B}{2000 \pi f_c} = \frac{1.536 \times 10^7 B}{f_c} \quad \text{Eq 1.5}$$

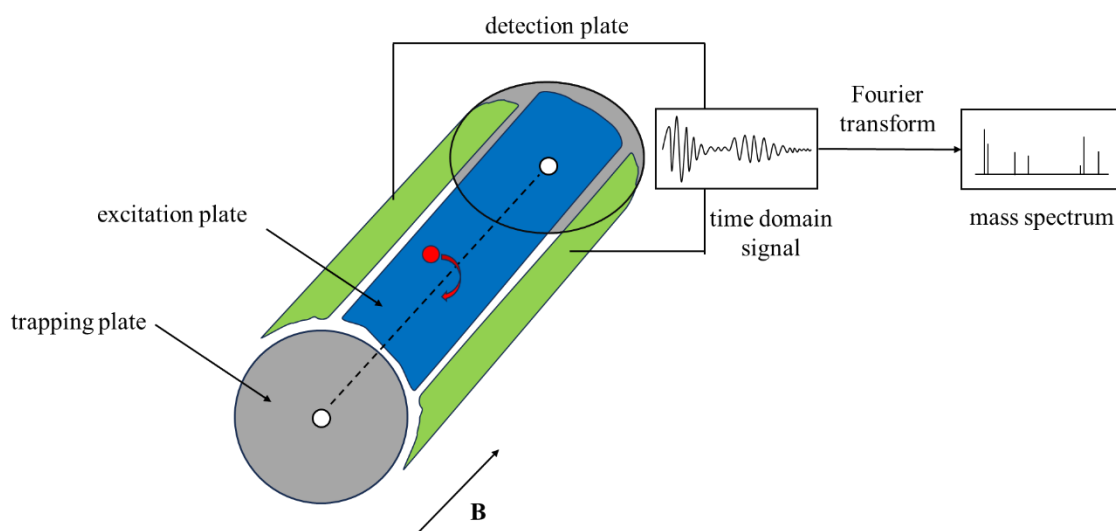


Figure 1.14 Schematic diagram of ion path and detection in FT-ICR.

When ions are initially transferred into the ICR cell, they are distributed around the central axis with only thermal kinetic energy and, therefore, a small cyclotron radius. As shown in Figure 1.14, the ICR cell consists of six plates, two excitation plates, two detection plates, and two trapping plates. The excitation and detection plates are parallel to the direction of the magnetic field, whereas the trapping plates are perpendicular to the direction of B . For detection, it is necessary to bring ions close to the detection plates. To achieve this a radio frequency (rf) sinusoidal signal is applied to the excitation plates. When

the frequency of the applied rf frequency is equal to or resonant with the cyclotron frequency of the ions in the ICR cell, the ions will absorb energy and be translationally excited, as a packet of ions, to a larger cyclotron radius. By scanning the rf frequencies, ions with all m/z values can be excited to a larger radius simultaneously. When the ion packet consisting of ions of a particular m/z passes each detection plate it will produce an image current. This sinusoidal image current is recorded over time and the frequency is equal to the frequency that the ions are passing the detection plates. A time domain spectrum is obtained, and if there are ions with more than one m/z , the time domain spectrum is a superposition of all the sinusoidal image currents of the ions in the ICR cell. The frequency domain signal is obtained by Fourier transformation of the time domain signal. Then the final mass spectrum in m/z can be obtained by Eq 1.5.

To prevent ions escaping along the magnetic field direction, trapping plates with a small direct current are placed at the two ends of excitation and detection plates. There is a hole on each trapping plate, one is for allowing ions being introduced and the other is for introduction of photons.

The FT-ICR MS consists of a superconducting magnet which has a super-strong magnetic field. The magnetic field strength, B , directly determines some of the main performance parameters of the FT-ICR such as mass resolution, mass accuracy, etc. The theoretical mass resolution of FT-ICR MS can be linearly improved by increasing the magnetic field strength.⁹⁰ Mass resolution also decreases with increasing of m/z . In addition, increasing the time of the acquisition cycle in the time domain can significantly improve the resolution of the FT-ICR MS. Comisarow and Marshall achieved mass resolution

analysis of the CH_4^+ ion at 0.005 Da based on their initial experimental design when the magnetic field intensity was only equivalent to 0.32 T.⁹¹ With the continuous development and improvement of FT-ICR MS, magnetic field intensity B, which represents its core performance, has also been significantly improved. For example, 4.7T, 7T and 9.4T correspond to proton Larmor frequencies of 200, 300 and 400MHz, respectively.⁹² Currently, commercial FT-ICR MS are equipped with superconducting magnets of 12T and 15T, but the National High Magnetic Field Laboratory at Florida State University recently reported 21.0 T FT-ICR MS for oil and DOM complex matrix samples.⁸⁵ The development of superconducting magnet technology brings about super strong magnetic field, which further improves the comprehensive analysis performance of FT-ICR MS. While mass resolution is an important aspect of FT-ICR mass spectrometry, it plays little role in the current research.

1.3.3 MS/MS

Ions with a certain m/z value can be selected by exciting and sweeping away all other undesired ions. Then the isolated ions are trapped in the ICR cell to allow further mass spectrometry. This two-step mass spectrometry, MS/MS, provides a way to identify and analyze ionic complexes. A very useful aspect of mass spectrometry is the ability to transfer internal energy to the precursor ion of interest resulting in its fragmentation. Structural information and composition of the precursor ion can be derived by measuring the m/z values of the fragment ions.

1.3.3.1 Sustained Off-Resonance Irradiation Collision Induced Dissociation (SORI-CID)

SORI-CID is a low energy, slow, collisional activation technique that is commonly used in this work in order to decompose precursor ions into fragments to probe their structures or relative binding energies.

In SORI-CID experiments, ions are first isolated and trapped in the ICR cell and accelerated by an rf frequency which is slightly off-resonance from the natural frequency of the cyclotron motion. The off-resonance results in acceleration-deceleration cycles of the ions, so that the ions remain confined in the ICR cell but are translationally excited by the sustained irradiation. By introducing a neutral collision gas (such as Ar), a portion of the translational energy will transfer to the internal energy of the precursor ion. Sustained off-resonance irradiation (SORI) results in 100s or even 1000's of low energy collisions which activate the ions slowly, resulting in the access of low-lying dissociation pathways. Thus, the slow heating dissociation technique is beneficial to study the structural information of ions. The maximum lab frame kinetic energy is given by:

$$E_{\text{lab}}^{\text{max}} = \frac{\beta^2 q^2 V_{\text{p-p}}}{32\pi^2 m d^2 \Delta\vartheta^2} \quad \text{Eq 1.6}$$

where β is the geometrical factor (0.9) and d is the diameter (0.06 m) of the ICR cell, q and m are the charge and mass of the ion of interest, respectively, $\Delta\vartheta$ is the frequency offset (500 Hz), $V_{\text{p-p}}$ is the peak-to-peak excitation voltage whose values are varied. The center of mass energy, $E_{\text{CM}}^{\text{max}}$, is given by the equation:

$$E_{CM}^{\max} = E_{lab}^{\max} \left(\frac{m_g}{m_g + m_p} \right) \quad \text{Eq 1.7}$$

where m_g is the mass of a collisional gas (Argon was used in my studies), and m_p is the mass of a precursor ion.

Energy resolved SORI-CID is performed to compare relative stabilities of ions. The ER-SORI-CID spectra are recorded by varying the V_{p-p} resulting in a range of precursor ion kinetic energies. By plotting the survival yield of a precursor ion as a function of center of mass energy, a sigmoidal-like shape curve is obtained. Relative binding energies of different complexes are compared using the E_{CM}^{\max} at half dissociation.

1.3.3.2 Instruments and Principles of Infrared Multiphoton Dissociation (IRMPD) Spectroscopy

Infrared multiphoton dissociation spectroscopy is a technique in which infrared spectral information of ions can be obtained directly, helping to infer the possible structure of ions. The basic principle of IRMPD is as follows. Following isolation of the ion of interest they are excited by external infrared laser irradiation. If a vibrational mode of the ion is in resonance with the frequency of the laser itself, the ions absorb photons. As shown in Figure 1.15, the process of IRMPD begins with the absorption of a single photon of infrared light, causing a vibrational transition from $\nu = 0$ to 1. Following this vibrational excitation, the redistribution of the energy across other internal states through a very fast process called intramolecular vibrational-energy redistribution (IVR), leaving the $\nu = 0$ to

1 of the absorbing mode available to absorb another photon. Subsequent absorption/IVR relaxation continues until the internal energy of the ion surpasses the dissociation threshold D_0 and the precursor ion undergoes fragmentation.

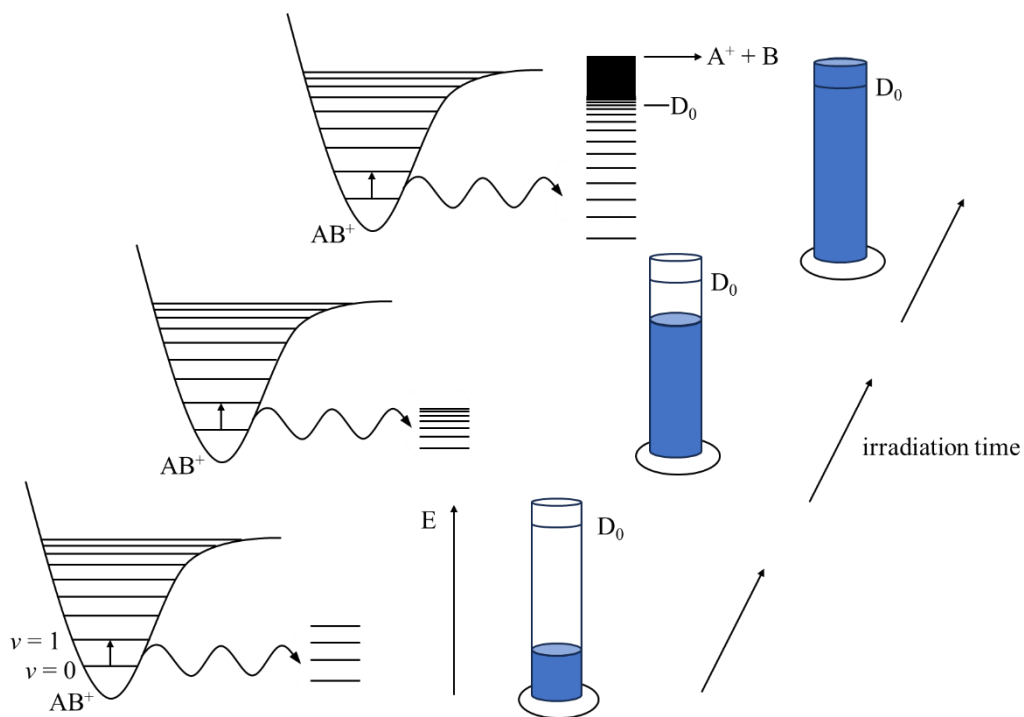


Figure 1.15 Mechanisms of IRMPD process. Adapted with permission from Dr. Travis D. Fridgen (Memorial University).

If a tunable IR laser is used, one can scan across the wavelength range of the laser to see what wavelengths are resonant with vibrational modes of the ion of interest. An IRMPD, or vibrational, spectrum can be obtained by plotting⁹³ the IRMPD efficiency:

$$\text{IRMPD efficiency} = -\log \frac{I_{\text{precursor ions}}}{I_{\text{precursor ions}} + I_{\text{precursor ions+product ions}}} \quad \text{Eq 1.8}$$

against the wavenumber value of the radiation. An example of IRMPD spectroscopy on $\text{Cs}^+(\text{TM9TP})$ complex is illustrated in Figure 1.16. Dissociation of $\text{Cs}^+(\text{TM9TP})$ complex, m/z 763.9, yielding Cs^+ , m/z 133.0, was observed when the laser scans close to 2978 cm^{-1} . This means that the aliphatic C-H stretching has a resonant mode at 2978 cm^{-1} . Figure 1.16 shows a small range of the actual spectrum recorded which was from 3150 cm^{-1} to 2700 cm^{-1} . IRMPD spectra of alkali metal (K, Rb, and Cs) cationized TM9TP will be discussed in chapter 2.

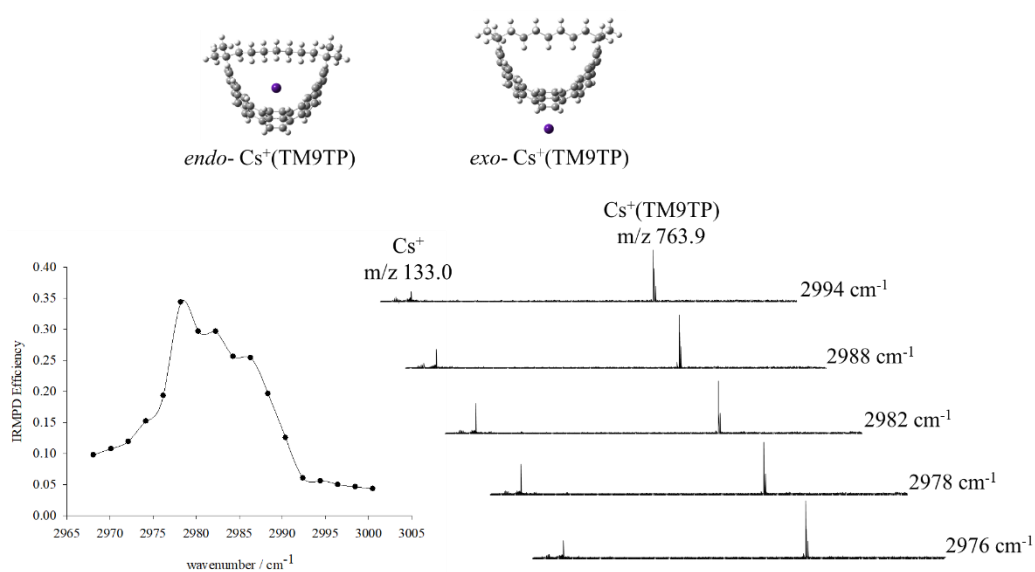


Figure 1.16 Fragmentations of $\text{Cs}^+(\text{TM9TP})$ during IRMPD scan. The band near 2978 cm^{-1} corresponds to aliphatic C-H stretching.

One of the most important parts of IRMPD spectroscopy is the laser source. Typically, vibrational spectra are recorded in the $400\text{--}4000\text{ cm}^{-1}$ to obtain structural

information. In this region, each photon carries roughly between 0.4 and 30 kJ mol⁻¹ of energy, so the absorption of many photons is required to surpass the dissociation threshold. Therefore, the laser source must be intense and tunable.⁹³ There are two different sources of suitable radiation which can be used to conduct IRMPD spectroscopy experiments, one is a free electron laser (FEL), which is a tunable laser with a wide range of wave numbers, mainly producing infrared spectra of 600-2500 cm⁻¹. 600-2500 cm⁻¹ encompassing infrared fingerprint regions that provide characteristic structural information. Another laser source is the optical parametric oscillation/amplifier (OPO/OPA) laser system, which mainly produces infrared spectra in the region of 2500-4000 cm⁻¹. An OPO laser (Figure 1.10) was used in this research at the Laboratory for the Study of Structures, Energetics and Reactions of Gas-Phase Ions at Memorial University of Newfoundland.⁹⁴ A neodymium-doped yttrium aluminium garnet (Nd:YAG) laser pumps light with a wavelength of 1064 nm onto a periodically poled lithium niobate (LiNbO₃) crystal which splits this input light into two beams with frequencies that sum to the input frequency. The beam of light produced in the 2200 – 4700 cm⁻¹ region is used for these experiments. This radiation is directed through a CaF₂ window fit into the ICR cell.

1.3.4 Blackbody Infrared Radiative Dissociation (BIRD)

Blackbody infrared radiative dissociation, BIRD, is another slow activation technique that can be used to obtain kinetic parameters for the dissociation of precursor ions. Temperature-dependent BIRD measurements can lead to dissociation thresholds of weakly-bound complex ions. BIRD is ideally studied in an FT-ICR cell, because the low pressure of the ICR cell minimizes collisions and allows for very long trapping times.

Every object above 0 K emits radiation. At ambient temperature, the FT-ICR cell acts as a black body and emits a broad range of infrared radiation determined by its temperature which can be absorbed by the ions isolated in the cell. Even though the energy of a single blackbody infrared photon is low, absorption of that photon by precursor ions at the high end the Boltzmann internal energy distribution leads to an increased dissociation rate and may be observed on the time scale of the experiment. The mechanism of dissociation can be described as:



where AB^+ is the precursor ion, A^+ and B are dissociation products, $h\nu$ is the energy of the photon in which h is Planck's constant and ν is the frequency of the electromagnetic radiation, k_{abs} is the photon absorption rate constant, k_{em} is the photon emission rate constant and k_d is the unimolecular dissociation rate constant. According to the steady-state approximation, the production of the intermediate in the mechanism, $(AB^+)^*$, is as fast as the consumption of it which can be expressed as

$$\frac{d[(AB^+)^*]}{dt} = 0 \quad \text{Eq 1.10}$$

where t is time and $[(AB^+)^*]$ is the concentration of $(AB^+)^*$. The rate of change in $[(AB^+)^*]$ can also be expressed as

$$\frac{d[(AB^+)^*]}{dt} = k_{abs}[AB^+] - k_{em}[(AB^+)^*] - k_d[(AB^+)^*] \quad \text{Eq 1.11}$$

Setting the expression in Eq 1.11 to 0 as in Eq 1.10 and rearranging yields:

$$k_{\text{abs}}[\text{AB}^+] = k_{\text{em}}[(\text{AB}^+)^*] + k_{\text{d}}[(\text{AB}^+)^*] \quad \text{Eq 1.12}$$

By further rearranging Eq 1.12, $[(\text{AB}^+)^*]$ is expressed as:

$$[(\text{AB}^+)^*] = \frac{k_{\text{abs}}}{k_{\text{em}} + k_{\text{d}}} [\text{AB}^+] \quad \text{Eq 1.13}$$

The overall rate of unimolecular dissociation is the same as the rate of forming product A^+ :

$$\frac{d[\text{A}^+]}{dt} = k_{\text{d}}[(\text{AB}^+)^*] \quad \text{Eq 1.14}$$

Substituting the expression of $[(\text{AB}^+)^*]$ in Eq 1.13 into Eq 1.14 gives:

$$\frac{d[\text{A}^+]}{dt} = \frac{k_{\text{abs}}k_{\text{d}}}{k_{\text{em}} + k_{\text{d}}} [\text{AB}^+] \quad \text{Eq 1.15}$$

Introducing a k_{uni} as the overall rate constant of the overall unimolecular dissociation, the overall rate of this reaction is:

$$\frac{d[\text{A}^+]}{dt} = k_{\text{uni}}[\text{AB}^+] \quad \text{Eq 1.16}$$

The two expressions of the rate of overall unimolecular dissociation in Eq 1.15 and Eq 1.16 are equivalent, thus k_{uni} is:

$$k_{\text{uni}} = \frac{k_{\text{abs}}k_{\text{d}}}{k_{\text{em}} + k_{\text{d}}} \quad \text{Eq 1.17}$$

For large molecules, the rate of emission from $(\text{AB}^+)^*$ is much faster than the dissociation of $(\text{AB}^+)^*$, $k_{\text{em}} \gg k_{\text{d}}$, so the value of k_{d} is negligible in the denominator of Eq 1.17 giving:

$$k_{\text{uni}} = \frac{k_{\text{abs}}k_{\text{d}}}{k_{\text{em}}} \quad \text{Eq 1.18}$$

Furthermore, when the rate of energy exchange between ions and the blackbody environment becomes equal ($k_{\text{abs}}=k_{\text{em}}$), the rapid energy exchange (REX) limit is achieved and the expression of k_{uni} is simplified to:

$$k_{\text{uni}} = k_{\text{d}} \quad \text{Eq 1.19}$$

Under these conditions, the dissociation threshold energy, E_0 , is equal to the experimentally obtained activation energy, E_a .

For small molecules, the dissociation rate constant is much higher than the energy exchange rate constants, and k_{uni} is underestimated, thus E_a underestimates E_0 . To get the true E_0 , a master equation modeling analysis is needed which will be briefly described in section 1.4.4.

For first order dissociation, the kinetics can be expressed by:

$$[I]_t = [I]_0 e^{-k_{\text{uni}}t} \quad \text{Eq 1.18}$$

where $[I]_t$ is the normalized intensity of precursor ion at a variable delay time t , and $[I]_0$ is the normalized initial precursor ion intensity which is unity due to normalization. respectively, k_{uni} is the first-order dissociation rate constant. The Arrhenius equation shows a relationship of rate constants at different temperatures (T) and is expressed as:

$$k_{\text{uni}} = A \exp\left(-\frac{E_a}{k_{\text{B}}T}\right) \quad \text{Eq 1.19}$$

where k_{uni} is the observed rate constant which is shown in Eq 1.17 using the steady state approximation, k_B is the Boltzmann constant, and E_a is the observed activation energy for the dissociation. Taking the natural logarithm of Arrhenius equation yields:

$$\ln(k_{\text{uni}}) = \ln(A) - \frac{E_a}{k_B T} \quad \text{Eq 1.20}$$

Thus, E_a can be obtained from the slope of the Arrhenius plot by performing BIRD experiments at different temperatures. The entropy of activation (ΔS^\ddagger) can be obtained by:

$$\Delta S^\ddagger = \left(\ln(A) - \ln\left(\frac{k_B T}{h}\right) - 1 \right) * R \quad \text{Eq 1.21}$$

where R is the gas constant and h is the Planck constant. BIRD experiments of $M^+(\text{TMnTP})$ and $\text{GlyH}^+(\text{TMnTP})$ will be discussed in chapter 2 and chapter 3 respectively.

1.4 Computational methods

Computational methods are commonly used to complement experimental results allowing us to extract as much information as possible from them, and help verify any conclusions based on our results. A computational method used to model the properties of chemical species consists of a level of theory and a basis set. Basis sets are a set of functions that describe atomic orbitals. In this work, density functional theory (DFT) is combined with the 6-31+g(d,p) basis set on C, H, O, N, Li, Na, K and the Def2SVP basis set on heavier metal atoms such as Rb and Cs. By optimizing chemical structures at a particular level of theory information such as bond lengths and angles, polarity, infrared frequencies, and energies including enthalpies H and Gibbs energies G are obtained at a particular level of theory.

1.4.1 Density Functional Theory (DFT)

Density functional theory is an important quantum mechanical method used in modern computational chemistry to study the electronic structure of atoms, molecules, and complexes. In contrast to the traditional quantum theory in which the Schrödinger equation is solved for each individual electron, DFT simplifies the $3N$ dimensional wave function problem to the three-dimensional particle density problem. DFT significantly simplifies the numerical processing and reduces the cost of computing.

The Thomas-Fermi model, formulated by Llewellyn Hilleth Thomas and Enrico Fermi, describes the electronic structure of atoms in terms of a statistical distribution of electrons and laid the foundation for the development of DFT.⁹⁵ In 1964, Walter Kohn and Pierre Hohenberg formulated the Hohenberg-Kohn theorems, which provided a foundation for DFT.⁹⁶ The theorems demonstrated that the electron density distribution in the non-degenerate ground state determines all the properties of the system. Shortly after the Hohenberg-Kohn theorems, Walter Kohn and his student Lu Jeu Sham, introduced the Kohn-Sham equations in 1965.⁹⁷ These equations reduced the many-body problem to a set of non-interacting particles with an effective potential. Over the following decades, several researchers made contributions to enhancing exchange-correlation functionals, thereby improving the accuracy and versatility of DFT. The widespread acceptance of DFT was further facilitated by the advancement of efficient numerical algorithms and the accessibility of robust computational resources.

There are various classes of DFT calculations, with one of those being a hybrid method in which functionals from other methods are combined, leading to more accurate

results. B3LYP is a hybrid method meaning it combines both Hartree-Fock exchange and DFT exchange-correlation components, where the Becke 3 parameter exchange functional (B3) is combined with the Lee-Yang-Parr correlation functional (LYP).⁹⁶ Grimme's D3 dispersion correction,⁹⁸ a method designed to account for dispersion (van der Waals) interactions in DFT calculations, was added to B3LYP in this research to enhance its accuracy in describing dispersion interactions. The D3 method considers both the attractive and repulsive components of dispersion interactions and is parameterized to be broadly applicable in many cases.

1.4.2 Basis Set

In the field of quantum chemistry and computational chemistry, basis sets are sets of mathematical functions used to approximate the wavefunctions (molecular orbitals) of electrons in a molecule. These functions are typically centered on the atomic nuclei and are used to describe the behavior of electrons around them. The selection of a basis set profoundly influences both the precision and computational costs of quantum chemical calculations. Typically, larger basis sets featuring more functions per atom offer heightened accuracy, albeit demanding greater computational resources. Conversely, smaller basis sets may lead to quicker calculations but could introduce more substantial errors.

Generally, the DFT computations are based on the solution to the Kohn-Sham DFT equation. To solve the Kohn-Sham DFT equation, it is necessary to expand molecular orbitals as linear combinations of single-electron basis functions. Gaussian type orbitals (GTO) can be used as basis functions but pure GTOs do not depict the shape of atomic orbital wavefunctions correctly. GTOs are rounded in the proximity of the nucleus whereas

wavefunction for atomic orbitals are steep near the nucleus. Slater type orbitals (STO) improve on this problem by linearly combining the primitive GTOs. In this research, the 6-31+g(d,p) basis set, is used on C, H, O and N atoms. It is a split valence double-zeta basis set. "6" refers to the number of GTOs that are contracted to STOs as basis functions that are used to describe the inner shell atomic orbitals. The two numbers of "31" means the valence orbitals are double zeta and split into an inner and outer valence region. "3" and "1" in "31" indicates that 3 primitive GTOs of the inner valence region and 1 primitive GTO of the outer valence are used to describe the valence shell orbitals. G(d,p) means that a set of Gaussian d polarization functions are used on heavy atoms and a set of Gaussian p functions is used for each hydrogen atom. Adding "+" to the basis set means adding diffuse functions on heavy atoms. When computing non-covalent interactions, it is necessary to add diffuse functions.⁹⁹ For alkali metal atoms, the def2svp basis set was used in this research. Def2svp belongs to the series of basis sets known as the "def2" family. SVP represents split, valence, and polarized.

1.4.3 Collecting and Processing Data

A structural guess of each host/guest complex was created with Gaussview before being submitted for electronic structure calculation using the Gaussian 16¹⁰⁰ package. Optimized structures, enthalpies, Gibbs energies, vibrational frequencies, and intensities are all computed. $\Delta_{\text{rel}}H$ and $\Delta_{\text{rel}}G$ are relative enthalpies and Gibbs energies to the lowest energy structure. All energies reported are at 298 K and 1 atm.

For a unimolecular decomposition of a host/guest complex ion:



The binding energies (BE) are the $\Delta_{\text{bind}}H$ computed using the following equation:

$$\Delta_{\text{bind}}H = \text{BE} = H_{\text{host}} + H_{\text{guest}^+} - H_{\text{host/guest}^+} \quad \text{Eq 1.25}$$

The Gibbs energies associated with the decomposition of the host/guest complex is computed using a similar equation:

$$\Delta_{\text{bind}}G = G_{\text{host}} + G_{\text{guest}^+} - G_{\text{host/guest}^+} \quad \text{Eq 1.26}$$

1.4.4 Master Equation Modeling (MEM)

The MEM procedure used to obtain experimental E_0 values is the same as that described previously.^{101,102} To determine whether an ion-molecule complex is in the so-called large molecule regime, the number of vibrational degrees of freedom as well as the reaction rate constant and Arrhenius frequency factors must be taken into account.¹⁰³ For complexes in the large molecule regime, the rates of radiation absorption and emission can be much greater than the rate of dissociation. Under the rapid energy exchange limit, also known as the high pressure limit, the internal energy can be described by a Boltzmann distribution at a certain ICR cell temperature. The kinetic and thermodynamic parameters can be obtained directly from BIRD experiments, for example, the threshold dissociation energy E_0 is equal to the observed activation energy E_a^{obs} determined from a BIRD Arrhenius plot. However, for smaller molecules, the dissociation rate constant can be larger than the rate of energy exchange with the surroundings, and therefore there may not be a true Boltzmann distribution of internal energies. In this situation, master equation modeling

(MEM) is used to obtain the true threshold dissociation energy. More detailed information of MEM has been discussed elsewhere.^{104,105} Briefly, a matrix formalism of the MEM was employed.

MEM models the time dependent change in population fraction in an internal energy level. The population fraction consists of the transport matrix that contains the information on absorption, emission and dissociation rate constants which provide the transfer probabilities from one energy state to another. These rate constants are calculated using formulas described in detail in other works.^{106,107} In our work, a 4000 x 4000 matrix with an energy bin of 20 cm⁻¹ was used. BIRD kinetics were simulated by “reacting” a Boltzmann distribution at a given temperature and following its time evolution. The population was allowed to react until a steady state energy distribution was reached. By plotting $\ln\left(\frac{[I]_t}{[I]_0}\right)$ vs. reaction time t , the first order BIRD rate constant can be obtained from the slope, where $[I]_t$ is the population at time t and $[I]_0$ is the initial population. For each host/guest complex, rate constants for the BIRD process were computed at both the highest and lowest temperatures of the experiments, and Arrhenius plots were constructed based on the modeling. The experimental data were then matched with these modeled Arrhenius plots to derive a range of E_0 values that properly reproduce the observed experimental Arrhenius plots. As discussed previously,^{101,102} two requirements are needed to be fulfilled for a good fit to the experimental data to be acceptable: (1) the modeled E_a value determined from the modeled Arrhenius plot was within one standard deviation of the experimental E_a value and (2) the modeled BIRD rate constants were within a factor of two of the experimental rate constants. Uncertainties in the nature of the transition state (TS) were

taken into account by systematically scanning TS frequencies to produce pre-exponential (A) factors corresponding to a range of neutral ($\log(A) = 14$) to loose ($\log(A) = 19$) TSs. E_0 values were varied over the 0.6 – 1.4 eV range in 0.1 eV increments.

For each set of E_0 and $\log(A)$ parameters, the E_a value determined from the modeled Arrhenius plot was compared with the experimental E_a value by calculating the squared difference. This squared difference was plotted as a function of both E_0 and $\log(A)$. We calculated the sum of squared differences of the modeled BIRD rate constants at the highest and lowest temperatures and their respective experimental values. Similarly, the difference was plotted as a function of both E_0 and $\log(A)$.

The range of optimal E_0 values was identified by examining the overlapping region in the two graphs that fulfilled the two fitting criteria mentioned earlier. To address uncertainties in calculated IR intensities, these were adjusted by a factor of 2, both upward and downward, in the ME modeling. The impact of these adjustments on the optimal E_0 values range was also taken into consideration.

1.4.5 Natural Energy Decomposition Analysis (NEDA)

To investigate the nature of the non-covalent interactions within the host/guest complexes, 1.4.5 Natural Energy Decomposition Analysis (NEDA) analysis was used. NEDA partitions the total energy of the interactions into physically understood components: electrostatic (ES), deformation (DEF), polarization (POL), charge transfer (CT), and exchange and correlation (XC).^{108,109}

To better understand these components, charge densities are defined as: $\rho_{A(r)}^0$ representing densities of relaxed monomers, $\rho_{A(r)}$ is the charge density of perturbed monomers, $\rho_{(r)}$ values are a sum of charge densities of perturbed monomers, also known as localized charge densities.

$$\rho_{(r)} = \sum_A \rho_{A(r)} \quad \text{Eq 1.27}$$

$\rho_{\text{tot}(r)}$ representing the total charge densities for the system. The interaction energy of the studied system can be described by:

$$\Delta E = E[\rho_{\text{tot}(r)}] - \sum_A E[\rho_{A(r)}^0] \quad \text{Eq 1.28}$$

The CT component is attributed to delocalization of electrons from occupied orbitals of one fragment to vacant orbitals of another fragment, otherwise known as covalent interactions. CT can be described as the energy difference between total and localized charge densities:

$$\text{CT} = E[\rho_{\text{tot}(r)}] - E[\rho_{(r)}] \quad \text{Eq 1.29}$$

DEF (core repulsion) is the deformation of the wave functions of perturbed fragments compared to that of isolated fragments, and can be described as:

$$\text{DEF}_A = E[\rho_{A(r)}] - E[\rho_{A(r)}^0] \quad \text{Eq 1.30}$$

$$\text{DEF} = \sum_A \text{DEF}_A \quad \text{Eq 1.31}$$

The remaining energy from the total interaction energy losing CT and DEF can be expressed by the sum of ES, POL and XC as shown below:

$$\Delta E - CT - DEF = ES + POL + XC \quad \text{Eq 1.32}$$

Where ES accounts for classical electrostatic interactions between permanent multipoles, POL arises from induced interactions between fragments and XC associates with the exchange and correlation interactions of electrons.

Additionally, the total energy can also be expressed as the sum of electrical interaction (EL), CT and core repulsions (CORE):

$$\Delta E = EL + CT + CORE \quad \text{Eq 1.33}$$

In which EL can be regarded as a sum of ES+POL+SE, where SE is self-polarization, it is an energy penalty for polarization that occurs within the monomer. The CORE component is expressed as:

$$CORE = DEF + XC - SE \quad \text{Eq 1.34}$$

1.4.6 Independent Gradient Model Based on Hirshfeld Partition (IGMH)

To visualize the interactions between hosts and guests, the independent gradient model based on Hirshfeld partition (IGMH) method,^{110,111} which was inspired by the independent gradient model (IGM)¹¹² method is used in this study. The general idea of IGM or IGMH is to use a three-dimensional function, δg , to reveal the regions and strength of intramolecular or intermolecular interactions. In general, the function of δg is expressed as

$$\delta g(\mathbf{r}) = g^{\text{IGM}}(\mathbf{r}) - g(\mathbf{r}) \quad \text{Eq 1.35}$$

where $g(\mathbf{r})$ is the sum of gradient of electron densities and can be expressed as

$$g(\mathbf{r}) = \left| \sum_i \nabla \rho_i^{\text{free}}(\mathbf{r}) \right| \quad \text{Eq 1.36}$$

where \mathbf{r} is the Cartesian coordinate vector, i is the number of all atoms.

The term, g^{IGM} , is the IGM type density gradient which is the sum of absolute values of the density gradients, and can be described as

$$g^{\text{IGM}}(\mathbf{r}) = \sum_i |\nabla \rho_i^{\text{free}}(\mathbf{r})| \quad \text{Eq 1.37}$$

where $\rho_i^{\text{free}}(\mathbf{r})$ represents spherically averaged density of atom i in its free state.

In this research on host-guest complexes, only intermolecular interactions are considered,

$$\delta g^{\text{inter}}(\mathbf{r}) = g^{\text{IGM,inter}}(\mathbf{r}) - g^{\text{inter}}(\mathbf{r}) \quad \text{Eq 1.38}$$

IGM employs the promolecular density approximation to compute electron densities (ED), assuming a spherically symmetric ED for an atom in its free state. In contrast, IGMH utilizes electron density derived from the Hirshfeld partition method based on quantum chemical calculations. Consequently, the difference of IGMH and IGH analyses lies in the fact that δg is determined using the Hirshfeld partition of molecular electron density. Isosurfaces of δg^{inter} are used for visualization of intermolecular interactions of host-guest complexes. Similar to the reduced density gradient (RDG)¹¹³ method, $\text{sign}(\lambda_2)\rho$ is introduced to color both the IGMH isosurface map and IGMH scatter

plot (δg^{inter} vs. $\text{sign}(\lambda_2)\rho$), where $\text{sign}(\lambda_2)$ denotes the sign of the second eigenvalue of the Hessian of the electron density (λ_2) and ρ represents electron density. The sign of λ_2 is used to distinguish the nature of the bond between attractive ($\lambda_2 < 0$) and repulsive ($\lambda_2 > 0$) interactions. When $-0.05 < \text{sign}(\lambda_2)\rho < 0.05$ a.u., this indicates that the intermolecular interactions are weak interactions. The range of $-0.005 < \text{sign}(\lambda_2)\rho < -0.05$ a.u. means stronger attractive noncovalent interactions and $0.005 < \text{sign}(\lambda_2)\rho < 0.05$ a.u. means stronger repulsive noncovalent interactions interaction.¹¹³

1.5 References

1. Villiers, A., Sur la fermentation de la fécule par l'action du ferment butyrique. *Compt. Rend. Acad. Sci* **1891**, 112, 536-538.
2. Szejtli, J., Introduction and general overview of cyclodextrin chemistry. *Chemical Reviews* **1998**, 98 (5), 1743-1754.
3. Freudenberg K., Cramer F., Plieninger H. Ger. Patent 895,769 (1953).
4. Singh, R.; Bharti, N.; Madan, J.; Hiremath, S., Characterization of cyclodextrin inclusion complexes—a review. *Journal of Pharmaceutical Science and Technology* **2010**, 2 (3), 171-183.
5. Zhang, J.; Ma, P. X., Cyclodextrin-based supramolecular systems for drug delivery: recent progress and future perspective. *Advanced Drug Delivery Reviews* **2013**, 65 (9), 1215-1233.
6. Lewis, G. N., The Atom and the Molecule. *Journal of the American Chemical Society* **1916**, 38 (4), 762-785.
7. Pedersen, C. J., Cyclic polyethers and their complexes with metal salts. *Journal of the American Chemical Society* **1967**, 89 (26), 7017-7036.

8. Lehn, J., Cryptates: inclusion complexes of macropolycyclic receptor molecules. In *Chemistry for the Welfare of Mankind*, Elsevier: 1979; pp 871-892.
9. Lehn, J. M., Supramolecular chemistry—scope and perspectives molecules, supermolecules, and molecular devices (Nobel Lecture). *Angewandte Chemie International Edition in English* **1988**, *27* (1), 89-112.
10. Cram, D. J.; Cram, J. M., Host-Guest Chemistry. *Science* **1974**, *183* (4127), 803-809.
11. Zhao, Y.; Wu, Y.; Liu, H.; Chen, S.-L.; Bo, S.-H., Accelerated Growth of Electrically Isolated Lithium Metal during Battery Cycling. *ACS Applied Materials & Interfaces* **2021**, *13* (30), 35750-35758.
12. Varnek, A.; Helissen, S.; Wipff, G.; Collet, A., van der Waals host–guest complexes: Can one predict complexation selectivity of neutral guests by a cryptophane? MD-FEP studies in gas phase and chloroform solution. *Journal of Computational Chemistry* **1998**, *19* (8), 820-832.
13. Rekharsky, M. V.; Inoue, Y., Complexation and chiral recognition thermodynamics of 6-amino-6-deoxy- β -cyclodextrin with anionic, cationic, and neutral chiral guests: counterbalance between van der Waals and coulombic interactions. *Journal of the American Chemical Society* **2002**, *124* (5), 813-826.
14. Park, I. W.; Yoo, J.; Adhikari, S.; Park, J. S.; Sessler, J. L.; Lee, C. H., Calix [4] pyrrole-Based Heteroditopic Ion-Pair Receptor That Displays Anion-Modulated, Cation-Binding Behavior. *Chemistry—A European Journal* **2012**, *18* (47), 15073-15078.
15. Luo, Y.-H.; Ge, S.-W.; Song, W.-T.; Sun, B.-W., Supramolecular assembly and host–guest interaction of crown ether with inorganic acid and organic amine containing carboxyl groups. *New Journal of Chemistry* **2014**, *38* (2), 723-729.
16. Steed, J. W.; Atwood, J. L., *Supramolecular Chemistry*. John Wiley & Sons: 2013.
17. Cram, D. J., The design of molecular hosts, guests, and their complexes (Nobel lecture). *Angew. Chem., Int. Ed. Engl.* **1988**, *27* (8), 1009-1020.

18. Li, W.; Gu, Q.; Su, F.; Sun, Y.; Sun, G.; Ma, S.; Yang, X., Intercalation of Azamacrocyclic Crown Ether into Layered Rare-Earth Hydroxide (LRH): Secondary Host–Guest Reaction and Efficient Heavy Metal Removal. *Inorganic chemistry* **2013**, *52* (24), 14010-14017.
19. Gupta, V. K.; Sethi, B.; Sharma, R.; Agarwal, S.; Bharti, A., Mercury selective potentiometric sensor based on low rim functionalized thiocalix [4]-arene as a cationic receptor. *Journal of Molecular Liquids* **2013**, *177*, 114-118.
20. Yeung, M. C.-L.; Yam, V. W.-W., Luminescent cation sensors: from host–guest chemistry, supramolecular chemistry to reaction-based mechanisms. *Chem. Soc. Rev.* **2015**, *44* (13), 4192-4202.
21. Rodrigo, F.; Gámez, F.; Avilés-Moreno, J. R.; Pedrosa, J. M.; Martínez-Haya, B., Enhanced cation recognition by a macrocyclic ionophore at the air–solution interface probed by mass spectrometry. *Phys. Chem. Chem. Phys.* **2016**, *18* (5), 3497-3503.
22. Kuwabara, T.; Tao, X.; Guo, H.; Katsumata, M.; Kurokawa, H., Monocationic ionophores capable of ion-responsive intramolecular charge transfer absorption variation. *Tetrahedron* **2016**, *72* (8), 1069-1075.
23. Wagner-Wysiecka, E.; Szarmach, M.; Chojnacki, J.; Łukasik, N.; Luboch, E., Cation sensing by diphenyl-azobenzocrowns. *Journal of Photochemistry and Photobiology A: Chemistry* **2017**, *333*, 220-232.
24. Gu, A.; Wheate, N. J., Macrocycles as drug-enhancing excipients in pharmaceutical formulations. *Journal of Inclusion Phenomena Macrocyclic Chemistry* **2021**, *100* (1-2), 55-69.
25. Georgiadis, T.; Markantonis-Kyroudis, S.; Triantafillidis, J., Prokinetic agents: current aspects with focus on cisapride. *Annals of Gastroenterology* **2000**.
26. Al Omari, M. M. H.; Zughul, M. B.; Davies, J. E. D.; Badwan, A. A., Cisapride/ β -cyclodextrin complexation: stability constants, thermodynamics, and guest–host interactions

probed by ¹H-NMR and molecular modeling studies. *Journal of Inclusion Phenomena Macrocyclic Chemistry* **2007**, *57*, 511-517.

27. Allen Jr, L. V.; Erickson III, M. A., Stability of alprazolam, chloroquine phosphate, cisapride, enalapril maleate, and hydralazine hydrochloride in extemporaneously compounded oral liquids. *American journal of health-system pharmacy* **1998**, *55* (18), 1915-1920.

28. Boonleang, J.; Tanthana, C.; Technology, Effect of hydroxypropyl- β -cyclodextrin on the stability of cisapride in oral suspensions. *Sonklanakar Journal of Science* **2010**, *32* (6), 605.

29. Dietrich-Buchecker, C. O.; Sauvage, J. P.; Kintzinger, J. P., Une nouvelle famille de molecules : les metallo-catenanes. *Tetrahedron Letters* **1983**, *24* (46), 5095-5098.

30. Adams, H.; Carver, F. J.; Hunter, C. A., [2] Catenane or not [2] catenane? *Journal of the Chemical Society, Chemical Communications* **1995**, (8), 809-810.

31. Evans, N. H., Recent advances in the synthesis and application of hydrogen bond templated rotaxanes and catenanes. *European Journal of Organic Chemistry* **2019**, *2019* (21), 3320-3343.

32. Anelli, P. L.; Spencer, N.; Stoddart, J. F., A molecular shuttle. *Journal of the American Chemical Society* **1991**, *113* (13), 5131-5133.

33. Baytekin, B.; Baytekin, H. T.; Schalley, C. A., Mass spectrometric studies of non-covalent compounds: why supramolecular chemistry in the gas phase? *Organic Biomolecular Chemistry* **2006**, *4* (15), 2825-2841.

34. Cram, D. J.; Steinberg, H., Macro Rings. I. Preparation and Spectra of the Paracyclophanes. *Journal of the American Chemical Society* **1951**, *73* (12), 5691-5704.

35. Cram, D. J.; Allinger, N. L., Macro Rings. XII. Stereochemical Consequences of Steric Compression in the Smallest Paracyclophane¹. *Journal of the American Chemical Society* **1955**, *77* (23), 6289-6294.

36. Alshamrani, N., Cation- π Interactions of Selected Alkali Metal Ions with Two Benzene Rings Connected through Linear Chains. **2018**. *Atlanta University Center Robert W. Woodruff Library*. 2010/2019, http://hdl.handle.net/20.500.12322/cau.td:2018_alshamrani_nouf.
37. Vaňura, P.; Sýkora, D.; Uhlíková, T., Interaction of the Silver (I) Cation with [2.2] Paracyclophane: Experimental and Theoretical Study. *ChemistrySelect* **2022**, 7 (38), e202203008.
38. Vaňura, P.; Sýkora, D.; Uhlíková, T., Reaction of the thallium(I) cation with [2.2]paracyclophane: Experimental and theoretical study. *Inorganica Chimica Acta* **2022**, 543, 121205.
39. Shannon, R. D., Revised effective ionic radii and systematic studies of interatomic distances in halides and chalcogenides. *Acta crystallographica section A: crystal physics, diffraction, theoretical general crystallography* **1976**, 32 (5), 751-767.
40. Vaňura, P.; Makrlík, E.; Sýkora, D.; Böhm, S., Interaction of the lithium cation with [2.2. 2] paracyclophane: Experimental and theoretical study. *Journal of Molecular Structure* **2021**, 1232, 130026.
41. Makrlík, E.; Sýkora, D.; Böhm, S.; Vaňura, P., Cation- π interaction of the univalent sodium cation with [2.2. 2] paracyclophane: Experimental and theoretical study. *Journal of Molecular Structure* **2018**, 1154, 79-82.
42. Makrlík, E.; Sýkora, D.; Böhm, S.; Vaňura, P., Experimental and Theoretical Study on Cation- π Interaction of the Potassium Cation with [2.2. 2] Paracyclophane. *Journal of Cluster Science* **2018**, 29, 21-25.
43. Merner, B. L.; Unikela, K. S.; Dawe, L. N.; Thompson, D. W.; Bodwell, G. J., 1, 1, n, n-Tetramethyl [n](2, 11) teropyrenophanes (n= 7–9): a series of armchair SWCNT segments. *Chemical Communications* **2013**, 49 (53), 5930-5932.
44. Ball, M.; Zhong, Y.; Wu, Y.; Schenck, C.; Ng, F.; Steigerwald, M.; Xiao, S.; Nuckolls, C., Contorted polycyclic aromatics. *Accounts of Chemical Research* **2015**, 48 (2), 267-276.

45. Dunbar, R. C., Binding of transition-metal ions to curved π surfaces: corannulene and coronene. *The Journal of Physical Chemistry A* **2002**, *106* (42), 9809-9819.
46. Zhao, G.; Zhu, H., Cation- π interactions in graphene-containing systems for water treatment and beyond. *Advanced Materials* **2020**, *32* (22), 1905756.
47. Kumar, K.; Woo, S. M.; Siu, T.; Cortopassi, W. A.; Duarte, F.; Paton, R. S., Cation- π interactions in protein-ligand binding: theory and data-mining reveal different roles for lysine and arginine. *Chemical Science* **2018**, *9* (10), 2655-2665.
48. Priyakumar, U. D.; Sastry, G. N., Cation- π interactions of curved polycyclic systems: M⁺ (M= Li and Na) ion complexation with buckybowls. *Tetrahedron Letters* **2003**, *44* (32), 6043-6046.
49. Vijay, D.; Sakurai, H.; Subramanian, V.; Sastry, G. N., Where to bind in buckybowls? The dilemma of a metal ion. *Physical Chemistry Chemical Physics* **2012**, *14* (9), 3057-3065.
50. Frash, M. V.; Hopkinson, A. C.; Bohme, D. K., Corannulene as a Lewis base: computational modeling of protonation and lithium cation binding. *Journal of the American Chemical Society* **2001**, *123* (27), 6687-6695.
51. Alexander I. Melker, M. A. K., Ruslan M. Zarafutdinov, Sumanene and fullerene C60. *Materials Physics and Mechanics* **2019**, *41*.
52. Rajesh, C.; Majumder, C., Structures and energetics of alkali and alkaline earth metal ion complexes of sumanene and corannulene: A systematic understanding of cation- π interactions. *SMC Bulletin*, 52.
53. Chen, Z.; Thiel, W.; Hirsch, A., Reactivity of the Convex and Concave Surfaces of Single-Walled Carbon Nanotubes (SWCNTs) towards Addition Reactions: Dependence on the Carbon-Atom Pyramidalization. *ChemPhysChem* **2003**, *4* (1), 93-97.
54. Udomvech, A.; Kerdcharoen, T.; Osotchan, T., First principles study of Li and Li⁺ adsorbed on carbon nanotube: Variation of tubule diameter and length. *Chemical Physics Letters* **2005**, *406* (1-3), 161-166.

55. Umadevi, D.; Sastry, G. N., Metal ion binding with carbon nanotubes and graphene: Effect of chirality and curvature. *Chemical Physics Letters* **2012**, *549*, 39-43.
56. Maleknia, S.; Brodbelt, J., Gas-phase selectivities of crown ethers for alkali metal ion complexation. *Journal of the American Chemical Society* **1992**, *114* (11), 4295-4298.
57. Pedersen, C. J.; Frensdorff, H., Macrocyclic polyethers and their complexes. *Angewandte Chemie International Edition in English* **1972**, *11* (1), 16-25.
58. Takeda, Y.; Kawarabayashi, A.; Endo, K.; Yahata, T.; Kudo, Y.; Katsuta, S., Solvent extraction of alkali metal (Li-Cs) picrates with 18-crown-6 into various diluents. Elucidation of fundamental equilibria which govern the extraction-ability and-selectivity. *Analytical sciences* **1998**, *14* (1), 215-223.
59. Brodbelt, J. S.; Liou, C.-C., New frontiers in host-guest chemistry: The gas phase. *Pure applied chemistry* **1993**, *65* (3), 409-414.
60. More, M. B.; Ray, D.; Armentrout, P., Intrinsic affinities of alkali cations for 15-crown-5 and 18-crown-6: bond dissociation energies of gas-phase M^+ crown ether complexes. *Journal of the American Chemical Society* **1999**, *121* (2), 417-423.
61. Glendening, E. D.; Feller, D.; Thompson, M. A., An ab initio investigation of the structure and alkali metal cation selectivity of 18-crown-6. *Journal of the American Chemical Society* **1994**, *116* (23), 10657-10669.
62. Dzidic, I.; Kebarle, P., Hydration of the alkali ions in the gas phase. Enthalpies and entropies of reactions $M^+ (H_2O)^{n-1} + H_2O = M^+ (H_2O)^n$. *The Journal of Physical Chemistry* **1970**, *74* (7), 1466-1474.
63. Jing, Z.; Wang, G.; Zhou, Y.; Pang, D.; Zhu, F.; Liu, H., Selectivity of 18-crown-6 ether to alkali ions by density functional theory and molecular dynamics simulation. *Journal of Molecular Liquids* **2020**, *311*, 113305.

64. Armentrout, P.; Austin, C.; Rodgers, M., Alkali metal cation interactions with 12-crown-4 in the gas phase: Revisited. *International Journal of Mass Spectrometry* **2012**, *330*, 16-26.
65. Armentrout, P.; Austin, C.; Rodgers, M., Alkali metal cation interactions with 15-crown-5 in the gas phase: Revisited. *The Journal of Physical Chemistry A* **2014**, *118* (37), 8088-8097.
66. Di Russo, N. V.; Estrin, D. A.; Martí, M. A.; Roitberg, A. E., pH-dependent conformational changes in proteins and their effect on experimental pK_as: The case of nitrophenol. *PLoS Computational Biology* **2012**, *8* (11).
67. Petukh, M.; Stefl, S.; Alexov, E., The role of protonation states in ligand-receptor recognition and binding. *Current Pharmaceutical Design* **2013**, *19* (23), 4182-4190.
68. Gabas, F.; Di Liberto, G.; Conte, R.; Ceotto, M., Protonated glycine supramolecular systems: the need for quantum dynamics. *Chemical Science* **2018**, *9* (41), 7894-7901.
69. Garcia, B.; Ramirez, J.; Wong, S.; Lebrilla, C. B., Thermal dissociation of protonated cyclodextrin-amino acid complexes in the gas phase. *International Journal of Mass Spectrometry* **2001**, *210*, 215-222.
70. Ma, F.; Zheng, X.; Xie, J.; Li, Z., Binding properties of cucurbit [7] uril to neutral and protonated amino acids: A theoretical study. *International Journal of Quantum Chemistry* **2020**, e26491.
71. Taylor, G. I., Disintegration of water drops in an electric field. *Proceedings of the Royal Society of London. Series A. Mathematical and Physical Sciences* **1964**, *280* (1382), 383-397.
72. Banerjee, S.; Mazumdar, S., Electrospray ionization mass spectrometry: a technique to access the information beyond the molecular weight of the analyte. *International journal of analytical chemistry* **2012**, *2012*.
73. Rayleigh, L., XX. On the equilibrium of liquid conducting masses charged with electricity. *The London, Edinburgh, and Dublin Philosophical Magazine and Journal of Science* **1882**, *14* (87), 184-186.

74. Cech, N. B.; Enke, C. G., Practical implications of some recent studies in electrospray ionization fundamentals. *Mass spectrometry reviews* **2001**, *20* (6), 362-387.
75. Konermann, L.; Ahadi, E.; Rodriguez, A. D.; Vahidi, S., Unraveling the Mechanism of Electrospray Ionization. *Analytical Chemistry* **2013**, *85* (1), 2-9.
76. Dole, M.; Mack, L.; Hines, R.; Mobley, R.; Ferguson, L.; Alice, M. d., Molecular beams of macroions. *J. Chem. Phys.* **1968**, *49* (5), 2240-2249.
77. Iribarne, J.; Thomson, B., On the evaporation of small ions from charged droplets. *J. Chem. Phys.* **1976**, *64* (6), 2287-2294.
78. Wilm, M., Principles of electrospray ionization. *Molecular & Cellular Proteomics* **2011**, *10* (7), M111. 009407.
79. Muneeruddin, K.; Bobst, C.; Frenkel, R.; Houde, D.; Turyan, I.; Sosic, Z.; Kaltashov, I., Characterization of a PEGylated protein therapeutic by ion exchange chromatography with on-line detection by native ESI MS and MS/MS. *Analyst* **2017**.
80. Kitova, E. N.; Yao, Y.; Klassen, J. S., Stabilizing protein-ligand complexes in ESI-MS using solution additives: Comparing the effects of amino acids and imidazole. *Int. J. Mass Spectrom.* **2017**.
81. Fabris, D., A role for the MS analysis of nucleic acids in the post-genomics age. *J. Am. Soc. Mass Spectrom.* **2010**, *21* (1), 1-13.
82. D'Atri, V.; Porrini, M.; Rosu, F.; Gabelica, V., Linking molecular models with ion mobility experiments. Illustration with a rigid nucleic acid structure. *J. Mass Spectrom.* **2015**, *50* (5), 711-726.
83. Wei, W.; Chu, Y.; Wang, R.; He, X.; Ding, C., Quantifying non-covalent binding affinity using mass spectrometry: A systematic study on complexes of cyclodextrins with alkali metal cations. *Rapid Communications in Mass Spectrometry* **2015**, *29* (10), 927-936.

84. Carroy, G.; Lemaire, V.; De Winter, J.; Isaacs, L.; De Pauw, E.; Cornil, J.; Gerbaux, P., Energy-resolved collision-induced dissociation of non-covalent ions: charge-and guest-dependence of decomplexation reaction efficiencies. *Physical Chemistry Chemical Physics* **2016**, *18* (18), 12557-12568.
85. Smith, D. F.; Podgorski, D. C.; Rodgers, R. P.; Blakney, G. T.; Hendrickson, C. L., 21 Tesla FT-ICR Mass Spectrometer for Ultrahigh-Resolution Analysis of Complex Organic Mixtures. *Analytical Chemistry* **2018**, *90* (3), 2041-2047.
86. Yan, J.; Zhou, M.; Gilbert, J. D.; Wolff, J. J.; Somogyi, Á.; Pedder, R. E.; Quintyn, R. S.; Morrison, L. J.; Easterling, M. L.; Paša-Tolić, L.; Wysocki, V. H., Surface-Induced Dissociation of Protein Complexes in a Hybrid Fourier Transform Ion Cyclotron Resonance Mass Spectrometer. *Analytical Chemistry* **2017**, *89* (1), 895-901.
87. Marshall, A. G.; Hendrickson, C. L.; Jackson, G. S., Fourier transform ion cyclotron resonance mass spectrometry: a primer. *Mass Spectrom Rev* **1998**, *17* (1), 1-35.
88. Hipple, J. A.; Sommer, H.; Thomas, H. A., A Precise Method of Determining the Faraday by Magnetic Resonance. *Physical Review* **1949**, *76* (12), 1877-1878.
89. Baldeschiwiler, J. D., Ion Cyclotron Resonance Spectroscopy. *Science* **1968**, *159* (3812), 263-273.
90. Marshall, A. G.; Guan, S., Advantages of High Magnetic Field for Fourier Transform Ion Cyclotron Resonance Mass Spectrometry. *Rapid Communications in Mass Spectrometry* **1996**, *10* (14), 1819-1823.
91. Comisarow, M. B.; Marshall, A. G., Fourier transform ion cyclotron resonance spectroscopy. *Chemical Physics Letters* **1974**, *25* (2), 282-283.
92. Marshall, A. G.; Hendrickson, C. L. J. A. r. o. a. c., High-resolution mass spectrometers. **2008**, *1* (1), 579.

93. Polfer, N. C.; Oomens, J., Reaction products in mass spectrometry elucidated with infrared spectroscopy. *Physical Chemistry Chemical Physics* **2007**, *9* (29), 3804-3817.
94. Fridgen, T. D., Infrared consequence spectroscopy of gaseous protonated and metal ion cationized complexes. *Mass spectrometry reviews* **2009**, *28* (4), 586-607.
95. Zangwill, A., Hartree and Thomas: the forefathers of density functional theory. *Archive for history of exact sciences* **2013**, *67*, 331-348.
96. Stephens, P. J.; Devlin, F. J.; Chabalowski, C. F.; Frisch, M. J., Ab Initio Calculation of Vibrational Absorption and Circular Dichroism Spectra Using Density Functional Force Fields. *The Journal of Physical Chemistry* **1994**, *98* (45), 11623-11627.
97. Kohn, W.; Sham, L. J., Self-Consistent Equations Including Exchange and Correlation Effects. *Physical Review* **1965**, *140* (4A), A1133-A1138.
98. Grimme, S.; Hansen, A.; Brandenburg, J. G.; Bannwarth, C., Dispersion-Corrected Mean-Field Electronic Structure Methods. *Chemical Reviews* **2016**, *116* (9), 5105-5154.
99. Gao, T.; Li, H.; Li, W.; Li, L.; Fang, C.; Li, H.; Hu, L.; Lu, Y.; Su, Z.-M., A machine learning correction for DFT non-covalent interactions based on the S22, S66 and X40 benchmark databases. *Journal of Cheminformatics* **2016**, *8* (1), 24.
100. Frisch, M. J.; Trucks, G. W.; Schlegel, H. B.; Scuseria, G. E.; Robb, M. A.; Cheeseman, J. R.; Scalmani, G.; Barone, V.; Petersson, G. A.; Nakatsuji, H.; Li, X.; Caricato, M.; Marenich, A. V.; Bloino, J.; Janesko, B. G.; Gomperts, R.; Mennucci, B.; Hratchian, H. P.; Ortiz, J. V.; Izmaylov, A. F.; Sonnenberg, J. L.; Williams; Ding, F.; Lipparini, F.; Egidi, F.; Goings, J.; Peng, B.; Petrone, A.; Henderson, T.; Ranasinghe, D.; Zakrzewski, V. G.; Gao, J.; Rega, N.; Zheng, G.; Liang, W.; Hada, M.; Ehara, M.; Toyota, K.; Fukuda, R.; Hasegawa, J.; Ishida, M.; Nakajima, T.; Honda, Y.; Kitao, O.; Nakai, H.; Vreven, T.; Throssell, K.; Montgomery Jr., J. A.; Peralta, J. E.; Ogliaro, F.; Bearpark, M. J.; Heyd, J. J.; Brothers, E. N.; Kudin, K. N.; Staroverov, V. N.; Keith, T. A.; Kobayashi, R.; Normand, J.; Raghavachari, K.; Rendell, A. P.;

Burant, J. C.; Iyengar, S. S.; Tomasi, J.; Cossi, M.; Millam, J. M.; Klene, M.; Adamo, C.; Cammi, R.; Ochterski, J. W.; Martin, R. L.; Morokuma, K.; Farkas, O.; Foresman, J. B.; Fox, D. *J. Gaussian 16 Rev. B.01*, Wallingford, CT, 2016.

101. Gillis, E. A.; Demireva, M.; Sarwar, M. G.; Chudzinski, M. G.; Taylor, M. S.; Williams, E. R.; Fridgen, T. D., Structure and energetics of gas phase halogen-bonding in mono-, bi-, and tri-dentate anion receptors as studied by BIRD. *Physical Chemistry Chemical Physics* **2013**, *15* (20), 7638-7647.

102. Gillis, E. A.; Demireva, M.; Nanda, K.; Beran, G.; Williams, E. R.; Fridgen, T. D., Structures and energetics of electrosprayed uracil n Ca²⁺ clusters (n= 14–4) in the gas phase. *Physical Chemistry Chemical Physics* **2012**, *14* (10), 3304-3315.

103. Dunbar, R. C., BIRD (blackbody infrared radiative dissociation): evolution, principles, and applications. *Mass Spectrometry Reviews* **2004**, *23* (2), 127-158.

104. Price, W. D.; Schnier, P. D.; Williams, E. R. *J. o. P. C. B.*, Binding Energies of the Proton-Bound Amino Acid Dimers Gly⁺Gly, Ala⁺Ala, Gly⁺Ala, and Lys⁺Lys Measured by Blackbody Infrared Radiative Dissociation. **1997**, *101* (4), 664-673.

105. Price, W. D.; Williams, E. R. *J. o. P. C. A.*, Activation of peptide ions by blackbody radiation: factors that lead to dissociation kinetics in the rapid energy exchange limit. **1997**, *101* (47), 8844-8852.

106. Dunbar, R. C., Kinetics of Thermal Unimolecular Dissociation by Ambient Infrared Radiation. *The Journal of Physical Chemistry* **1994**, *98* (35), 8705-8712.

107. Price, W. D.; Schnier, P. D.; Williams, E. R., Binding Energies of the Proton-Bound Amino Acid Dimers Gly·Gly, Ala·Ala, Gly·Ala, and Lys·Lys Measured by Blackbody Infrared Radiative Dissociation. *The Journal of Physical Chemistry B* **1997**, *101* (4), 664-673.

108. Glendening, E. D., Natural energy decomposition analysis: Extension to density functional methods and analysis of cooperative effects in water clusters. *The Journal of Physical Chemistry A* **2005**, *109* (51), 11936-11940.
109. Glendening, E. D.; Streitwieser, A., Natural energy decomposition analysis: An energy partitioning procedure for molecular interactions with application to weak hydrogen bonding, strong ionic, and moderate donor–acceptor interactions. *The Journal of Chemical Physics* **1994**, *100* (4), 2900-2909.
110. Baykov, S. V.; Tarasenko, M. V.; Semenov, A. V.; Katlenok, E. A.; Shetnev, A. A.; Boyarskiy, V. P., Dualism of 1, 2, 4-oxadiazole ring in noncovalent interactions with carboxylic group. *Journal of Molecular Structure* **2022**, *1262*, 132974.
111. Rozhkov, A. V.; Katlenok, E. A.; Zhmykhova, M. V.; Ivanov, A. Y.; Kuznetsov, M. L.; Bokach, N. A.; Kukushkin, V. Y., Metal-Involving Chalcogen Bond. The Case of Platinum (II) Interaction with Se/Te-Based σ -Hole Donors. *Journal of the American Chemical Society* **2021**, *143* (38), 15701-15710.
112. Lefebvre, C.; Rubez, G.; Khartabil, H.; Boisson, J.-C.; Contreras-García, J.; Henon, E., Accurately extracting the signature of intermolecular interactions present in the NCI plot of the reduced density gradient versus electron density. *Physical Chemistry Chemical Physics* **2017**, *19* (27), 17928-17936.
113. Johnson, E. R.; Keinan, S.; Mori-Sánchez, P.; Contreras-García, J.; Cohen, A. J.; Yang, W., Revealing noncovalent interactions. *Journal of the American Chemical Society* **2010**, *132* (18), 6498-6506.

Chapter 2: Endo or Exo? Structures of Gas Phase Alkali Metal Cation/Aromatic Half-Belt Complexes

1,1,9,9-Tetramethyl[9](2,11)teropyrenophane (TM9TP), a belt-shaped molecule, has a sizable cavity that molecules or ions could occupy. In this study, the question of whether TM9TP forms gas phase ion-molecule complexes with metal cations (K^+ , Rb^+ , Cs^+) situated inside or outside the TM9TP cavity was addressed using both experimental and computational methods. Complexes were trapped in a Fourier transform ion cyclotron resonance mass spectrometer and their structures were explored by some novel physical chemistry/mass spectrometry methods. Blackbody infrared radiative dissociation kinetics revealed two populations of ions, a fast-dissociating fraction and a persistent fraction. Infrared multiphoton dissociation spectra (vibrational spectra) provided very strong evidence that the most abundant population is a complex where the metal cation is inside the TM9TP cavity, *endo*-TM9TP. Red-shifted C-H stretching bands revealed in the gas-phase vibrational spectra of these ionic complexes show that there is an interaction between the metal cation and a bridge C-H bond due to the cation sitting inside the cavity of TM9TP. B3LYP/6-31+G(d,p) calculations showed the *endo* complexes to be the lowest in energy and about 50 kJ mol^{-1} more thermodynamically stable and more than 100 kJ mol^{-1} kinetically more stable than the *exo* complexes.

A version of this chapter has been published:

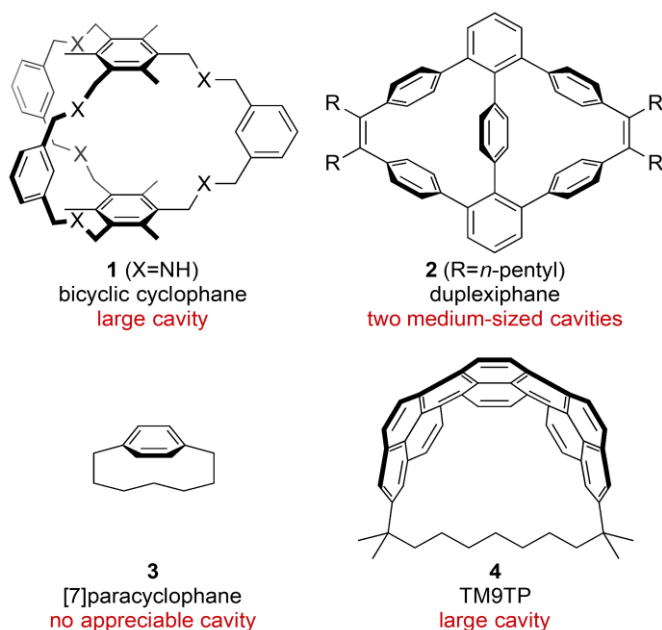
Y. Chen, Y. Jami-Alahmadi, K. S. Unikela, G. J. Bodwell, T. D. Fridgen, *ChemPhysChem* 2018, 19, 2194.

2.1. Introduction

The pioneering work of the 1987 Nobel laureates¹ Pederson,^{2, 3} Lehn⁴⁻⁶ and Cram⁷,⁸ laid much of the groundwork for modern supramolecular chemistry.⁹ A central theme in this area is the formation of host-guest complexes, whereby organic molecules with a cavity of some description can accommodate a guest molecule and/or ion. Not only the shape and size of the cavity, but a variety of non-covalent interactions¹⁰⁻¹⁵ such as hydrogen bonding, electrostatic effects, van der Waals forces, hydrophobic forces, π - π stacking interactions, and cation- π interactions contribute to provide a welcoming and selective environment for guests.¹⁶

Cyclophanes, which can be loosely defined as assemblies of aromatic units and bridging aliphatic units,¹⁷ have played an important role in the development of host-guest chemistry.^{18, 19} From a structural perspective, the aromatic units¹⁷ of a host cyclophane not only provide a degree of rigidity that contributes to the formation of a non-collapsible cavity,²⁰ but also offer π electron clouds that are able to interact with cations, anions and neutral molecules.²¹⁻²³ On the other hand, the bridges provide a degree of flexibility that enables the host some latitude to adjust the dimensions of its cavity in response to a guest. For example, cyclophane **1** (5 aromatic units, 6 bridges; Scheme 2.1) has a cavity that enables it to serve as a host for neutral molecules such as acetone and anions such as $\text{Cl}^- \cdots \text{H}_2\text{O}$, and I^- .²⁴ On the other hand, duplexiphane (**2**) was found to be a suitable host for Ag^+ .²⁵

Until now, all the cyclophanes that have been employed in the context of host-guest chemistry have had more than one aromatic unit and more than one bridge, e.g. **1**. In other words, no $[n]$ cyclophane (1 aromatic unit and 1 bridge) has ever seen application in this area. This is simply because the aromatic systems (usually benzene) that have been used to construct host cyclophanes are far too small to be able to form $[n]$ cyclophanes with an appropriately-sized and sufficiently shape-persistent cavity. For example, [7]paracyclophane (**3**) has no appreciable cavity. Substantially larger $[n]$ paracyclophanes can have significant cavities, but lack shape-persistence. Upon moving to larger aromatic systems, there are very few examples of $[n]$ cyclophanes with arenes larger than pyrene.¹⁷ Indeed, a variety of $[n](2,7)$ pyrenophanes have been synthesized and characterized crystallographically, but none of them has anything more than a very small cavity.²⁶⁻³⁸



Scheme 2.1 Homoditopic hexamino bicyclic cyclophane (**1**), duplexiphane (**2**), [7]paracyclophane (**3**), and TM9TP (**4**).

Teropyrene is the largest aromatic system to have been incorporated into a [n]cyclophane.^{39, 40} A short series, of 1,1,*n,n*-tetramethyl[n](2,11)teropyrenophanes was recently reported, the highest homologue of which is 1,1,9,9-tetramethyl[9](2,11)teropyrenophane (**4**, TM9TP).⁴⁰ TM9TP has a relatively large, roughly semicircular-shaped cavity. A distance of 9.80 Å between the two bridgehead carbon atoms was determined using X-ray crystallography.⁴⁰ As such, a range of molecules or ions could conceivably be hosted by TM9TP.

Host-guest complexes of cyclophanes have been studied almost exclusively in solution.⁴¹⁻⁴⁵ However, in order to explore the fundamental nature and extent of non-covalent interactions between a host and its guest, the effects of solvents should be excluded. This can be accomplished using gas-phase analytical methods. Although mass spectrometry (MS) used to be an unsuitable method for the study of non-covalent complexes, the development of soft ionization techniques has enabled nondestructive ionization of weakly-bound complexes. Consequently, MS investigation of high molecular weight molecules and their non-covalent interactions with molecules and ions has become feasible.^{46, 47} Mass spectrometry has been used to investigate the interaction between halogenated dodecaborate dianions (ie. B₁₂C₁₁₂²⁻) with non-polar aromatic organic host molecules.⁴⁸ Collision induced dissociation of these ions required excitation energies approaching those used to dissociate covalent bonds. The self-assembly of these complexes was explained to be driven by strong dispersion interactions. Infrared multiphoton dissociation (IRMPD) spectroscopy has also been used to determine that crown-ether molecules bind strongly to ions such as H₃O⁺ and NH₄⁺,⁴⁹ diatomic cations such as Zn²⁺

and Cd^{2+} ,⁵⁰ and alkali metal cations.⁵¹ For the alkali metal cations, a size dependence was observed in complex structures where the larger cations sit above the crown ether whereas the crown ether folds to encapsulate the smaller metal cations. We report here the formation and study of gas-phase ion-molecule complexes of TM9TP with the alkali cations, K^+ , Rb^+ , and Cs^+ using Fourier transform ion cyclotron resonance (FT-ICR) MS in conjunction with sustained off-resonance irradiation collision-induced dissociation (SORI-CID), blackbody infrared radiative dissociation (BIRD) kinetics, and IRMPD spectroscopy.

2.2 Methods

2.2.1 Experimental

All experiments were performed using a Bruker ApexQe 7 FT-ICR mass spectrometer in the Laboratory for the Study of Structures, Energetics, and Reactions of Gas-Phase Ions^{52, 53} at Memorial University. The TM9TP used in these experiments was synthesized using a recently reported gram-scale synthesis.⁴⁰ Solutions were prepared by adding 1-2 drops of 50 mM (in 18 M Ω -cm H_2O) metal chloride (KCl , RbCl , or CsCl) solution into a saturated TM9TP/acetonitrile solution. All solutions were injected at the rate of 120 $\mu\text{L h}^{-1}$ into an Apollo II electrospray ionization (ESI) source. Ions were accumulated for between 1.0 s to 3.0 s in the hexapole ion accumulation cell prior to being transferred to the ICR cell. Prior to activation of the $\text{M}(\text{TM9TP})$ ions by SORI-CID, BIRD, or IRMPD, ions with the desirable mass were selected by standard FTICR techniques.

SORI-CID experiments were carried out by increasing the translational energy to a maximum of 1.5 eV (centre of mass) using a 500 Hz offset from the cyclotron frequency,

and pulsing Ar into the ICR cell at a pressure of about 10^{-5} mbar for 250 ms. For BIRD experiments, the FTICR cell was heated to increase the internal energy of the ions by increasing the blackbody radiation field.^{54, 55} The magnet was protected from the heat source using a water-cooled heating jacket on the outside of the ICR cell vacuum tube.⁵⁶ Parent and fragment ion intensities were measured as a function of time.

IRMPD spectroscopy was done with a tunable OPO laser with a bandwidth of 2 cm^{-1} scanned from 2700 cm^{-1} to 3150 cm^{-1} in 2 cm^{-1} steps. Irradiation times were 1 s for $\text{Cs}(\text{TM9TP})^+$ and 2 s for $\text{Rb}(\text{TM9TP})^+$ at each wavelength. The OPO is built around a periodically-poled LiNbO_3 crystal which is pumped by a diode-pumped solid state Nd:YAG laser. The OPO operates at 20 kHz, with a pulse duration of a few nanoseconds and operated with an output power near 1 W at $3\text{ }\mu\text{m}$.

2.2.2 Computational

B3LYP density functional theory was used for all geometry optimizations, frequency calculations, and electrostatic potential maps with the 6-31+g(d,p) basis set on C and H and with the Def2SVP basis set on Rb and Cs using the Gaussian 09 suite of programs and were corrected with the D3 dispersion correction.⁵⁷ Some calculations were repeated with the CAM-B3LYP set of functionals which incorporates a long range correction.⁵⁸ Calculated frequencies of $\text{Rb}(\text{TM9TP})^+$ and $\text{Cs}(\text{TM9TP})^+$ were scaled by 0.948. QST3, a synchronous transit-guided quasi-Newton (STQN) method, was used to search for the transition states from *endo*-M(TM9TP)⁺ (M=K, Rb, and Cs) to *exo*-

M(TM9TP)⁺. Transition states were characterized by an imaginary frequency involving the correct relative atomic motions.

2.2.3 Master Equation Modelling

The master equation is used to simulate energy changes in populations of the internal energy levels of a system over a period of time. A set of coupled linear first-order ordinary differential equations and the radiative absorption, emission, and dissociation rate constants of all state-to-state transitions are used to find the probability of energy transfer between all possible internal energy states. Once a Boltzmann distribution of ion populations and a steady-state is reached, the unimolecular decomposition rate constants can be obtained. To compute the dissociation and radiative rate constants, the computed vibrational frequencies and intensities were used for the *endo* and *exo* complexes. The Arrhenius pre-exponential factors depend on the looseness of the transition states. In the present case the transition states are expected to be medium to loose, i.e. the transition state resembles the complex or, since it is dissociating, the transition state is more loose than the complex. To obtain transition state entropies, ΔS^\ddagger , of between 0 and 50 J K⁻¹ mol⁻¹—neutral to slightly loose—the computed vibrational frequencies of the complex are scaled by a factor less than one. The master equation analysis done here was developed in the Williams lab.⁵⁹

2.3 Results and Discussion

In Figure 2.1 the SORI-CID mass spectra of $\text{K}(\text{TM9TP})^+$, m/z 669; $\text{Rb}(\text{TM9TP})^+$, m/z 715; and $\text{Cs}(\text{TM9TP})^+$, m/z 763, are displayed. These complexes readily dissociate upon collisional activation by losing only the TM9TP, leaving the bare metal cations K^+ , Rb^+ , and Cs^+ at m/z 39, 85, or 133, respectively.

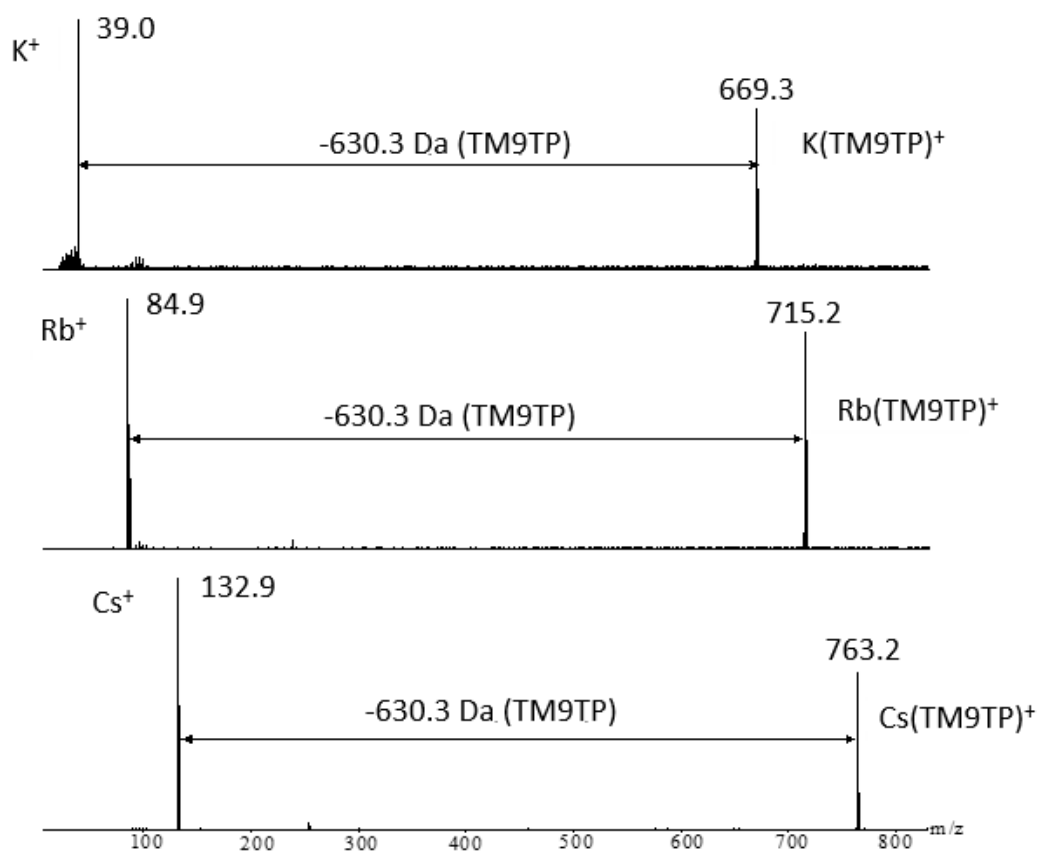


Figure 2.1 SORI-CID mass spectra of potassiated, rubidiated, and cesiated TM9TP complexes.

Relative to SORI-CID, BIRD can be considered a very soft activation technique. Ionic complexes are trapped and stored in the ICR cell ($\sim 10^{-10}$ mbar) and absorb a single ambient blackbody infrared photon from the ICR vacuum chamber. If the complexes are weakly bound, those at the top of the Boltzmann internal energy distribution are observed to dissociate.^{54, 60-62} Since the activation process involves absorption of a photon, the observed kinetics are expected to be first order as in Eq. 1 with I_t and I_0 being the time dependent and initial precursor ion intensities, respectively, k is the first order rate constant and t is time.

$$I_t = I_0 e^{-kt} \quad \text{Eq. 1}$$

In Figure 2.2 the time dependencies of the parent complex ions and their dissociation products (BIRD plots) are presented. It is apparent from the BIRD plots (Fig. 2) that the ion dissociation is not observed to be first order. In fact, the decay can be fitted to a biexponential, two first order dissociations:

$$I_{A,t} + I_{B,t} = I_{A,0} e^{-k_A t} + I_{B,0} e^{-k_B t} \quad \text{Eq. 2}$$

suggesting two distinct populations of ions—one which is weakly bound (A) and undergoes fast BIRD kinetics and a second, significantly more persistent, population of ions (B) which is relatively more strongly bound and is actually not observed to dissociate on the time frame of the experiments, ie. k_B , the first order dissociation rate constant is essentially 0 s^{-1} . For the experiments shown, population A consists of between 5 and 15% of the mixture, depending on the cation. It is likely that initially the percentage of population A is larger,

but that many of them decompose *en route* to the ICR cell from the ion source. It is tantalizing to surmise that populations A and B might be the *exo*-M(TM9TP)⁺ and *endo*-M(TM9TP)⁺ complexes, respectively, as shown in Figure 2.2, but that is merely conjecture at this point.

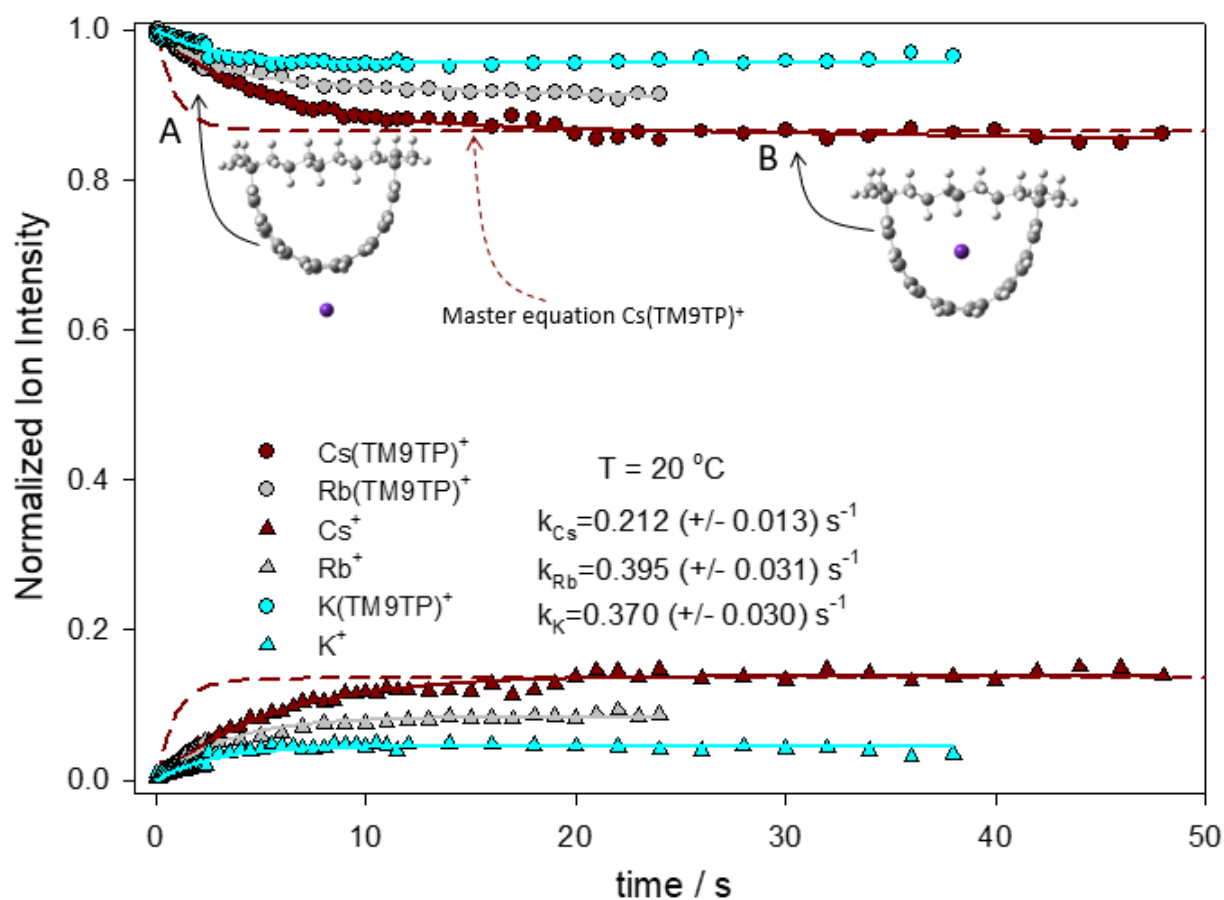


Figure 2.2 Normalized ion intensity vs time plots for BIRD of K(TM9TP)⁺, Rb(TM9TP)⁺, and Cs(TM9TP)⁺. The ICR cell temperature was 20 °C. The dashed red lines are theoretical BIRD plots computed using the master equation.

Electronic structure calculations were conducted and a potential energy diagram for the $\text{Rb}(\text{TM9TP})^+$ complex is shown in Figure 2.3. It was determined that *exo*- $\text{Rb}(\text{TM9TP})^+$ is significantly higher in energy (63 kJ mol^{-1}) than *endo*- $\text{Rb}(\text{TM9TP})^+$, consistent with two populations of ions observed in the BIRD experiments. Furthermore, the *endo* and *exo* complexes are separated by a significant barrier.

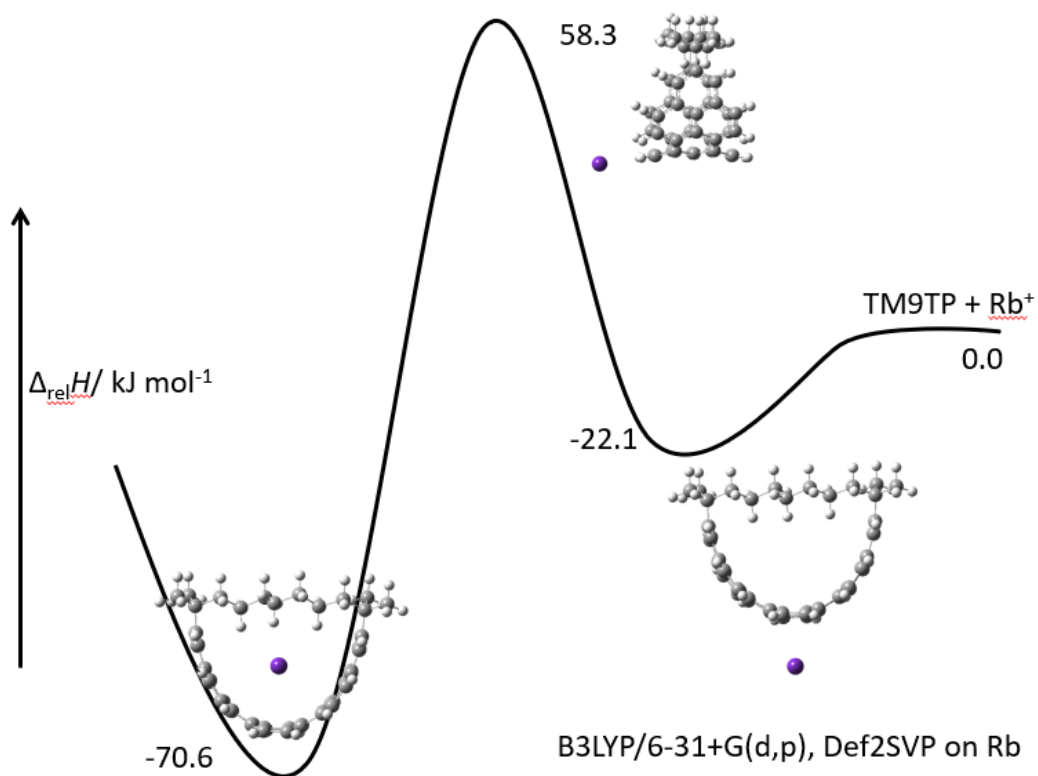


Figure 2.3 B3LYP/6-31+G(d,p), Def2SVP on Rb, computed 298 K enthalpy diagram for the dissociation of *endo*- $\text{Rb}(\text{TM9TP})^+$.

To dissociate, *exo*-Rb(TM9TP)⁺ simply loses TM9TP at a cost of merely 22.1 kJ mol⁻¹. However, the lowest energy route to dissociation for *endo*-Rb(TM9TP)⁺ is through the barrier to the *exo* complex as shown in Figure 2.3, with an activation enthalpy computed to be almost 130.0 kJ mol⁻¹. The results of these calculations are summarized in Table 2.1. To confirm the lowest-energy dissociation pathway, a relaxed potential energy scan was also conducted beginning with *endo*-Rb(TM9TP)⁺ and moving the ion outward from its lowest energy position in the centre of the TM9TP molecule and perpendicular to the plane containing the alkyl bridge. During these potential energy scan calculations, the TM9TP molecule itself was frozen but the position of ion with respect to the TM9TP was relaxed and allowed to optimize independently of TM9TP except for the fixed distance from the centre during each step of the calculation. The results of the scan are provided in Figure A1. These calculations show that the *endo*-Rb(TM9TP)⁺ cation prefers to interact with the aromatic π electrons while dissociating and isomerizes from the *endo* to the *exo* complex prior to dissociation. This makes sense since the cation would be expected to be stabilized by the large electron density of the π system, rather than dissociating through a complex where the cation is interacting with aliphatic C-H groups.

Table 2.1 Computed potential energy surface for the dissociation of $M(\text{TM9TP})^+$. Values are relative 298 K enthalpies computed using B3LYP-D3 (and CAM-B3LYP) with 6-31+G(d,p) basis on C and H, and def2-SVP basis on metal atoms.

| Species | M = K | M = Rb | M = Cs |
|------------------------------------|-------|---------------|--------|
| TM9TP + M ⁺ | 0.0 | 0.0 (0.0) | 0.0 |
| <i>exo</i> -M(TM9TP) ⁺ | -18.0 | -22.1 (5.9) | -13.7 |
| TS- <i>exo-endo</i> | 56.3 | 58.3 | 62.2 |
| <i>endo</i> -M(TM9TP) ⁺ | -74.3 | -70.6 (-57.6) | -68.5 |

The red dashed lines in Figure 2.2 are the master equation simulated BIRD dissociation plots for a population of ions containing 86.5% *endo*-Cs(TM9TP)⁺ and 13.5% *exo*-Cs(TM9TP)⁺ which are determined experimentally. The BIRD dissociation rate constants computed using the master equation were $4.0 \times 10^{-7} \text{ s}^{-1}$ for *endo*-Cs(TM9TP)⁺ and 1.1 s^{-1} for *exo*-Cs(TM9TP)⁺ using dissociation energies of 1.3 and 0.1 eV, respectively, for a neutral transition state (A values of between $10^{16} - 10^{14}$ or ΔS^\ddagger values of between 50 and $10 \text{ J K}^{-1} \text{ mol}^{-1}$). It is clear that *endo*-Cs(TM9TP)⁺, due to its much higher binding energy does not observably dissociate on the timescale of these experiments. Using the master equation modeling a larger dissociation rate constant is computed than observed experimentally (0.2 s^{-1}) for *exo*-Cs(TM9TP)⁺, but still less than an order of magnitude difference. These kinetic modelling results agree with the hypothesis that the fast dissociating population is *exo*-Cs(TM9TP)⁺ and the persistent population is *endo*-Cs(TM9TP)⁺. The very weakly-bound *exo* complexes dissociate rapidly, on the timescale that can be observed in the BIRD experiments. However, the more strongly bound *endo* complex, requiring 130 kJ mol^{-1} to reach the threshold for dissociation, persists and is not observed to dissociate on the timeframe of these experiments. It is not unreasonable to expect such strongly-bound ions as the *endo* $M(\text{TM9TP})^+$ complexes to not dissociate strongly under BIRD conditions. For example the BIRD dissociation rate constants for

complexes such as (dimethylether)₃(H₂O)H⁺ and (H₂O)₄H⁺ were determined to be 9.5x10⁻² and 4.6x10⁻³ s⁻¹, respectively,⁶³ with binding energies of 71⁶⁴ and 73⁶⁵ kJ mol⁻¹, respectively. However, in these cases, the complexes have strongly IR-absorbing functional groups whereas the endo M(TM9TP)⁺ complexes have only aliphatic and aromatic C-C and C-H groups which have far less intense IR absorptions. A comparison of the computed IR spectra for endo-Rb(TM9TP)⁺ and (H₂O)₄H⁺ is provided in Figure A4 and shows that the water complex is far more strongly absorbing in the IR region.

The frequency calculations for the *endo* complexes revealed red-shifted C-H stretching vibrations, with respect to the *exo* complexes (see black traces in Figures 4 and S3) such that it was anticipated that IRMPD spectroscopy (a form of vibrational spectroscopy for gaseous ions)^{52, 53, 66} might be useful to distinguish between the *endo* and *exo* complexes.

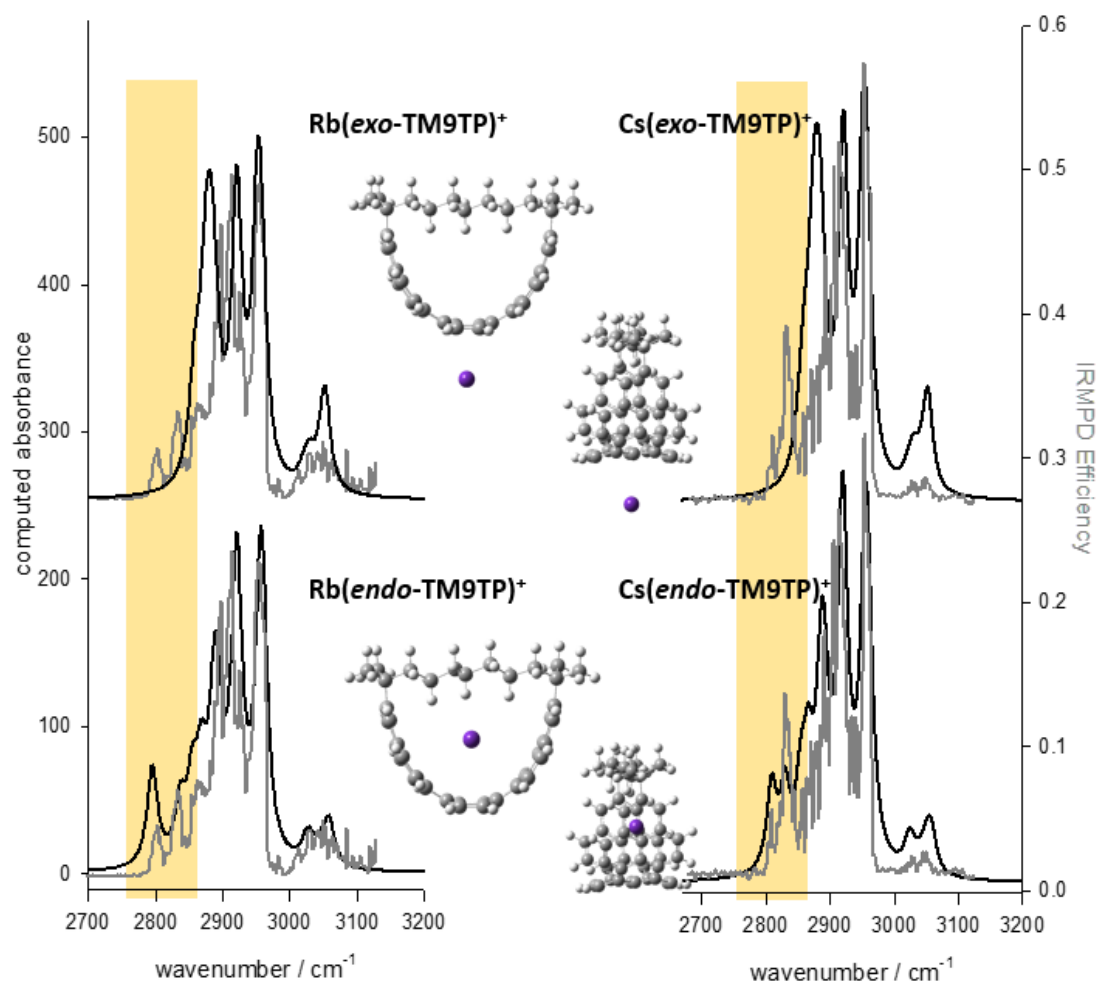


Figure 2.4 Comparison of the IRMPD spectra (grey traces) and computed spectra (black traces) for the $\text{Rb}(\text{TM9TP})^+$ (left) and $\text{Cs}(\text{TM9TP})^+$ (right) complexes in the *exo* (top) and *endo* (bottom) configurations.

The experimental IRMPD spectra of all three complexes are compared in Figure A2 (in Figure 2.4, the spectra for the Rb^+ and Cs^+ complexes are shown (grey traces)). The spectra contain absorptions between 3000 and 3100 cm^{-1} which correspond to the aromatic $\text{C}(\text{sp}^2)\text{-H}$ stretching vibrations as well as strong, sharp absorptions between 2825 and 2950

cm⁻¹ due to the C(sp³)–H bonds of the aliphatic bridge (see Figure A2A for a comparison of all three spectra). Most interestingly, there are sharp absorptions below 2850 cm⁻¹. These red-shifted C–H stretches are assigned to the bridge C(sp³)–H bonds that are interacting with the K⁺, Rb⁺, and Cs⁺ ions. Due to the C–H--M⁺ interaction, the C–H bond is apparently weakened slightly; similar to the weakening of a hydrogen bonded O–H or N–H stretch. This weakening, in turn, causes a significant and clearly measurable red shift in the observed wavenumber position of the stretching vibration. The most red-shifted C–H stretch will be discussed further below.

The experimental IRMPD spectra (grey traces) in Figure 2.4 for Rb(TM9TP)⁺ and Cs(TM9TP)⁺ and in Figure A2 for K(TM9TP)⁺ are compared to the computed IR spectra for the endo and exo complexes. The computed IR spectra for the endo complexes, in fact, agree very well with the experimental IRMPD spectra, including reproducing the red shifted C–H stretches. These bands below 2850 cm⁻¹ are not predicted for the exo complexes.

The most red-shifted absorption belongs to the C–H stretch of the centre-most carbon in the bridge. It is also interesting to compare the position of this feature between the three different complexes. The band position changes from 2786 cm⁻¹ in K(TM9TP)⁺ to 2803 and 2810 cm⁻¹ for the Rb(TM9TP)⁺ and Cs(TM9TP)⁺ complexes, respectively—the smaller, more densely-charged K⁺ interacting with this bridge C–H causes the strongest red shift, followed by Rb⁺ and Cs⁺. This trend is expected if one considers the smaller, more densely charged K⁺ interacts more strongly with the C–H bond, weakening it more with respect to Rb⁺ and Cs⁺ and causing a stronger red-shift. The position of that most red-

shifted C-H stretch is plotted against the ionization energy of the metal in Figure 2.5 and an obvious inverse relationship is seen. Trends such as this, between the wavenumber position of a vibrational mode when it is interacting with another species have been seen before. For example, the hydrogen-bonded O-H⁺-O stretch for mixed protonated dimers was found to be linearly dependent upon the difference in proton affinity between the two monomers.⁶⁷⁻⁶⁹ The position of that band predicted by the electronic structure calculations also shows this trend providing more evidence that the complex observed—the persistent population—is the endo M(TM9TP)⁺.

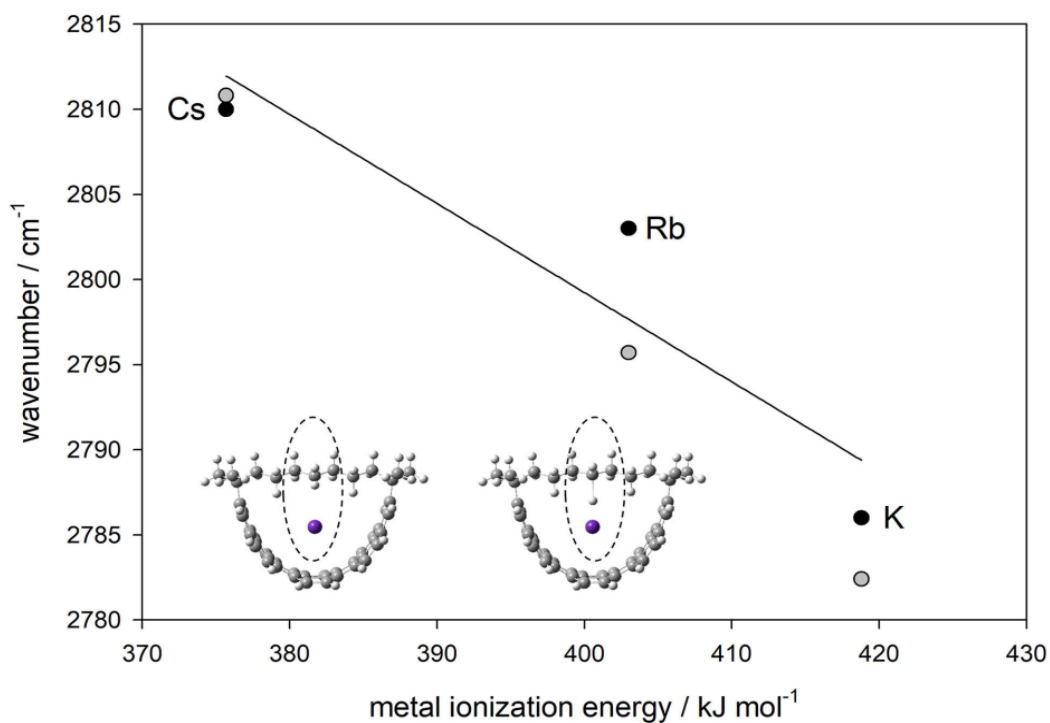


Figure 2.5 A plot of the computed (grey circles) and observed (black circles) central bridge C-H stretch (see inset structures) positions vs the ionization energy of the metal.

The IRMPD spectroscopic data presented here is the first direct evidence for *endo*-ion-molecule complexes in the gas phase, where the host is a non-polar molecule, and shows that the potassium, rubidium, and cesium cations sit inside the TM9TP cavity. The BIRD data clearly shows that two populations of ions are produced. This work shows that the persistent population is the *endo* complex. We can only speculate that population A, the fast-dissociating complex is the weakly-bound *exo* complex where the ion sits outside the cavity, bound to the outer π electron system.

2.4 Conclusions

Blackbody infrared radiative dissociation experiments revealed two populations of ions for K^+ , Rb^+ and Cs^+ complexes with TM9TP, an aromatic half-belt. One population dissociated readily in the ICR cell while the other population persisted for very long times such that no BIRD was even observed. Red-shifted aliphatic C-H stretching absorptions observed in the IRMPD spectra of the persistent population revealed it to be the *endo* complex where the metal cation was inside (*wearing*) the aromatic half-belt. Calculations of the potential energy surface for these ions are consistent with the BIRD active population being the *exo* complexes with a very low dissociation threshold energy while the *endo* complex has a much higher dissociation threshold energy and most likely dissociates through the *exo* complex.

2.5 Acknowledgements

Financial support of this work from the Natural Sciences and Engineering Research Council (NSERC) of Canada (G.J.B., T.D.F.) is gratefully acknowledged. The Canada Foundation for Innovation (CFI), Industrial Research and Innovation Fund (IRIF), and Bruker are gratefully acknowledged for their support of the Laboratory for the Study of Gaseous Ion Structures, Energetics and Reactions (T.D.F.). Computational support from the Atlantic Computational Excellence Network (ACE-NET) and Western Canada Research Grid (West-Grid) is also gratefully acknowledged (T.D.F.). Y. Chen also extends gratitude to the China

Scholarship Council. B. Linford is acknowledged for his technical help at the beginning of the research.

2.6 References

1. Zhao, Y.; Wu, Y.; Liu, H.; Chen, S.-L.; Bo, S.-H., Accelerated Growth of Electrically Isolated Lithium Metal during Battery Cycling. *ACS Applied Materials & Interfaces* **2021**, *13* (30), 35750-35758.
2. Gokel, G. W.; Leevy, W. M.; Weber, M. E., Crown ethers: sensors for ions and molecular scaffolds for materials and biological models. *Chem. Rev.* **2004**, *104* (5), 2723-2750.
3. Pedersen, C. J., The discovery of crown ethers (Nobel Lecture). *Angew. Chem., Int. Ed. Engl.* **1988**, *27* (8), 1021-1027.
4. Gazit, E., Self-assembled peptide nanostructures: the design of molecular building blocks and their technological utilization. *Chem. Soc. Rev.* **2007**, *36* (8), 1263-1269.
5. Lehn, J. M., Supramolecular chemistry—scope and perspectives molecules, supermolecules, and molecular devices (Nobel Lecture). *Angew. Chem., Int. Ed. Engl.* **1988**, *27* (1), 89-112.
6. Mahdizadeh, S.; Rounaghi, G.; Mohajeri, M.; Karimian, F., Study of Complex Formation between Kryptofix 21 with La³⁺. *Russ. J. Inorg. Chem.* **2016**, *61* (6), 791-798.
7. Cram, D. J., The design of molecular hosts, guests, and their complexes (Nobel lecture). *Angew. Chem., Int. Ed. Engl.* **1988**, *27* (8), 1009-1020.
8. Paik, M.-J.; Kang, J. S.; Huang, B.-S.; Carey, J. R.; Lee, W., Development and application of chiral crown ethers as selectors for chiral separation in high-performance liquid chromatography and nuclear magnetic resonance spectroscopy. *J. Chromatogr. A* **2013**, *1274*, 1-5.

9. Atwood, J. L.; Steed, J. W., *Encyclopedia of Supramolecular Chemistry*. CRC Press: 2004; Vol. 1, p 261.
10. Yuan, Y.; Gao, G.; Jiang, Z.-L.; You, J.-S.; Zhou, Z.-Y.; Yuan, D.-Q.; Xie, R.-G., Synthesis and selective anion recognition of imidazolium cyclophanes. *Tetrahedron* **2002**, *58* (44), 8993-8999.
11. Kano, K.; Hayakawa, T.; Hashimoto, S., Strong van der Waals interactions in water. Molecular complexes of porphyrins and quinones in organic and aqueous media. *Bull. Chem. Soc. Jpn.* **1991**, *64* (3), 778-784.
12. Cooke, G.; Rotello, V. M., Methods of modulating hydrogen bonded interactions in synthetic host-guest systems. *Chem. Soc. Rev.* **2002**, *31* (5), 275-286.
13. Biedermann, F.; Nau, W. M.; Schneider, H. J., The Hydrophobic Effect Revisited—Studies with Supramolecular Complexes Imply High-Energy Water as a Noncovalent Driving Force. *Angew. Chem., Int. Ed.* **2014**, *53* (42), 11158-11171.
14. Meyer, E. A.; Castellano, R. K.; Diederich, F., Interactions with aromatic rings in chemical and biological recognition. *Angew. Chem., Int. Ed.* **2003**, *42* (11), 1210-1250.
15. Dougherty, D. A., The cation- π interaction. *Acc. Chem. Res.* **2012**, *46* (4), 885-893.
16. Diederich, F.; Stang, P. J.; Tykwinski, R. R., *Modern Supramolecular Chemistry: Strategies for Macrocyclic Synthesis*. John Wiley & Sons: 2008; p XIII.
17. Ghasemabadi, P. G.; Yao, T.; Bodwell, G. J., Cyclophanes containing large polycyclic aromatic hydrocarbons. *Chem. Soc. Rev.* **2015**, *44* (18), 6494-6518.
18. Diederich, F., *Cyclophanes*. Royal society of chemistry: London, UK: 1991.
19. Pochorovski, I.; Diederich, F., Fluorophore-Functionalized and Top-Covered Resorcin [4] arene Cavitands. *Isr. J. Chem.* **2012**, *52* (1-2), 20-29.
20. Rajakumar, P.; Srisailas, M., Synthesis of bicyclic cyclophanes with chiral cages by sixfold coupling. *Tetrahedron Lett.* **2002**, *43* (10), 1909-1913.

21. Bartoli, S.; Roelens, S., Binding of acetylcholine and tetramethylammonium to a cyclophane receptor: Anion's contribution to the cation- π interaction. *J. Am. Chem. Soc.* **2002**, *124* (28), 8307-8315.
22. Yoon, J.; Kim, S. K.; Singh, N. J.; Kim, K. S., Imidazolium receptors for the recognition of anions. *Chem. Soc. Rev.* **2006**, *35* (4), 355-360.
23. Li, C., Pillararene-based supramolecular polymers: from molecular recognition to polymeric aggregates. *Chem. Commun.* **2014**, *50* (83), 12420-12433.
24. Arunachalam, M.; Ravikumar, I.; Ghosh, P., A New Hexaaza Bicyclic Cyclophane with Dual Binding Sites. *J. Org. Chem.* **2008**, *73* (22), 9144-9147.
25. Emond, S. J.; Debroy, P.; Rathore, R., Duplexiphane: A Polyaromatic Receptor Containing Two Adjoined Δ -Shaped Cavities for an Efficient Hopping of a Single Silver Cation. *Org. Lett.* **2008**, *10* (3), 389-392.
26. Bodwell, G. J.; Bridson, J. N.; Houghton, T. J.; Kennedy, J. W.; Mannion, M. R., Dioxo [8](2, 7) pyrenophan, ein stark verzerrter, polycyclischer, aromatischer Kohlenwasserstoff. *Angew. Chem.* **1996**, *108* (12), 1418-1420.
27. Bodwell, G. J.; Bridson, J. N.; Houghton, T. J.; Kennedy, J. W.; Mannion, M. R., 1, 8-Dioxo [8](2, 7) pyrenophane, a Severely Distorted Polycyclic Aromatic Hydrocarbon. *Angew. Chem., Int. Ed. Engl.* **1996**, *35* (12), 1320-1321.
28. Bodwell, G. J.; Bridson, J. N.; Houghton, T. J.; Kennedy, J. W.; Mannion, M. R., 1, 7-Dioxo [7](2, 7) pyrenophane: The Pyrene Moiety Is More Bent than That of C70. *Chem. - Eur. J.* **1999**, *5* (6), 1823-1827.
29. Bodwell, G. J.; Fleming, J. J.; Mannion, M. R.; Miller, D. O., Nonplanar aromatic compounds. 3. A proposed new strategy for the synthesis of buckybowls. Synthesis, structure and reactions of [7]-, [8]- and [9](2, 7) pyrenophanes. *J. Org. Chem.* **2000**, *65* (17), 5360-5370.

30. Bodwell, G. J.; Fleming, J. J.; Miller, D. O., Non-planar aromatic compounds. Part 4: Fine tuning the degree of bend in the pyrene moiety of [7](2, 7) pyrenophanes by modifying the nature of the bridge. *Tetrahedron* **2001**, *57* (17), 3577-3585.
31. Bodwell, G. J.; Miller, D. O.; Vermeij, R. J., Nonplanar aromatic compounds. 6.[2] Paracyclo [2](2, 7) pyrenophane. A novel strained cyclophane and a first step on the road to a "Vögtle" Belt. *Org. Lett.* **2001**, *3* (13), 2093-2096.
32. Bodwell, G. J.; Bridson, J. N.; Cyrański, M. K.; Kennedy, J. W.; Krygowski, T. M.; Mannion, M. R.; Miller, D. O., Nonplanar Aromatic Compounds. 8.1 Synthesis, Crystal Structures, and Aromaticity Investigations of the 1, n-Dioxa [n](2, 7) pyrenophanes. How Does Bending Affect the Cyclic π -Electron Delocalization of the Pyrene System? *J. Org. Chem.* **2003**, *68* (6), 2089-2098.
33. Zhang, B.; Manning, G. P.; Dobrowolski, M. A.; Cyranski, M. K.; Bodwell, G. J., Nonplanar aromatic compounds. 9. Synthesis, structure, and aromaticity of 1: 2, 13: 14-dibenzo [2] paracyclo [2](2, 7)-pyrenophane-1, 13-diene. *Org. Lett.* **2008**, *10* (2), 273-276.
34. Dobrowolski, M. A.; Cyrański, M. K.; Merner, B. L.; Bodwell, G. J.; Wu, J. I.; Schleyer, P. v. R., Interplay of π -Electron Delocalization and Strain in [n](2, 7) Pyrenophanes. *J. Org. Chem.* **2008**, *73* (20), 8001-8009.
35. Vermeij, R. J.; Miller, D. O.; Dawe, L. N.; Aprahamian, I.; Sheradsky, T.; Rabinovitz, M.; Bodwell, G. J., Mixed [2.2] Cyclophanes of Pyrene and Benzene. *Aust. J. Chem.* **2010**, *63* (12), 1703-1716.
36. Yang, Y.; Mannion, M. R.; Dawe, L. N.; Kraml, C. M.; Pascal Jr, R. A.; Bodwell, G. J., Synthesis, Crystal Structure, and Resolution of [10](1, 6) Pyrenophane: An Inherently Chiral [n] Cyclophane. *J. Org. Chem.* **2011**, *77* (1), 57-67.
37. Kahl, P.; Wagner, J. P.; Balestrieri, C.; Becker, J.; Hausmann, H.; Bodwell, G. J.; Schreiner, P. R., [2](1, 3) Adamantano [2](2, 7) pyrenophane: A Hydrocarbon with a Large Dipole Moment. *Angew. Chem.* **2016**, *128* (32), 9423-9427.

38. Zhang, B.; Zhao, Y.; Bodwell, G. J., Kinetic Stabilization of a Highly Bent Pyrene System. *Synlett* **2016**, *27* (14), 2113-2116.
39. Merner, B. L.; Dawe, L. N.; Bodwell, G. J., 1, 1, 8, 8-Tetramethyl [8](2, 11) teropyrenophane: Half of an Aromatic Belt and a Segment of an (8, 8) Single-Walled Carbon Nanotube. *Angew. Chem., Int. Ed.* **2009**, *48* (30), 5487-5491.
40. Merner, B. L.; Unikela, K. S.; Dawe, L. N.; Thompson, D. W.; Bodwell, G. J., 1, 1, n, n-Tetramethyl [n](2, 11) teropyrenophanes (n= 7–9): a series of armchair SWCNT segments. *Chem. Commun.* **2013**, *49* (53), 5930-5932.
41. Bisson, A. P.; Lynch, V. M.; Monahan, M. K. C.; Anslyn, E. V., Recognition of Anions through NH π Hydrogen Bonds in a Bicyclic Cyclophane—Selectivity for Nitrate. *Angew. Chem., Int. Ed. Engl.* **1997**, *36* (21), 2340-2342.
42. Diederich, F.; Dick, K., A new water-soluble macrocyclic host of the cyclophane type: host-guest complexation with aromatic guests in aqueous solution and acceleration of the transport of arenes through an aqueous phase. *J. Am. Chem. Soc.* **1984**, *106* (26), 8024-8036.
43. Forman, J.; Marsh, R.; Schaefer, W.; Dougherty, D., Structure of a cyclophane host molecule. *Acta Crystallogr., Sect. B: Struct. Sci.* **1993**, *49* (5), 892-896.
44. Gavin, J. A.; Deng, N.; Alcalá, M.; Mallouk, T. E., Host-guest chemistry of a chiral cyclohexanediamine-viologen cyclophane in solution and in the solid state. *Chem. Mater.* **1998**, *10* (7), 1937-1944.
45. Zhelezina, Y. A.; Balueva, A. S.; Ignatieva, S. N.; Karasik, A. A.; Sinyashin, O. G., Host-Guest Complexes of P, N-Containing Cyclophanes with Heteroaromatic Ammonium Salts in Solution. *Phosphorus, Sulfur Silicon Relat. Elem.* **2013**, *188* (1-3), 19-20.
46. Schalley, C. A., Supramolecular chemistry goes gas phase: the mass spectrometric examination of noncovalent interactions in host–guest chemistry and molecular recognition. *Int. J. Mass Spectrom.* **2000**, *194* (1), 11-39.

47. Schalley, C. A., *Analytical Methods in Supramolecular Chemistry: Vol. 1*. 2012; p 129-135.
48. Warneke, J.; Jenne, C.; Bernarding, J.; Azov, V. A.; Plaumann, M., Evidence for an intrinsic binding force between dodecaborate dianions and receptors with hydrophobic binding pockets. *Chemical Communications* **2016**, 52 (37), 6300-6303.
49. Hurtado, P.; Gámez, F.; Hamad, S.; Martínez-Haya, B.; Steill, J. D.; Oomens, J., Crown Ether Complexes with H₃O⁺ and NH₄⁺: Proton Localization and Proton Bridge Formation. *The Journal of Physical Chemistry A* **2011**, 115 (25), 7275-7282.
50. Cooper, T. E.; Carl, D. R.; Oomens, J.; Steill, J. D.; Armentrout, P. B., Infrared Spectroscopy of Divalent Zinc and Cadmium Crown Ether Systems. *The Journal of Physical Chemistry A* **2011**, 115 (21), 5408-5422.
51. Martínez-Haya, B.; Hurtado, P.; Hortal, A. R.; Hamad, S.; Steill, J. D.; Oomens, J., Emergence of Symmetry and Chirality in Crown Ether Complexes with Alkali Metal Cations. *The Journal of Physical Chemistry A* **2010**, 114 (26), 7048-7054.
52. Burt, M.; Fridgen, T., Structures and physical properties of gaseous metal cationized biological ions. *Eur. J. Mass Spectrom.* **2012**, 18 (2), 235.
53. Fridgen, T. D., Infrared consequence spectroscopy of gaseous protonated and metal ion cationized complexes. *Mass spectrometry reviews* **2009**, 28 (4), 586-607.
54. Dunbar, R. C.; McMahon, T. B.; Thoelmann, D.; Tonner, D. S.; Salahub, D. R.; Wei, D., Zero-Pressure Thermal-Radiation-Induced Dissociation of Gas-Phase Cluster Ions: Comparison of Theory and Experiment for (H₂O)₂Cl⁻ and (H₂O)₃Cl⁻. *J. Am. Chem. Soc.* **1995**, 117 (51), 12819-12825.
55. Price, W. D.; Schnier, P. D.; Williams, E. R., Binding Energies of the Proton-Bound Amino Acid Dimers Gly⁻Gly, Ala⁻Ala, Gly⁻Ala, and Lys⁻Lys Measured by Blackbody Infrared Radiative Dissociation. *J. Phys. Chem. B* **1997**, 101 (4), 664-673.

56. Rajabi, K.; Easterling, M. L.; Fridgen, T. D., Solvation of electrosprayed ions in the accumulation/collision hexapole of a hybrid Q-FTMS. *J. Am. Soc. Mass Spectrom.* **2009**, *20* (3), 411-418.
57. Frisch, M. J.; Trucks, G. W.; Schlegel, H. B.; Scuseria, G. E.; Robb, M. A.; Cheeseman, J. R.; Scalmani, G.; Barone, V.; Mennucci, B.; Petersson, G. A.; Nakatsuji, H.; Caricato, M.; Li, X.; Hratchian, H. P.; Izmaylov, A. F.; Bloino, J.; Zheng, G.; Sonnenberg, J. L.; Hada, M.; Ehara, M.; Toyota, K.; Fukuda, R.; Hasegawa, J.; Ishida, M.; Nakajima, T.; Honda, Y.; Kitao, O.; Nakai, H.; Vreven, T.; Montgomery Jr., J. A.; Peralta, J. E.; Ogliaro, F.; Bearpark, M. J.; Heyd, J.; Brothers, E. N.; Kudin, K. N.; Staroverov, V. N.; Kobayashi, R.; Normand, J.; Raghavachari, K.; Rendell, A. P.; Burant, J. C.; Iyengar, S. S.; Tomasi, J.; Cossi, M.; Rega, N.; Millam, N. J.; Klene, M.; Knox, J. E.; Cross, J. B.; Bakken, V.; Adamo, C.; Jaramillo, J.; Gomperts, R.; Stratmann, R. E.; Yazyev, O.; Austin, A. J.; Cammi, R.; Pomelli, C.; Ochterski, J. W.; Martin, R. L.; Morokuma, K.; Zakrzewski, V. G.; Voth, G. A.; Salvador, P.; Dannenberg, J. J.; Dapprich, S.; Daniels, A. D.; Farkas, Ö.; Foresman, J. B.; Ortiz, J. V.; Cioslowski, J.; Fox, D. J. *Gaussian 09*, Gaussian, Inc.: Wallingford, CT, USA, 2009.
58. Yanai, T.; Tew, D. P.; Handy, N. C., A new hybrid exchange–correlation functional using the Coulomb-attenuating method (CAM-B3LYP). *Chemical Physics Letters* **2004**, *393* (1-3), 51-57.
59. Gillis, E. A. L.; Demireva, M.; Nanda, K.; Beran, G.; Williams, E. R.; Fridgen, T. D., Structures and energetics of electrosprayed uracilnCa²⁺ clusters (n = 14–4) in the gas phase. *Physical Chemistry Chemical Physics* **2012**, *14* (10), 3304-3315.
60. Azargun, M.; Jami-Alahmadi, Y.; Fridgen, T., The intrinsic stabilities and structures of alkali metal cationized guanine quadruplexes. *Phys. Chem. Chem. Phys.* **2017**, *19* (2), 1281-1287.

61. Gillis, E. A.; Demireva, M.; Sarwar, M. G.; Chudzinski, M. G.; Taylor, M. S.; Williams, E. R.; Fridgen, T. D., Structure and energetics of gas phase halogen-bonding in mono-, bi-, and tridentate anion receptors as studied by BIRD. *Phys. Chem. Chem. Phys.* **2013**, *15* (20), 7638-7647.
62. Blackbody chemistry. *Science* **1998**, *279* (5348), 149b-149b.
63. Thoelmann, D.; Tonner, D. S.; McMahon, T. B., Spontaneous Unimolecular Dissociation of Small Cluster Ions, $(\text{H}_3\text{O}^+)_{\text{Ln}}$ and $\text{Cl}-(\text{H}_2\text{O})_{\text{n}}$ ($n = 2-4$), under Fourier Transform Ion Cyclotron Resonance Conditions. *The Journal of Physical Chemistry* **1994**, *98* (8), 2002-2004.
64. Hiraoka, K.; Grimsrud, E. P.; Kebarle, P., Gas phase ion equilibrium studies of the hydrogen ion in water-dimethyl ether and methanol-dimethyl ether mixtures. *Journal of the American Chemical Society* **1974**, *96* (11), 3359-3364.
65. Meot-Ner, M.; Speller, C. V., Filling of solvent shells about ions. 1. Thermochemical criteria and the effects of isomeric clusters. *The Journal of Physical Chemistry* **1986**, *90* (25), 6616-6624.
66. Polfer, N. C.; Oomens, J., Vibrational spectroscopy of bare and solvated ionic complexes of biological relevance. *Mass Spectrom. Rev.* **2009**, *28* (3), 468-494.
67. Burt, M. B.; Fridgen, T. D., Heterogeneous Proton-Bound Dimers with a High Dipole Moment Monomer: How Could We Experimentally Observe These Anomalous Ionic Hydrogen Bonds? *The Journal of Physical Chemistry A* **2007**, *111* (42), 10738-10744.
68. Fridgen, T. D.; MacAleese, L.; Maitre, P.; McMahon, T. B.; Boissel, P.; Lemaire, J., Infrared spectra of homogeneous and heterogeneous proton-bound dimers in the gas phase. *Physical Chemistry Chemical Physics* **2005**, *7* (14), 2747-2755.
69. Roscioli, J. R.; McCunn, L. R.; Johnson, M. A., Quantum Structure of the Intermolecular Proton Bond. *Science* **2007**, *316* (5822), 249-254.

Chapter 3: Glycine in a Basket: Protonated 1,1,n,n-tetramethyl[n](2,11)teropyrenophane (n=7, 8, 9) Complexes With Glycine in the Gas-Phase

Protonated complexes composed of a basket-like host molecule 1,1,n,n-tetramethyl[n](2,11)teropyrenophanes (TMnTP) (n=7, 8, 9) and glycine as a guest were studied in the gas phase by experimental and computational methods. Blackbody infrared radiative dissociation (BIRD) experiments of [(TMnTP)(Gly)]H⁺ not only provided the observed Arrhenius parameters (activation energies, E_a^{obs}, and frequency factors, A) but also suggested the existence of two populations of isomeric complexes of [(TMnTP)(Gly)]H⁺, termed fast dissociating (FD) and slow dissociating (SD), due to their relative BIRD rate constants. Master equation modeling was conducted to obtain the threshold dissociation energies E₀ of the host-guest complexes. The relative stabilities of the most stable of the n=7, 8, or 9 [(TMnTP)(Gly)]H⁺ complexes followed the trend SD-[(TM7TP)(Gly)]H⁺ > SD-[(TM8TP)(Gly)]H⁺ > SD-[(TM9TP)(Gly)]H⁺ by both BIRD and energy resolved sustained off-resonance irradiation collision-induced dissociation experiments (ER-SORI-CID). Computed structures and energies of [(TMnTP)(Gly)]H⁺ were obtained using B3LYP-D3/6-31+G(d,p) and for all TMnTP molecules, the lowest-energy structures were ones where protonated glycine was within the cavity of the TMnTP, despite the TMnTP molecules having a proton affinity 100 kJ mol⁻¹ higher than glycine. An independent gradient model based on the Hirshfeld partition (IGMH) and natural energy decomposition analysis (NEDA) were applied to visualize and reveal the nature of interactions between hosts and guest. The NEDA analysis suggested that the polarization

(POL) component which describes interactions between induced multipoles contributed the most to the stability of [(TMnTP)(Gly)]H⁺ (n=7, 8, 9) complexes.

A version of this chapter has been published:

Chen, Y.; Ghasemabadi, P. G.; Bodwell, G. J.; Demireva, M.; Fridgen, T. D., *Physical Chemistry Chemical Physics* **2023**, 25 (24), 16597-16612.

3.1 Introduction

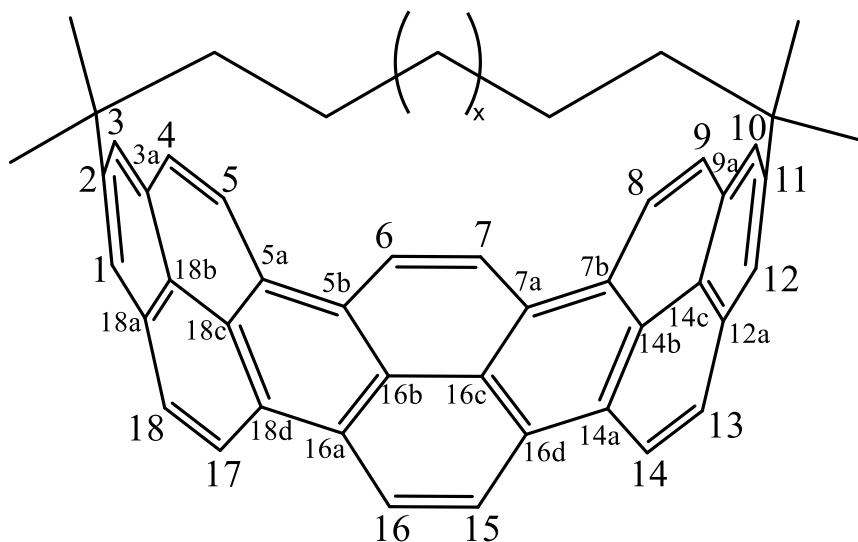
The history of supramolecular chemistry can be traced back to 1891, when Villiers first discovered cyclodextrin (CD, originally called cellulosine) which has a cyclic structure with an internal cavity.^{1,2} Beginning in the 1950s, the encapsulation properties of CDs were widely investigated.^{3, 4} Lehn introduced the term “supramolecular”^{5, 6} to describe the chemistry of systems consisting of two or more molecules held together through intermolecular or non-covalent interactions such as dipole-dipole, hydrogen bonding, etc.⁷⁻
¹⁰ Within the field of supramolecular chemistry, host-guest chemistry has garnered much attention.

The gap in time between the first discovery of CD and extensive studies on the physical properties of host/guest molecules was mainly due to limitations of the methods used for studying complexes held together by weak interactions and the inability to eliminate interactions with solvents. Different soft ionization sources coupled with different mass analyzers contribute greatly to the fundamental study of complexes held together by non-covalent interactions.¹¹ In this study, electrospray ionization (ESI)/Fourier transform ion cyclotron resonance mass spectrometry (FT-ICR-MS) was used. ESI is a soft source of ions, enabling the extraction of ions from the solution phase to the gas phase keeping supramolecular complexes intact.^{12, 13} FT-ICR-MS provides a low pressure environment, $\sim 10^{-10}$ mbar, to minimize ion-molecule collisions during experiments and the capability for tandem mass spectrometry analysis to probe the physical properties of ion-molecule complexes.^{14, 15} Slow activation methods such as sustained off-resonance irradiation

collision-induced dissociation (SORI-CID)¹⁶ and BIRD^{17, 18} are used to provide information on the strength of non-covalent interactions.

Non-planar or contorted polycyclic aromatics¹⁹ show unique structures containing different π -faces compared with planar PAHs whose two surfaces are identical. For example, corannulene has both concave (*endo*) and convex (*exo*) π -surfaces²⁰ which allow guests like cations²¹⁻²⁴ and aromatics²⁵ to bind by cation- π interactions or π - π stacking interactions. Since the dipole moment of corannulene is directed from the concave surface to the convex surface, it is more electrostatically negative on the convex (*exo*) surface. Thus, alkali metal cations (Li^+ , Na^+ , K^+) have a slight preference, of only few kJ mol^{-1} , for the convex surface of corannulene.²⁰ It was also found that these cations have a preference for binding in an η^6 site vs an η^5 site in corannulene. Single walled carbon nanotubes (SWCNTs) also contain non-planar π -surfaces,²⁶ which are able to involve cation- π interactions with cations,²⁷ π - π stacking interactions with aromatic compounds,²⁸ and aromatic hydrogen bond with XH (X = C, O, N, etc.) containing molecules.²⁹ The curvature of the carbon nanotube (CNT) affects the binding energy to metal cations. For example, when the diameter of armchair CNTs increases (the curvature decreases), the binding energies of *exo*-alkali metal cations and *exo*-alkaline earth metal cations with CNTs increase.³⁰ 1,1,*n*-Tetramethyl[*n*](2,11)teropyrenophanes (*n*=7-9), Scheme 3.1, are cyclophanes that are composed of an aliphatic chain with *n* carbons on its main chain and a large non-planar PAH which can be seen as a segment of armchair SWCNTs.³¹ The differences between the shapes of TMnTP molecules are caused by the length of the bridging aliphatic chain. In a previous study³² employing infrared multiple photon dissociation spectroscopy, alkali

metal cations were found to predominantly occupy the *endo* position of the half belt shaped TMnTP while the *exo* complexes dissociated too fast to properly observe.



Scheme 3.1 1,1,n,n-Tetramethyl(2,11)teropyrenophane (TMnTP) ($x=1-3$, $n = 7-9$)

In the present study, protonated glycine (Gly) was used as a guest molecule in protonated Gly/TMnTP complexes. Protonation is an important influencer of chemical properties of biological systems. For instance, protonation of amino acid residues plays important roles not only on structures and stabilities of proteins, but also on protein-ligand binding and enzymatic mechanisms.³³⁻³⁵ Protonated glycine is the simplest of the protein building blocks and studies on host-guest complexes involving protonated glycine have been performed in the past decades. For example, Lebrilla and coworkers have explored the thermal dissociation of protonated amino acid/CD complexes in the gas phase³⁶ to compare the interaction strength of different protonated amino acids (Gly, Val, Phe, Tyr and Trp) with tri-O-methyl- β -cyclodextrin (TMCD) and di-O-methyl- β -cyclodextrin (DMCD).

In general, they found that hydrogen bonding interactions between the protonated amino acid and the CD as well as steric locking of the protonated amino acid within the CD were the key players in strengthening the interactions of the inclusion complexes. For example, protonated amino acids with more basic groups for hydrogen bonding interactions increased the dissociation temperature. However, the dissociation temperature of the [TMCD:Gly + H]⁺ complex is higher than for other protonated amino acid/TMCD complexes because TMCD has 14 methyl groups in the upper rim creating a “steric lock” so that it is difficult for small compact amino acids inside the CD to escape. Structures, binding energies, and binding natures of cucurbit[7]uril (CB7) complexes with protonated amino acids and neutral amino acid complexes were explored by Ma’s group using computational methods.³⁷ Protonation of the amino acids including Gly brings into play ion-dipole and stronger ionic hydrogen bonding into the host/guest system. Thus, the binding energy between a protonated amino acid and a CB7 is significantly larger than the corresponding amino acid and the CB7. Protonated glycine was also investigated as a guest of crown ethers.^{38, 39} For example, McNary *et al.* investigated the structures of protonated complexes of amino acids with 18-crown-6 (18C6) ether using infrared multiphoton dissociation (IRMPD) spectroscopy and computational methods.³⁹ Interestingly, IRMPD of (Gly)H⁺(18C6) leads to loss of neutral Gly whereas the spectroscopy and calculations were consistent with the complex being amino protonated glycine bound to 18C6. The other amino acids studied lost 18C6 leaving the protonated amino acids and the complexes with 18C6 also involved protonated amino acids.

To experimentally investigate the thermodynamics and reaction kinetics of a host/guest complex, ER-SORI-CID and BIRD techniques can be employed. ER-SORI-CID experiments were used to compare the relative stability of the complex ions in the gas phase. Azargun and Fridgen used ER-SORI-CID experiments to compare the relative stabilities of alkali metal cationized 9-ethylguanine tetrad complexes in the gas phase, concluding that the trend in binding energies decreased over the series $\text{Na}(9\text{eG})_4^+ > \text{Li}(9\text{eG})_4^+ > \text{K}(9\text{eG})_4^+ > \text{Rb}(9\text{eG})_4^+ > \text{Cs}(9\text{eG})_4^+$.⁴⁰ Carroy et al. used this method and observed the relative binding energies at half dissociation of three protonated amine complexes (*para*-phenylenediamine, *para*-xylylenediamine, and adamantylamine) with the nor-seco-cucurbit[10]uril host in either the 2+ or 3+ charge state. Dissociation thresholds were dependent on both the guest molecules and the charge state of the complex.⁴¹

BIRD is a method used to measure the observed activation energy, E_a^{obs} . The threshold dissociation energy, E_0 is equivalent to E_a^{obs} when the rapid energy exchange (REX) limit is reached, for large, slow-dissociating complexes. Otherwise E_0 can be obtained by master equation modeling (MEM) of the temperature dependent kinetic plots. Williams and co-workers performed BIRD and MEM to determine the binding energies of H_2O with lithiated lysine ($\text{LysLi}^+(\text{H}_2\text{O})$), and some related amino acids.⁴² While calculations show the lowest energy $\text{LysLi}^+(\text{H}_2\text{O})$ structure is zwitterionic, by about 7 kJ mol^{-1} , the BIRD experiments resulted in the conclusion that $\text{LysLi}^+(\text{H}_2\text{O})$ was non-zwitterionic. BIRD experiments in our lab have been fruitful in determining binding energies and helping elucidate structures of various ion-molecule complexes.⁴³⁻⁴⁶

In this study, the gas-phase stabilities of [(TMnTP)(Gly)]H⁺ (*n*=7, 8, 9) complexes were studied by ER-SORI-CID and BIRD techniques. Density functional theory (DFT) was used to compute the structures and binding energies of the [(TMnTP)(Gly)]H⁺ complexes. The interactions between the host and the guest of [(TMnTP)(Gly)]H⁺ complexes were also explored by the independent gradient model based on the Hirshfeld partition⁴⁷ and by natural energy decomposition analysis.⁴⁸

3.2 Methods

3.2.1 Experimental

All experiments were performed in the Laboratory for the Study of Structures, Energetics, and Reactions of Gas-Phase Ions at Memorial University^{49, 50} using a Bruker 7T Apex-Qe FT-ICR mass spectrometer equipped with an Appollo II ESI source. The three TMnTP compounds were synthesized by the Bodwell Group at Memorial University.^{31, 51} The TMnTP solutions (~70 μmol L⁻¹) were prepared in acetonitrile. Protonated glycine solutions were prepared at 1 mmol L⁻¹ in 18 MΩ-cm water (Millipore) with a few drops of 1% formic acid. Final solutions were prepared by adding a few drops of protonated glycine solution into 5 mL of the TMnTP solution. This solution was then pumped into the ESI source with a flow rate of 120 μL h⁻¹. Ions were accumulated in an accumulation hexapole for 1 s before being transferred to the ICR cell where they underwent SORI-CID or BIRD experiments.

3.2.1.1 Energy-Resolved SORI-CID

SORI-CID provides a slow heating process achieved by applying a radio frequency (rf) pulse slightly off-resonance with the ion's cyclotron frequency. SORI-CID experiments were carried out by selecting and isolating the host-guest complex ions in the ICR cell at 10^{-10} mbar followed by pulsing in argon collision gas ($\sim 10^{-6}$ - 10^{-5} mbar in the ICR cell), and exciting precursor ions for 250 ms by an offset frequency of 500 Hz off the cyclotron frequency to increase their translation energy. The maximum lab frame kinetic energy, $E_{\text{lab}}^{\text{max}}$, can be calculated through the following equation:^{52, 53}

$$E_{\text{lab}}^{\text{max}} = \frac{\beta^2 q^2 V_{\text{p-p}}}{32\pi^2 m d^2 \Delta\vartheta^2} \quad \text{Eq 3.1}$$

where β and d are the geometrical factor (0.9) and the diameter (0.06 m) of the ICR cell, q and m are the charge and mass of the ion of interest, respectively, $\Delta\vartheta$ is the frequency offset (500 Hz) at which SORI is carried out, $V_{\text{p-p}}$ is the peak-to-peak excitation voltage whose values are varied. The center of mass energy, $E_{\text{CM}}^{\text{max}}$, was determined from $E_{\text{lab}}^{\text{max}}$ using the following equation:

$$E_{\text{CM}}^{\text{max}} = E_{\text{lab}}^{\text{max}} \left(\frac{m_{\text{g}}}{m_{\text{g}} + m_{\text{p}}} \right) \quad \text{Eq 3.2}$$

where m_{g} is the mass of a collisional gas and m_{p} is the mass of a precursor ion.

ER-SORI-CID spectra are recorded by varying the $V_{\text{p-p}}$ resulting in a range of precursor ion kinetic energies. A sigmoidal-like shaped curve is obtained by plotting the

survival yield of a precursor ion as a function of center of mass energy. Relative binding energies of different complexes are compared using the E_{CM}^{\max} at half dissociation.

3.2.1.2 BIRD measurements

Temperature-dependent BIRD measurements, another slow activation technique, was used to obtain kinetic parameters for dissociation of the $[(\text{TMnTP})(\text{Gly})]\text{H}^+$ complexes in this study. A single blackbody infrared photon emitted from the FT-ICR cell chamber is absorbed by precursor ions. Loosely-bound complexes with high internal energies, at the top of the Boltzmann internal energy distribution can dissociate. First order kinetics can be used to describe the time dependence of the intensity of precursor ions:

$$[I]_t = [I]_0 e^{-kt} \quad \text{Eq 3.3}$$

where $[I]_t$ is the normalized intensity of precursor ion at a delay time t , $[I]_0$ is the initial precursor ion intensity ($[I]_0=1$ due to normalization), and k is the first-order dissociation rate constant. By determining rate constants at different temperatures (T) under BIRD conditions, Arrhenius parameters can be obtained by:

$$\ln(k) = \ln(A) - \frac{E_a}{k_B T} \quad \text{Eq 3.4}$$

where A is the Arrhenius factor, E_a is the activation energy for dissociation, and k_B is Boltzmann constant. The entropy of activation (ΔS^\ddagger) can be obtained by:

$$\Delta S^\ddagger = \left(\ln(A) - \ln\left(\frac{k_B T}{h}\right) - 1 \right) * R \quad \text{Eq 3.5}$$

where R and h are the gas constant and the Planck constant respectively.

3.2.2 Computational

Structural optimizations, frequency calculations and natural energy decomposition analysis (NEDA) were done at the B3LYP-D3/6-31+g(d,p) level using the Gaussian 16 package.⁵⁴ All reported computed thermochemistries are at 298 K and 1 atm. The proton affinities of TMnTP were obtained by

$$\text{PA} = H_{\text{TMnTP}} + H_{\text{H}^+} - H_{(\text{TMnTP})\text{H}^+}$$

The enthalpy (H) of each species consists of the total electronic energy, the correction to the thermal energy and $k_{\text{B}}T$. The zero-point energies were not scaled. The Gibbs energy (G) is computed from these computed enthalpies and the vibrational, rotational, and translational contributions to the entropies.

The determination of the length, height, and width of TMnTP molecules and the independent gradient model based on Hirshfeld partition analysis which have been described elsewhere^{47,55} were obtained using the Multiwfn program⁵⁶ and visualized using the VMD program.⁵⁷

3.2.2.1 Independent gradient model based on Hirshfeld partition

IGMH is a useful technique to visually study the interactions between fragments,^{58,59} and it is inspired by the IGM⁵⁵ method. IGM introduced a descriptor, δ_{g} , to reveal the regions and strength of intramolecular or intermolecular interactions. In general, the function of δ_{g} is expressed as

$$\delta g(\mathbf{r}) = g^{IGM}(\mathbf{r}) - g(\mathbf{r}) \quad \text{Eq 3.6}$$

where g is the sum of the gradient of electron densities, g^{IGM} is the IGM type density gradient which is the sum of the absolute value of the density gradient. If only intermolecular interactions are considered,

$$\delta g^{inter}(\mathbf{r}) = g^{IGM,inter}(\mathbf{r}) - g^{inter}(\mathbf{r}) \quad \text{Eq 3.7}$$

The difference between IGM and IGMH is the way to consider the atomic electron densities (ED). IGM calculates ED by promolecular density approximation which assumes spherically symmetric ED of an atom in its free state, whereas IGMH considers ED based on the Hirshfeld partition of molecular electron density based on the quantum chemical calculations. Thus, the difference between the IGMH and IGH analysis is that the δg is calculated using the Hirshfeld partition of molecular electron density. Similar to the reduced density gradient (RDG)⁶⁰ method, $\text{sign}(\lambda_2)\rho$, the sign of the second eigenvalue of the Hessian of the electron density (λ_2) times the electron density (ρ) is introduced to color both the IGMH isosurface map and IGMH scatter plot (δg^{inter} vs. $\text{sign}(\lambda_2)\rho$). The sign of λ_2 is used to distinguish the nature of the bond between attractive ($\lambda_2 < 0$) and repulsive ($\lambda_2 > 0$) interactions. When $\lambda_2 \approx 0$ and $\rho < 0.005$ au, it maps the van der Waals interaction.⁶⁰

3.2.2.2 Natural Energy Decomposition Analysis

To investigate the nature of the non-covalent interactions within the ion/molecule complexes, a natural energy decomposition analysis was used. NEDA partitions the total energy of the interactions into physically understood components: electrostatic (ES), deformation (DEF), polarization (POL), charge transfer (CT), and exchange and correlation

(XC).^{48, 61} ES accounts for classical electrostatic interactions between permanent multipoles and POL arises from induced interactions between fragments. The CT component is attributed to delocalization of electrons from occupied orbitals of one fragment to vacant orbitals of another fragment, otherwise known as covalent interactions. XC associates with the exchange and correlation interactions of electrons. DEF (core repulsion) is the deformation of the wave functions of isolated fragments compared to that of perturbed fragments.

The NEDA calculations were carried out as implemented in Gaussian 16 Revision C.01.

3.2.3 Master Equation Modeling

The MEM procedure to obtain experimental E_0 values is the same as that described previously.^{44, 46} For those molecules whose dissociation rates are much faster than the rates of absorption and emission of infrared radiation, master equation modeling (MEM) needs to be used to obtain the true threshold dissociation energy. Briefly, a matrix formalism of the MEM was employed. Detailed rate constants for absorption, emission, and dissociation are contained in the matrix and provide the transfer probabilities from one energy state to another. These rate constants are calculated using formulas described in detail in other works.^{62, 63} Here, a 4000 x 4000 matrix with an energy bin of 20 cm^{-1} was used. BIRD kinetics were simulated by “reacting” a Boltzmann distribution at a given temperature and following its time evolution. Linear kinetics in a plot of $\ln([I]_t/[I]_0)$ as a function of reaction time (t), where $[I]_0$ is the initial Boltzmann population and $[I]_t$ corresponds to the population

remaining at time t , indicated that a steady-state population had been reached. The first order BIRD rate constant was then determined from the slope of the linear portion of the $\ln([I]_t/[I]_0)$ vs. t graph. For each *exo*- and *endo*- [(TMnTP)(Gly)]H⁺ ($n = 7, 8, 9$) complex, BIRD rate constants were calculated at the highest and lowest temperatures of the experiments and modeled Arrhenius plots were constructed. Experimental data were fitted with the modeled Arrhenius plots to extract a range of E_0 values that could properly reproduce the experimental results. As discussed previously,^{44, 46} two requirements are needed to be satisfied for a fit to the experimental data to be deemed acceptable: (1) the E_a value determined from the modeled Arrhenius plot was within one standard deviation of the experimental value and (2) the modeled BIRD rate constants were within a factor of two of the experimental rate constants. To account for uncertainties in the nature of the transition state (TS), TS frequencies were changed to produce pre-exponential (A) factors corresponding to a range of neutral to loose TSs. These A factors were systematically scanned from $\log(A) = 14$ (neutral TS) to $\log(A) = 19$ (loose TS). E_0 values were varied over the 0.6 – 1.4 eV range in 0.1 eV increments. For each set of E_0 and $\log(A)$ parameters, the E_a value determined from the modeled Arrhenius plot was compared with the experimental E_a value by computing the squared difference. This squared difference was plotted as a function of E_0 and $\log(A)$. Similarly, the modeled BIRD rate constants at the highest and lowest temperatures were compared with their respective experimental values by calculating the sum of squared differences and plotting these as a function of E_0 and $\log(A)$. The range of optimal E_0 values was determined from the overlap of the two graphs that satisfied the two fitting criteria (*vide supra*). Uncertainties in calculated IR intensities

were accounted for by scaling these up and down by a factor of 2 in the ME modeling and including their effect on the range of optimal E_0 values.

3.3 Results and Discussions

3.3.1 SORI-CID and Computed Proton Affinities

In a previous study, alkali metal cationized TMnTP complexes $M(\text{TMnTP})^+$ were observed to dissociate by losing neutral TMnTP, leaving the bare alkali metal cations.³² When the present host-guest complexes $[(\text{TMnTP})(\text{Gly})]\text{H}^+$ at m/z 678.4, $n=7$; m/z 692.5, $n=8$; and m/z 706.4, $n=9$ were submitted to SORI-CID, in all cases the loss was neutral glycine, leaving protonated TM7TP, TM8TP, or TM9TP at m/z 603.4, 617.5 and 631.4 respectively, see Figure 3.1. That the fragment ion is TMnTPH^+ indicates that in all cases, TMnTP likely has a higher proton affinity than glycine.

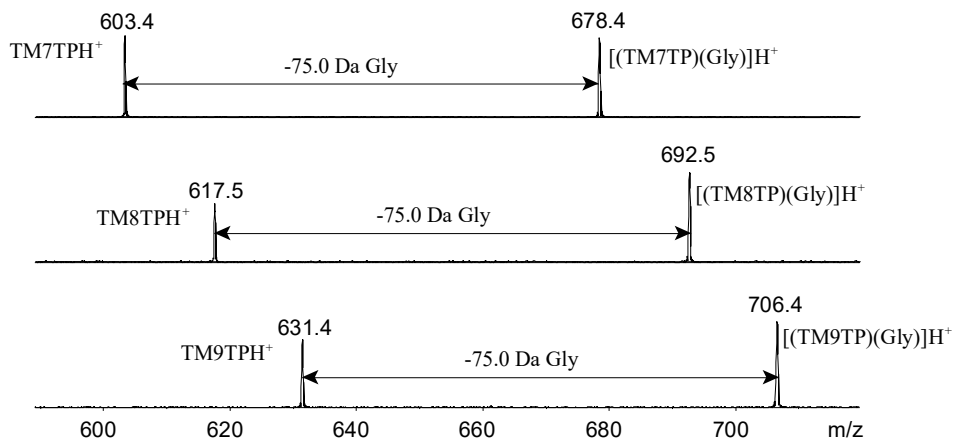


Figure 3.1 SORI-CID mass spectra of $[(\text{TMnTP})(\text{Gly})]\text{H}^+$ ($n=7, 8, 9$) decomposing to protonated TMnTP.

Experimental and computational proton affinities (PAs) of aromatic hydrocarbons have been explored. Hunter and Lias reported the experimental PAs of benzene (750.4 kJ mol⁻¹), toluene (784.0 kJ mol⁻¹), naphthalene (802.9 kJ mol⁻¹) and 1-methylnaphthalene (834.8 kJ mol⁻¹).⁶⁴ The computational PAs of benzene (762.3 kJ mol⁻¹),⁶⁵ toluene (802.8 kJ mol⁻¹),⁶⁶ naphthalene (820.9 kJ mol⁻¹),⁶⁵ and 1-methylnaphthalene (832.3 kJ mol⁻¹) at the level of B3LYP-D3/6-311++G(d,p) are shown in Table B1. By performing B3LYP-D3/6-31+G(d,p) calculations, the most stable protonated structures of the aromatic hydrocarbons gave the PAs of benzene (773.2 kJ mol⁻¹), toluene (803.0 kJ mol⁻¹), naphthalene (825.5 kJ mol⁻¹), 1-methylnaphthalene (835.9 kJ mol⁻¹). The PA values under B3LYP-D3/6-31+G(d,p) are at most 11 kJ mol⁻¹ higher than those computed using B3LYP-D3/6-311++G(d,p) and at most 23 kJ mol⁻¹ higher than the experimental PAs. This shows that the 6-31+G(d,p) basis set is adequate to estimate the PAs of aromatic compounds such as TMnTP.

The PAs of each carbon of the aromatic system of TMnTP, both *endo* and *exo* positions where applicable, were computed and are shown in Table B2. TM7TP and TM9TP belong to the C_s point group, aromatic carbons which are symmetric about the mirror plane that are perpendicular to the tether and teropyrene are equivalent. TM8TP belongs to the C_2 point group, so aromatic atoms are centro-symmetric about the C_2 axis that crosses through the middle of the aromatic system and the aliphatic chain. For all three TMnTP molecules, carbon 1 is computed to have the highest PA. The PA of carbon 1 is larger than that of position 18 followed by 16 and 17. According to Bodwell and coworkers,⁶⁷ based on electron paramagnetic resonance spectroscopy, the 1 positions of teropyrenes are known

to be innately preferred in electrophilic aromatic substitution, followed by carbon 18, carbon 16 and carbon 17. This trend agrees with the computed proton affinities in this study. Additionally, as shown in Table B1, the PAs of methyl substituted benzene and methyl substituted naphthalene are larger than benzene and naphthalene itself due to the electron donating methyl group. Thus, the presence of the inductive donating effect of the alkyl bridge of teropyrene would be expected to slightly enrich electron clouds near carbon 1, 3, 10 and 12 positions. While carbon 1 and carbon 3 are the same distance from the tether, carbon 3 is less basic due to the steric effect of the alkyl group that lies right over it (Figure B1). It should be noted that the bridge flips rapidly back and forth at room temperature to render the 1 and 3 positions (and 10 and 12) equivalent. The evidence for this is the sharp singlets in the NMR for the protons on these positions.³¹ The computed PAs of the TMnTPs show that they increase slightly from TM7TP (971.5 kJ mol⁻¹) to TM8TP (975.7 kJ mol⁻¹) and TM9TP (979.1 kJ mol⁻¹) with increasing length of the aliphatic tether. For glycine, the computed PA on the amine site using B3LYP-D3/6-31+G(d,p) is 888.3 kJ mol⁻¹ which compares favorably to the experimental value⁶⁴ of 886.5 kJ mol⁻¹ and the G3MP2 value of 886.6 kJ mol⁻¹.⁶⁸ It can be safely concluded that the PAs of the TMnTP molecules are significantly larger than that of glycine, by almost 100 kJ mol⁻¹ and which is in agreement with the observed dissociation pathways.

3.3.2 BIRD Experiments

The BIRD kinetic plots for all three [(TMnTP)(Gly)]H⁺ ($n=7, 8, 9$) complexes are shown in Figure 3.2. Similar to the BIRD kinetic plots for the M(TMnTP)⁺ (M=Rb and

Cs),³² two populations of [(TMnTP)(Gly)]H⁺ were observed, a slow decaying (SD) population and a much faster decaying (FD) population.

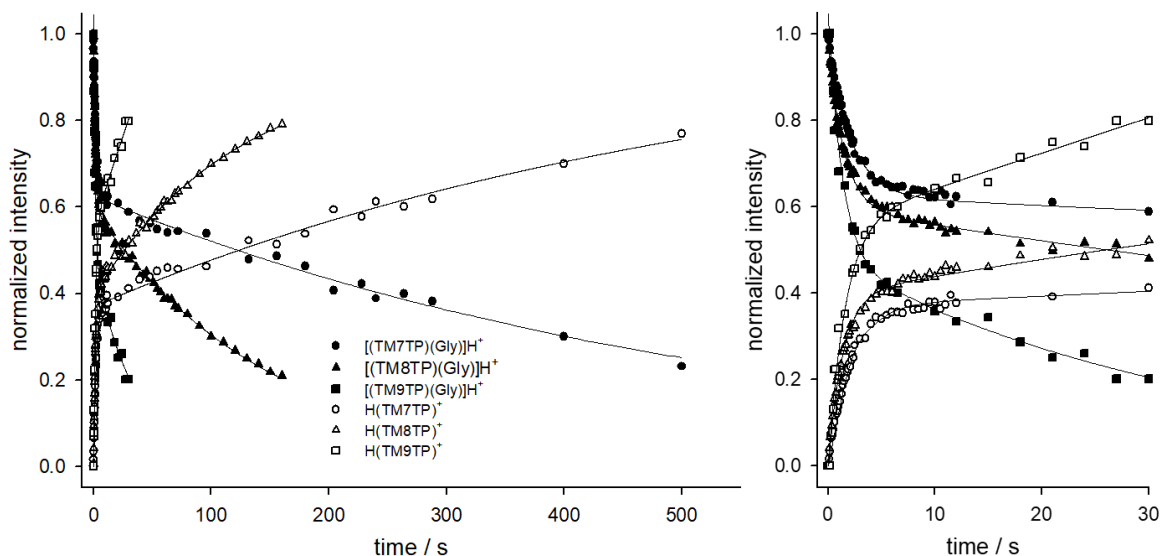


Figure 3.2 BIRD kinetic plots of [(TMnTP)(Gly)]H⁺ (n=7, 8, 9) at 342 K, precursor ions [(TMnTP)(Gly)]H⁺ are denoted as solid shapes and fragment ions TMnTPH⁺ are denoted as hollow shapes. Circles, triangles and squares corresponded to the n=7, 8, 9 complexes respectively. The solid curved lines are biexponential fits of the experimental data. The data plotted in a) and b) are the same with different scales on the abscissa.

The experimental decay curve was fit to a biexponential equation representing two separate first order decays:

$$I_{SD,t} + I_{FD,t} = I_{SD,0}e^{-k_{SD}t} + I_{FD,0}e^{-k_{FD}t} \quad \text{Eq 3.8}$$

which is shown to nicely reproduce the data in the BIRD plots of the three [(TMnTP)(Gly)]H⁺ complexes at 342 K as shown in Figure 3.2. In BIRD experiments where [(TMnTP)(Gly)]H⁺ complexes were exposed to 295 K an ambient blackbody environment, the SD complexes barely dissociate. Thus, BIRD experiments were

conducted at relatively higher temperatures between 329 and 371 K, and the temperature-dependent rate constants for each [(TMnTP)(Gly)]H⁺ species are summarized in Table B3. At the same temperature, FD-[(TM7TP)(Gly)]H⁺, FD-[(TM8TP)(Gly)]H⁺ and FD-[(TM9TP)(Gly)]H⁺ species dissociated at least 85, 35, 16 times faster than their corresponding SD species respectively. The rate constant for dissociation of SD-[(TM7TP)(Gly)]H⁺ is smaller than for SD-[(TM8TP)(Gly)]H⁺ which, in turn, is smaller than for SD-[(TM9TP)(Gly)]H⁺ at the same temperatures. As for the fast-decaying species, FD-[(TM9TP)(Gly)]H⁺ has the largest dissociation rate constant, larger than both FD-[(TM7TP)(Gly)]H⁺ and FD-[(TM8TP)(Gly)]H⁺, the latter two which are similar at the same temperature.

Table 3.1 Experimental observed activation energy E_a^{obs} , logarithm of pre-exponential factors $\log A_{\text{obs}}$, activation entropies ΔS^\ddagger , MEM threshold dissociation energy E_0 and computed binding energies at 298K, 1 atm

| species | E_a^{obs} / kJ mol ⁻¹ | $\log A_{\text{obs}}$ | ΔS^\ddagger / J mol ⁻¹ K ⁻¹ | E_0 / kJ mol ⁻¹ | $\Delta_r H$ / kJ·mol ⁻¹ | species |
|-------------------------------------|--|-----------------------|--|---------------------------------|---|--|
| | | | | 91.7 ± 5.8 | 42.6 | <i>exo</i> - (TM7TP)(GlyH ⁺) |
| FD- [(TM7TP)(Gly)]H ⁺ | 42.6 ± 3.1 | 6.2 ± 0.5 | -134.6 ± 8.9 | 91.7 ± 5.8 | 45.8 | <i>exo</i> - (TM7TPH ⁺)(Gly) |
| | | | | 91.7 ± 4.8- | 69.3 | <i>endo</i> - (TM7TPH ⁺)(Gly) |
| SD- [(TM7TP)(Gly)]H ⁺ | 94.8 ± 3.2 | 11.8 ± 0.5 | -27.4 ± 9.6 | 111.0 ± 4.8 | 94.3 | <i>endo</i> - (TM7TP)(GlyH ⁺) |
| | | | | 91.7 ± 7.7 | 39.1 | <i>exo</i> - (TM8TP)(GlyH ⁺) |
| FD- [(TM8TP)(Gly)]H ⁺ | 43.7 ± 6.3 | 6.3 ± 0.9 | -131.7 ± 18.2 | 90.7 ± 6.8 | 44.6 | <i>exo</i> - (TM8TPH ⁺)(Gly) |
| | | | | 90.7 ± 6.8 | 76.2 | <i>endo</i> - (TM8TPH ⁺)(Gly) |
| SD- [(TM8TP)(Gly)]H ⁺ | 82.3 ± 3.7 | 10.4 ± 0.6 | -54.2 ± 11.0 | 111.0 ± 4.8 | 102.5 | <i>endo</i> - (TM8TP)(GlyH ⁺) |
| | | | | 90.7 ± 5.8 | 36.6 | <i>exo</i> - (TM9TP)(GlyH ⁺) |
| FD- [(TM9TP)(Gly)]H ⁺ | 48.1 ± 5.2 | 7.2 ± 0.8 | -114.6 ± 14.9 | 91.7 ± 5.8 | 43.9 | <i>exo</i> - (TM9TPH ⁺)(Gly) |
| | | | | 91.7 ± 5.8 | 74.4 | <i>endo</i> - (TM9TPH ⁺)(Gly) |
| SD- [(TM9TP)(Gly)]H ⁺ | 68.7 ± 4.6 | 8.9 ± 0.7 | -82.3 ± 13.8 | 101.3 ± 5.8 | 100.9 | <i>endo</i> - (TM9TP)(GlyH ⁺) |

The Arrhenius plots for the dissociation of [(TMnTP)(Gly)]H⁺ are shown in Figure 3.3 and the observed activation energies (E_a^{obs}), base-10 logarithm of the pre-exponential

factors ($\log(A_{\text{obs}})$) and activation entropies (ΔS^\ddagger) are tabulated in Table 3.1. The Arrhenius data are well fit with linear regressions having $R^2 = 0.94-0.99$. As expected, the observed activation energy of the slow-dissociating complex is larger than its corresponding fast-dissociating complex. The E_a^{obs} values of SD complexes follow the trend: SD-[(TM7TP)(Gly)]H⁺ ($94.8 \pm 3.2 \text{ kJ mol}^{-1}$) > SD-[(TM8TP)(Gly)]H⁺ ($82.3 \pm 3.7 \text{ kJ mol}^{-1}$) > SD-[(TM9TP)(Gly)]H⁺ ($68.7 \pm 4.6 \text{ kJ mol}^{-1}$). However, for FD complexes, the observed activation energies range from 42.6 to 48.1 kJ mol⁻¹, only differing by 5.5 kJ mol⁻¹ while the maximum error in these values is 6.3 kJ mol⁻¹. Therefore, it is difficult to differentiate the relative stabilities of FD-[(TMnTP)(Gly)]H⁺ complexes by their activation energies from the BIRD experiments. However, they do differ substantially from the SD complexes. The experimental activation entropies of [(TMnTP)(Gly)]H⁺ range from -27.4 ± 9.6 to $-134.6 \pm 8.9 \text{ J mol}^{-1} \text{ K}^{-1}$. The large negative activation entropies may suggest that the dissociation reactions occur with a tight transition state involving an activation energy barrier. The error in these E_a^{obs} values are due to the scatter in the Arrhenius plots and propagate the error in the individual rate constants.

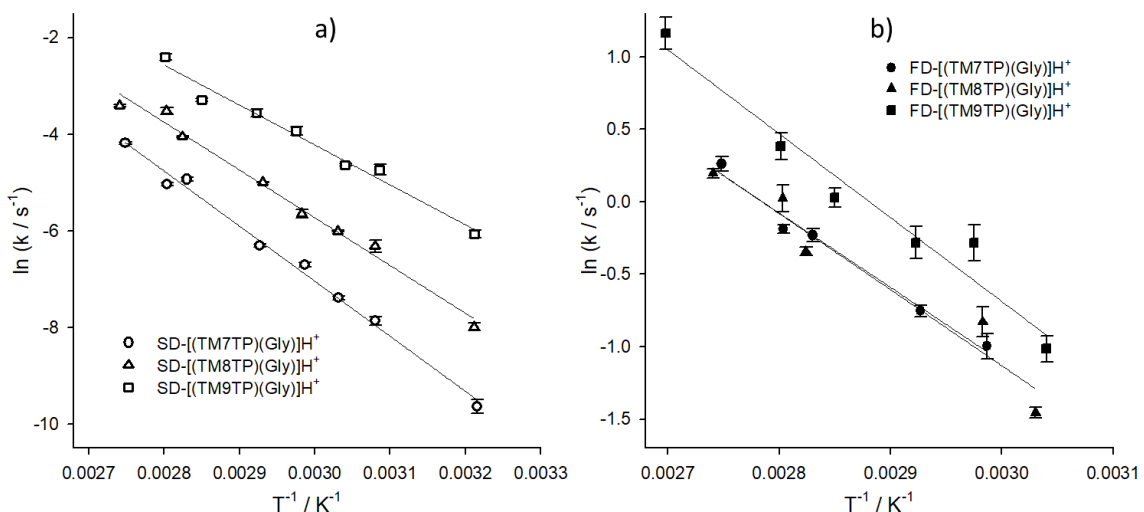


Figure 3.3 Arrhenius plots for the BIRD of a) SD-[(TMnTP)(Gly)]H⁺ and b) FD-[(TMnTP)(Gly)]H⁺, (n=7, 8, 9). The error bars are due to the standard error in fitting the kinetic plots.

Although the degrees of freedom of [(TM7TP)(Gly)]H⁺ (282), [(TM8TP)(Gly)]H⁺ (291) and [(TM9TP)(Gly)]H⁺ (300) are not small, the dissociation rate constants of the fast-dissociating species are large enough that these complexes lie in the realm of the small-to-medium-molecule kinetics.¹⁷ While smaller, the dissociation rate constants for the slow dissociating species still lie close to the boundary of the small-to-medium-molecule regime.¹⁷ Thus, MEM needs to be performed to extract threshold dissociation energies. The threshold dissociation energies (E_0) from MEM as well as experimental activation energies (E_a^{obs}) are compared in Table 3.1. The modeled E_0 values of both the slow- and fast-dissociating complexes are larger than the E_a^{obs} values obtained from BIRD experiments as is expected for complexes displaying small-to-medium-molecule kinetics suggesting that the dissociation rates of [(TMnTP)(Gly)]H⁺ are higher than the rates of energy

exchange between the $[(\text{TMnTP})(\text{Gly})]\text{H}^+$ and the blackbody radiation. The E_0 values determined from the MEM analysis for the SD- $[(\text{TM7TP})(\text{Gly})]\text{H}^+$ and SD- $[(\text{TM8TP})(\text{Gly})]\text{H}^+$ are $111.0 \pm 4.8 \text{ kJ mol}^{-1}$, while that of SD- $[(\text{TM9TP})(\text{Gly})]\text{H}^+$ was found to be slightly smaller at $101.3 \pm 5.8 \text{ kJ mol}^{-1}$. The E_0 values for the FD- $[(\text{TMnTP})(\text{Gly})]\text{H}^+$ complexes were as follows: FD- $[(\text{TM7TP})(\text{Gly})]\text{H}^+$ ($91.7 \pm 5.8 \text{ kJ mol}^{-1}$), FD- $[(\text{TM8TP})(\text{Gly})]\text{H}^+$ ($91.7 \pm 7.7 \text{ kJ mol}^{-1}$) and FD- $[(\text{TM9TP})(\text{Gly})]\text{H}^+$ ($90.7 \pm 5.8 \text{ kJ mol}^{-1}$), virtually identical. Furthermore, the values of E_0 were not sensitive to the computed structure (Figure 3.5) from which the frequencies/intensities were used in the MEM analysis. For all tether lengths ($n=7, 8, 9$), both the E_0 value and E_a^{obs} value of slow-dissociating species is larger than the corresponding fast-dissociating species.

3.3.3 Energy-resolved SORI-CID

ER-SORI-CID experiments were carried out as an additional means to compare the relative stabilities of the more strongly bound population of the three $[(\text{TMnTP})(\text{Gly})]\text{H}^+$ complexes. Prior to the isolation of the SD complexes, the FD complex populations were decomposed by applying a low energy SORI pulse. Then parent ions (SD complexes) were excited to center-of-mass collisional energies (E_{CM}) from 0 to 1.1 eV and exposed to Ar gas from a reservoir at 10 mbar. In Figure 3.4 are the plots of the center of mass energy-dependent survival yields of the three SD- $[(\text{TMnTP})(\text{Gly})]\text{H}^+$ complexes.

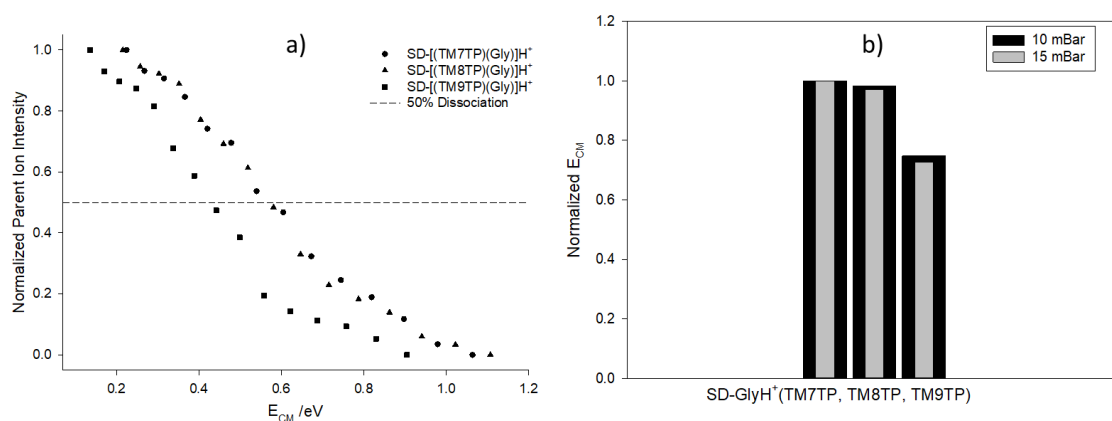


Figure 3.4 a) Intensity vs. the center-of-mass energy survival yields curves for ER-SORI-CID of SD-[(TMnTP)(Gly)]H⁺ complexes exposed to Ar gas pulsed with 10 mbar reservoir pressure; b) Relative center-of-mass collisional energies at half dissociation of SD-[(TMnTP)(Gly)]H⁺ ($n=7, 8, 9$) under 10 and 15 mbar reservoir pressures.

The horizontal dashed line in Figure 3.4 is where 50% of the ion population survives and the center of mass energies are 0.58, 0.57 and 0.43 eV for the TM7TP, TM8TP, and TM9TP complexes, respectively. Another set of ER-SORI-CID experiments were repeated with a reservoir pressure of 15 mbar—and therefore higher Ar pulse pressure during SORI-CID than those conducted with a reservoir pressure of 10 mbar—and gave similar results. The relative center-of-mass collisional energies for ER-SORI-CID of all host-guest complexes are summarized in Figure 3.4b. To better compare the gas phase stabilities of the SD-[(TMnTP)(Gly)]H⁺ complexes and because these values are not quantitative, the center-of-mass collisional energies at half dissociation are normalized to the E_{CM} of the most stable complex in Figure 3.4b. In agreement with the BIRD results, the relative gas phase stabilities of the SD-[(TMnTP)(Gly)]H⁺ complexes followed the trend SD-[(TM7TP)(Gly)]H⁺ > SD-[(TM8TP)(Gly)]H⁺ > SD-[(TM9TP)(Gly)]H⁺. It is worth stating

that the $E_{CM,50\%}$ difference between $SD-[(TM7TP)(Gly)]H^+$ and $SD-[(TM8TP)(Gly)]H^+$ is only 0.01 eV (10 mBar) or 0.005 eV (15 mbar), while the $E_{CM,50\%}$ of $SD-[(TM9TP)(Gly)]H^+$ is significantly lower than that of the other two complexes. These results are consistent with the E_0 values obtained for the $SD-[(TMnTP)(Gly)]H^+$ complexes from the temperature-dependent BIRD experiments.

3.3.4 Computed Structures and Energies

As discussed above, the BIRD experiments reveal two species, a SD and a FD population, for each of the $[(TMnTP)(Gly)]H^+$ complexes. In the previous study, it was shown that the SD, and therefore more strongly bound, population of $M(TMnTP)^+$ complexes were *endo* complexes with the metal (M) cation inside the TMnTP cavity and it was speculated that the FD population was an *exo* complex with the metal cation bound to the external face of the teropyrenophane.³² With that in mind it might be tempting to once again postulate that the glycine/TMnTP complexes also form *endo* and *exo* complexes with the *exo* and *endo* complexes being the FD and SD populations respectively. Thus, we computed both *endo* and *exo* glycine/TMnTP complexes.

Some of the computed structures of the *endo* and *exo* protonated glycine/TMnTP complexes are summarized in Figure 3.5, others are displayed in Figures S3-S5. The lowest energy structures for all values of n are the *endo*- $(TMnTP)(GlyH^+)$ complexes and interestingly, these structures are composed of protonated glycine inside the neutral TMnTP host, despite that TMnTP has a significantly higher proton affinity, by about 100 kJ mol⁻¹ (*vide supra*). This can be explained in that the energy lost by protonating glycine instead of

TMnTP is more than offset by forming an ion-molecule complex with presumably very strong non-covalent interactions between protonated glycine and the electron-rich aromatic. That protonation of TMnTP is favoured by almost 100 kJ mol^{-1} implies that the non-covalent interactions between protonated glycine and the TMnTPs (which will be discussed later) are more than 100 kJ mol^{-1} . This type of behaviour, where the monomer with the lower proton affinity is protonated in the protonated complex has been observed and discussed previously with respect to proton-bound complexes with high dipole moment monomers^{69,70} and protonated nucleic acid base pairs.⁷¹⁻⁷⁶ Similarly, the lowest energy structure of the $(\text{Gly})\text{H}^+(18\text{C}6)$ complex determined by McNary *et al.*,³⁹ as discussed above, was protonated Gly bound to neutral 18C6 despite the proton affinity of 18C6 being $935.3 \text{ kJ mol}^{-1}$,⁷⁷ some 50 kJ mol^{-1} higher than that of glycine.

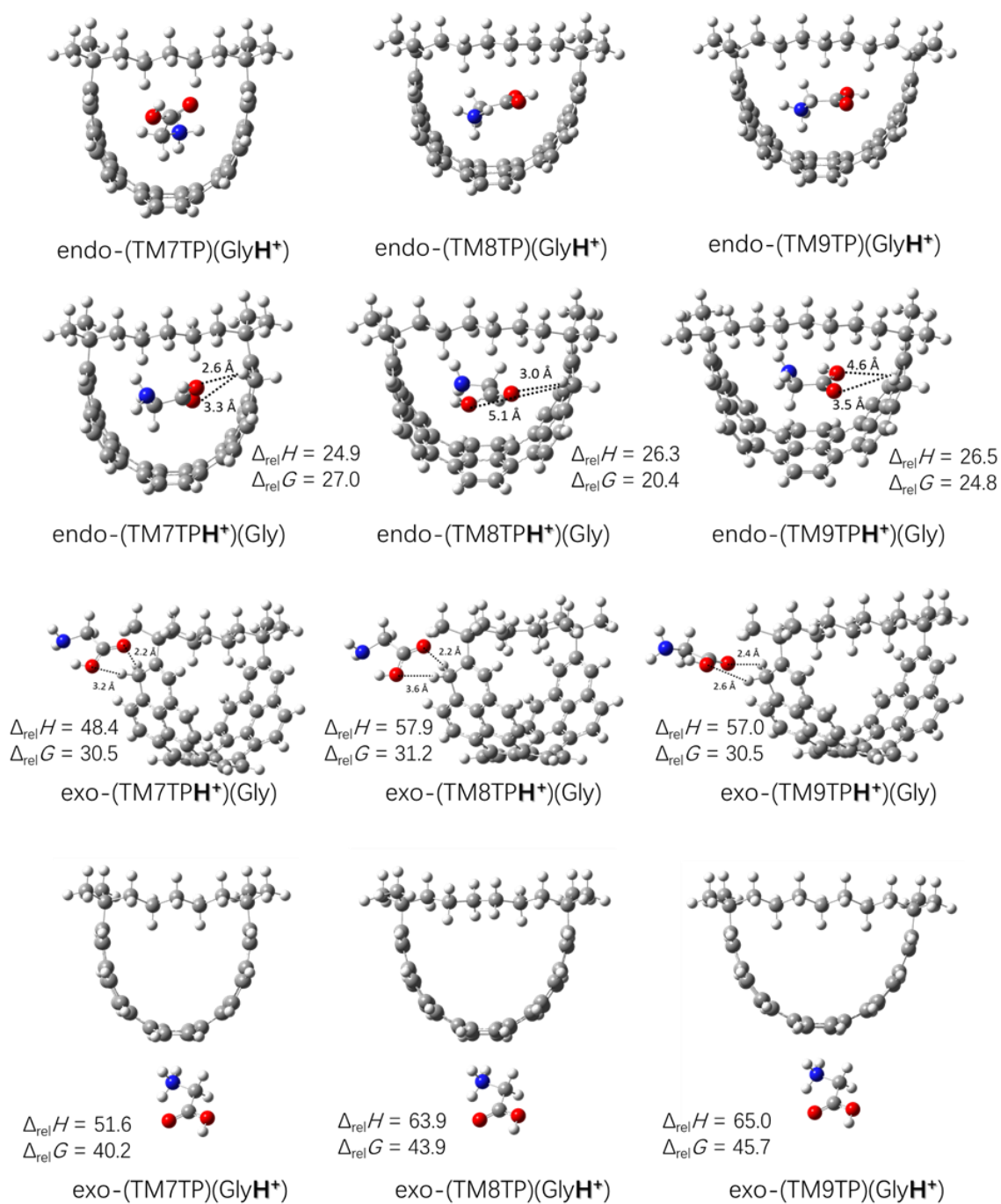


Figure 3.5 Global minimum structures of [(TMnTP)(Gly)]H⁺ $n=7, 8, 9$, first row, respectively; the lowest energy structures of *endo*-(TMnTPH⁺)(Gly) $n=7, 8, 9$, second row, respectively; the lowest energy structures of *exo*-(TMnTPH⁺)(Gly) $n=7, 8, 9$, third row, respectively; and the lowest energy structures of *exo*-(TMnTP)(Gly)H⁺ $n=7, 8, 9$, fourth row, respectively. Structures and energies were computed by B3LYP-D3/6-31+g(d,p). Thermochemical values are in kJ mol⁻¹ and are 298 K values. Bond lengths are in Å.

What is also interesting about these three lowest-energy complexes is the difference in the orientation of the protonated glycine sitting inside the three TMnTP molecules. The TMnTP molecules and the protonated glycine molecule with van der Waals surfaces (isosurface value = 0.001 a.u.) were enclosed in rectangular boxes. Lengths, widths, and heights of the TMnTP molecules determined using the Multiwfn package are shown in Figure B2. TM9TP is the longest (17.0 Å) because it has the longest aliphatic chain, followed by TM8TP (15.7 Å) and TM7TP (14.5 Å). The heights of TMnTP molecules follow the trend TM7TP (11.6 Å) > TM8TP (11.3 Å) > TM9TP (11.1 Å), decreasing over the series because there is less distortion of the teropyrene. The widths of these molecules do not differ, since the widths are mainly due to the teropyrene which are the same for all three TMnTP molecules. Since TM9TP has the longest cavity, the O-O-N plane of protonated glycine sits in the cavity almost parallel to the aliphatic chain and the aromatic system. The distance from the nitrogen of glycine to the carbon 16a of TM9TP is computed to be 3.4 Å, which is only 0.2 Å larger than the distance (3.6 Å) from the carbonyl-oxygen of glycine to carbon 16d of TM9TP. TM7TP has the shortest aliphatic chain length, so structures in which the protonated glycine sits parallel to the aliphatic chain were significantly higher in energy. The lowest energy structure (Gibbs energy) is a complex with the protonated amine inside the cavity and the hydroxy projecting outside the cavity somewhat. A structure where the protonated glycine is perpendicular to the aliphatic chain and sitting in the cavity and is slightly lower in enthalpy (2.1 kJ mol⁻¹), but 6.0 kJ mol⁻¹ higher in Gibbs energy (Fig S3). A similar structure where the protonated glycine sits in the cavity perpendicular to the aliphatic chain could not be obtained for the TM8TP and TM9TP hosts since the cavities are not tall enough. For TM8TP, the lowest energy structure has protonated glycine sitting

almost parallel to the aliphatic chain and teropyrene similar to protonated glycine in TM9TP. The nitrogen of glycine is 3.3 Å from the carbon 16a of TM8TP, while the distance from the carbonyl-oxygen of glycine to the carbon 16d of TM8TP is 4.0 Å. The coordinates of the lowest energy structures of each type of [(TMnTP)(Gly)]H⁺ can also be found in the supplementary information.

The next most stable class of structures are also *endo* with neutral glycine inside the C1-protonated TMnTP cavity, *endo*-(TMnTPH⁺)(Gly) and are shown in Figure 3.5. The enthalpies and Gibbs energies relative to the *endo*-(TMnTP)(GlyH⁺) structures are also provided in Figure 3.5 and are all between 20 and 30 kJ mol⁻¹ higher in energy. In these *endo*-(TMnTPH⁺)(Gly) structures glycine interacts with protonated TMnTP mainly through the carboxyl group, and the hydroxyl group is hydrogen bonded to the amine nitrogen which has been seen in previous ionic complexes of glycine.⁷⁸⁻⁸⁰ In order to interact with the proton, glycine needs to be parallel to the aliphatic chain and since TM7TP has a narrower cavity than TM8TP and TM9TP, the amine group of glycine extends out of the cavity slightly.

In contrast to the *endo* complexes, the lowest energy *exo* complexes, are those between protonated TMnTP and neutral glycine, *exo*-(TMnTPH⁺)(Gly). In all three complexes (*n*=7, 8, and 9) both oxygens of neutral glycine are interacting with the hydrogens on protonated C1 with the carbonyl oxygen to proton distance being the shortest (Figure 3.5). The lowest energy structures of *exo*-(TMnTPH⁺)(Gly) are higher in enthalpy than the global minima *endo*-(TMnTP)(GlyH⁺) structures by between 48 and 58 kJ mol⁻¹. The *exo*-(TMnTP)(GlyH⁺) are computed to be slightly higher in enthalpy than those of the

the lowest energy *exo*-(TMnTPH⁺)(Gly) complexes. The protonated glycine in these complexes resides outside of the teropyrene cavity at the bottom. Structures where the protonated glycine are on the side of the TMnTP (Figure B3-B5) are within a few kJ mol⁻¹ higher in enthalpy than structures where the protonated glycine are at the bottom.

Structures in which neutral glycine was zwitterionic were attempted but as expected, they optimized back to canonical glycine. To our knowledge, zwitterionic glycine has never been observed in the gas phase in any ionic complexes to date. However, the stability of the zwitterionic aliphatic amino acids, including glycine, is expected to increase when complexed with smaller more densely-charged cations.^{81, 82}

The four lowest energy structures for each teropyrenophane were submitted to an optimization and frequency calculation using the wB97XD⁸³ range-separated functional capable of capturing short- and long-range interactions along with the 6-31+G(d,p) basis set. The computed structures are quite similar to the B3LYP/6-31+G(d,p) calculated structures. The relative energies of the complexes at both levels of theory are summarized in Table B5. With wB97XD/6-31+G(d,p) the lowest energy structure is still the *endo*-(TMnTP)(GlyH⁺). Similarly, the *endo*-(TMnTPH⁺)(Gly) is the second highest energy structure type and is between 36 and 47 kJ mol⁻¹ higher in energy than *endo*-(TMnTP)(GlyH⁺), making the global minimum more thermodynamically stable with respect to the lowest energy structures of the other three groups using wB97XD/6-31+G(d,p). While using B3LYP, the *exo*-(TMnTPH⁺)(Gly) structure is lower in Gibbs energy than *exo*-(TMnTP)(GlyH⁺) by some 15-20 kJ mol⁻¹, but using wB97XD it is the *exo*-(TMnTP)(GlyH⁺) complexes that are lower in Gibbs energy by 3-4 kJ mol⁻¹ and both *exo*-

(TMnTPH⁺)(Gly) and *exo*-(TMnTP)(GlyH⁺) are more thermodynamically less stable compared to the global minimum.

The computed relative binding energies ($\Delta_r H$) of the lowest energy structures of the four types of [(TMnTP)(Gly)]H⁺ complexes are provided in Table 3.1 along with the observed E_a and MEM E_0 values. The computed binding energies were obtained by using the equation:

$$\Delta_r H = H_{\text{Gly}} + H_{(\text{TMnTP})\text{H}^+} - H_{[(\text{Gly})(\text{TMnTP})]\text{H}^+}$$

For each one of the [(TMnTP)(Gly)]H⁺ ($n=7, 8, 9$) complexes, the computed binding energies of the *exo* structures are significantly less than those of the *endo* structures. The same trend also can be found for the alkali metal cationized TMnTP complexes.³² The trend in computed binding energies decreases as follows *endo*-(TMnTP)(GlyH⁺) > *endo*-(TMnTPH⁺)(Gly) > *exo*-(TMnTPH⁺)(Gly) > *exo*-(TMnTP)(GlyH⁺). The computed binding energies for the *endo*-(TMnTP)(GlyH⁺) complexes are in decent agreement with the E_0 values obtained from the BIRD experiments and MEM analysis. The order of the computed binding energies for the *endo*-(TMnTP)(GlyH⁺) does not match the ordering of the BIRD/MEM values, but the computed values differ by only 8.2 kJ mol⁻¹, far below the sensitivity of the BIRD/MEM results and the accuracy of the calculations.

Based on a comparison of the MEM-extracted E_0 values and the computed dissociation enthalpies, it is likely that the SD population is the *endo*-(TMnTP)(GlyH⁺) complex and that the FD population is the *endo*-(TMnTPH⁺)(Gly) complex. For this to be true, there would also need to be a barrier separating these two protomers. Similarly, for

the *endo*-(TMnTP)(GlyH⁺) species to lose neutral glycine, a proton transfer from the glycine to the TMnTP must occur at some point prior to dissociation. A possible dissociation pathway for each of the three *endo*-(TMnTP)(GlyH⁺) complexes to lose neutral glycine were computed and are shown in Figures S6, S7, and S8. In all cases, a transition state for the transfer of a proton from Gly to TMnTP was found and was characterized by an imaginary frequency with the appropriate coordinate, the proton motion from the amine group of protonated glycine to C1 of TMnTP. In all cases there is a significant energy barrier to proton transfer, computed to be between 66 and 70 kJ mol⁻¹, but still some 30 kJ mol⁻¹ lower than the computed dissociation threshold.

3.3.5 Non-covalent Interactions Analysis

3.3.5.1 Independent Gradient Model Based on Hirshfeld Partition Analysis

The IGMH approach provides a way to visualize the non-covalent interactions of [(TMnTP)(Gly)]H⁺ (*n*=7, 8, 9) complexes. IGMH isosurfaces and scatter graphs (δg vs. $\text{sign}(\lambda_2)\rho$) for the four types of [(Gly)(TM9TP)]H⁺ complexes are shown in Figure 3.6 and for [(Gly)(TM7TP)]H⁺ and [(Gly)(TM8TP)]H⁺ in Figure B9 and B10, respectively.

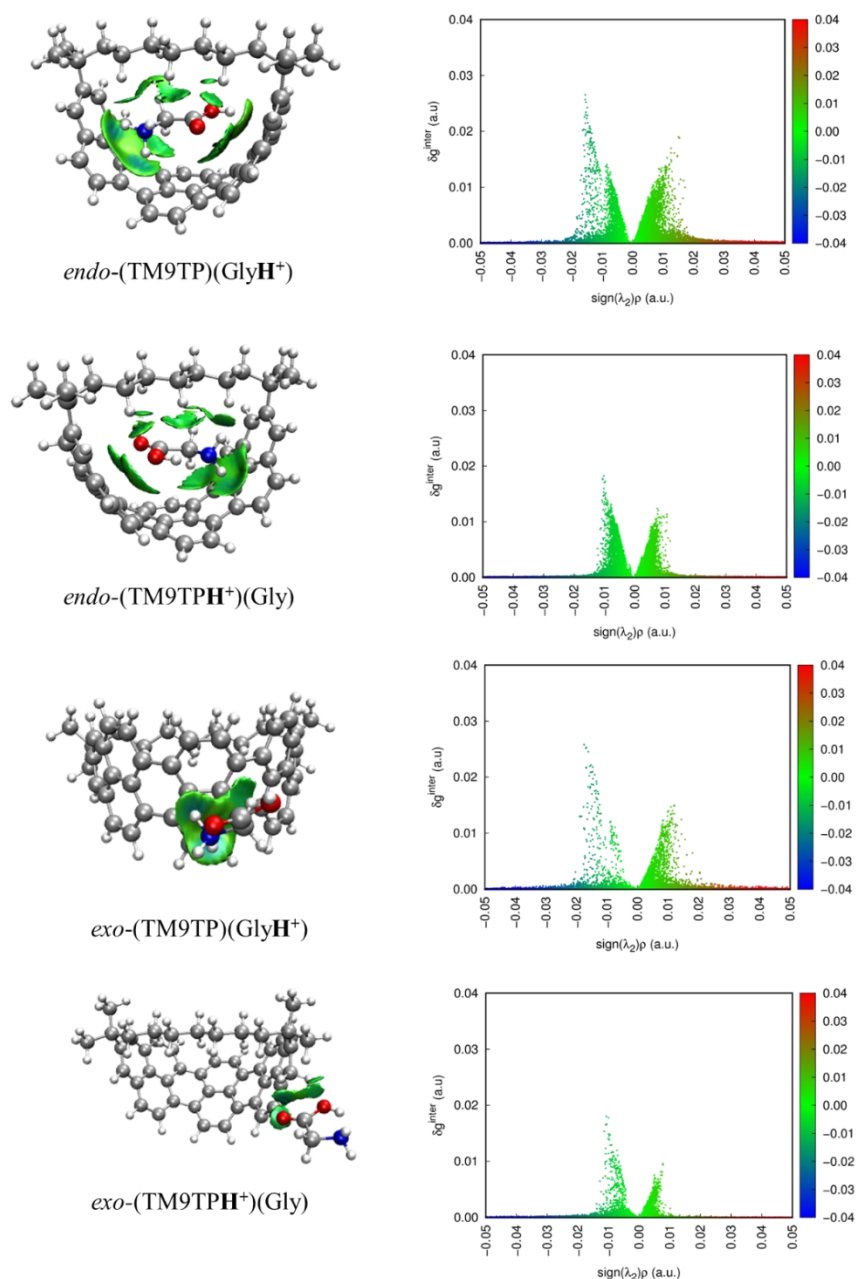


Figure 3.6 Results of the IGMH analysis of the lowest energy structures of each type of $[(\text{TM9TP})(\text{Gly})]\text{H}^+$ complexes. Upper figures are three dimensional isosurfaces (isovalued = 0.005 a.u.), lower figures are IGMH scatter plots. Both are colored according to the BGR scheme over the range of $-0.04 < \text{sign}(\lambda_2)\rho < 0.04$ au, where the blue, green, and red correspond to strong attraction, weak attraction, and steric repulsion respectively. To make a better view of the isosurfaces, structures of *endo*-(TM9TP) (GlyH⁺) and *endo*-(TMnTPH⁺)(Gly) are rotated slightly from the corresponding structures of Figure 3.5; structures of *exo*-(TM9TP)(GlyH⁺) are rotated up almost 90° from the corresponding structure of Figure 3.5; and the structures of *exo*-(TMnTPH⁺)(Gly) are flipped and rotated 90° from the corresponding structure of Figure 3.5.

The cyanspikes in $\text{sign}(\lambda_2)\rho$ near -0.02 a.u. in the IGMH scatter plot for *endo*-(TM9TP) (GlyH⁺) and *exo*-(TM9TP)(GlyH⁺) complexes reveals the relatively stronger -NH₃⁺— π interactions. As shown for the *exo*-(TM9TP)(GlyH⁺) complex, when the ammonium hydrogen is closer to the aromatic ring, the stronger (cyan) the interaction. Additionally, the hydroxyl group of protonated glycine in the *endo* complex also interacts with the aromatic system of TM9TP by way of an O-H— π interaction. The aliphatic chain also weakly interacts with the guest molecule in the way of C-H—O attractive and C-H—H-C interactions. As for *endo*-(TM9TPH⁺)(Gly) and *exo*-(TM9TPH⁺)(Gly) complexes, there are no obvious cyan spikes observed indicating the -NH₂— π interactions are not stronger than other interactions in the complexes. However, small cyan spikes in the $\text{sign}(\lambda_2)\rho$ range of -0.01 a.u. to -0.02 a.u. are observed in *exo*-(TM7TPH⁺)(Gly) and *exo*-(TM8TPH⁺)(Gly), indicating that there are relatively stronger interactions than van der Waals interactions. C-H—O and C-H—H-C interactions are found in *endo*-(TMnTPH⁺)(Gly) (n = 7, 8 and 9).

3.3.5.2 Natural energy decomposition analysis

To better understand the nature of the non-covalent interactions in the [(TMnTP)(Gly)]H⁺ complexes, NEDA calculations were conducted. As shown in Figure 3.7 and Table B4, there is little in the way of permanent electrostatic (ES) forces or covalent (CT) interactions. In fact, the binding of the *endo*-(TMnTP)(GlyH⁺) and *exo*-(TMnTP)(GlyH⁺) complexes, where protonated glycine is complexed to neutral TMnTP, is dominated by induced dipole interactions (POL). These interactions would be best characterized as ion-induced dipole (or cation- π) interactions and dipole-induced dipole

interaction which are calculated to be between 460 and 600 kJ mol⁻¹ for *endo*-(TMnTP)(GlyH⁺) and close to 400 kJ mol⁻¹ for *exo*-(TMnTP)(GlyH⁺).

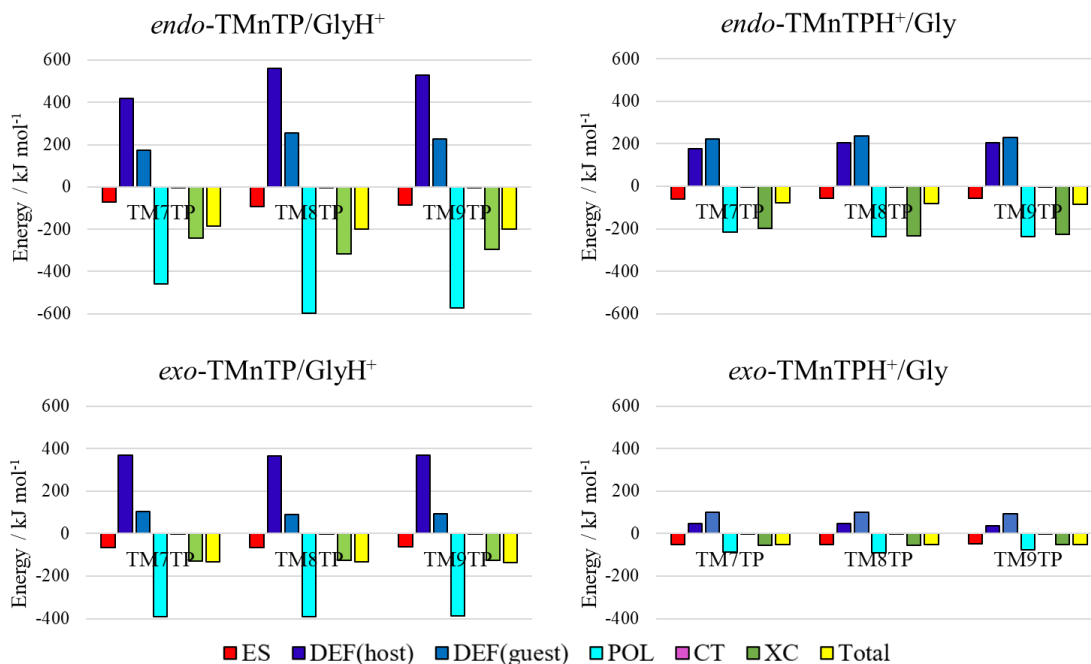


Figure 3.7 Computed NEDA component energies (in kJ mol⁻¹) at the B3LYP-D3/6-31+G(d,p) level for the lowest energy structures of each type of [(TMnTP)(Gly)]H⁺ complex.

This is in stark contrast to the comparatively weaker POL energies, about 200 kJ mol⁻¹ and less than 100 kJ mol⁻¹ for the *endo*-(TMnTPH⁺)(Gly) and *exo*-Gly(TMnTPH⁺)(Gly) complexes, respectively. It is the POL contributions to the binding that results in the *endo*-(TMnTP)(GlyH⁺) structure being the lowest in energy, despite the energy advantage that the *endo*-(TMnTPH⁺)(Gly) and *exo*-Gly(TMnTPH⁺)(Gly) complexes would have by TMnTP, with the much larger proton affinity, being protonated.

It is also interesting to compare the deformation energies (DEF) displayed in Figure 3.7. The DEF values are due to the deformation of the isolated fragment electron

distributions compared to the optimized electron densities in the complex. For the *endo*- and *exo*-(TMnTP)(GlyH⁺) complexes, the TMnTP electron distributions are distorted significantly by the GlyH⁺ guest. It is, in fact, the distortion of the TMnTP electron densities that contribute to the stabilizing ion-induced dipole and dipole-induced dipole interactions. For the two TMnTPH⁺ complexes, there is significantly less DEF because the TMnTP molecule is the ionic species and, therefore, there is not as significant a contribution from the stabilizing POL component.

Note that the total binding energies computed in the *endo*-(TMnTP)(GlyH⁺) and *exo*-(TMnTP)(GlyH⁺) complexes do not take into account the proton transfer energy. Therefore, for *endo*-(TMnTP)(GlyH⁺) and *exo*-(TMnTP)(GlyH⁺), the computed binding energies are about 200 and 130 kJ mol⁻¹, respectively, but that is computed for dissociation to GlyH⁺ and neutral TMnTP. These complexes would dissociate to the lower energy products Gly and TMnTP⁺, a threshold that is lower by the proton affinity difference between Gly and TMnTP, approximately 100 kJ mol⁻¹.

3.4 Conclusions

Structures and relative stabilities of gas-phase [(TMnTP)(Gly)]H⁺ were investigated in this study by a combination of experimental and computational techniques. The proton affinity of glycine is expected to be at least 100 kJ mol⁻¹ smaller than that of most favourable protonation site of TMnTP, carbon-1. Thus, during the unimolecular dissociation process in the gas phase, that [(TMnTP)(Gly)]H⁺ decomposes to neutral Gly and protonated TMnTP is entirely expected. Under the influence of blackbody infrared

radiation, two populations of [(TMnTP)(Gly)]H⁺ ions, SD and FD, were observed. With master equation modelling of the Arrhenius plots, it was found that the SD population of ions have an energy barrier for dissociation that was 10-20 kJ mol⁻¹ higher than the FD population. This is consistent with the ~25 kJ mol⁻¹ larger binding energies computed for the *endo*-(TMnTP)(GlyH⁺) over the *endo*-(TMnTPH⁺)(Gly), making these the two likely candidates for the SD and FD populations, respectively. Calculations also show there to be a significant proton transfer energy barrier separating the *endo*-(TMnTP)(GlyH⁺) and *endo*-(TMnTPH⁺)(Gly) structures which would be required to observe two separate populations of the structural isomers. An IGMH analysis shows there to be significant non-covalent interactions between the π electrons of the TMnTP and both the protonated amine and hydroxyl of the glycine. A NEDA clearly indicates that the *endo*-(TMnTP)(GlyH⁺) structure is favoured over the *exo*-(TMnTPH⁺)(Gly) because of the very strong ion-induced dipole interactions (cation- π interactions) which outweighs the ~100 kJ mol⁻¹ energy deficit by glycine being protonated over TMnTP in the complex.

3.5 Acknowledgements

The authors extend gratitude to the Natural Sciences and Engineering Research Council (NSERC) of Canada. We also thank the Canada Foundation for Innovation (CFI), the Industrial Research and Innovation Fund (IRIF), and Bruker for funding to build the Laboratory for the Study of Gaseous Ion Structures, Energetics and Reactions. Computational resources provided by Compute Canada are acknowledged for computational resources supporting. YC acknowledges funding from the China Scholarship Council (CSC).

3.6 References

1. Villiers, A., Sur la fermentation de la fécule par l'action du ferment butyrique. *Comptes Rendus de l'Académie des Sciences* **1891**, 112, 536-538.
2. Szejtli, J., Introduction and general overview of cyclodextrin chemistry. *Chemical Reviews* **1998**, 98 (5), 1743-1754.
3. Singh, R.; Bharti, N.; Madan, J.; Hiremath, S., Characterization of cyclodextrin inclusion complexes—a review. *Journal of Pharmaceutical Science and Technology* **2010**, 2 (3), 171-183.
4. Zhang, J.; Ma, P. X., Cyclodextrin-based supramolecular systems for drug delivery: recent progress and future perspective. *Advanced Drug Delivery Reviews* **2013**, 65 (9), 1215-1233.
5. Lehn, J. M., Supramolecular chemistry—scope and perspectives molecules, supermolecules, and molecular devices (Nobel Lecture). *Angewandte Chemie International Edition in English* **1988**, 27 (1), 89-112.
6. Steed, J. W.; Atwood, J. L., *Supramolecular Chemistry*. John Wiley & Sons: 2013.
7. Varnek, A.; Helissen, S.; Wipff, G.; Collet, A., van der Waals host–guest complexes: Can one predict complexation selectivity of neutral guests by a cryptophane? MD-FEP studies in gas phase and chloroform solution. *Journal of Computational Chemistry* **1998**, 19 (8), 820-832.
8. Rekharsky, M. V.; Inoue, Y., Complexation and chiral recognition thermodynamics of 6-amino-6-deoxy- β -cyclodextrin with anionic, cationic, and neutral chiral guests: counterbalance between van der Waals and coulombic interactions. *Journal of the American Chemical Society* **2002**, 124 (5), 813-826.
9. Park, I. W.; Yoo, J.; Adhikari, S.; Park, J. S.; Sessler, J. L.; Lee, C. H., Calix [4] pyrrole-Based Heteroditopic Ion-Pair Receptor That Displays Anion-Modulated, Cation-Binding Behavior. *Chemistry—A European Journal* **2012**, 18 (47), 15073-15078.

10. Luo, Y.-H.; Ge, S.-W.; Song, W.-T.; Sun, B.-W., Supramolecular assembly and host-guest interaction of crown ether with inorganic acid and organic amine containing carboxyl groups. *New Journal of Chemistry* **2014**, *38* (2), 723-729.
11. Baytekin, B.; Baytekin, H. T.; Schalley, C. A., Mass spectrometric studies of non-covalent compounds: why supramolecular chemistry in the gas phase? *Organic Biomolecular Chemistry* **2006**, *4* (15), 2825-2841.
12. Schalley, C. A.; Rivera, J. M.; Martín, T.; Santamaría, J.; Siuzdak, G.; Rebek Jr., J., Structural Examination of Supramolecular Architectures by Electrospray Ionization Mass Spectrometry. *European Journal of Organic Chemistry* **1999**, *1999* (6), 1325-1331.
13. Konermann, L.; Ahadi, E.; Rodriguez, A. D.; Vahidi, S., Unraveling the Mechanism of Electrospray Ionization. *Analytical Chemistry* **2013**, *85* (1), 2-9.
14. Azargun, M.; Jami-Alahmadi, Y.; Fridgen, T. D., The intrinsic stabilities and structures of alkali metal cationized guanine quadruplexes. *Physical Chemistry Chemical Physics* **2017**, *19* (2), 1281-1287.
15. Jami-Alahmadi, Y.; Fridgen, T. D., Distinguishing complexes of isomeric peptides: Structures, energetic, and reactions of sodium cation-coordinated ProLeu or LeuPro trimers in the gas phase. *International Journal of Mass Spectrometry* **2018**, *429*, 136-141.
16. Mirgorodskaya, E.; O'Connor, P. B.; Costello, C. E., A general method for precalculation of parameters for sustained off resonance irradiation/collision-induced dissociation. *Journal of the American Society for Mass Spectrometry* **2002**, *13* (4), 318-324.
17. Dunbar, R. C., BIRD (blackbody infrared radiative dissociation): evolution, principles, and applications. *Mass Spectrometry Reviews* **2004**, *23* (2), 127-158.
18. Dunbar, R. C.; McMahon, T. B.; Thoelmann, D.; Tonner, D. S.; Salahub, D. R.; Wei, D., Zero-pressure thermal-radiation-induced dissociation of gas-phase cluster ions: comparison of

theory and experiment for (H₂O) 2Cl-and (H₂O) 3Cl. *Journal of the American Chemical Society* **1995**, *117* (51), 12819-12825.

19. Ball, M.; Zhong, Y.; Wu, Y.; Schenck, C.; Ng, F.; Steigerwald, M.; Xiao, S.; Nuckolls, C., Contorted polycyclic aromatics. *Accounts of Chemical Research* **2015**, *48* (2), 267-276.

20. Dunbar, R. C., Binding of transition-metal ions to curved π surfaces: corannulene and coronene. *The Journal of Physical Chemistry A* **2002**, *106* (42), 9809-9819.

21. Zhao, G.; Zhu, H., Cation- π interactions in graphene-containing systems for water treatment and beyond. *Advanced Materials* **2020**, *32* (22), 1905756.

22. Kumar, K.; Woo, S. M.; Siu, T.; Cortopassi, W. A.; Duarte, F.; Paton, R. S., Cation- π interactions in protein-ligand binding: theory and data-mining reveal different roles for lysine and arginine. *Chemical Science* **2018**, *9* (10), 2655-2665.

23. Priyakumar, U. D.; Sastry, G. N., Cation- π interactions of curved polycyclic systems: M⁺ (M= Li and Na) ion complexation with buckybowls. *Tetrahedron Letters* **2003**, *44* (32), 6043-6046.

24. Vijay, D.; Sakurai, H.; Subramanian, V.; Sastry, G. N., Where to bind in buckybowls? The dilemma of a metal ion. *Physical Chemistry Chemical Physics* **2012**, *14* (9), 3057-3065.

25. Denis, P. A., Theoretical investigation of the stacking interactions between curved conjugated systems and their interaction with fullerenes. *Chemical Physics Letters* **2011**, *516* (1-3), 82-87.

26. Chen, Z.; Thiel, W.; Hirsch, A., Reactivity of the Convex and Concave Surfaces of Single-Walled Carbon Nanotubes (SWCNTs) towards Addition Reactions: Dependence on the Carbon-Atom Pyramidalization. *ChemPhysChem* **2003**, *4* (1), 93-97.

27. Udomvech, A.; Kerdcharoen, T.; Osotchan, T., First principles study of Li and Li⁺ adsorbed on carbon nanotube: Variation of tubule diameter and length. *Chemical Physics Letters* **2005**, *406* (1-3), 161-166.

28. Billing, B. K.; Agnihotri, P. K.; Singh, N., Development of pyrene-stacked carbon nanotube-based hybrid: measurement of NO_3^- ions using fluorescence spectroscopy. *Analyst* **2018**, *143* (14), 3343-3352.
29. Kozłowska, M.; Meyer, B.; Rodziewicz, P., Single-walled carbon nanotubes in tetrahydrofuran solution: microsolvation from first-principles calculations. *Journal of Molecular Modeling* **2019**, *25* (7), 206.
30. Umadevi, D.; Sastry, G. N., Metal ion binding with carbon nanotubes and graphene: Effect of chirality and curvature. *Chemical Physics Letters* **2012**, *549*, 39-43.
31. Merner, B. L.; Unikela, K. S.; Dawe, L. N.; Thompson, D. W.; Bodwell, G. J., 1, 1, n, n-Tetramethyl [n](2, 11) teropyrenophanes (n= 7–9): a series of armchair SWCNT segments. *Chemical Communications* **2013**, *49* (53), 5930-5932.
32. Chen, Y.; Jami-Alahmadi, Y.; Unikela, K. S.; Bodwell, G. J.; Fridgen, T. D., Endo or Exo? Structures of Gas-Phase Alkali Metal Cation/Aromatic Half-Belt Complexes. *ChemPhysChem* **2018**, *19* (17), 2194-2199.
33. Di Russo, N. V.; Estrin, D. A.; Martí, M. A.; Roitberg, A. E., pH-dependent conformational changes in proteins and their effect on experimental pK_as: The case of nitrophenol. *PLoS Computational Biology* **2012**, *8* (11).
34. Petukh, M.; Stefl, S.; Alexov, E., The role of protonation states in ligand-receptor recognition and binding. *Current Pharmaceutical Design* **2013**, *19* (23), 4182-4190.
35. Gabas, F.; Di Liberto, G.; Conte, R.; Ceotto, M., Protonated glycine supramolecular systems: the need for quantum dynamics. *Chemical Science* **2018**, *9* (41), 7894-7901.
36. Garcia, B.; Ramirez, J.; Wong, S.; Lebrilla, C. B., Thermal dissociation of protonated cyclodextrin-amino acid complexes in the gas phase. *International Journal of Mass Spectrometry* **2001**, *210*, 215-222.

37. Ma, F.; Zheng, X.; Xie, J.; Li, Z., Binding properties of cucurbit [7] uril to neutral and protonated amino acids: A theoretical study. *International Journal of Quantum Chemistry* **2020**, e26491.
38. Lee, S.-W.; Lee, H.-N.; Kim, H. S.; Beauchamp, J., Selective binding of crown ethers to protonated peptides can be used to probe mechanisms of H/D exchange and collision-induced dissociation reactions in the gas phase. *Journal of the American Chemical Society* **1998**, *120* (23), 5800-5805.
39. McNary, C. P.; Nei, Y.-W.; Maitre, P.; Rodgers, M.; Armentrout, P., Infrared multiple photon dissociation action spectroscopy of protonated glycine, histidine, lysine, and arginine complexed with 18-crown-6 ether. *Physical Chemistry Chemical Physics* **2019**, *21* (23), 12625-12639.
40. Azargun, M.; Fridgen, T. D., Guanine tetrads: an IRMPD spectroscopy, energy resolved SORI-CID, and computational study of M (9-ethylguanine) 4+(M= Li, Na, K, Rb, Cs) in the gas phase. *Physical Chemistry Chemical Physics* **2015**, *17* (39), 25778-25785.
41. Carroy, G.; Lemaire, V.; De Winter, J.; Isaacs, L.; De Pauw, E.; Cornil, J.; Gerbaux, P., Energy-resolved collision-induced dissociation of non-covalent ions: charge-and guest-dependence of decomplexation reaction efficiencies. *Physical Chemistry Chemical Physics* **2016**, *18* (18), 12557-12568.
42. Lemoff, A. S.; Bush, M. F.; O'Brien, J. T.; Williams, E. R., Structures of lithiated lysine and structural analogues in the gas phase: effects of water and proton affinity on zwitterionic stability. *The Journal of Physical Chemistry A* **2006**, *110* (27), 8433-8442.
43. Azargun, M.; Meister, P. J.; Gauld, J. W.; Fridgen, T. D., The K² (9-ethylguanine)₂²⁺ quadruplex is more stable to unimolecular dissociation than the K (9-ethylguanine)₈⁺ quadruplex in the gas phase: a BIRD, energy resolved SORI-CID, IRMPD spectroscopic, and computational study. *Physical Chemistry Chemical Physics* **2019**, *21* (28), 15319-15326.

44. Gillis, E. A.; Demireva, M.; Sarwar, M. G.; Chudzinski, M. G.; Taylor, M. S.; Williams, E. R.; Fridgen, T. D., Structure and energetics of gas phase halogen-bonding in mono-, bi-, and tri-dentate anion receptors as studied by BIRD. *Physical Chemistry Chemical Physics* **2013**, *15* (20), 7638-7647.
45. Burt, M. B.; Decker, S. G.; Fridgen, T. D., Water binding energies of [Pb (amino acid-H) H₂O]⁺ complexes determined by blackbody infrared radiative dissociation. *Physical Chemistry Chemical Physics* **2012**, *14* (43), 15118-15126.
46. Gillis, E. A.; Demireva, M.; Nanda, K.; Beran, G.; Williams, E. R.; Fridgen, T. D., Structures and energetics of electrosprayed uracil n Ca²⁺ clusters (n= 14–4) in the gas phase. *Physical Chemistry Chemical Physics* **2012**, *14* (10), 3304-3315.
47. Lu, T.; Chen, Q., Independent gradient model based on Hirshfeld partition: A new method for visual study of interactions in chemical systems. *Journal of Computational Chemistry* **2022**, *43* (8), 539-555.
48. Glendening, E. D.; Streitwieser, A., Natural energy decomposition analysis: An energy partitioning procedure for molecular interactions with application to weak hydrogen bonding, strong ionic, and moderate donor–acceptor interactions. *The Journal of Chemical Physics* **1994**, *100* (4), 2900-2909.
49. Burt, M. B.; Fridgen, T. D., Structures and physical properties of gaseous metal cationized biological ions. *European Journal of Mass Spectrometry* **2012**, *18* (2), 235-250.
50. Fridgen, T. D., Infrared consequence spectroscopy of gaseous protonated and metal ion cationized complexes. *Mass Spectrometry Reviews* **2009**, *28* (4), 586-607.
51. Unikela, K. S.; Ghasemabadi, P. G.; Houska, V.; Dawe, L. N.; Zhao, Y.; Bodwell, G. J., Gram-Scale Synthesis of the 1,1,n,n-Tetramethyl[n](2,11)teropyrenophanes. *Chemistry – A European Journal* **2021**, *27* (1), 390-400.

52. Peltz, C.; Drahos, L.; Vékey, K., SORI excitation: Collisional and radiative processes. *Journal of the American Society for Mass Spectrometry* **2007**, *18* (12), 2119-2126.
53. Guo, X.; Duursma, M. C.; Al-Khalili, A.; Heeren, R. M., Experimental calibration of the SORI-CID internal energy scale: energy uptake and loss. *International Journal of Mass Spectrometry* **2003**, *225* (1), 71-82.
54. Frisch, M. J.; Trucks, G. W.; Schlegel, H. B.; Scuseria, G. E.; Robb, M. A.; Cheeseman, J. R.; Scalmani, G.; Barone, V.; Petersson, G. A.; Nakatsuji, H.; Li, X.; Caricato, M.; Marenich, A. V.; Bloino, J.; Janesko, B. G.; Gomperts, R.; Mennucci, B.; Hratchian, H. P.; Ortiz, J. V.; Izmaylov, A. F.; Sonnenberg, J. L.; Williams; Ding, F.; Lipparini, F.; Egidi, F.; Goings, J.; Peng, B.; Petrone, A.; Henderson, T.; Ranasinghe, D.; Zakrzewski, V. G.; Gao, J.; Rega, N.; Zheng, G.; Liang, W.; Hada, M.; Ehara, M.; Toyota, K.; Fukuda, R.; Hasegawa, J.; Ishida, M.; Nakajima, T.; Honda, Y.; Kitao, O.; Nakai, H.; Vreven, T.; Throssell, K.; Montgomery Jr., J. A.; Peralta, J. E.; Ogliaro, F.; Bearpark, M. J.; Heyd, J. J.; Brothers, E. N.; Kudin, K. N.; Staroverov, V. N.; Keith, T. A.; Kobayashi, R.; Normand, J.; Raghavachari, K.; Rendell, A. P.; Burant, J. C.; Iyengar, S. S.; Tomasi, J.; Cossi, M.; Millam, J. M.; Klene, M.; Adamo, C.; Cammi, R.; Ochterski, J. W.; Martin, R. L.; Morokuma, K.; Farkas, O.; Foresman, J. B.; Fox, D. *J. Gaussian 16 Rev. B.01*, Wallingford, CT, 2016.
55. Lefebvre, C.; Rubez, G.; Khartabil, H.; Boisson, J.-C.; Contreras-García, J.; Henon, E., Accurately extracting the signature of intermolecular interactions present in the NCI plot of the reduced density gradient versus electron density. *Physical Chemistry Chemical Physics* **2017**, *19* (27), 17928-17936.
56. Lu, T.; Chen, F., Multiwfn: a multifunctional wavefunction analyzer. *Journal of Computational Chemistry* **2012**, *33* (5), 580-592.
57. Humphrey, W.; Dalke, A.; Schulten, K., VMD: visual molecular dynamics. *Journal of Molecular Graphics* **1996**, *14* (1), 33-38.

58. Baykov, S. V.; Tarasenko, M. V.; Semenov, A. V.; Katlenok, E. A.; Shetnev, A. A.; Boyarskiy, V. P., Dualism of 1, 2, 4-oxadiazole ring in noncovalent interactions with carboxylic group. *Journal of Molecular Structure* **2022**, *1262*, 132974.
59. Rozhkov, A. V.; Katlenok, E. A.; Zhmykhova, M. V.; Ivanov, A. Y.; Kuznetsov, M. L.; Bokach, N. A.; Kukushkin, V. Y., Metal-Involving Chalcogen Bond. The Case of Platinum (II) Interaction with Se/Te-Based σ -Hole Donors. *Journal of the American Chemical Society* **2021**, *143* (38), 15701-15710.
60. Johnson, E. R.; Keinan, S.; Mori-Sánchez, P.; Contreras-García, J.; Cohen, A. J.; Yang, W., Revealing noncovalent interactions. *Journal of the American Chemical Society* **2010**, *132* (18), 6498-6506.
61. Glendening, E. D., Natural energy decomposition analysis: Extension to density functional methods and analysis of cooperative effects in water clusters. *The Journal of Physical Chemistry A* **2005**, *109* (51), 11936-11940.
62. Dunbar, R. C., Kinetics of Thermal Unimolecular Dissociation by Ambient Infrared Radiation. *The Journal of Physical Chemistry* **1994**, *98* (35), 8705-8712.
63. Price, W. D.; Schnier, P. D.; Williams, E. R., Binding Energies of the Proton-Bound Amino Acid Dimers Gly·Gly, Ala·Ala, Gly·Ala, and Lys·Lys Measured by Blackbody Infrared Radiative Dissociation. *The Journal of Physical Chemistry B* **1997**, *101* (4), 664-673.
64. Hunter, E. P.; Lias, S. G., Evaluated gas phase basicities and proton affinities of molecules: an update. *Journal of Physical Chemical Reference Data* **1998**, *27* (3), 413-656.
65. Kapinus, V. A., *Photophysical properties of protonated aromatic hydrocarbons*. California Institute of Technology: 2005.
66. Nam, P.-C.; Nguyen, M. T.; Chandra, A. K., Methyl and phenyl substitution effects on the proton affinities of hydrides of first and second row elements and substituent effects on the proton

- affinities of ring carbons in benzene: A DFT study. *The Journal of Physical Chemistry A* **2006**, *110* (13), 4509-4515.
67. Unikela, K. S.; Roemmele, T. L.; Houska, V.; McGrath, K. E.; Tobin, D. M.; Dawe, L. N.; Boéré, R. T.; Bodwell, G. J., Gram-Scale Synthesis and Highly Regioselective Bromination of 1, 1, 9, 9-Tetramethyl [9](2, 11) teropyrenophane. *Angewandte Chemie International Edition* **2018**, *130* (6), 1723-1727.
68. Gronert, S.; Simpson, D. C.; Conner, K. M., A reevaluation of computed proton affinities for the common α -amino acids. *Journal of the American Society for Mass Spectrometry* **2009**, *20* (11), 2116-2123.
69. Burt, M. B.; Fridgen, T. D., Heterogeneous proton-bound dimers with a high dipole moment monomer: How could we experimentally observe these anomalous ionic hydrogen bonds? *The Journal of Physical Chemistry A* **2007**, *111* (42), 10738-10744.
70. Fridgen, T. D., Structures of heterogeneous proton-bond dimers with a high dipole moment monomer: Covalent vs electrostatic interactions. *The Journal of Physical Chemistry A* **2006**, *110* (18), 6122-6128.
71. Cheng, R.; Loire, E.; Martens, J.; Fridgen, T. D., An IRMPD spectroscopic and computational study of protonated guanine-containing mismatched base pairs in the gas phase. *J Physical Chemistry Chemical Physics* **2020**, *22* (5), 2999-3007.
72. Cheng, R.; Martens, J.; Fridgen, T. D., A vibrational spectroscopic and computational study of gaseous protonated and alkali metal cationized G–C base pairs. *Physical Chemistry Chemical Physics* **2020**, *22* (20), 11546-11557.
73. Cruz-Ortiz, A. F.; Rossa, M.; Berthias, F.; Berdakin, M.; Maitre, P.; Pino, G. A., Fingerprints of Both Watson–Crick and Hoogsteen Isomers of the Isolated (Cytosine–Guanine) H⁺ Pair. *The Journal of Physical Chemistry Letters* **2017**, *8* (22), 5501-5506.

74. Han, S. Y.; Lee, S. H.; Chung, J.; Oh, H. B., Base-pair interactions in the gas-phase proton-bonded complexes of C+ G and C+ GC. *The Journal of chemical physics* **2007**, *127* (24), 12B611.
75. Park, J. J.; Han, S. Y., Alternated Branching Ratios by Anomaly in Collision-Induced Dissociation of Proton-Bound Hoogsteen Base Pairs of 1-Methylcytosine with 1-Methylguanine and 9-Methylguanine. *Journal of The American Society for Mass Spectrometry* **2019**, *30* (5), 846-854.
76. Park, J. J.; Lee, C. S.; Han, S. Y., Proton transfer accounting for anomalous collision-induced dissociation of proton-bound Hoogsteen base pair of cytosine and guanine. *Journal of The American Society for Mass Spectrometry* **2018**, *29* (12), 2368-2379.
77. Chen, Y.; Rodgers, M., Re-Evaluation of the Proton Affinity of 18-Crown-6 Using Competitive Threshold Collision-Induced Dissociation Techniques. *Analytical Chemistry* **2012**, *84* (17), 7570-7577.
78. Atkins, C. G.; Rajabi, K.; Gillis, E. A.; Fridgen, T. D., Infrared Multiple Photon Dissociation Spectra of Proton-and Sodium Ion-Bound Glycine Dimers in the N– H and O– H Stretching Region. *The Journal of Physical Chemistry A* **2008**, *112* (41), 10220-10225.
79. Raspopov, S. A.; McMahon, T. B., A high-pressure mass spectrometric and density functional theory investigation of the thermochemical properties and structure of protonated dimers and trimers of glycine. *Journal of Mass Spectrometry* **2005**, *40* (12), 1536-1545.
80. Wu, R.; McMahon, T. B., Infrared multiple photon dissociation spectra of proline and glycine proton-bound homodimers. Evidence for zwitterionic structure. *Journal of the American Chemical Society* **2007**, *129* (16), 4864-4865.
81. Wytenbach, T.; Witt, M.; Bowers, M. T., On the stability of amino acid zwitterions in the gas phase: the influence of derivatization, proton affinity, and alkali ion addition. *Journal of the American Chemical Society* **2000**, *122* (14), 3458-3464.

82. Drayß, M. K.; Armentrout, P.; Oomens, J.; Schäfer, M., IR spectroscopy of cationized aliphatic amino acids: stability of charge-solvated structure increases with metal cation size. *International Journal of Mass Spectrometry* **2010**, *297* (1-3), 18-27.
83. Chai, J.-D.; Head-Gordon, M., Long-range corrected hybrid density functionals with damped atom–atom dispersion corrections. *Physical Chemistry Chemical Physics* **2008**, *10* (44), 6615-6620.

Chapter 4: Complexation of Tetraanisoyl-Anthraquinodimethanes with Alkali

Metal Ions: A Combined Mass Spectrometric and Computational Study

In this work, a group of tetraanisoyl-functionalized anthraquinodimethane (TAAQ) derivatives were investigated in view of their intriguing structures and metal binding properties that are analogous to crown ethers and spherands. The binding of TAAQs with a range of alkali metal cations (Li^+ , Na^+ , K^+ , Rb^+ and Cs^+) resulted in guest-host complexes, $\text{M}^+(\text{TAAQ})$, which were subjected to mass spectrometric analysis using the sustained off-resonance irradiation collision-induced dissociation (SORI-CID) to determine their fragmentation behavior in the gas phase. It was found that except for $\text{Li}^+(\text{TAAQ})$ and $\text{Na}^+(\text{o-TAAQ})$, all the complexes lost the neutral TAAQ moiety leaving alkali metal cations as fragments. The possible dissociation pathways for $\text{Li}^+(\text{TAAQ})$ and $\text{Na}^+(\text{o-TAAQ})$ were deduced from these mass spectrometry experiments and density functional theory (DFT) computational modeling. Furthermore, energy-resolved (ER) SORI-CID results allowed the relative gas-phase stability of $\text{M}^+(\text{TAAQ})$ to be compared and ranked. The experimentally established trend of stability in general concurs with the binding energies computed based on our proposed structures for these complexes. Moreover, electrostatic interactions were identified as the key driving force for the assembly of $\text{M}^+(\text{TAAQ})$ according to a natural energy decomposition analysis.

4.1 Introduction

Lithium is an important and finite raw material used in various industries, most notably in the production of lithium-ion batteries, which power many electronic devices and electric vehicles.¹⁻⁴ As the global demand for lithium-ion batteries has increased dramatically in recent years due to the growing popularity of electric vehicles and renewable energy storage systems, recovering lithium from various sources has become increasingly important. The average content of lithium in the earth's crust has been estimated to be approximately 0.007%.⁵ Economical concentrations of lithium are usually found in hydro-mineral resources of brines and geothermal water. There have been numerous efforts to develop innovative technologies for lithium recovery such as ion-sieve adsorption,^{6,7} membrane separation,^{8,9} electrochemical approaches,¹⁰ solvent extraction,^{11,12} as well as separation technologies based on photocatalytic nanocomposites.^{13,14} Among them, solvent extraction is an established process for efficient separation and extraction of a variety of metals from aqueous media owing to its simplicity and convenient handling.¹⁵⁻¹⁷ However, the solvent extraction process for lithium is always affected by co-existing cations, resulting in low efficiency. Crown ethers are cyclic compounds that contain multiple repeating [-CH₂-CH₂-O-] units in their structures. They show variable selectivities toward different metal ions, especially alkali and alkaline earth metals through the ion-dipole interaction, and therefore can be tuned as efficient ligands for metal extraction. Since their discovery by Pedersen,¹⁸ crown ethers have been used in isotope separations,^{19,20} heavy metal ion sensors,^{21,22} phase transfer catalysts,²³ and ion separation.^{24,25} Recently, Zhao and co-workers found that benzo-15-crown-5 ether (B15C5)

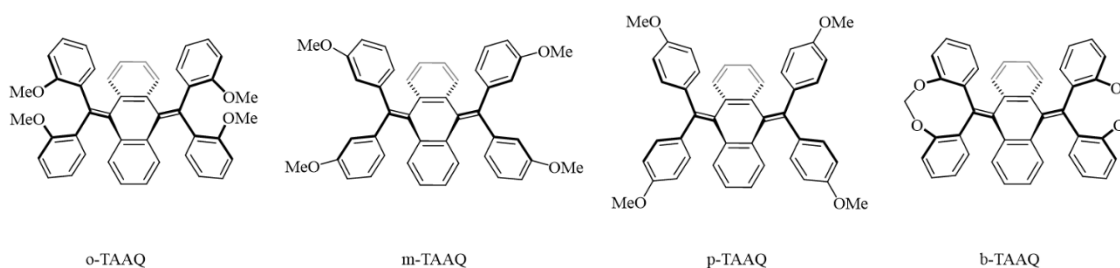
can strongly coordinate with Li^+ , but not as well with other metals such as Co^{2+} , Ni^{2+} and Mn^{2+} and this was explained with the help of hard soft acid base (HSAB) theory.²⁶ Selective separation of Li^+ from spent lithium-ion batteries leaching solution using B15C5 as an extracting agent has been achieved.²⁷ Based on the cavity-cation size compatibility strategy, Zhao and co-workers synthesized 14-crown-4 ether derivatives whose cavity sizes match best with Li^+ and found them to show excellent selectivity for binding with Li^+ and hence useful as efficient extractants for the selective recovery of lithium from brine.²⁸ Overall, crown ethers can be flexibly tailored for efficient extraction and recovery of lithium while minimizing the co-extraction of other metal ions. This selectivity is crucial for ensuring the high purity of the recovered lithium, especially in applications like battery manufacturing, where purity is essential for optimal battery performance.

The encapsulation of ions by macrocyclic structures can be traced back to the discovery of cryptands by Donald J. Cram in 1947. Built upon cryptands, the discovery and synthesis of crown ethers broadened the knowledge base of macrocyclic compounds and their ion encapsulation properties. In the 1960s, Pederson reported synthetic approaches to crown ethers²⁹ and determined that they had the ability to form complexes with alkali metal cations and alkaline earth metal cations.¹⁸ Since then, a diversity of crown ethers have been developed which show different selectivity towards alkali metal cations. This selectivity is mainly dependent on the cavity size of crown ethers, the coordination number for crown ethers available for binding and energetic considerations. In the gas phase, the binding ability of 18-crown-6 to alkali metal cations follows the order of $\text{Li}^+ > \text{Na}^+ > \text{K}^+ > \text{Rb}^+ > \text{Cs}^+$.³⁰ However, in aqueous solution, the selectivity order of 18-crown-6 is $\text{K}^+ > \text{Rb}^+ > \text{Cs}^+ >$

$\text{Na}^+ > \text{Li}^+$.³¹ Zhou used two different solvent/water models to theoretically analyze the selectivity of 18-crown-6 towards alkali metal cations in aqueous solution. In all cases, K^+ has the strongest interaction with 18-crown-6. In contrast to the highest selectivity of 18-crown-6 for Li^+ in the gas phase, lithiated 18-crown-6 shows the weakest interaction in aqueous solution. Of the alkali metal cations, lithium cation is the most strongly solvated in aqueous media. The resulting hydrated lithium cation possesses a diameter of 3.8 Å, which is larger than the cavity of 18-crown-6 (2.6-3.2 Å). The strong hydration effect of lithium cation is the main cause for its weak interaction with 18-crown-6 in aqueous solution. Not only crown ethers, other types of ethers such as dimethyl ether (DME) and 1,2-dimethoxyethane (DXE) were also found to interact with alkali metal cations. It was determined that the computed binding enthalpies and experimental bond dissociation energies (losing one DME or DXE) of $\text{M}^+(\text{DME})_x$ and $\text{M}^+(\text{DXE})_y$ ($\text{M} = \text{Li},^{32,33} \text{Na},^{34} \text{K},^{35} \text{Rb}$ and Cs^{36}) ($x = 1-2, y = 1-2$), followed the order $\text{Li}^+ > \text{Na}^+ > \text{K}^+ > \text{Rb}^+ > \text{Cs}^+$ complexes in the gas phase, as expected for electrostatically bound complexes.

Since its initiation by crown ethers, supramolecular chemistry has vigorously grown. Studying supramolecular chemistry in the gas phase laid the groundwork for investigating the intrinsic properties of non-covalent interactions within a supramolecule involving, for example, hydrogen bonds,³⁷ cation- π interactions,³⁸ anion- π interaction^{39,40} etc. In the present study, we explore the intrinsic properties of alkali metal cation complexes with four host molecules consisting of an anthraquinodimethane (AQ) substituted by four anisoles. The four structures of ortho-, meta-, para-, and bridge-TAAQ are displayed in Scheme 4.1. Ortho, meta, and para correspond to the position of the tetra-

anisole (TA) substituents on the AQ. Bridging-TAAQ describes the structure where each two ortho-substituted phenoxy groups on the same carbon of anthraquinodimethane are connected by a methylene bridge. The presence of oxygen atoms and aromatic rings in the TAAQs enable them to interact with alkali metal cations through non-covalent interactions.



Scheme 4.1 Structures of four tetra-anisole substituted anthraquinodimethane (TAAQ) host molecules, from top left to right corresponding to the ortho-, meta-, para- and bridging- TAAQ respectively.

Mass spectrometry in the gas phase provides a suitable technique to study the intrinsic properties of host/guest complexes by eliminating the effect of interactions with solvents.⁴¹ In this study, electrospray ionization (ESI) was used in order to keep the fragile supramolecular complex intact, and Fourier transform ion cyclotron resonance (FT-ICR) mass spectrometer was used to identify the supramolecular complexes and allowed for tandem mass spectrometry experiments to further investigate them. Energy-resolved sustained off-resonance irradiation collision-induced dissociation (ER-SORI-CID) on these $M^+(\text{TAAQs})$ ($M=\text{Li, Na, K, Rb and Cs}$) complexes were performed to obtain the relative

stabilities of the metal cation associating with the different host molecules in the gas phase. To further investigate the structures, unimolecular dissociation, and energetics, density functional theory (DFT) calculations were also carried out.

4.2 Methods

4.2.1 Experimental

All experiments were conducted using a Bruker 7T Apex-Qe FT-ICR mass spectrometer equipped with an Appollo II electrospray ionization (ESI) source in the Laboratory for the Study of Structures, Energetics, and Reactions of Gas-Phase Ions at Memorial University.^{42,43} All host compounds were synthesized at Memorial University. The TAAQ solutions ($\sim 71 \mu\text{mol L}^{-1}$) were prepared in acetonitrile. The alkali metal cation/TAAQ solutions were prepared by adding a few drops of 5 mmol L^{-1} alkali salt solutions into 5 mL of the TAAQ solutions. The mixtures were injected into the ESI source at a rate of $120 \mu\text{L h}^{-1}$ in positive ion mode. Gaseous ions were transferred to, and mass selected in the ICR cell (pressure = 10^{-10} mbar). Ions were activated by applying an off-resonant rf electric field pulse and pulsing in an argon collision gas to an estimated pressure of $\sim 10^{-5}$ mbar.

The maximum center-of-mass (CM) frame kinetic energy E_{CM}^{max} achieved in SORI-CID is calculated using the following equation:^{44,45}

$$E_{CM}^{max} = E_{lab}^{max} \left(\frac{m_g}{m_g + m_p} \right) = \frac{\beta^2 q^2 V_{p-p}}{32\pi^2 m_p d^2 \Delta\theta^2} \left(\frac{m_g}{m_g + m_p} \right)$$

where the geometry factor $\beta = 9$ and the diameter of the ICR cell $d = 0.06$ m in this case, q is the charge of the selected parent ion, m_g and m_p are the mass of collisional gas (argon in this study) and of the precursor ion respectively. The frequency offset $\Delta\theta$ was set to 500 Hz. V_{p-p} represents the peak-to-peak excitation voltage which is related to the SORI power. Energy-resolved (ER) SORI-CID experiments were conducted by recording intensities of the precursor and fragment ions as a function of various E_{CM}^{max} ranging from 0.01 eV to 2.90 eV calculated from various SORI powers that were set during the experiment. E_{CM}^{max} values at half dissociation ($E_{50\%}$) of different precursor ions were arbitrarily used to compare the relative gas-phase stabilities of these ions.

4.2.2 Computational

DFT calculations were performed using the B3LYP functional with Grimme's D3 dispersion correction⁴⁶ implemented in the Gaussian 16 software package.⁴⁷ In calculating the $M^+(\text{TAAQ})$ complexes, C, H and O atoms were described by the Pople-style basis set, 6-31+G(d,p), while Rb and Cs were treated with the Ahlrichs Def2-SVP basis set, Li, Na and K were described using both basis sets. The initial structures of TAAQs for optimization were constructed according to X-ray diffraction (XRD) data determined in the solid state. Possible trial structures for optimizing $M^+(\text{TAAQ})$ complexes in the gas phase were constructed according to chemical intuition. Alkali metal cations were placed around respective TAAQs with consideration of cation- π interactions and/or electrostatic interactions with oxygens. The optimized geometries were subjected to frequency calculations at the same level of theory to validate there are energy minima (no presence of imaginary frequencies) and to obtain thermodynamic energies. Gibbs energies (G) and

enthalpies (H) relative to the lowest energy structure are reported as $\Delta_{\text{rel}}H$ and $\Delta_{\text{rel}}G$. Binding enthalpies (BE) for $M^+(\text{TAAQ})$ complexes were calculated by the following equation,

$$\text{BE} = \Delta_{\text{bind}}H = H[M^+] + H[\text{TAAQ}] - H[M^+(\text{TAAQ})]$$

where $H[M^+]$, $H[\text{TAAQ}]$, and $H[M^+(\text{TAAQ})]$ are the enthalpies of metal cation (M^+), TAAQ, and their complex $M^+(\text{TAAQ})$, respectively. A similar equation was used to compute the Gibbs energy of binding, $\Delta_{\text{bind}}G$.

Natural energy decomposition analysis (NEDA)^{48,49} was performed to provide an understanding of the individual interactions making up the overall binding in each complex. These forces include electrostatic (ES), polarization (POL), charge transfer (CT), exchange and correlation (XC), and deformation (DEF) components, which contribute to the total binding energy in the $M^+(\text{TAAQ})$ complexes. The ES and POL components account for permanent and induced electrostatic interactions between two monomers (in this case, hosts and guests), respectively. The CT term arises from interactions between filled orbitals and vacant ones between the two species, otherwise known as covalent interactions. The XC energy is attributed to exchange and correlation interactions of electrons arising from putting the host and guest species together. The DEF component is associated with the deformation of wave functions of isolated fragments compared to perturbed fragments in optimized structures. The NEDA calculations were done by the NBO 7 program implemented in the Gaussian 16 Revision C.01 software package.⁵⁰

4.3 Results and Discussion

4.3.1 SORI-CID Reactions.

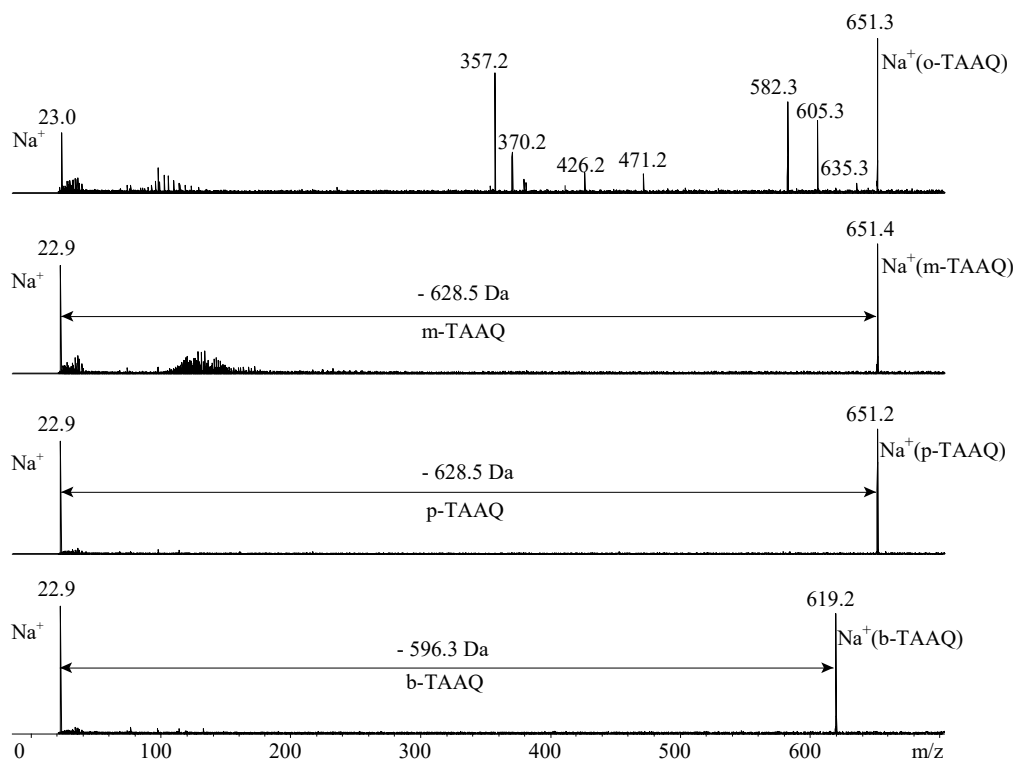


Figure 4.1 SORI-CID mass spectra of the complexes of Na⁺ with o-, m-, p- and b-TAAQs, respectively.

In Figure 4.1 and Figure C1, the SORI-CID mass spectra of M⁺(TAAQ) complexes (where TAAQ = o-, m-, p- and b-TAAQ, and M⁺ = Li⁺, Na⁺, K⁺, Rb⁺ and Cs⁺) are displayed. Note that when the metal cation is Li⁺, if Li⁺ is formed upon fragmentation it would not be seen because its mass is not detectable using the FT-ICR used in these studies. The SORI-CID mass spectra for complexes of Na⁺ with o-TAAQ and Li⁺ with o-, m-, p- and b-TAAQ,

show significant fragmentation of the TAAQ host. The possible chemical identities and formulae of fragments of lithiated o-, m-, and p-TAAQ are summarized in Table C1. All other complexes of alkali metal cations with TAAQs simply lose the TAAQ host, leaving the alkali metal cations observed in the spectra. To facilitate our description of the dissociation pathways, oxygen atoms in each TAAQ are numbered as shown in Scheme C1. The numbers of oxygens start from the top left corner and go counterclockwise, respectively, giving O1, O2, O3 and O4. O1 and O2 are on the same side of anthracene, so are O3 and O4.

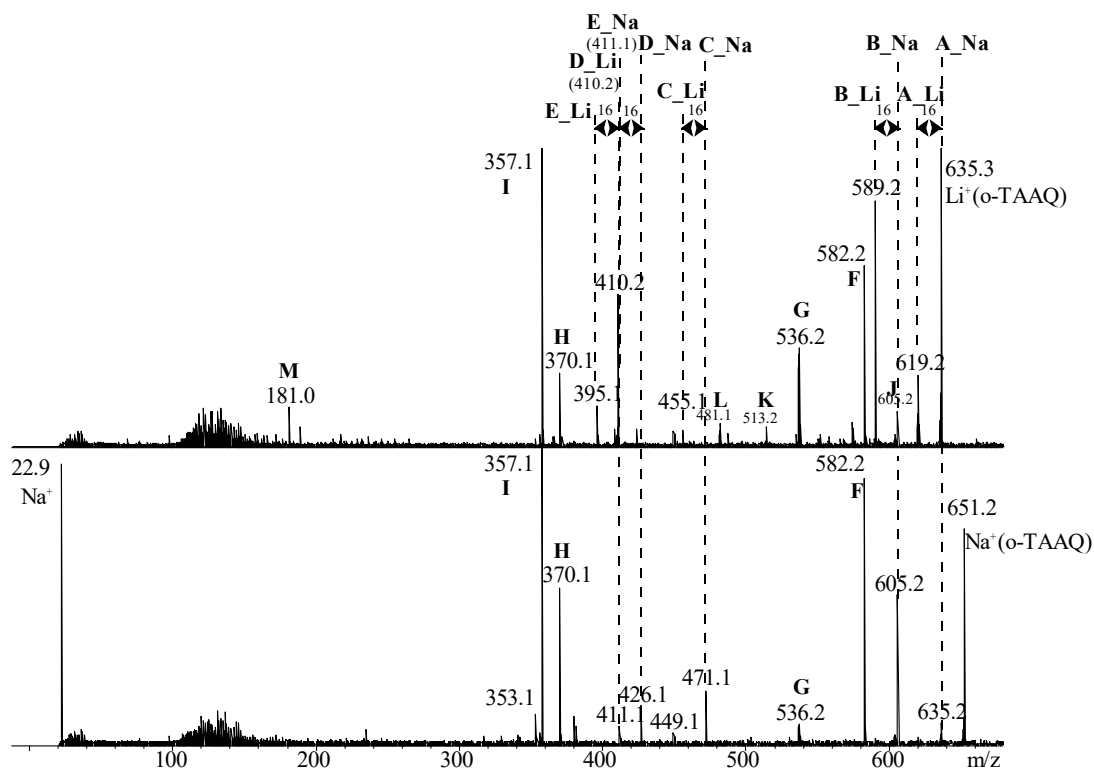


Figure 4.2 Comparison of the SORI-CID mass spectra for $\text{Li}^+(\text{o-TAAQ})$ and $\text{Na}^+(\text{o-TAAQ})$.

As shown in Figure 4.2, the SORI-CID spectrum for the $\text{Li}^+(\text{o-TAAQ})$ complex (m/z 635.3) and $\text{Na}^+(\text{o-TAAQ})$ complex (m/z 651.3) produce four fragment ions with the same m/z values at 582.2 (**F**), 536.2 (**G**), 370.1 (**H**) and 357.1 (**I**) whose structures are proposed to be identical and not to contain metal cation. The m/z values of the fragments resulting from $\text{Li}^+(\text{o-TAAQ})$ are observed at 619.2 (**A_Li**), 589.2 (**B_Li**), 455.1 (**C_Li**), 410.2 (**D_Li**), 395.1 (**E_Li**). Each of them is 16.0 Da less than the corresponding fragment observed in the spectrum of $\text{Na}^+(\text{o-TAAQ})$, which are at m/z 635.2 (**A_Na**), 605.2 (**B_Na**), 471.1 (**C_Na**), 426.1 (**D_Na**), and 411.1 (**E_Na**), respectively. The proposed structures of the same letter labeled fragments are proposed to be the same except for the metal cation, since the molar mass difference of Li and Na is 16 Da. Besides the fragments mentioned above, there are four fragments unique to $\text{Li}^+(\text{o-TAAQ})$, which can be seen at m/z 605.2 (**J**), 513.2 (**K**), 481.1 (**L**), 181.0 (**M**). Na^+ is observed as a fragment in the spectrum of $\text{Na}^+(\text{o-TAAQ})$.

Possible dissociation pathways for $\text{Li}^+(\text{o-TAAQ})$ and $\text{Na}^+(\text{o-TAAQ})$ are shown in Schemes 4.2 and 4.3, respectively.

4.3.1.1 Fragment ions of $\text{Li}^+(\text{o-TAAQ})$ and $\text{Na}^+(\text{o-TAAQ})$ with similar structures containing the metal cation.

The fragment ion **A_Li** (m/z 619.2) was formed by losing 16 Da which is CH_4 . Two different proposed structures of **A_Li** are given in Figure C5. The lost CH_4 could come from a CH_3 radical on O4 and a H radical of a methyl group on O1, and this path results in the **A_Li_diff** structure. It is also possible for a CH_3 radical on O2 and a H radical of a methyl group on O1 to be lost leading to the **A_Li_same** structure. The **A_Li_diff** ion is computed to be 13.3 kJ mol^{-1} lower in enthalpy than the **A_Li_same** ion. A similar loss of CH_4 from $\text{Na}^+(\text{o-TAAQ})$ was observed. Thus, structures similar to **A_Li** were proposed for **A_Na**, which are shown in Figure C6. The **A_Na_diff** ion was also found to be lower in enthalpy than the **A_Na_same** ion by 15.8 kJ mol^{-1} . Based on the energetics presented, the proposed structures for the **A_Li** and **A_Na** fragment ions are most likely due to the loss of methane consisting of CH_3 and H radicals from opposite sides of the anisole as shown in Scheme 4.2 and 4.3.

The loss of 46.0 Da from both $\text{Li}^+(\text{o-TAAQ})$ and $\text{Na}^+(\text{o-TAAQ})$ are identified as losses of the dimethyl ether, CH_3OCH_3 , giving rise to mass peaks at m/z 589.2 and 605.2, respectively. The possible dissociation mechanism and two possible structures for both the **B_Li** and **B_Na** ions are shown in Figures S7 and S8. The structures with the loss of a methyl radical from O2 and a methoxy radical from O1 are 29.6 and 45.2 kJ mol^{-1} lower in enthalpy than the structures with the loss of a methyl radical from O2 and a methoxy radical from O3 for **B_Li** and **B_Na**, respectively. According to the tandem SORI-CID experiments (MS/MS) on **B_Na**, as shown in Figure C4, **B_Na** (605.2 Da) loses 582.2 Da

to yield a small amount of Na^+ as a fragment, with no other fragment observed. This indicates that the electron prefers staying in the neutral **F** (582.2 Da), rather than transferring to Na^+ . The computed ionization energy at the B3LYP-D3/def2svp level of theory for Na is $516.7 \text{ kJ mol}^{-1}$, which is 13.0 kJ mol^{-1} lower than that of the neutral fragment, $529.7 \text{ kJ mol}^{-1}$, accounting for the observation of Na^+ rather than a m/z 582.2 ion. The ionization energy of Li is $534.4 \text{ kJ mol}^{-1}$ at the B3LYP-D3/def2svp level of theory which is 4.7 kJ mol^{-1} larger than that of neutral **F**, meaning that we would expect to see m/z 582.2, fragment **F**, rather than Li^+ . A tandem SORI-CID spectrum of **B_Li** (589.2 Da) as shown in Figure C3 suggests the parent ion dissociated to form **G** (m/z 536.2) and **L** (m/z 481.2). Li^+ was not experimentally detected and **F** was not observed either. **G** is a fragment of **F**, which suggests a possibility that **B_Li** first lost Li to form **F** and then dissociated to yield **G**.

The loss of 180.1 Da from $\text{Li}^+(\text{o-TAAQ})$ and $\text{Na}^+(\text{o-TAAQ})$ results in the formation of fragment ion **C_Li** at m/z 455.1 and **C_Na** at m/z 471.1, respectively. Based solely on the mass of the fragment, the 180.1 Da could be $\text{C}_{14}\text{H}_{12}$ or $\text{C}_{12}\text{H}_4\text{O}_2$ as shown in Figures S9 and S10. The two possible fragmentation pathways would both involve some rearrangement, but the loss of $\text{C}_{12}\text{H}_4\text{O}_2$ that makes the **C** ions carry an isopropyl group would require extensive rearrangement and result in an overly unsaturated structure for the neutral loss. The structure presented for loss of $\text{C}_{14}\text{H}_{12}$ assumes two anisoles on the same side of the anthracene unit are lost and the two oxygens migrate to the adjacent carbon of the anthraquinodimethane moiety, forming a didydroxylalkene substituent. This loss

requires much less rearrangement and a neutral fragment structure that is easily accounted for from the precursor ion.

Fragment **D_Li** (m/z 410.2) of $\text{Li}^+(\text{o-TAAQ})$ and **D_Na** (m/z 426.1) of $\text{Na}^+(\text{o-TAAQ})$ were formed through the loss of 225 Da ($\text{C}_{15}\text{H}_{13}\text{O}_2$) from their parent ions. It is proposed that the fragmentation occurred by cleaving the carbon-carbon double bond connected to the anthracene at carbon 9 of the parent ion and abstracting a H radical. The remaining radical in the anthracene was delocalized along the π -orbitals in the anthracene group and the other carbon-carbon double bond connected to the other side of the anthracene at carbon 10. The proposed mechanism and structures of **D_Li** and **D_Na** are provided in Figures S11-12.

Figures S13-14 show the product of the loss of a neutral moiety with a mass of 240 Da ($\text{C}_{16}\text{H}_{16}\text{O}_2$) from $\text{Li}^+(\text{o-TAAQ})$ and $\text{Na}^+(\text{o-TAAQ})$, leading to the observation of **E_Li** and **E_Na** fragment ions. The fragmentation is proposed to undergo a pathway that involves the cleavage of the carbon-carbon double bond connected to the anthracene at carbon 9 of the parent ion and concerted back migration of two hydrogens from the neutral, as well as loss of 16 Da (CH_4) from the remaining two anisoles. In these structures, Li^+ and Na^+ ions are proposed to bind with the remaining two oxygens, while adjacent aromatic groups may offer some stabilization via cation- π interactions.

4.3.1.2 SORI-CID of Fragment ions without a metal cation in Li⁺(o-TAAQ) and Na⁺(o-TAAQ)

The proposed structure of **F** fragment ion (m/z 582.2) that was observed in the SORI-CID spectra of Li⁺(o-TAAQ) and Na⁺(o-TAAQ) is shown in Figure 4.2. It was formed by neutral losses of 53.1 and 69.0 Da, which are equivalent to neutral losses of the metal (Li and Na, respectively) and dimethyl ether. As shown in Figure C3, MS/MS on the m/z 589 and 605 fragment ions resulting from losses of dimethyl ether from Li⁺(o-TAAQ) and Na⁺(o-TAAQ), respectively, did not show any m/z 582 ion. Such observation means that the loss of the neutral metal and dimethyl ether probably occurs as a primary fragmentation, or the activation that results in neutral metal loss from the precursor ion rapidly follows through dimethyl ether loss as well, since there is no fragment ion resulting from neutral metal loss observed in the CID spectra. The methyl (from O1) and methoxy groups (from O2) lost in these fragmentations are proposed to be from anisoles on the same side of anthracene forming **F**_same, or by anisoles from different side of anthracene (O2 and O3) forming **F**_diff, or by diagonal anisoles (O2 and O4) forming **F**_diag. **F**_same was about 100 kJ mol⁻¹ lower in energy than the other two structures. The three possible structures of **F** are shown in Figure C15.

For both Li⁺(o-TAAQ) and Na⁺(o-TAAQ), the formation of **G** (m/z 536.2) is attributed to the loss of a CH₃OCH₃ molecule (m/z 46.0) from **F**, as evidenced by the MS/MS spectra as shown in Figures C3-4. The mechanism for forming **G** from **F** is shown in Figure C16. As shown in Figure C3, the tandem MS spectra on Li⁺(o-TAAQ) showed that **G** also comes from **B**_Li by loss of 53.0 Da (CH₃OCH₃ and Li).

As shown in Figures C3-4 fragment **H** (m/z 370.1) is formed from **F** (m/z 582.2) upon loss of $C_{14}H_{12}O_2$ (m/z 212.1 Da). The possible structure of **H** is shown in Figure C17. Two anisoles (containing O3 and O4) of **F** were lost following a concerted back migration of two hydrogens from the leaving anisoles.

Fragment **I** (m/z 357.1) was the dominant fragment of both **D_Li** and **D_Na** by losing 53.1 Da and 69.1 Da, respectively, as shown in Figures C3-4. As shown in Figure C18, the structure of **I** can be regarded as losing CH_3OCH_3 as well as Li from **D_Li** or Na from **D_Na**. According to the tandem mass spectra shown in Figure C3-4, **I** (m/z 357.1) further dissociates to yield m/z 353.1, which was a 4.0 Da ($2xH_2$) loss from **I**.

4.3.1.3 Fragment ions only observed in the SORI-CID spectra of $Li^+(o-TAAQ)$

Fragment **J** (m/z 605.2) was formed by loss of 30.0 Da from $Li^+(o-TAAQ)$. Two proposed structures of **J** are shown in Figure C19. The loss of 30.0 Da is loss of formaldehyde (CH_2O). This loss likely originates from a CH_3O group, which may come from either O1 or O3 forming **J_O1** or from O2 or O4 forming **J_O4**, and a concerted back migration of H to the CH_3O leaving site. The lowest energy structure is **J_O4** which is 18.6 kJ mol^{-1} lower in enthalpy than **J_O1**.

Fragment **K** (m/z 513.2) was formed by a concomitant loss of C_7H_6O and CH_4 . The C_7H_6O was proposed to be an anisole radical ($C_6H_4OCH_3$) and one hydrogen from the anisole radical migrating back to the remaining part of $Li^+(o-TAAQ)$. The CH_4 could come from a CH_3 radical from O2 and a H radical from the methyl group on O3 giving the **K_diff**

structure, or CH₃ from O4 and a H from methyl group on O3 giving **K_{same}**. Two proposed structures were shown in Figure C20. **K_{diff}** is 31.6 kJ mol⁻¹ lower in energy than **K_{same}**.

Fragment **L** (m/z 481.2) (Figure C21), is likely formed by loss of 108.0 Da (C₇H₈O) from **B_{Li}**. The C₇H₈O was proposed to be composed of an anisole radical (C₆H₄OCH₃·) and a proton radical (H·). The remaining CH₂· bonded with the alkene radical to form a heterocycle.

Two structures were proposed for fragment **M** (m/z 181.0) as shown in Figure C22. The computed energy of **M_{C10a}** in which the carbon cation at carbon 10a was 72.6 kJ mol⁻¹ less in enthalpy than the **M_{C9}**, where the carbon cation was on carbon 9. The vacant orbitals of carbon 10a enabled the π-electrons on the carbon-carbon double bond close to carbon 10a to delocalize, thus providing stabilization to **M_{C10a}**.

4.3.1.4 Fragmentation of Li⁺(m-TAAQ)

The proposed dissociation pathways for Li⁺(m-TAAQ) are shown in Figure C24 and the proposed structures for fragments of Li⁺(m-TAAQ) are displayed in Figure C25-31. Since the values of m/z of Li⁺(m-TAAQ) and Li⁺(o-TAAQ) are the same, fragments of which with the same m/z are proposed to have similar structures except the different TAAQs. These fragments include m/z **619**, **605**, and **513**.

Fragment **619** (m/z 619.3) is a loss of 16.0 Da from the parent Li⁺(m-TAAQ) ion. As shown in Figure C25, the basic dissociation resulting in loss of CH₄ is similar to the formation of fragment **A_{Li}** from Li⁺(o-TAAQ). Two possible structures are proposed, and

the lowest energy structure is **619_1**, where Li^+ is bound to anisole oxygens O2 and O3. When Li^+ interacts with the O1 and O4, that are bridged by a CH_2 group to give **619_2**, the enthalpy is 53.2 kJ mol^{-1} larger than **619_1**.

Fragment **605_m** (m/z 605.3) is a primary fragment of $\text{Li}^+(\text{m-TAAQ})$ formed by loss of 30.0 Da (CH_2O). As shown in Figure C28, OCH_3 group was lost from an anisole at a distance from Li^+ with a concerted back migration of hydrogen radical from the OCH_3 moiety, leading to the **605_m** fragment ion. A similar loss was observed in the dissociation of $\text{Li}^+(\text{o-TAAQ})$.

Fragment **603** (m/z 603.2) ion was formed by losing 16.0 Da from fragment **619**. It was fair to propose that the loss of 16.0 Da was CH_4 from the anisoles close to Li^+ as shown in Figure C26.

$\text{Li}^+(\text{m-TAAQ})$ (m/z 635.3) loses 44.0 Da to yield **591** fragment (m/z 591.3). The proposed dissociation mechanism involves two types of bond cleavage as shown in Figure C28. One is the cleavage of an O-CH_3 with a concerted hydrogen back migration to the remaining O radical. The second is a Ph-OCH_3 bond cleavage taking place on another anisole with a hydrogen back migration to the remaining Ph radical. It is most likely that these CH_2 and OCH_2 fragments leave as oxirane or acetaldehyde (44 Da). As discussed above, $\text{Li}^+(\text{o-TAAQ})$ undergoes a loss of dimethyl ether forming a Ph-O-Ph structure. In the present case, back migration of hydrogen atoms and the formation of oxirane instead of dimethyl ether is likely driven by the fact that making a cross-link is too high in energy (53.8 kJ mol^{-1} in enthalpy at the level of B3LYP-D3/6-31+G(d,p) on C, H, O and def2svp on Li) for the meta substituted anisoles.

Fragment **575** (m/z 575.2) was formed by losing 16.0 Da from fragment **591** or by losing 43.9 Da from fragment **619**. As shown in Figure C29, a CH_3 on O3 and a H of the methyl group connected to O2 were lost from **591**. The 43.9 Da loss from **619** was proposed to be oxirane or acetaldehyde, which was also observed in the formation of **591** from the parent $\text{Li}^+(\text{m-TAAQ})$.

Both **591** and **619** primary fragment ions of the parent $\text{Li}^+(\text{m-TAAQ})$ dissociated to form fragment **547** (m/z 547.2) by losing 44.1 Da and 72.0 Da, respectively. The 44.1 Da is proposed to be neutral oxirane, similar to the formation of **591** from **635** as described above (see Figure C30). The 72.0 Da loss from **619** forming **547** is proposed to be $\text{C}_3\text{H}_4\text{O}_2$. As displayed in Figure C30, $\text{O}(1)\text{CH}_2\text{O}(4)$ was lost but the two remaining benzene radicals abstracted back two H radicals. The two CH_3 groups on O2 and O3 were lost and the two remaining O2 and O3 radicals abstracted back two H radicals.

Fragment **513** (m/z 513.2) is a primary fragment of $\text{Li}^+(\text{m-TAAQ})$ (m/z 635.3). A similar fragmentation pathway was also observed when $\text{Li}^+(\text{o-TAAQ})$ (m/z 635.3) was dissociated to yield **K** (m/z 513.2) as mentioned above. As shown in Figure C31, the loss of 122.1 Da is due to CH_3 (16.0 Da) and $\text{C}_7\text{H}_7\text{O}$ (106.1 Da), following the mechanism proposed in Figure C20.

4.3.1.5 Fragmentation of $\text{Li}^+(\text{p-TAAQ})$

As shown in Figure C1, two fragments **620** (m/z 620.3) and **605_p** (m/z 605.2) were observed in the unimolecular decomposition of $\text{Li}^+(\text{p-TAAQ})$. The **620** fragment ion was

formed by loss of 15.0 Da (CH_3) from $\text{Li}^+(\text{p-TAAQ})$. It is worth noting that the loss of 15.0 Da (CH_3) from $\text{Li}^+(\text{p-TAAQ})$ is different from the loss of 16.0 Da (CH_4) from $\text{Li}^+(\text{o-TAAQ})$ and $\text{Li}^+(\text{m-TAAQ})$. Since these are para-substituted anisoles on AQ, presumably the methoxyl group of each anisoles are too far from each other to be able to participate in concerted rearrangements leading to CH_4 loss, resulting in simple cleavage of the O- CH_3 bond Figure C33.

The mechanism for the formation of **605_p** (Figure C34) from $\text{Li}^+(\text{p-TAAQ})$ is the same as for the formation of **605_m** from $\text{Li}^+(\text{m-TAAQ})$ and **J** (m/z 605.3) from $\text{Li}^+(\text{o-TAAQ})$.

4.3.1.6 Fragmentation of $\text{Li}^+(\text{b-TAAQ})$

The m/z values and proposed chemical formulae for the fragments resulting from $\text{Li}^+(\text{b-TAAQ})$ are listed in Table C1. The fragments of $\text{Li}^+(\text{b-TAAQ})$ are very different than those from Li^+ complexes with o-, m- and p-TAAQ because of their significant structural differences in the ether units. Nevertheless, the fragment 181.0 of $\text{Li}^+(\text{b-TAAQ})$ can still be proposed as the same fragment 181.0 (**M**) observed for $\text{Li}^+(\text{o-TAAQ})$, since 181.0 is only relevant to the anthracene part of the precursor ion.

4.3.2 Energy-resolved SORI-CID

Energy-resolved SORI-CID experiments were performed to determine the relative gas-phase stabilities of the $\text{M}^+(\text{TAAQ})$ host-guest complexes where the only decomposition

observed was loss of neutral TAAQ. The breakdown curves are shown in Figure 4.3 for the $\text{Na}^+(\text{TAAQ})$ complexes at both 10 and 15 mbar of Ar reservoir pressure. Similar figures for other metals are shown in Figure C35 and comparisons of the different metals with each of the TAAQs are shown in Figures C36-39.

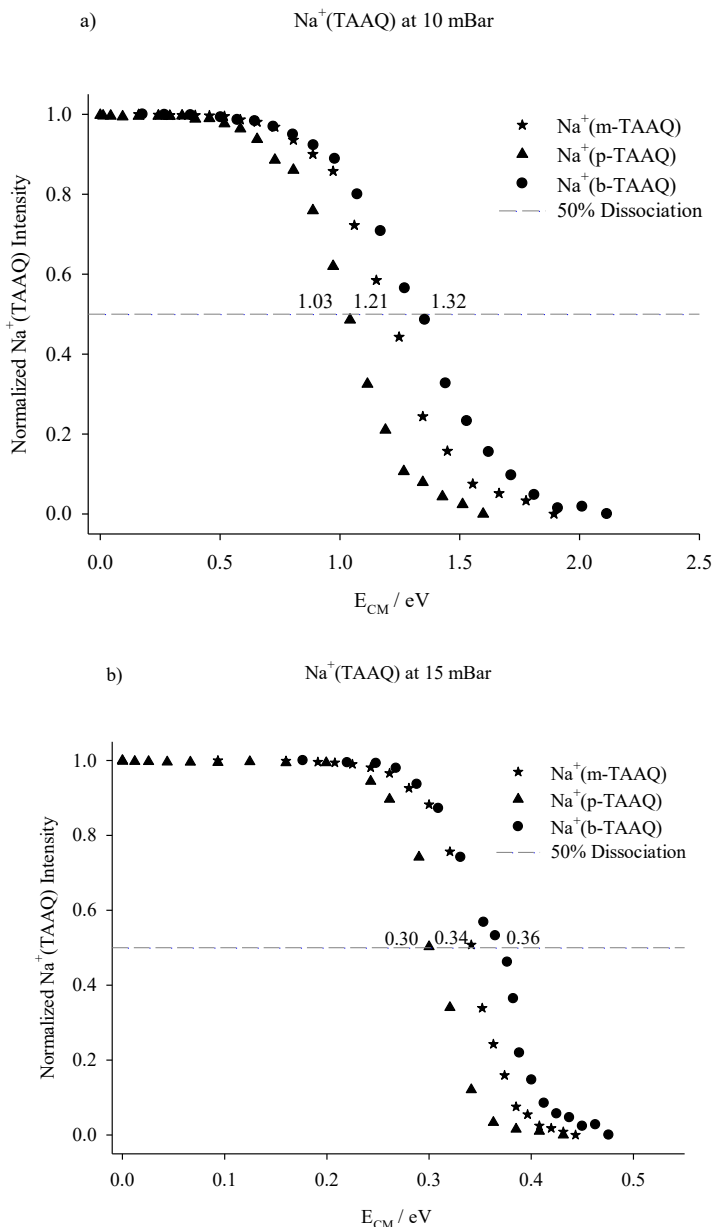


Figure 4.3 Energy-resolved SORI-CID breakdown curves for the $\text{Na}^+(\text{TAAQ})$ complexes under a) 10 mBar and b) 15 mBar Ar reservoir pressure.

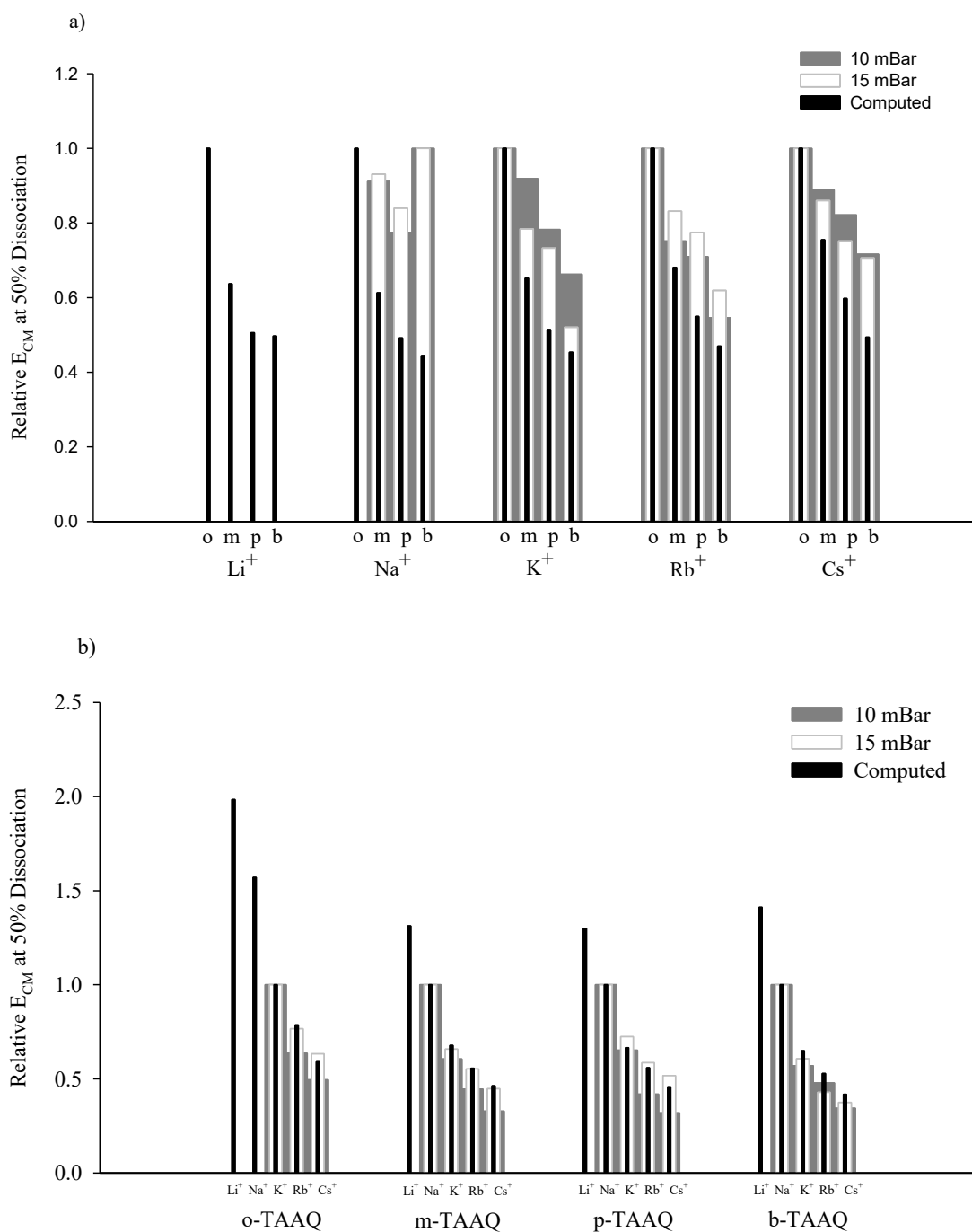


Figure 4.4 Relative center of mass collision energies at half dissociation for loss of neutral TAAQ from the $M^+(TAAQ)$ complex ions at 15 mbar (black bars) and 10 mbar (grey bars) of reservoir Ar pressure. Plot a) compares the metal cation binding to each of the TAAQs and plot b) compares the TAAQ binding to each of the metal cations. Also shown are the relative binding energies computed at the B3LYP-D3/6-31+G(d,p) on C, H, O and def2svp on metals level and basis set (black bars).

The relative center-of-mass energies ($E_{50\%}$) for dissociation of the K^+ complexes with o-, m-, p- and b-TAAQs are 1.00, 0.92, 0.78 and 0.66 eV, respectively, with 10 mbar reservoir pressure as seen in Figure 4.4a, with the same decreasing trend over this series at 15 mbar reservoir pressure. These experimental results indicate that the binding energies decrease over the series $K^+(\text{o-TAAQ}) > K^+(\text{m-TAAQ}) > K^+(\text{p-TAAQ}) > K^+(\text{b-TAAQ})$ in the gas phase. Like the K^+ complexes, Rb^+ and Cs^+ also show the strongest binding to o-TAAQ, followed by m-TAAQ, p-TAAQ and b-TAAQ in the gas phase. Although Li^+ cannot be detected by FT-ICR mass spectrometer, the computed binding energy of lithiated TAAQs are displayed in Figure 4.4a the trend of which is predicted to also follow the order $Li^+(\text{o-TAAQ}) > Li^+(\text{m-TAAQ}) > Li^+(\text{p-TAAQ}) > Li^+(\text{b-TAAQ})$.

The $Na^+(\text{o-TAAQ})$ complex is different from the other sodiated TAAQs as discussed in Section 3.1 in that metal cation is not lost, but the ion undergoes complex fragmentation, suggesting strong $Na^+/\text{o-TAAQ}$ binding compared to Na^+ binding to the other TAAQs. It is surprising to note that the breakdown curves for the other Na^+ complexes suggest that the most strongly bound complex is with b-TAAQ ($E_{50\%} = 1.32$ eV) followed by m-TAAQ ($E_{50\%} = 1.21$ eV) and p-TAAQ ($E_{50\%} = 1.03$ eV) under 10 mbar reservoir with the same trend observed under 15 mbar reservoir pressure. These experiments suggest that the binding energies of Na^+ to the TAAQs decrease over the series $Na^+(\text{o-TAAQ}) > Na^+(\text{b-TAAQ}) > Na^+(\text{m-TAAQ}) > Na^+(\text{p-TAAQ})$. For Na^+ , binding to b-TAAQ is the second strongest of the four TAAQ's and for the other metal cations the $M^+(\text{b-TAAQ})$ displays the weakest binding. However, the computed binding energy of $M^+(\text{b-TAAQ})$ follows the trend $Na^+(\text{o-TAAQ}) > Na^+(\text{m-TAAQ}) > Na^+(\text{p-TAAQ}) > Na^+(\text{b-TAAQ})$ which is different from

the experimental result. Thus, the proposed structures of $\text{Na}^+(\text{b-TAAQ})$ are worth a more detailed look and will be discussed in Section 4.3.3.4.

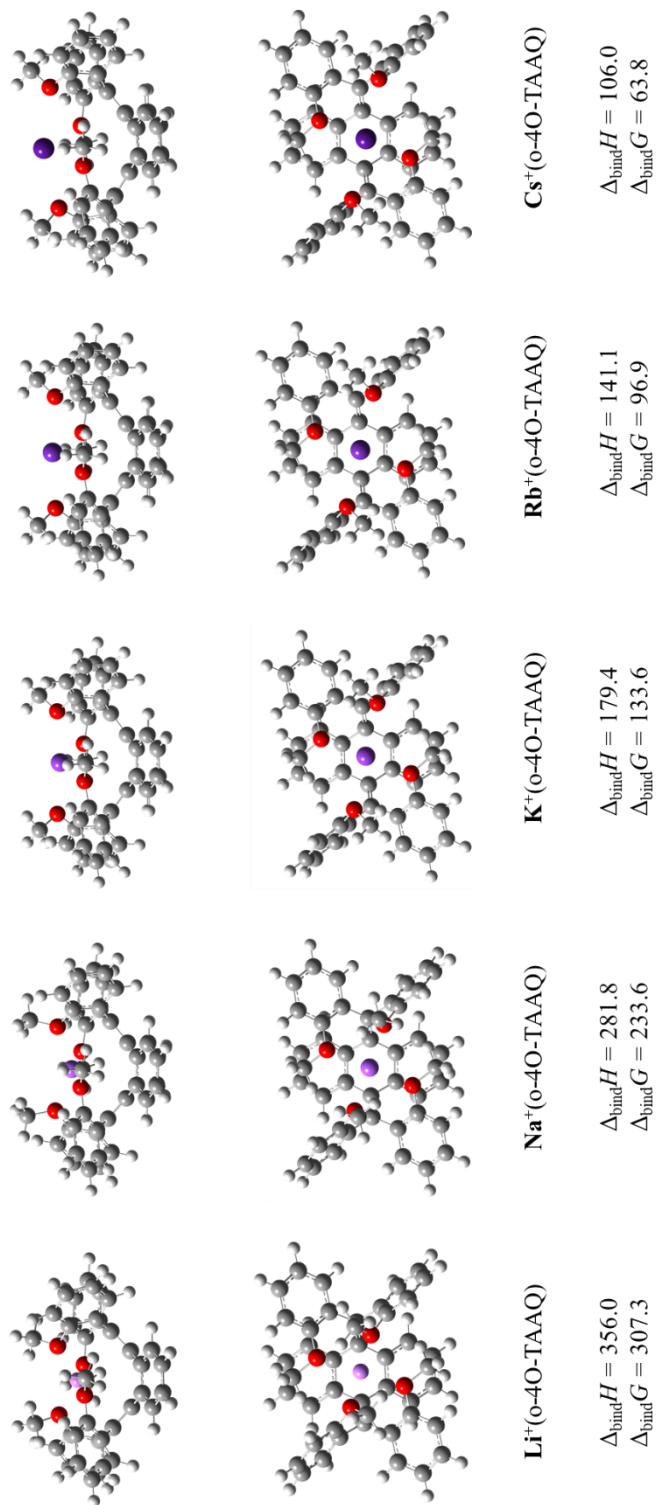
In Figure 4.4b, the results of the ER-SORI-CID experiments are arranged to compare the relative gas-phase stability of a particular TAAQ host binding with each of the different alkali metal cations. In all cases, the trend in gas-phase stabilities for the $\text{M}^+(\text{TAAQ})$ is found to be $\text{Na}^+(\text{TAAQ}) > \text{K}^+(\text{TAAQ}) > \text{Rb}^+(\text{TAAQ}) > \text{Cs}^+(\text{TAAQ})$ under both 10 mbar and 15 mbar reservoir pressure. These results are expected for electrostatic ion-dipole and ion-induced dipole complexes.

Before discussing the relative computed binding energies, we discuss the computed structures of the $\text{M}^+(\text{TAAQ})$ complexes.

4.3.3 Computed Structures for the $\text{M}^+(\text{TAAQ})$ Complexes.

Alkali metal cations can not only interact with oxygen atoms, but also with the π environment of TAAQs. As shown in Scheme C1, the π environment consists of three aromatic systems, the two anisoles on each side of anthracene and the anthracene itself. Structures of an alkali metal cation occupying these positions were all computed, but in this discussion, we focused on the lowest energy structures.

Figure 4.5 B3LYP-D3/6-31+G(d,p)/Def2-SVP computed lowest energy structures of M^+ (o-TAAQ) $\Delta_{\text{bind}}H$ and $\Delta_{\text{bind}}G$ are in unit kJ mol^{-1} at 298 K, 1 atm.



4.3.3.1 Computed structures for M^+ (o-TAAQ).

As shown in Scheme 4.1, all four methoxy oxygens of o-TAAQ are above the anthracene, forming an eagle-paw like structure. In the lowest energy structure of M^+ (o-TAAQ), M^+ (o-4O-TAAQ) seen in Figure 4.5, the metal cation is bound to the four oxygens in a tetrahedral-like shape. In Table 4.1, it can be seen that the distances from O2 and O4 to the alkali metal cation are the same, as are the distances from O1 and O3 to the alkali metal cations and the differences in the distances from M^+ to O2/O4 and to O1/O3 are not that different, at most 0.2 Å. The side view structures in Figure 4.5 and the data in Table 4.1, show that as M^+ increases in size, from Li^+ to Cs^+ , its distance from the centre of the structures also increases, from 2.63 Å to 4.03 Å. As is also shown in Figure 4.5 and Figure 4.4b, the binding energies or relative binding energies, respectively, decrease as the metal cation increases from Li^+ to Cs^+ , and that also agrees with the experimental trends determined from the ER-SORI-CID experiments from K^+ to Cs^+ .

Table 4.1 Distances (Å) from alkali metal cations to the oxygens nearby and distances (Å) from Li^+ to the middle of anthracene computed by B3LYP- D3/6-31+G(d,p) on C, H, O and def2svp on metal.

| | o-TAAQ ^a | | | m-TAAQ ^b | | p-TAAQ ^c | | b ^d |
|---------------|---------------------|--------|------------|---------------------|------|---------------------|------|---|
| | O2, O4 | O1, O3 | Anthracene | O2 | O3 | O2 | O3 | O |
| Li^+ | 2.19 | 1.99 | 2.63 | 1.96 | 1.91 | 4.32 | 5.2 | 2.03 (O1, O2) 1.92 (O4) 2.85 (O3) |
| Na^+ | 2.35 | 2.34 | 2.82 | 2.43 | 2.33 | 4.34 | 4.45 | 2.41 |
| K^+ | 2.68 | 2.70 | 3.41 | 2.92 | 2.75 | 4.40 | 4.40 | 2.97 |
| Rb^+ | 2.84 | 2.87 | 3.67 | 3.10 | 3.10 | 4.40 | 4.41 | 3.15 |
| Cs^+ | 3.02 | 3.05 | 4.03 | 3.31 | 3.31 | 4.53 | 4.46 | 3.37 |

^a $\text{M}^+(\text{o-4O-TAAQ})$ (M=Li, Na, K, Rb and Cs)

^b $\text{M}^+(\text{m}_1\text{-2O-3Ph-TAAQ})$ (M=Li, Na, K, Rb and Cs)

^c $\text{M}^+(\text{p-2O-3Ph-TAAQ})$ (M=Li, Na, K, Rb and Cs)

^d $\text{M}^+(\text{b}_{2u}\text{-4O-TAAQ})$ (M = Li, Na) and $\text{M}^+(\text{b}_{2d}\text{-2O-TAAQ})$ (M = K, Rb, and Cs)

4.3.3.2 Computed structures for $\text{M}^+(\text{m-TAAQ})$.

Two structures for neutral m-TAAQ were found (Figure C1). One is $\text{m}_1\text{-TAAQ}$ in which the O1/O4 and O2/O3 pairs are close to each other and above the anthracene. The other, $\text{m}_2\text{-TAAQ}$ in which all the oxygen atoms are pointing away from the anthracene and is only 1.0 kJ mol^{-1} lower in Gibbs energy and 0.7 kJ mol^{-1} higher in enthalpy than $\text{m}_1\text{-TAAQ}$. The lowest energy structures for $\text{M}^+(\text{m-TAAQ})$ are those where the metal is bound to m-TAAQ that resembles $\text{m}_1\text{-TAAQ}$, $\text{M}^+(\text{m}_1\text{-2O-3Ph-TAAQ})$ and are shown in Table C2, (and Figure 4.6 for Na^+) where the metal cation is bound to two of the oxygen atoms. As the size of the metal cation increases, its binding distance to the oxygen atoms increases from 1.91 to 3.31 Å (Table 4.1). Based on the geometry of the m-TAAQ, it is not possible

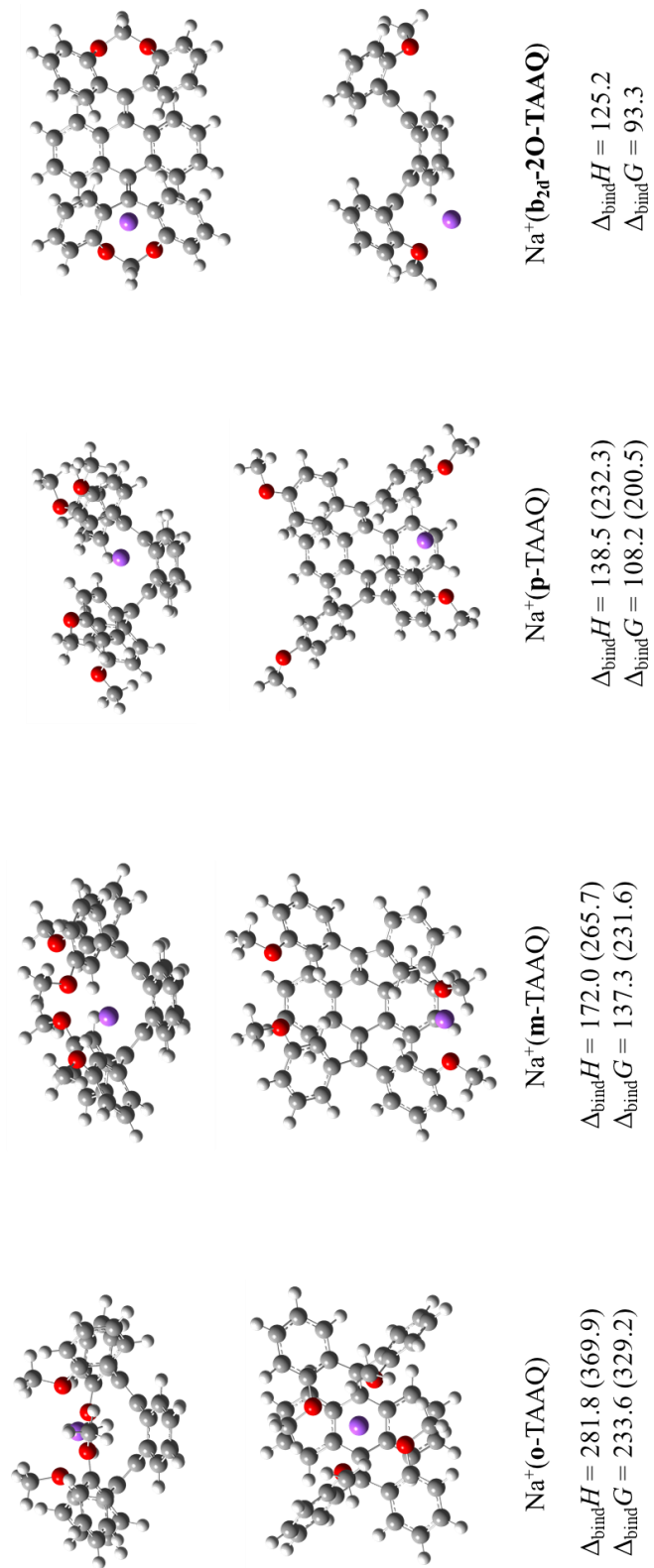
for the metal cation to bind all four oxygens. The computed binding energies of the metal cations to m-TAAQ follow the trend of $\text{Li}^+ > \text{Na}^+ > \text{K}^+ > \text{Rb}^+ > \text{Cs}^+$ and agree with the experimental trends observed from the ER-SORI-CID experiments (Figure 4.4b).

4.3.3.3 Computed Structures for $\text{M}^+(\text{p-TAAQ})$.

The lowest energy structures for the $\text{M}^+(\text{p-TAAQ})$ complexes, $\text{M}^+(\text{p-2O-3Ph})$ are those where the metal cation interacts with the π system of one of the anthracene rings and is relatively close to two oxygen atoms, O2 and O3, and much further from O1 and O4, as shown in Table C3 and Figure 4.6 for the Na^+ complex. As seen in Table 4.1, the distances from M^+ to the nearby oxygens of $\text{M}^+(\text{p-TAAQ})$ are larger than the metal to oxygen distances in $\text{M}^+(\text{o-TAAQ})$ and $\text{M}^+(\text{m-TAAQ})$. The computed binding energies of p-TAAQ binding with different alkali metal cations, follow the trend of $\text{Li}^+ > \text{Na}^+ > \text{K}^+ > \text{Rb}^+ > \text{Cs}^+$ and agree with the experimental trend from the ER-SORI-CID experiments.

According to the computed binding energies presented for the $\text{M}^+/\text{o-,m-,p-TAAQ}$ complexes, for a particular metal cation, the binding energies decrease across the series $\text{o-TAAQ} > \text{m-TAAQ} > \text{p-TAAQ}$. The most likely reason for the stronger binding with o-TAAQ is that the metal cation interacts with all four oxygen atoms. Two oxygen atoms as well as the π aromatics of m-TAAQ interact with the metal cations, however the metal cations barely interact with the oxygen atoms and bind to p-TAAQ through cation- π interactions.

Figure 4.6 Computed lowest energy structures of M^+ (o-TAAQ) by the B3LYP-D3 method with the 6-31+G(d,p) basis set used on C, H and O, and the Def2-SVP basis set on alkali metal atoms.



4.3.3.4 Computed Structures for M⁺(b-TAAQ).

The lowest energy structure for the M⁺(b-TAAQ) complexes, M⁺(b_{2d}-TAAQ), has the metal cation bound to two oxygens on one side of the anthracene (O1 and O2), as shown in Table C4 and Figure 4.6 for Na⁺. Note that other, higher binding energy structures of M⁺(b-TAAQ) complexes are shown in Tables C5 and C6. The distances between the Li⁺, Na⁺, K⁺, Rb⁺, Cs⁺ and the oxygens they are bound to in M⁺(b_{2d}-TAAQ) are 2.03, 2.47, 2.97, 3.15 and 3.37 Å, respectively (Table 4.1). The computed metal binding energies (Table 4.2) decrease across the series Li⁺ > Na⁺ > K⁺ > Rb⁺ > Cs⁺ as would be expected for electrostatically bound complexes and agree with the experimental trend from the ER-SORI-CID results.

Table 4.2 Computed binding energies (values in the bracket are computed dissociation Gibbs free energies) of the lowest energy structure of alkali metal cationized o-, m-, p-, b_{2u}-, b_{1u1d}- and b_{2d}-TAAQs. Energies are listed in kJ mol⁻¹ and calculated by B3LYP-D3/6-31+G(d,p) on C, H, O and B3LYP-D3/Def2-SVP on metal at 298K, 1atm. Values in bold are computed under the level of M06-2x/6-31+G(d,p) on C, H, O and B3LYP-D3/Def2-SVP on metal at 298K, 1atm.

| | o-TAAQ ^a | m-TAAQ ^b | p-TAAQ ^c | b-TAAQ | | |
|-----------------|-------------------------------|-------------------------------|-------------------------------|-------------------------------|-------------------------------|-------------------------------|
| | | | | b _{2u} -4O-TAAQ | b _{1u1d} -3Ph-TAAQ | b _{2d} -2O-TAAQ |
| Li ⁺ | 356 (307) 403 (358) | 227 (190) 260 (218) | 180 (146) 226 (189) | 264 (221) 306 (263) | 211(172) 250 (211) | 177 (143) 220 (185) |
| Na ⁺ | 282 (234) 311 (275) | 172 (137) 203 (161) | 138 (108) 177 (142) | 190 (149) 225 (183) | 155 (116) 189 (149) | 125 (93) 164 (129) |
| K ⁺ | 179 (134) 204 (168) | 116 (86) 154 (117) | 92 (62) 133 (93) | 107 (65) 138 (94) | 97 (61) 137 (97) | 81 (49) 120 (86) |
| Rb ⁺ | 141 (97) 161 (127) | 96 (65) 132 (94) | 77 (45) 113 (75) | 83 (43) 114 (71) | 78 (41) 116 (77) | 66 (34) 104 (72) |
| Cs ⁺ | 106 (64) 130 (97) | 80 (49) 118 (80) | 63 (32) 101 (66) | 63 (23) 99 (57) | 63 (25) 102 (64) | 52 (24) 93 (58) |

According to the computed binding energies for the lowest energy M⁺(b-TAAQ) complexes, they are the weakest of all four host/guest complexes for each of the metals, which is consistent with the ER-SORI-CID trends except that experimentally, the Na⁺(b-

TAAQ) complex was observed to be more strongly bound than the $\text{Na}^+(\text{m-TAAQ})$ and $\text{Na}^+(\text{p-TAAQ})$ complexes.

More structures of $\text{M}^+(\text{b-TAAQ})$ need to be proposed to try to explain the observed experimental trend that $\text{Na}^+(\text{o-TAAQ}) > \text{Na}^+(\text{b-TAAQ}) > \text{Na}^+(\text{m-TAAQ}) > \text{Na}^+(\text{p-TAAQ})$. A $\text{b}_{1\text{u}1\text{d}}$ -TAAQ structure as shown in Scheme 4.1 was proposed, which describes the structure that at one side of anthracene, the two oxygens (O1 and O2) are higher in position with respect to their connected benzene rings and at the other side of anthracene, the two oxygens (O3 and O4) are lower in position than their connected aromatics. As shown in Table C5, the lowest energy structure of alkali metal cationized $\text{b}_{1\text{u}1\text{d}}$ -TAAQ is $\text{M}^+(\text{b}_{1\text{u}1\text{d}}\text{-3Ph-TAAQ})$ ($\text{M} = \text{Li}, \text{Na}, \text{K}, \text{and Rb}$) where the metal cation occupies the region 3Ph as marked in Scheme 4.1. As for cesiated $\text{b}_{1\text{u}1\text{d}}$ -TAAQ, the lowest energy structure is where the Cs^+ is close to O1 and O2, named $\text{Cs}^+(\text{b}_{1\text{u}1\text{d}}\text{-2O-TAAQ})$. $\text{Cs}^+(\text{b}_{1\text{u}1\text{d}}\text{-2O-TAAQ})$ is only a few kJ mol^{-1} higher in enthalpy and Gibbs free energy than $\text{Cs}^+(\text{b}_{1\text{u}1\text{d}}\text{-3Ph-TAAQ})$. The computed binding energy of $\text{Na}^+(\text{b}_{1\text{u}1\text{d}}\text{-3Ph-TAAQ})$ is $154.8 \text{ kJ mol}^{-1}$ which is larger than that of $\text{Na}^+(\text{p-2O-3Ph-TAAQ})$ ($138.5 \text{ kJ mol}^{-1}$) but smaller than that of the $\text{Na}^+(\text{m}_1\text{-2O-3Ph-TAAQ})$ ($172.0 \text{ kJ mol}^{-1}$). The computed energy trend of this type of structure- $\text{M}^+(\text{b}_{1\text{u}1\text{d}}\text{-TAAQ})$ does not agree with the experimental trend.

Additionally, another structure of $\text{M}^+(\text{b-TAAQ})$ was proposed. As shown in Scheme C1, from the side view of these structures, $\text{b}_{2\text{u}}$ -TAAQ displays the structure that the phenolic oxygens at both sides of anthracene are at higher positions than their connected benzene ring. Among the three structures of b-TAAQ, the lowest Gibbs energy structure is $\text{b}_{2\text{d}}$ -TAAQ. The structure of $\text{b}_{1\text{u}1\text{d}}$ -TAAQ is 3.7 kJ mol^{-1} lower in enthalpy than $\text{b}_{2\text{d}}$ -TAAQ but

2.1 kJ mol⁻¹ higher in Gibbs energy than b_{2d}-TAAQ. B_{2u}-TAAQ is 29.8 kJ mol⁻¹ and 37.0 kJ mol⁻¹ higher in enthalpy and Gibbs energy respectively than b_{2d}-TAAQ. As shown in Tables C6, the lowest energy structure of Li⁺ or Na⁺ complexed with b_{2u}-TAAQ is that Li⁺ or Na⁺ sits in the middle of four oxygens of b_{2u}-TAAQ, named M⁺(b_{2u}-4O-TAAQ) (M = Li, Na). As for the complexes of K⁺, Rb⁺ and Cs⁺ with b_{2u}-TAAQ (see Tables 6), the lowest energy structures show the alkali metal cations sitting in the 3Ph region of b_{2u}-TAAQ, named M⁺(b_{2u}-3Ph-TAAQ) (M=K, Rb and Cs). Optimization of the structures of Li⁺ and Na⁺ complexed with b_{2u}-3Ph-TAAQ always led to M⁺(b_{2u}-4O-TAAQ) (M = Li, Na). It was also noticed that optimization of the structure of Cs⁺(b_{2u}-TAAQ) where Cs⁺ in the middle of four oxygens always ended with the structure where Cs⁺ sits in the region of three aromatics, Cs⁺(b_{2u}-3Ph-TAAQ). It is therefore proposed that the size of Cs⁺ is too large to be near the oxygens. The energies of potassiated and rubidiated b_{2u}-4O-TAAQ are 11.4 and 23.2 kJ mol⁻¹ higher in enthalpy than those of b_{2u}-3Ph-TAAQ, respectively.

According to the computed binding energies of the lowest energy structures as recorded in Tables S2-S6, M⁺(o-4O-TAAQ) > M⁺(b_{2u}-TAAQ) > M⁺(m₁-2O-3Ph-TAAQ) > M⁺(p-2O-3Ph-TAAQ) (M = Li, Na, K, Rb and Cs). When M = Na, the computed trend agrees with the trend of relative stability of sodiated TAAQs obtained from ER-SORI-CID experiments; that is, Na⁺(b-TAAQ) > Na⁺(m-TAAQ) > Na⁺(p-TAAQ). Although, the computed trend in the energies for complexes of K⁺, Rb⁺ and Cs⁺ with b_{2u}-TAAQ does not agree with the experimental trend, they are the lowest energy structures of M⁺(b-TAAQ).

However, the lowest energy structure of b-TAAQ is b_{2d}-TAAQ, thus the most likely structure for alkali metal cationized b-TAAQ is M⁺(b_{2d}-2O-TAAQ) (M = Na, K, Rb, and

Cs). Although the computed energy trend of sodiated TAAQ agrees with the experimental trend: $\text{Na}^+(\text{b}_{2\text{u}}\text{-4O-TAAQ}) > \text{Na}^+(\text{m-TAAQ}) > \text{Na}^+(\text{p-TAAQ})$, the most likely structure of sodiated b-TAAQ is $\text{Na}^+(\text{b}_{2\text{d}}\text{-2O-TAAQ})$ rather than $\text{Na}^+(\text{b}_{2\text{u}}\text{-4O-TAAQ})$. Additionally, there is no obvious evidence that an energy barrier exists when $\text{Na}^+(\text{b}_{2\text{d}}\text{-2O-TAAQ})$ dissociates to explain its larger binding energy versus $\text{Na}^+(\text{m-TAAQ})$ and $\text{Na}^+(\text{p-TAAQ})$. What is more, the M06-2x computational method was also used to obtain binding energies of $\text{M}^+(\text{TAAQ})$ complexes. As shown in Table 4.2, under the level of M06-2x, the trend of binding energies does not differ from the binding energies determined using the level of B3LYP-D3. Thus, the trend of gas phase stabilities observed from ER-SORI-CID, which is $\text{Na}^+(\text{b-TAAQ}) > \text{Na}^+(\text{m-TAAQ}) > \text{Na}^+(\text{p-TAAQ})$, cannot be well explained theoretically. It is inferred that there is a lower energy structure of $\text{Na}^+(\text{b}_{2\text{d}}\text{-TAAQ})$ that has not yet been found.

4.3.3.5. Analysis of Computed Binding Energies.

The computed binding energies of the lowest energy structure of each type of alkali metal cationized TAAQ complexes, $\text{M}^+(\text{o-4O-TAAQ})$, $\text{M}^+(\text{m}_1\text{-2O-3Ph-TAAQ})$, $\text{M}^+(\text{p-2O-3Ph-TAAQ})$ ($\text{M} = \text{Li, Na, K, Rb}$ and Cs) and the lowest energy structures of $\text{M}^+(\text{b-TAAQ})$ which are $\text{M}^+(\text{b}_{2\text{u}}\text{-4O-TAAQ})$ ($\text{M} = \text{Li, Na}$) and $\text{M}^+(\text{b}_{2\text{d}}\text{-2O-TAAQ})$ ($\text{M} = \text{K, Rb, and Cs}$), are summarized in Table 4.2 and displayed in Figure 4.4.

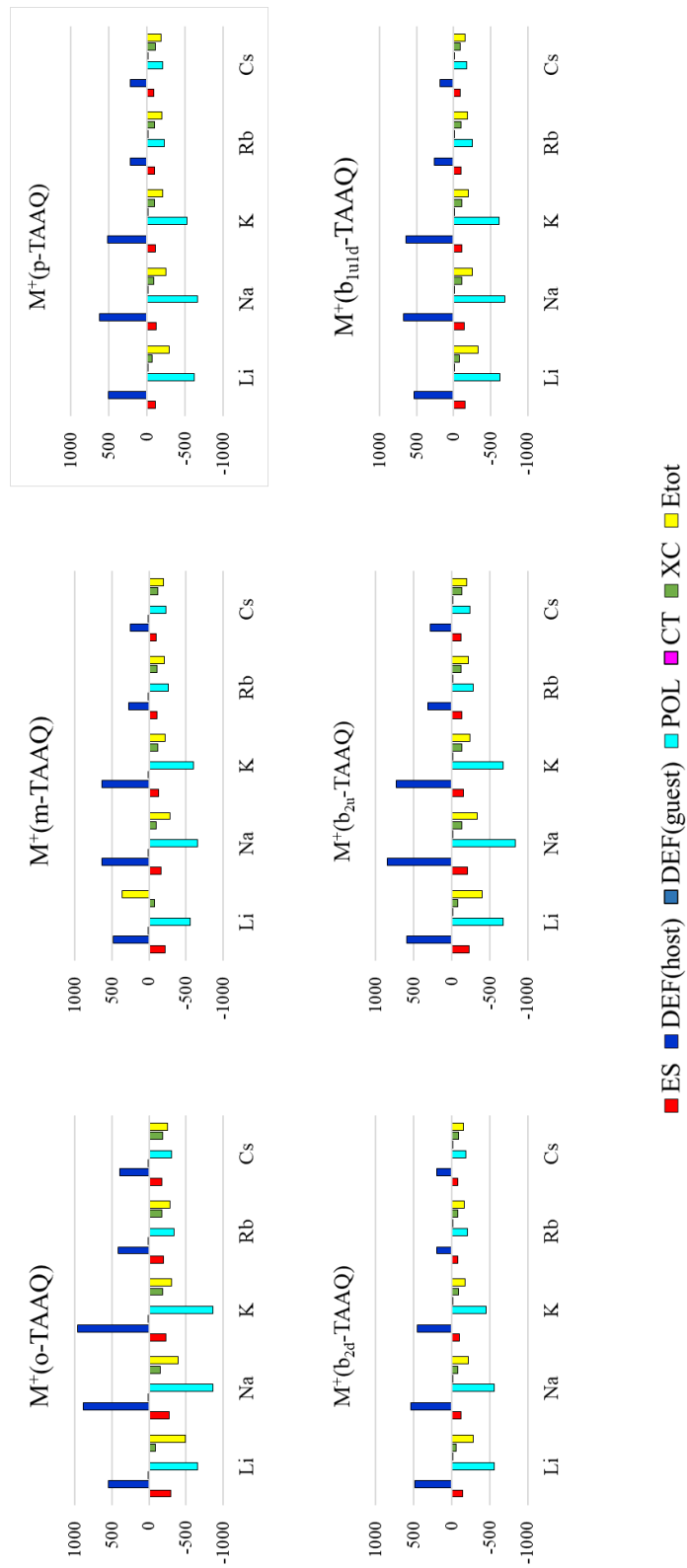
When considering the association of a certain host with different alkali metal cations, it shows the trend of $\text{Li}^+(\text{TAAQ}) > \text{Na}^+(\text{TAAQ}) > \text{K}^+(\text{TAAQ}) > \text{Rb}^+(\text{TAAQ}) > \text{Cs}^+(\text{TAAQ})$.

This trend agrees with the experimental ER-SORI-CID results. When it comes to comparing the computed and experimental relative stability of a certain M^+ complexing with different TAAQs, for K^+ , Rb^+ and Cs^+ , the experimental stability trend agrees with the computed trend showing $M^+(\text{o-TAAQ}) > M^+(\text{m-TAAQ}) > M^+(\text{p-TAAQ}) > M^+(\text{b-TAAQ})$. As for sodiated TAAQ, the ER-SORI-CID experiments show a trend of $Na^+(\text{b-TAAQ}) > Na^+(\text{m-TAAQ}) > Na^+(\text{p-TAAQ})$, which agrees with the that of computed lowest energy structures of sodiated TAAQ: $Na^+(\text{o-4O-TAAQ})$ (281.8 kJ mol⁻¹) $>$ $Na^+(\text{b}_{2u}\text{-4O-TAAQ})$ (190.1 kJ mol⁻¹) $>$ $Na^+(\text{m}_1\text{-2O-3Ph-TAAQ})$ (172.7 kJ mol⁻¹) $>$ $Na^+(\text{p-2O-3Ph-TAAQ})$ (138.5 kJ mol⁻¹).

4.3.4 Natural Energy Decomposition Analysis (NEDA)

The interactions between alkali metal cations and the TAAQs were examined by the NEDA approach to obtain deeper insights into the nature of interactions between the metal cations and TAAQ in their lowest energy structures.

Figure 4.7 Results of the NEDA computations on the lowest energy structures of M^+ (TAAQs) which are M^+ (o-4O-TAAQ), M^+ (m-2O-3Ph-TAAQ), M^+ (p-2O-3Ph-TAAQ) ($M = \text{Li, Na, K, Rb, Cs}$) and M^+ (b_{2u}-4O-TAAQ) ($M = \text{Li, Na}$), M^+ (b_{2d}-2O-TAAQ) ($M = \text{K, Rb, and Cs}$). Calculations were done by B3LYP-D3/6-31+G(d,p) on C, H, O and B3LYP-D3/Def2-SVP on alkali metals.



As shown in Figure 4.7 and Table C7, NEDA suggests that polarization (POL) components, consisting of electrostatic attractive interactions arising from induced multipoles, contribute the most (45.7%-75.5%) to the total stabilization energies of the $M^+(\text{TAAQ})$ complexes. The second largest stabilization energy (13.2%-28.1% of the total stabilization energies) comes from the electrostatic (ES) component consisting of classical interactions of permanent multipoles. The steric exchange XC component which comes from the anti-symmetry of the wavefunction accounts for 8.1%- 27.5% of the total attractive interactions. The charge transfer (CT), or covalent, component only contributes less than 1.0% to the total stabilization interactions. Overall, the attractive interactions between alkali metal cations and the TAAQs are mainly contributed by electrostatic interaction involving interactions of permanent and induced multipoles.

The POL component of $\text{Li}^+(\text{TAAQ})$ is smaller than that of $\text{Na}^+(\text{TAAQ})$, but the ES component of $\text{Li}^+(\text{TAAQ})$ is larger than that of $\text{Na}^+(\text{TAAQ})$. These results suggests that the interactions involving induced multipoles caused by Li^+ are not as strong as induced multipoles caused by Na^+ , but interactions between Li^+ and permanent multipoles are stronger than those between Na^+ and permanent multipoles.

Finally, the deformation (DEF) components which contribute to destabilizing effects due mainly to deformation of the electron cloud of the TAAQs are almost 2 times larger for Na^+ and K^+ than for of Rb^+ and Cs^+ indicating that Na^+ and K^+ distort the electron distributions of TAAQs more than Rb^+ and Cs^+ do. The DEF effect of Li^+ is between Na^+/K^+ and Rb^+/Cs^+ (see Figure 4.7).

4.4 Conclusions

In summary, this paper presents a systematic study of the structures, energies, fragmentation pathways, and interactions of $M^+(\text{TAAQ})$ complexes. Our study reveals that, except $\text{Na}^+(\text{o-TAAQ})$ and the Li^+ complexes with *o*-, *m*-, *p*- and *b*-TAAQ, all other $M^+(\text{TAAQ})$ complexes (where $M = \text{Na}, \text{K}, \text{Rb}, \text{and Cs}$) decompose to M^+ and TAAQ upon collisional activation. Both experimental and computational results indicate the relative stabilities of the $M^+(\text{TAAQ})$ complexes follow the trend: $\text{Na}^+(\text{TAAQ}) > \text{K}^+(\text{TAAQ}) > \text{Rb}^+(\text{TAAQ}) > \text{Cs}^+(\text{TAAQ})$. For the gas-phase binding energies of TAAQs with a given metal cation ($\text{K}^+, \text{Rb}^+, \text{or Cs}^+$), the experimental trend is $M^+(\text{o-TAAQ}) > M^+(\text{m-TAAQ}) > M^+(\text{p-TAAQ}) > M^+(\text{b-TAAQ})$. This trend aligns with the computationally determined stability order: $M^+(\text{o-4O-TAAQ}), M^+(\text{m}_1\text{-2O-3Ph-TAAQ}), M^+(\text{p-2O-3Ph-TAAQ})$ and $M^+(\text{b}_{2d}\text{-2O-TAAQ})$ (where $M = \text{K}, \text{Rb}, \text{and Cs}$) structures. The gas-phase relative stability of Na^+ complexes with different TAAQs, however, shows a discrepancy between experimental and computational results. Experimentally, the trend is $\text{Na}^+(\text{b-TAAQ}) > \text{Na}^+(\text{m-TAAQ}) > \text{Na}^+(\text{p-TAAQ})$, whereas the computational trend predicts: $M^+(\text{m}_1\text{-2O-3Ph-TAAQ}) > M^+(\text{p-2O-3Ph-TAAQ}) > \text{Na}^+(\text{b}_{2d}\text{-2O-TAAQ})$. The observed discrepancy between the experimental and computational trends for $\text{Na}^+(\text{TAAQ})$ complexes highlights the complexity of accurately modeling these systems. To address this challenging question, a more systematic search for the lowest-energy structures combined with the use of higher-level theoretical methods is essential.

Overall, our experimental and theoretical studies have provided significant understanding into how alkali metal ions interact with ether-functionalized arene ligands.

This knowledge has important implications for advancing selective lithium extraction techniques. The strong binding of Li^+ with *o*-TAAQ is due to its well-organized multiple ether groups, which resemble the structure of crown ethers or spherands. Understanding these interactions offers valuable insights for designing highly selective extractants to recover lithium from complex mixtures.

4.5 Acknowledgments

The authors thank NSERC, CFI, IRIF and the Laboratory for the Study of Gaseous Ion Structures, Energetics and Reactions of Memorial University. The computational resources provided by Digital Research Alliance of Canada (The Alliance) are acknowledged. YC extends gratitude to the China Scholarship Council (CSC) for funding support.

4.6 References

1. Paranthaman, M. P.; Li, L.; Luo, J.; Hoke, T.; Ucar, H.; Moyer, B. A.; Harrison, S., Recovery of Lithium from Geothermal Brine with Lithium–Aluminum Layered Double Hydroxide Chloride Sorbents. *Environmental Science & Technology* **2017**, *51* (22), 13481-13486.
2. Yao, Y.; Zhu, M.; Zhao, Z.; Tong, B.; Fan, Y.; Hua, Z., Hydrometallurgical Processes for Recycling Spent Lithium-Ion Batteries: A Critical Review. *ACS Sustainable Chemistry & Engineering* **2018**, *6* (11), 13611-13627.
3. Zhao, Y.; Wu, Y.; Liu, H.; Chen, S.-L.; Bo, S.-H., Accelerated Growth of Electrically Isolated Lithium Metal during Battery Cycling. *ACS Applied Materials & Interfaces* **2021**, *13* (30), 35750-35758.
4. Wu, X.-W.; Cui, S.-L.; Liu, S.; Li, G.-R.; Gao, X.-P., From Dendrites to Hemispheres: Changing Lithium Deposition by Highly Ordered Charge Transfer Channels. *ACS Applied Materials & Interfaces* **2021**, *13* (5), 6249-6256.
5. Swain, B., Recovery and recycling of lithium: A review. *Separation and Purification Technology* **2017**, *172*, 388-403.
6. Wang, S.; Li, P.; Zhang, X.; Zheng, S.; Zhang, Y., Selective adsorption of lithium from high Mg-containing brines using HxTiO₃ ion sieve. *Hydrometallurgy* **2017**, *174*, 21-28.
7. Zhao, Q.; Gao, J.-m.; Guo, Y.; Cheng, F., Facile Synthesis of Magnetically Recyclable Fe-doped Lithium Ion Sieve and Its Li Adsorption Performance. *Chemistry Letters* **2018**, *47* (10), 1308-1310.
8. Li, W.; Shi, C.; Zhou, A.; He, X.; Sun, Y.; Zhang, J., A positively charged composite nanofiltration membrane modified by EDTA for LiCl/MgCl₂ separation. *Separation and Purification Technology* **2017**, *186*, 233-242.

9. Zhang, H.-Z.; Xu, Z.-L.; Ding, H.; Tang, Y.-J., Positively charged capillary nanofiltration membrane with high rejection for Mg^{2+} and Ca^{2+} and good separation for Mg^{2+} and Li^+ . *Desalination* **2017**, *420*, 158-166.
10. Kim, S.; Lee, J.; Kim, S.; Kim, S.; Yoon, J., Electrochemical Lithium Recovery with a $LiMn_2O_4$ -Zinc Battery System using Zinc as a Negative Electrode. *Energy Technology* **2018**, *6* (2), 340-344.
11. Shi, C.; Jing, Y.; Xiao, J.; Wang, X.; Yao, Y.; Jia, Y., Solvent extraction of lithium from aqueous solution using non-fluorinated functionalized ionic liquids as extraction agents. *Separation and Purification Technology* **2017**, *172*, 473-479.
12. Shi, D.; Cui, B.; Li, L.; Peng, X.; Zhang, L.; Zhang, Y., Lithium extraction from low-grade salt lake brine with ultrahigh Mg/Li ratio using TBP – kerosene – $FeCl_3$ system. *Separation and Purification Technology* **2019**, *211*, 303-309.
13. Yousefi, S. R.; Amiri, O.; Salavati-Niasari, M., Control sonochemical parameter to prepare pure $Zn_{0.35}Fe_{2.65}O_4$ nanostructures and study their photocatalytic activity. *Ultrasonics Sonochemistry* **2019**, *58*, 104619.
14. Yousefi, S. R.; Ghanbari, M.; Amiri, O.; Marzhoseyni, Z.; Mehdizadeh, P.; Hajizadeh-Oghaz, M.; Salavati-Niasari, M., $Dy_2BaCuO_5/Ba_4DyCu_3O_{9.09}$ S-scheme heterojunction nanocomposite with enhanced photocatalytic and antibacterial activities. *Journal of the American Ceramic Society* **2021**, *104* (7), 2952-2965.
15. Kumar, V.; Sahu, S. K.; Pandey, B. D., Prospects for solvent extraction processes in the Indian context for the recovery of base metals. A review. *Hydrometallurgy* **2010**, *103* (1), 45-53.
16. Torrejos, R. E. C.; Nisola, G. M.; Park, M. J.; Shon, H. K.; Seo, J. G.; Koo, S.; Chung, W.-J., Synthesis and characterization of multi-walled carbon nanotubes-supported dibenzo-14-crown-4 ether with proton ionizable carboxyl sidearm as Li^+ adsorbents. *Chemical Engineering Journal* **2015**, *264*, 89-98.

17. Swain, B., Separation and purification of lithium by solvent extraction and supported liquid membrane, analysis of their mechanism: a review. *Journal of Chemical Technology & Biotechnology* **2016**, *91* (10), 2549-2562.
18. Pedersen, C. J., Cyclic polyethers and their complexes with metal salts. *Journal of the American Chemical Society* **1967**, *89* (10), 2495-2496.
19. Davoudi, M.; Mallah, M. H., Enrichment of ^6Li using dispersive liquid-liquid microextraction as a highly efficient technique. *Annals of Nuclear Energy* **2013**, *62*, 499-503.
20. Kim, D. W.; Jeon, B. K.; Kang, B. M.; Lee, N.-S.; Ryu, H.-i.; Lee, Y.-i., Adsorption and isotope effects by ion exchange with 1-aza-12-crown-4 bonded Merrifield peptide resin. *Journal of Colloid and Interface Science* **2003**, *263* (2), 528-532.
21. Hassan, R. Y. A.; Kamel, M. S.; Hassan, H. N. A.; Khaled, E., Voltammetric determination of mercury in biological samples using crown ether/multiwalled carbon nanotube-based sensor. *Journal of Electroanalytical Chemistry* **2015**, *759*, 101-106.
22. Mameli, M.; Lippolis, V.; Caltagirone, C.; Capelo, J. L.; Faza, O. N.; Lodeiro, C., Hg^{2+} Detection by New Anthracene Pendant-Arm Derivatives of Mixed N/S- and N/S/O-Donor Macrocycles: Fluorescence, Matrix-Assisted Laser Desorption/Ionization Time-of-Flight Mass Spectrometry and Density Functional Theory Studies. *Inorganic Chemistry* **2010**, *49* (18), 8276-8286.
23. Rapi, Z.; Grün, A.; Nemcsok, T.; Hessz, D.; Kállay, M.; Kubinyi, M.; Keglevich, G.; Bakó, P., Crown ether derived from d-glucose as an efficient phase-transfer catalyst for the enantioselective Michael addition of malonates to enones. *Tetrahedron: Asymmetry* **2016**, *27* (19), 960-972.
24. Kafashi, S.; Yaftian, M. R.; Zamani, A. A., Binding Ability of Crown Ethers Towards Pb(II) Ions in Binary Water/Organic Solvents Using Solvent Extraction Method. *Journal of Solution Chemistry* **2015**, *44* (9), 1798-1811.

25. Yi, R.; Ye, G.; Wu, F.; Lv, D.; Chen, J., Magnetic solid-phase extraction of strontium using core-shell structured magnetic microspheres impregnated with crown ether receptors: a response surface optimization. *Journal of Radioanalytical and Nuclear Chemistry* **2016**, *308* (2), 599-608.
26. Yan ZHAO, Y.-Y. A., Jian CHEN, Hong-Tao SONG, Wei HUANG, Jing PENG. Density Functional Theory Studies of the Structures and Thermodynamic Parameters of Li⁺-Crown Ether Complexes[J]. *Acta Phys. -Chim. Sin.*, 2016, 32(7): 1681-1690.
27. Sun, Y.; Zhu, M.; Yao, Y.; Wang, H.; Tong, B.; Zhao, Z., A novel approach for the selective extraction of Li⁺ from the leaching solution of spent lithium-ion batteries using benzo-15-crown-5 ether as extractant. *Separation and Purification Technology* **2020**, *237*, 116325.
28. Xiong, Y.; Ge, T.; Xu, L.; Wang, L.; He, J.; Zhou, X.; Tian, Y.; Zhao, Z., A fundamental study on selective extraction of Li⁺ with dibenzo-14-crown-4 ether: Toward new technology development for lithium recovery from brines. *Journal of Environmental Management* **2022**, *310*, 114705.
29. Pedersen, C. J., Cyclic polyethers and their complexes with metal salts. *Journal of the American Chemical Society* **1967**, *89* (26), 7017-7036.
30. Jing, Z.; Wang, G.; Zhou, Y.; Pang, D.; Zhu, F.; Liu, H., Selectivity of 18-crown-6 ether to alkali ions by density functional theory and molecular dynamics simulation. *Journal of Molecular Liquids* **2020**, *311*, 113305.
31. Takeda, Y.; Kawarabayashi, A.; Endo, K.; Yahata, T.; Kudo, Y.; Katsuta, S., Solvent extraction of alkali metal (Li-Cs) picrates with 18-crown-6 into various diluents. Elucidation of fundamental equilibria which govern the extraction-ability and-selectivity. *Analytical sciences* **1998**, *14* (1), 215-223.

32. More, M. B.; Glendening, E. D.; Ray, D.; Feller, D.; Armentrout, P. J. T. J. o. P. C., Cation– Ether Complexes in the Gas Phase: Bond Dissociation Energies and Equilibrium Structures of $\text{Li}^+ [\text{O}(\text{CH}_3)_2]_x$, $x=1-4$. **1996**, *100* (5), 1605-1614.
33. Ray, D.; Feller, D.; More, M. B.; Glendening, E. D.; Armentrout, P. J. T. J. o. P. C., Cation– Ether Complexes in the Gas Phase: Bond Dissociation Energies and Equilibrium Structures of Li^+ (1, 2-dimethoxyethane) x , $x=1$ and 2, and Li^+ (12-crown-4). **1996**, *100* (40), 16116-16125.
34. More, M. B.; Ray, D.; Armentrout, P. J. T. J. o. P. C. A., Cation– Ether Complexes in the Gas Phase: Bond Dissociation Energies of Na^+ (dimethyl ether) x , $x=1-4$; Na^+ (1, 2-dimethoxyethane) x , $x=1$ and 2; and Na^+ (12-crown-4). **1997**, *101* (5), 831-839.
35. More, M. B.; Ray, D.; Armentrout, P. J. T. J. o. P. C. A., Cation– Ether Complexes in the Gas Phase: Bond Dissociation Energies of K^+ (dimethyl ether) x , $x=1-4$; K^+ (1, 2-dimethoxyethane) x , $x=1$ and 2; and K^+ (12-crown-4). **1997**, *101* (23), 4254-4262.
36. More, M. B.; Ray, D.; Armentrout, P. J. T. J. o. P. C. A., Cation– Ether Complexes in the Gas Phase: Bond Dissociation Energies of M^+ (dimethyl ether) x , $x=1-3$, M^+ (1, 2-dimethoxyethane) x , $x=1$ and 2, and M^+ (12-crown-4) Where $\text{M}=\text{Rb}$ and Cs . **1997**, *101* (37), 7007-7017.
37. Noh, D. H.; Lee, S. J. C.; Lee, J. W.; Kim, H. I., Host–guest chemistry in the gas phase: complex formation of cucurbit [6] uril with proton-bound water dimer. *Journal of The American Society for Mass Spectrometry* **2014**, *25* (3), 410-421.
38. Chen, Y.; Jami-Alahmadi, Y.; Unikela, K. S.; Bodwell, G. J.; Fridgen, T. D., Endo or Exo? Structures of Gas-Phase Alkali Metal Cation/Aromatic Half-Belt Complexes. *ChemPhysChem* **2018**, *19* (17), 2194-2199.
39. Kan, X.; Liu, H.; Pan, Q.; Li, Z.; Zhao, Y., Anion- π interactions: From concept to application. *Chinese Chemical Letters* **2018**, *29* (2), 261-266.

40. Ballester, P., Experimental quantification of anion- π interactions in solution using neutral host-guest model systems. *Accounts of chemical research* **2013**, *46* (4), 874-884.
41. Cera, L.; Schalley, C. A., Supramolecular reactivity in the gas phase: investigating the intrinsic properties of non-covalent complexes. *Chemical Society Reviews* **2014**, *43* (6), 1800-1812.
42. Burt, M. B.; Fridgen, T. D., Structures and physical properties of gaseous metal cationized biological ions. *European Journal of Mass Spectrometry* **2012**, *18* (2), 235-250.
43. Fridgen, T. D., Infrared consequence spectroscopy of gaseous protonated and metal ion cationized complexes. *Mass Spectrometry Reviews* **2009**, *28* (4), 586-607.
44. Peltz, C.; Drahos, L.; Vékey, K., SORI excitation: Collisional and radiative processes. *Journal of the American Society for Mass Spectrometry* **2007**, *18* (12), 2119-2126.
45. Guo, X.; Duursma, M. C.; Al-Khalili, A.; Heeren, R. M., Experimental calibration of the SORI-CID internal energy scale: energy uptake and loss. *International Journal of Mass Spectrometry* **2003**, *225* (1), 71-82.
46. Grimme, S.; Antony, J.; Ehrlich, S.; Krieg, H. J. T. J. o. c. p., A consistent and accurate ab initio parametrization of density functional dispersion correction (DFT-D) for the 94 elements H-Pu. **2010**, *132* (15).
47. Frisch, M. J.; Trucks, G. W.; Schlegel, H. B.; Scuseria, G. E.; Robb, M. A.; Cheeseman, J. R.; Scalmani, G.; Barone, V.; Petersson, G. A.; Nakatsuji, H.; Li, X.; Caricato, M.; Marenich, A. V.; Bloino, J.; Janesko, B. G.; Gomperts, R.; Mennucci, B.; Hratchian, H. P.; Ortiz, J. V.; Izmaylov, A. F.; Sonnenberg, J. L.; Williams; Ding, F.; Lipparini, F.; Egidi, F.; Goings, J.; Peng, B.; Petrone, A.; Henderson, T.; Ranasinghe, D.; Zakrzewski, V. G.; Gao, J.; Rega, N.; Zheng, G.; Liang, W.; Hada, M.; Ehara, M.; Toyota, K.; Fukuda, R.; Hasegawa, J.; Ishida, M.; Nakajima, T.; Honda, Y.; Kitao, O.; Nakai, H.; Vreven, T.; Throssell, K.; Montgomery Jr., J. A.; Peralta, J. E.; Ogliaro, F.; Bearpark, M. J.; Heyd, J. J.; Brothers, E. N.;

Kudin, K. N.; Staroverov, V. N.; Keith, T. A.; Kobayashi, R.; Normand, J.; Raghavachari, K.; Rendell, A. P.; Burant, J. C.; Iyengar, S. S.; Tomasi, J.; Cossi, M.; Millam, J. M.; Klene, M.; Adamo, C.; Cammi, R.; Ochterski, J. W.; Martin, R. L.; Morokuma, K.; Farkas, O.; Foresman, J. B.; Fox, D. J. *Gaussian 16 Rev. B.01*, Wallingford, CT, 2016.

48. Glendening, E. D.; Streitwieser, A., Natural energy decomposition analysis: An energy partitioning procedure for molecular interactions with application to weak hydrogen bonding, strong ionic, and moderate donor–acceptor interactions. *The Journal of Chemical Physics* **1994**, *100* (4), 2900-2909.

49. Glendening, E. D., Natural energy decomposition analysis: Extension to density functional methods and analysis of cooperative effects in water clusters. *The Journal of Physical Chemistry A* **2005**, *109* (51), 11936-11940.

50. Frisch, M. J.; Trucks, G. W.; Schlegel, H. B.; Scuseria, G. E.; Robb, M. A.; Cheeseman, J. R.; Scalmani, G.; Barone, V.; Petersson, G. A.; Nakatsuji, H.; Li, X.; Caricato, M.; Marenich, A. V.; Bloino, J.; Janesko, B. G.; Gomperts, R.; Mennucci, B.; Hratchian, H. P.; Ortiz, J. V.; Izmaylov, A. F.; Sonnenberg, J. L.; Williams; Ding, F.; Lipparini, F.; Egidi, F.; Goings, J.; Peng, B.; Petrone, A.; Henderson, T.; Ranasinghe, D.; Zakrzewski, V. G.; Gao, J.; Rega, N.; Zheng, G.; Liang, W.; Hada, M.; Ehara, M.; Toyota, K.; Fukuda, R.; Hasegawa, J.; Ishida, M.; Nakajima, T.; Honda, Y.; Kitao, O.; Nakai, H.; Vreven, T.; Throssell, K.; Montgomery Jr., J. A.; Peralta, J. E.; Ogliaro, F.; Bearpark, M. J.; Heyd, J. J.; Brothers, E. N.; Kudin, K. N.; Staroverov, V. N.; Keith, T. A.; Kobayashi, R.; Normand, J.; Raghavachari, K.; Rendell, A. P.; Burant, J. C.; Iyengar, S. S.; Tomasi, J.; Cossi, M.; Millam, J. M.; Klene, M.; Adamo, C.; Cammi, R.; Ochterski, J. W.; Martin, R. L.; Morokuma, K.; Farkas, O.; Foresman, J. B.; Fox, D. J. *Gaussian 16 Rev. C.01*, Wallingford, CT, 2016.

Chapter 5-Conclusions and Future work

5.1 Summary

In this thesis, structural and energetic information of host/guest complexes were investigated by both experimental and computational methods. The experimental studies were carried out using an ESI coupled with an FT-ICR mass spectrometer. The m/z ratios of precursor ions provided information on whether or not the predicted host/guest ions were formed. Fragmentation of precursor ions occurred using SORI-CID. The m/z of fragments helped elucidate the composition of the precursor ions. When applying BIRD on TMnTP/guest ions, two species of precursor ions were observed, and kinetic parameters were obtained. Two types of structures were proposed and the energies of which were determined computationally. IRMPD spectroscopy helped structural investigations on TMnTP/M⁺ by comparing the experimental spectra with the computed IR spectra of the computed lowest energy structure. Furthermore, ER-SORI-CID experiments were performed to obtain relative stabilities of the host/guest ions in the gas phase. The computed binding energies of the lowest energy structures of each type of host/guest ions can also provide relative stabilities. The interactions between a host and a guest can be visualized by IGMH analysis and the nature of which can be analysed by the NEDA method.

In chapter 2, the structures and energies of alkali metal cationized TM9TP were explored. M⁺(TM9TP) (M=K, Rb, Cs) decomposed yield alkali metal cations

by losing neutral TM9TP. This indicates that the composition of the precursor ions does include the alkali metal cations and TM9TP. The BIRD kinetics revealed two species of the precursor ions. One is weakly bound and undergoes fast BIRD kinetics, the structure of which is proposed to be the alkali metal cation sitting on the outside of the teropyrene giving an *exo*-metal TM9TP structure. The other one is more strongly bound and does not dissociate under BIRD (the first order dissociation rate constant is essentially 0 s^{-1}), the structure of which is proposed to be the metal cation inside of the cavity of TM9TP. To probe more information about the geometry of the proposed two types of structures, IRMPD spectroscopy were done. Absorptions between 3000 and 3100 cm^{-1} were observed in the IRMPD spectra of $M^+(\text{TM9TP})$ ($M=\text{K, Rb, Cs}$) indicating the aromatic $C(sp^2)\text{-H}$ stretching. Strong absorptions between 2825 and 2950 cm^{-1} indicate the $C(sp^3)\text{-H}$ bonds of the aliphatic bridge. Interactions between bridge $C(sp^3)\text{-H}$ bonds and alkali metal cations ions are responsible for the red-shifted C-H stretches bands below 2850 cm^{-1} . The red-shifted band occurred in the spectrum of the *endo* complex where the metal cation was inside the aromatic half-belt. Potential energy surface calculations for these ions align with the notion that the BIRD active population corresponds to *exo* complexes characterized by a notably low dissociation threshold energy. In contrast, the *endo* complex exhibits a considerably higher dissociation threshold energy and is likely to dissociate primarily through conversion to the *exo* complex.

In chapter 3, structures and relative stabilities of gas-phase $[(\text{TMnTP})(\text{Gly})]\text{H}^+$ were investigated. The SORI-CID spectra showed that the

$[(\text{TMnTP})(\text{Gly})]\text{H}^+$ precursor ions underwent neutral glycine loss leaving protonated TMnTPs. The proton transfer indicated differences with respect to proton affinity. The proton affinity of glycine is computed to be at least 100 kJ mol^{-1} smaller than that of most favourable protonation site of TMnTP, carbon 1. Therefore, in the gas phase unimolecular dissociation process, the decomposition of $[(\text{TMnTP})(\text{Gly})]\text{H}^+$ into neutral Gly and protonated TMnTP is entirely expected. BIRD was also conducted on $[(\text{TMnTP})(\text{Gly})]\text{H}^+$ and is discussed chapter 3. According to BIRD kinetics, two species one involving a slow decaying species and the other a fast decaying species were observed. The intuition says that these two species are *endo* and *exo* protonated glycine species. Several structures consisting of *endo* and *exo* neutral glycine protonated TMnTP along with *endo* and *exo* protonated glycine neutral TMnTP were computed. The lowest two types of structures are *endo*-(TMnTP)(GlyH⁺) and *endo*-(TMnTPH⁺)(Gly). With master equation modelling of the Arrhenius plots, it was found that SD population encounters an energy barrier that is $10\text{-}20 \text{ kJ mol}^{-1}$ higher than that of the FD population for dissociation. This aligns with the computed binding energies, which are approximately 25 kJ mol^{-1} higher for *endo*-(TMnTPH⁺)(Gly) compared to *endo*-(TMnTP)(GlyH⁺). Consequently, these two entities are the probable candidates for the SD and FD populations, respectively. The calculations indicate a substantial energy barrier for proton transfer between the *endo*-(TMnTP)(GlyH⁺) and *endo*-(TMnTPH⁺)(Gly) structures. This barrier is crucial to explain the observation of distinct populations of these structural isomers. By IGMH analysis, the non-covalent interactions between the π electrons of the TMnTP and both the protonated amine and hydroxyl

of the glycine were visualized. NEDA helped to understand the nature of the interaction between host and guest. A NEDA analysis distinctly reveals the preference for the *endo*-(TMnTP)(GlyH⁺) structure over the *exo*-(TMnTPH⁺)(Gly). This preference is attributed to the dominant ion-induced dipole interactions, which outweigh the energy deficit of approximately 100 kJ mol⁻¹ caused by glycine being protonated instead of TMnTP in the complex. DEF components provide information about the interactions within protonated glycine/TMnTP and glycine/protonated TMnTP. In the case of the *endo*-protonated glycine/TMnTP complex, the DEF component is notably greater compared to the *endo*-neutral glycine/protonated TMnTP complex. This discrepancy arises from the significant distortion of TMnTP electron distributions induced by the GlyH⁺ guest. The distortion in TMnTP electron densities contributes to the stabilization of ion-induced dipole and dipole-induced dipole interactions. Conversely, the DEF components for protonated TMnTP and neutral glycine are small, given that TMnTP is being protonated, and its electron density is less susceptible to distortion by neutral glycine.

In chapter 4, we focused on studying the structures, energies, decomposition pathways and interactions of M⁺(TAAQ) complexes, where M represents alkali metal cations (Li⁺, Na⁺, K⁺, Rb⁺, and Cs⁺). The study combines experimental and computational approaches to elucidate the behavior of these complexes under collisional activation and their relative stabilities. With the exception of Na⁺(o-TAAQ) and the Li⁺ complexes with o-, m-, p-, and b-TAAQ, all other M⁺(TAAQ) complexes were found to dissociate into their constituent M⁺ cations and neutral

TAAQ molecules following collisional activation. The relative stabilities of the $M^+(\text{TAAQ})$ complexes were determined both experimentally and computationally, revealing a consistent trend across the series: $\text{Na}^+(\text{TAAQ}) > \text{K}^+(\text{TAAQ}) > \text{Rb}^+(\text{TAAQ}) > \text{Cs}^+(\text{TAAQ})$. This trend suggests that the binding affinity between the metal cation and the TAAQ ligand decreases as the size of the alkali metal cation increases, likely due to reduced electrostatic interactions and increased steric effects. Furthermore, the gas-phase binding energies of the TAAQ associating with K^+ , Rb^+ , and Cs^+ cations exhibited a distinct trend: $M^+(\text{o-TAAQ}) > M^+(\text{m-TAAQ}) > M^+(\text{p-TAAQ}) > M^+(\text{b-TAAQ})$. This experimental trend aligns well with the computational predictions for the corresponding structures: $M^+(\text{o-4O-TAAQ})$, $M^+(\text{m1-2O-3Ph-TAAQ})$, $M^+(\text{p-2O-3Ph-TAAQ})$, and $M^+(\text{b2d-2O-TAAQ})$. The agreement between experimental and computational results underscores the reliability of the theoretical models used in this study. However, an interesting discrepancy arises in the case of Na^+ complexes. The experimental gas-phase relative stability trend for Na^+ with different TAAQ ligands was observed as $\text{Na}^+(\text{o-TAAQ}) > \text{Na}^+(\text{b-TAAQ}) > \text{Na}^+(\text{m-TAAQ}) > \text{Na}^+(\text{p-TAAQ})$, which contrasts with the computational trend: $\text{Na}^+(\text{m1-2O-3Ph-TAAQ}) > \text{Na}^+(\text{p-2O-3Ph-TAAQ}) > \text{Na}^+(\text{b2d-2O-TAAQ})$. This divergence suggests that more structures of $\text{Na}^+(\text{b-TAAQ})$ need to be explored. Nevertheless, the computational results for $\text{Na}^+(\text{o-4O-TAAQ})$, $\text{Na}^+(\text{m1-2O-3Ph-TAAQ})$, $\text{Na}^+(\text{p-2O-3Ph-TAAQ})$, and $\text{Na}^+(\text{b2u-4O-TAAQ})$ structures remain consistent with the broader trends observed for other alkali metal cations.

5.2 Future Work

Based on the structures and energies of the host/guest complexes investigated in this work, a number of new directions became apparent to make the system more diverse. First, the cavity and large aromatic rings provided by TMnTP offer opportunities to study its interactions with other metal cations or protonated amino acids to interact with. Some work has been done on the $\text{Ag}^+(\text{TMnTP})$ complex. Following the introduction of Ag^+ to the acetonitrile solvated TMnTP solution, not only the m/z of $\text{Ag}^+(\text{TMnTP})$ was observed, but also the m/z of $\text{Ag}^+(\text{TMnTP})(\text{ACN})$. As shown in Figure 5.1, the SORI-CID spectra shows that $\text{Ag}^+(\text{TMnTP})$ loses neutral Ag leaving a TMnTP radical cation. An electron transfer process is observed. When another SORI-CID experiment was performed on TMnTP radical cations, a set of fragments were observed. By comparing these fragments as shown in Figure 5.2 of TMnTP radical cations ($n=7-9$), it will be interesting to figure out the identity of these fragments. Furthermore, singly charged metal cations of the same group of Ag also have the potential to interact with TMnTP, such as Cu^+ and Au^+ aiming to find out whether the electron transfer process is observed as was the case for the Ag^+ complex. As shown in Figure 5.3, IRMPD spectroscopy was carried out on $\text{Ag}^+(\text{TM9TP})$, the red shifted aliphatic C-H stretching indicates that the Ag^+ occupies the cavity of TMnTP forming *endo*- $\text{Ag}^+(\text{TM9TP})$ structure. Structures of $\text{Cu}^+(\text{TMnTP})$ and $\text{Au}^+(\text{TMnTP})$ can also be explored by IRMPD spectroscopy and the energies of each proposed structure can be obtained by computational chemistry. Additionally, a loss of ACN from $\text{Ag}^+(\text{TMnTP})(\text{ACN})$ was also observed. This inspires future investigations on $\text{Ag}^+(\text{TMnTP})(\text{H}_2\text{O})$ and $\text{Cu}^+(\text{TMnTP})(\text{ACN})$, $\text{Cu}^+(\text{TMnTP})(\text{H}_2\text{O})$, $\text{Au}^+(\text{TMnTP})(\text{ACN})$

and $\text{Au}^+(\text{TMnTP})(\text{H}_2\text{O})$. Also, ER-SORI-CID experiments have the potential to obtain the relative stability of $\text{M}^+(\text{TMnTP})$ ($\text{M}=\text{Cu}, \text{Ag}$ and Au). In addition to TMnTP as a host, Cu^+ , Ag^+ and Au^+ also have the potential to interact with TAAQs. It will be interesting to observe whether or not the electron transfer process is observed. A bunch of structures can be proposed, and the interactions between Cu^+ , Ag^+ , Au^+ and TAAQs can be investigated by several experimental and computational methods. BIRD experiments were done on alkali metal cationized TAAQs, however no fragmentation was observed. It is curious to figure out Cu^+ , Ag^+ , Au^+ /TAAQs complexes will undergo dissociation using the soft dissociation technique.

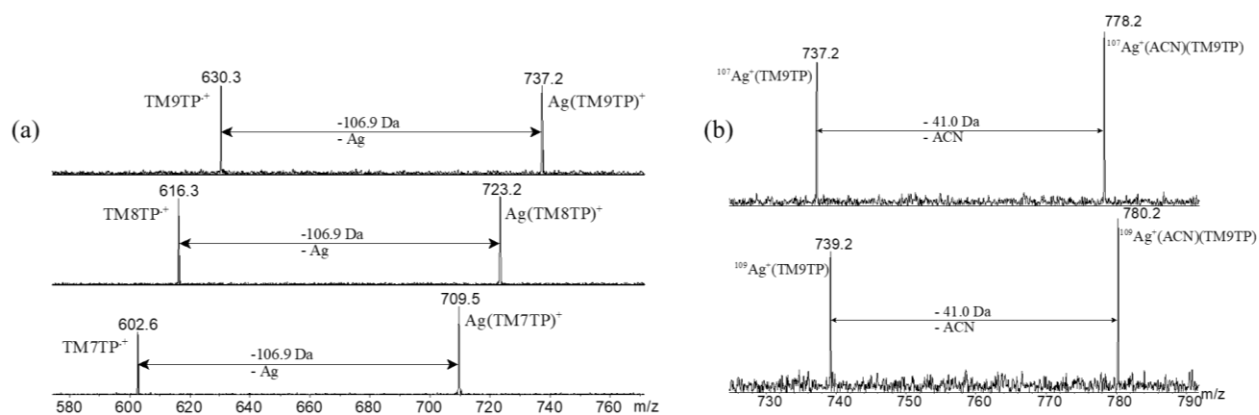


Figure 5.1 SORI-CID spectra of (a) $\text{Ag}(\text{TMnTP})^+$ and (b) $\text{Ag}^+(\text{ACN})(\text{TM9TP})$

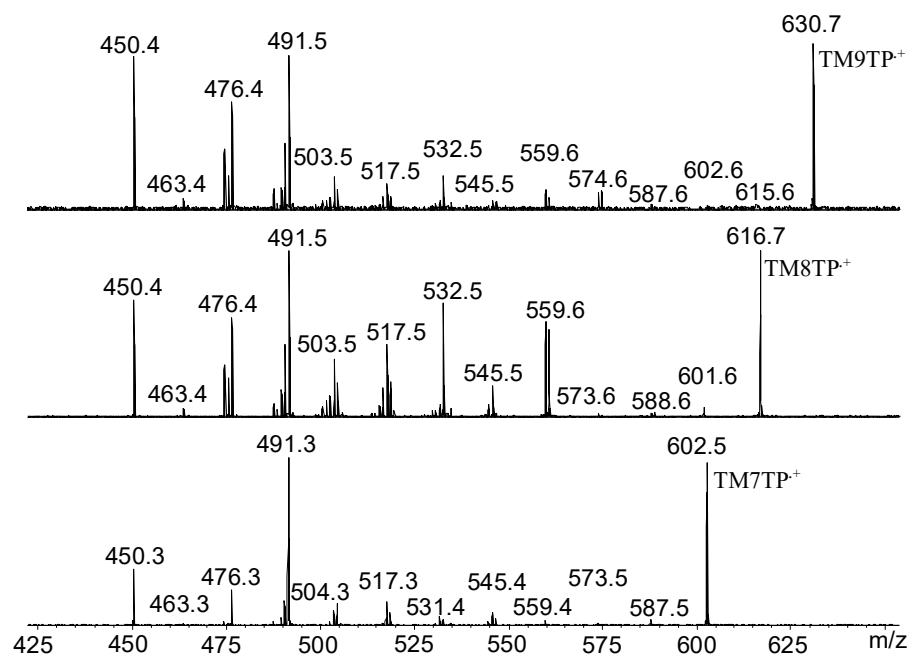


Figure 5.2 SORI-CID spectra of TM_nTP⁺

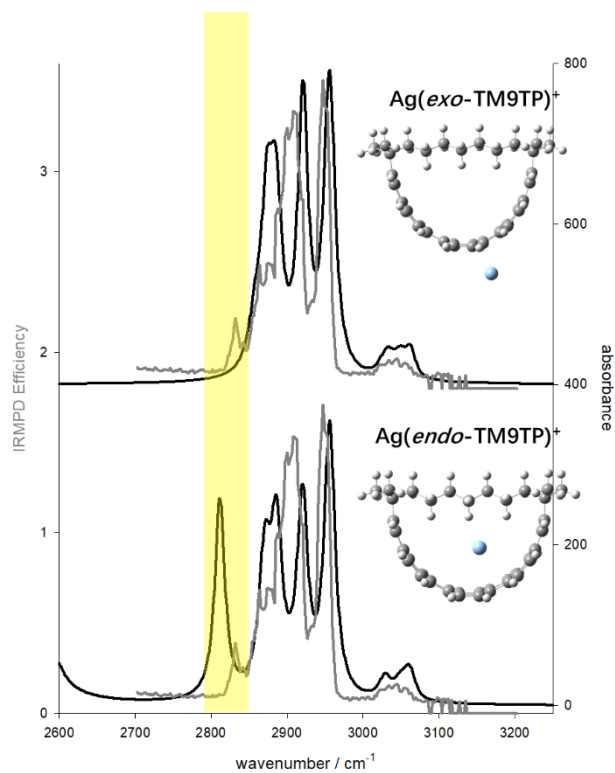


Figure 5.3 IRMPD spectra (gray traces) overlaid by computed IR spectra (black traces) of *endo*- and *exo*-Ag(TM9TP)⁺.

Secondly, the smallest protonated AA (GlyH⁺) showed its ability to interact with TMnTP in the *endo* and *exo* position. Other protonated AAs can also be studied interacting with TMnTP. It will be interesting to figure out how other protonated AAs occupy the cavity, and if some of them are too large to occupy the cavity of TMnTP. IGMH and NEDA analysis on protonated AA/TMnTP can help to visualize the potential complicated interactions between protonated AAs and TMnTP. Also, whether or not the proton transfer process occurs when protonated AA/TMnTP dissociates under SORI-CID. Furthermore, protonated AAs can bind with o-TAAQ. Some protonated AAs/o-TAAQ complexes dissociate yield to protonated glycine (Figure 5.4), some dissociate to yield both protonated glycine and protonated o-TAAQ (Figure 5.5), and some dissociate more to yield protonated o-TAAQ (Figure 5.6). Structures of AAs/o-TAAQ can be proposed and optimized by computational methods. Also, the proton affinities can be compared between AAs and o-TAAQ. Not only o-TAAQ complexes, but protonated AAs with m-, p- and b-TAAQs can also be investigated.

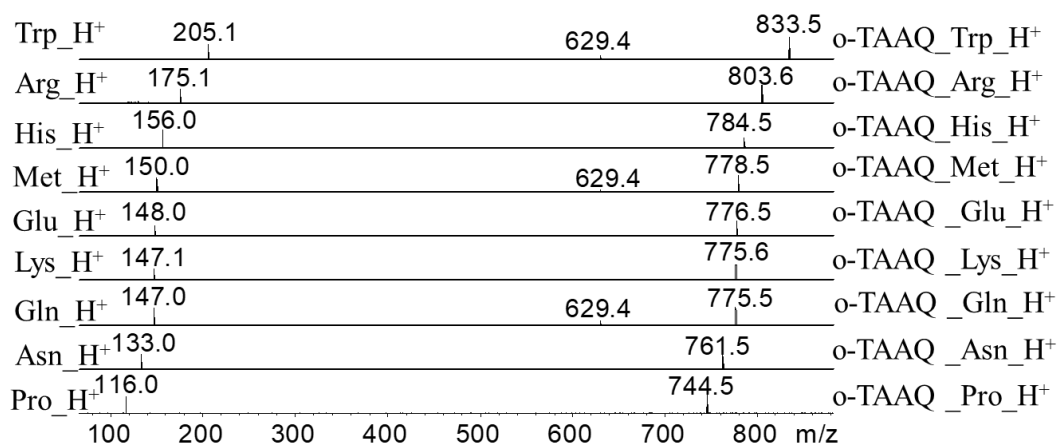


Figure 5.4 SORI-CID spectra of protonated AAs/o-TAAQ.

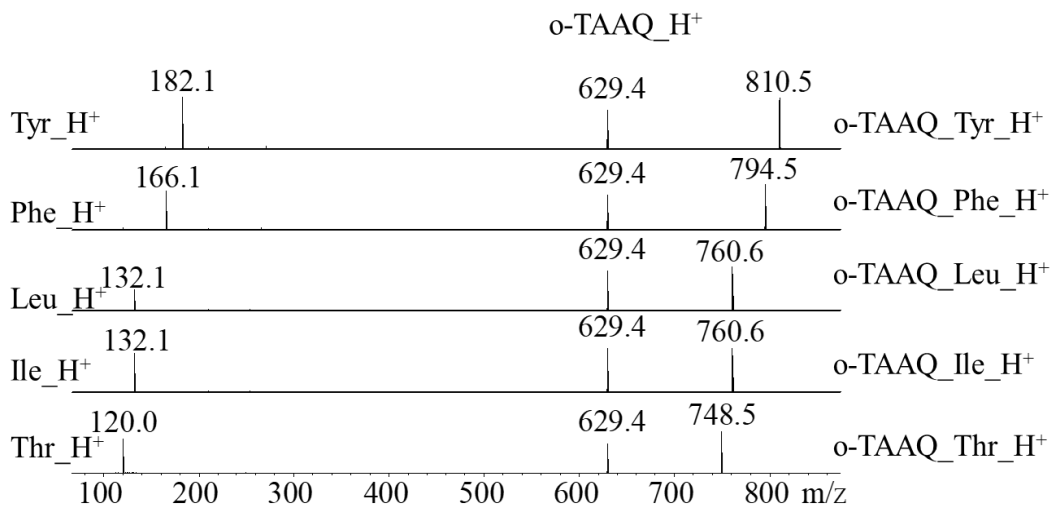


Figure 5.5 SORI-CID spectra of protonated AAs/o-TAAQ.

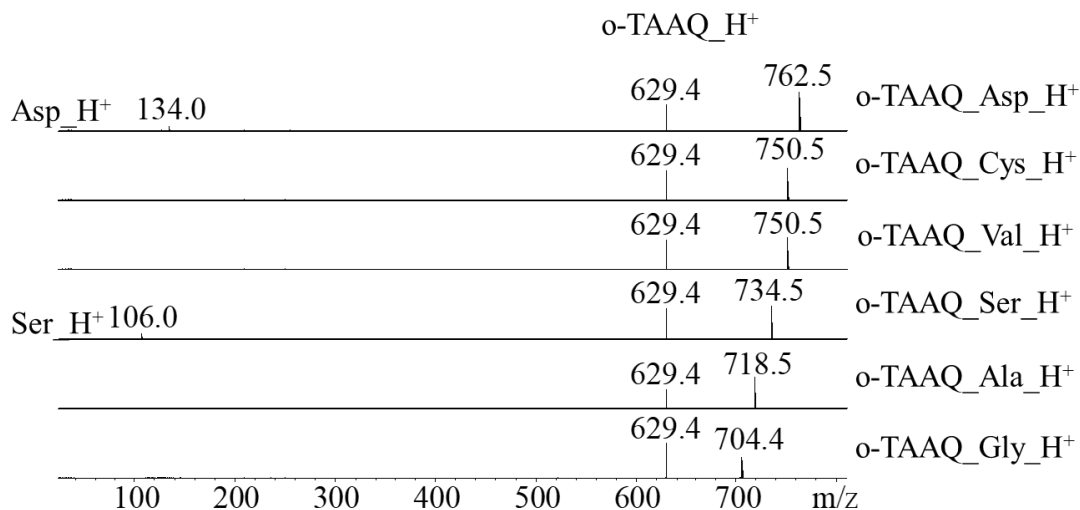


Figure 5.6 SORI-CID spectra of protonated AAs/o-TAAQ.

Above all, several areas remain unexplored and could be addressed in future research. One is a study of the structures, energies, fragmentation pathways, and interactions of $M^+(\text{TMnTP})$ and $M^+(\text{TAAQ})$ complexes, where M^+ represents Cu, Ag, and Au. The interesting part is predicted to be the electron transfer process. The other is a

structural and energetic study on (protonated amino acid)/(TAAQ) complexes. The proton transfer process could be interesting.

Appendix A: Chapter 2 Supplemental Information

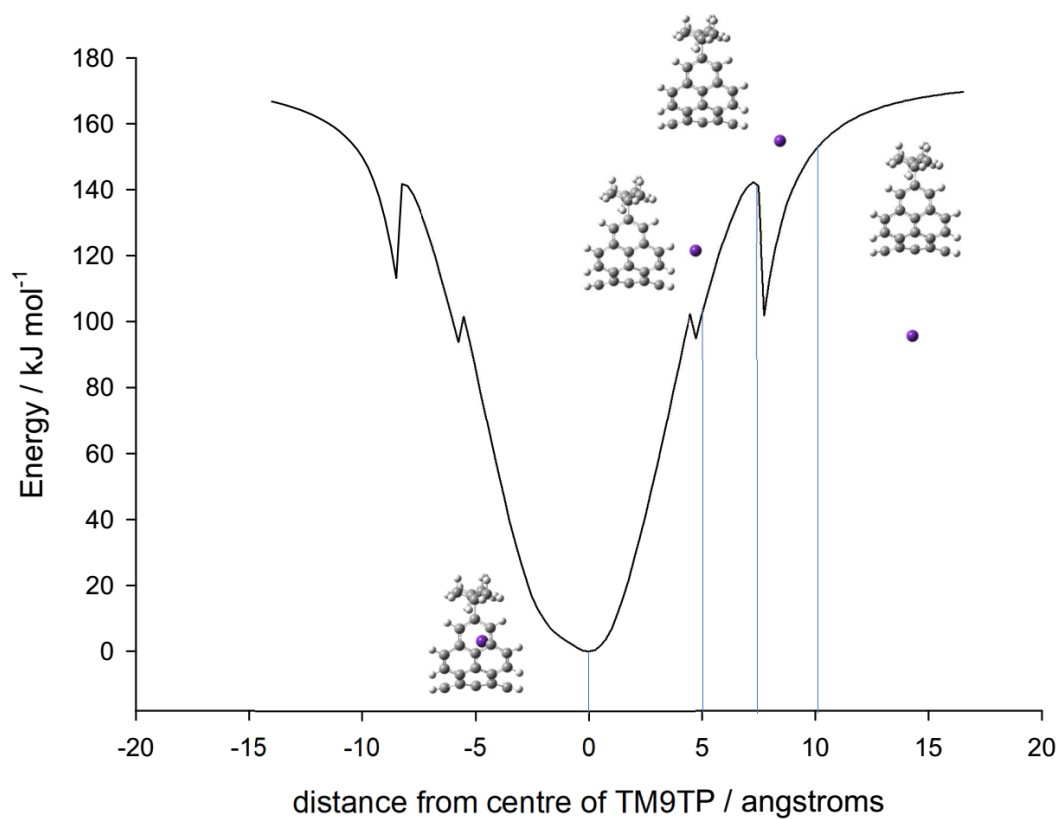


Figure A1. Computed potential energy scan (B3LYPD3/6-31+G(d,p) – Def2SVP on Rb). During the scan, the TM9TP structure was frozen and the position of the ion was completely relaxed except for the position from the centre of TM9TP. The blue lines indicate the position on the scan of the four structures shown.

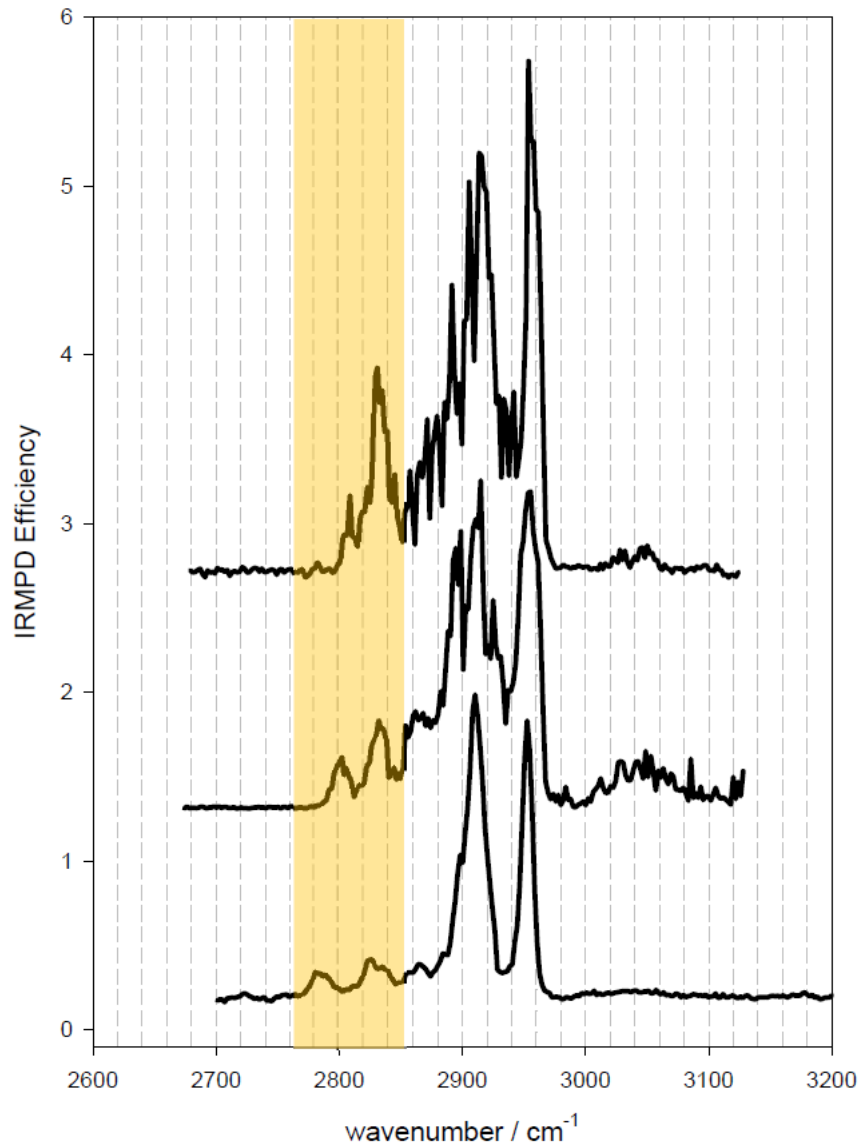


Figure A2. A) Comparison of the IRMPD spectra for $\text{K}(\text{TM9TP})^+$, $\text{Rb}(\text{TM9TP})^+$, and $\text{Cs}(\text{TM9TP})^+$ (top to bottom, respectively). The highlighted portion is the region where the C-H stretching absorptions occur and which are red-shifted from the $2850 - 2975 \text{ cm}^{-1}$ region due to their interaction with the metal cation.

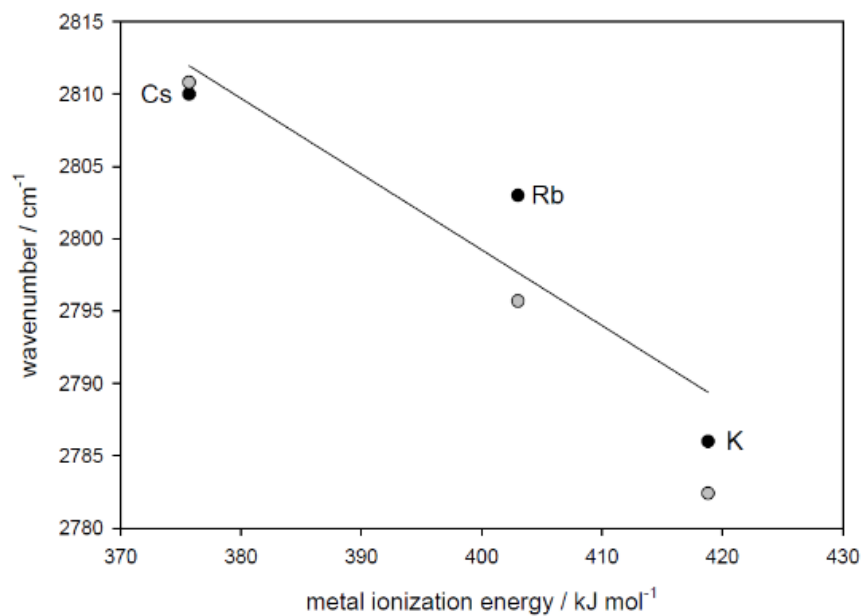


Figure A2. B) Plot of wavenumber position of the central bridge C-H stretching vibration against the ionization energy of the metal. The black filled circles are the experimental positions and the grey are the computed positions.

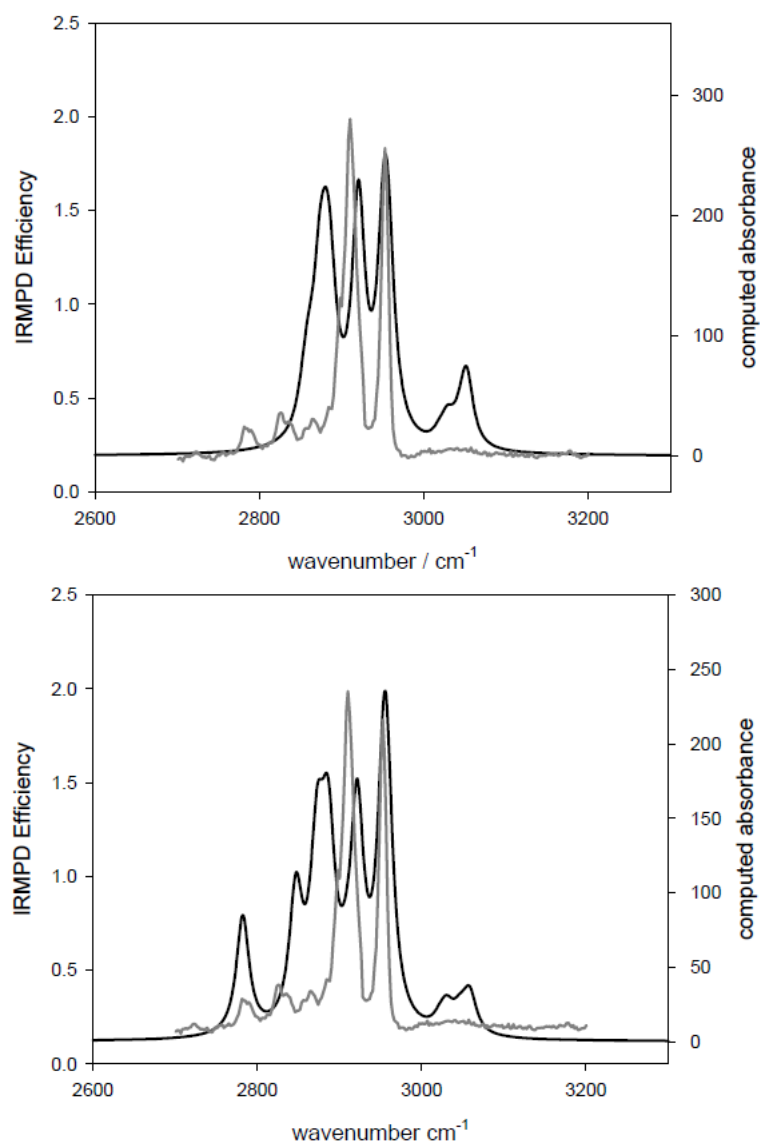


Figure A3. Comparison of the IRMPD spectrum (grey) and computed IR spectra (black traces) of the endo-K(TM9TP)⁺ (bottom) and exo-K(TM9TP)⁺ complexes.

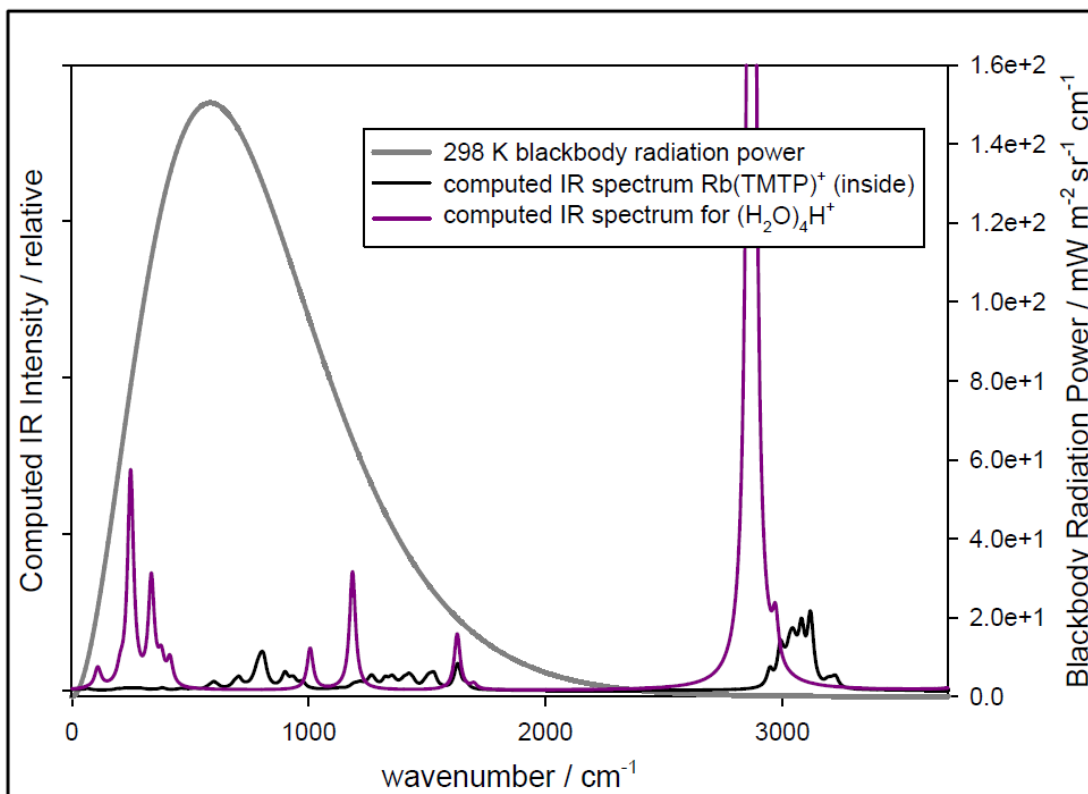


Figure A4. A comparison of the computed IR spectrum for the protonated water tetramer and endo-Rb(TM9TP)⁺. The 298 K blackbody radiation power spectrum is overlaid.

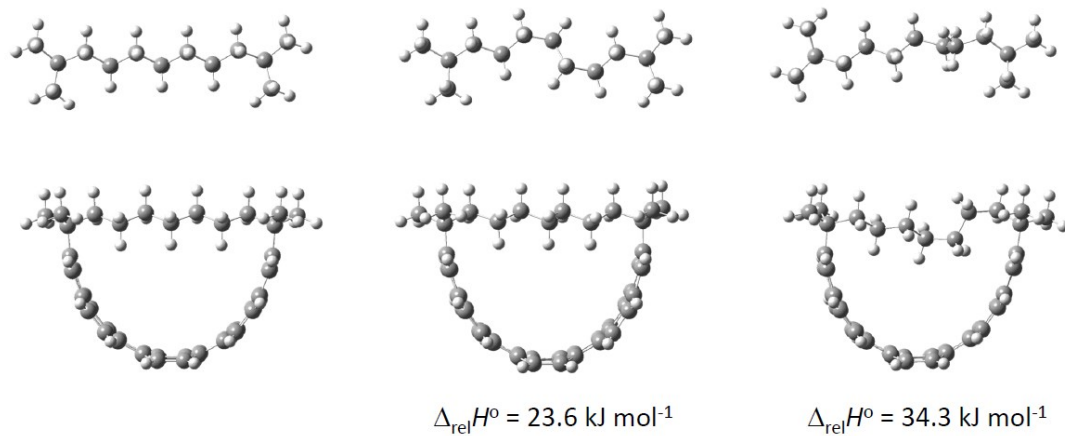


Figure A5. Three structures and relative energies for TM9TP computed using B3LYPD3/6-31+G(d,p). The structures on top are looking down on the TM9TP with the pyrenophane removed.

Information of Alkali metal cationized TMnTP (n=7-9)

As shown in Scheme 3.1 (Chapter 3), 1,1,*n,n*-Tetramethyl[*n*](2,11)teropyrenophanes (*n*=7-9) are abbreviated as TMnTP, which are composed of an aliphatic chain with *n* carbons on its main chain and a large non-planar polycyclic aromatics. Structures of alkali metal cationized TMnTP (*n*=7-9) are computed under the level of B3LYP-D3 with 6-31+G(d,p) basis on C and H, and def2-SVP basis on metal atoms. Both *endo*-K⁺(TMnTP) and *exo*-K⁺(TMnTP) are displayed in Table A1. Structures of Rb⁺ and Cs⁺(TMnTP) are similar to K⁺(TMnTP). The computed binding energies which are computed using B3LYP-D3 (and CAM-B3LYP in bold) with 6-31+G(d,p) basis on C and H, and def2-SVP basis on metal atoms are shown in Table A2. The *endo*-M⁺(TMnTP) are more strongly bound than the corresponding *exo*-M⁺(TMnTP). Generally, K⁺ binds with TMnTP the most strongly, followed by Rb⁺ and Cs⁺, which suggest the alkali metal cation binds with TMnTP electrostatically. Additionally, energy-resolved SORI-CID experiments were performed. The relative E_{CM} values at half dissociation of *endo*-M⁺(TMnTP) complexes were recorded in Figure A6. The trend agrees with the computed trend discussed above.

Table A1. Computed structures of $K^+(TMnTP)$ ($n=7-9$) using B3LYP-D3 with 6-31+G(d,p) basis on C and H, and def2-SVP basis on metal atoms.

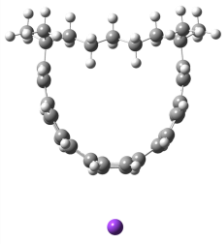
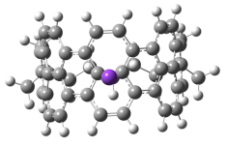
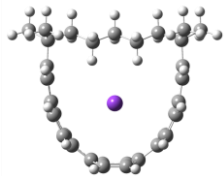
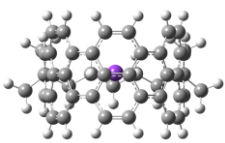
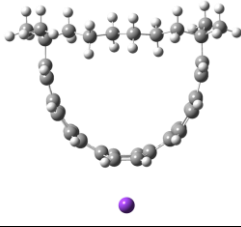
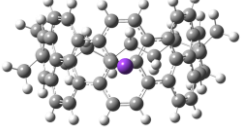
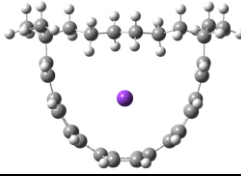
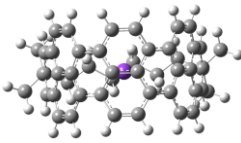
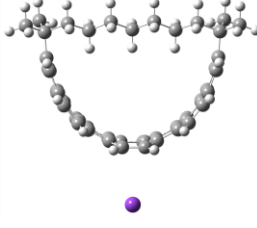
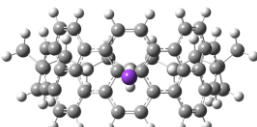
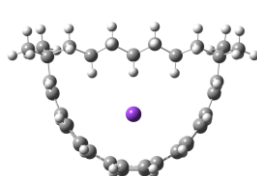
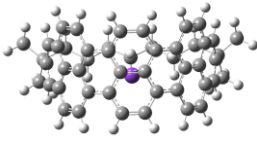
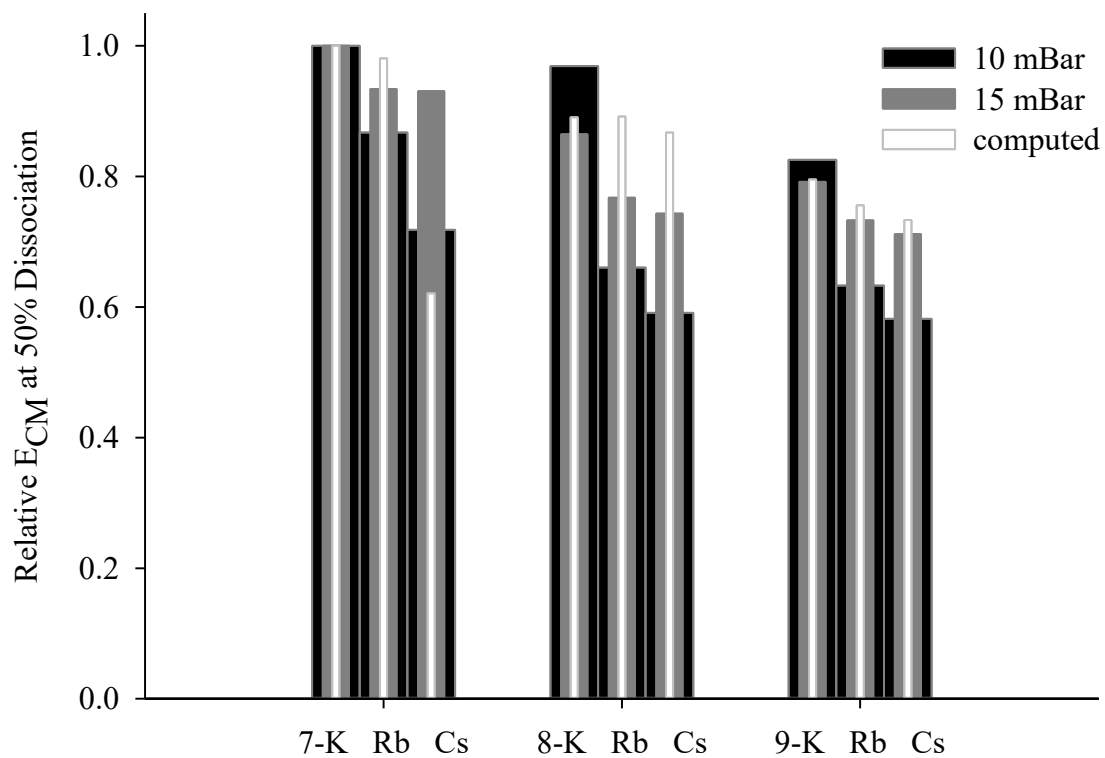
| | | Side view | Bottom view |
|-------|---------------------------|---|---|
| TM7TP | <i>exo-K⁺</i> |  |  |
| | <i>endo-K⁺</i> |  |  |
| TM8TP | <i>exo-K⁺</i> |  |  |
| | <i>endo-K⁺</i> |  |  |
| TM9TP | <i>exo-K⁺</i> |  |  |
| | <i>endo-K⁺</i> |  |  |

Table A2. Computed binding energies of alkali metal cationized TMnTP (n=7-9). Values are relative 298 K enthalpies computed using B3LYP-D3 (and CAM-B3LYP in bold) with 6-31+G(d,p) basis on C and H, and def2-SVP basis on metal atoms.

| | | K ⁺ | Rb ⁺ | Cs ⁺ |
|-------|-------------|----------------|-----------------|-----------------|
| TM7TP | <i>exo</i> | 36.5 | 25.1 | 16.7 |
| | | 30.3 | -2.3 | -14.8 |
| | <i>endo</i> | 93.4 | 91.6 | 85.0 |
| | | 81.2 | 76.6 | 72.1 |
| TM8TP | <i>exo</i> | 35.3 | 23.5 | 15.1 |
| | | 28.4 | -4.2 | -16.6 |
| | <i>endo</i> | 83.2 | 83.3 | 81.0 |
| | | 70.3 | 68.3 | 66.9 |
| TM9TP | <i>exo</i> | 18.0 | 22.1 | 13.7 |
| | | 26.5 | -5.9 | -18.4 |
| | <i>endo</i> | 74.3 | 70.6 | 68.5 |
| | | 65.0 | 57.6 | 55.9 |

Figure A6. Relative center of mass collision energies at half dissociation for loss of M^+ from the $M^+(TMnTP)$ complex ions at 15 mbar (grey bars) and 10 mbar (black bars) of reservoir Ar pressure. Also shown are the relative binding energies computed at the B3LYP-D3/6-31+G(d,p) on C and H, and def2svp on metals level and basis set (white bars).



Appendix B: Chapter 3 Supplementary Information

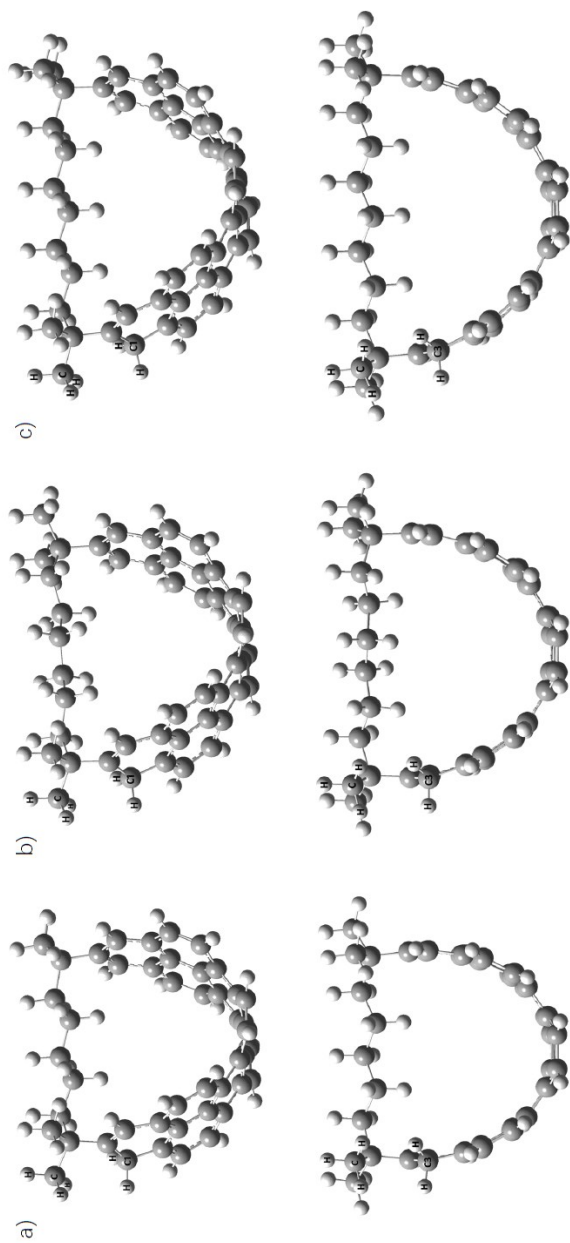


Figure B1. Computed structures of a) TM7TPH⁺; b) TM8TPH⁺; c) TM9TPH⁺ where the protonation sites are at carbon 1 (C1) and carbon 3 (C3) at the level of B3LYP-D3/6-31+G(d,p). The two hydrogens on C1 and the two hydrogens of methyl group close to C1 are staggered. When the protonation site is on C3, the two hydrogens on C3 are face to face with the two hydrogens of the methyl group right above C3.

Another perspective view of protonation on C1



Figure B1 continuous.

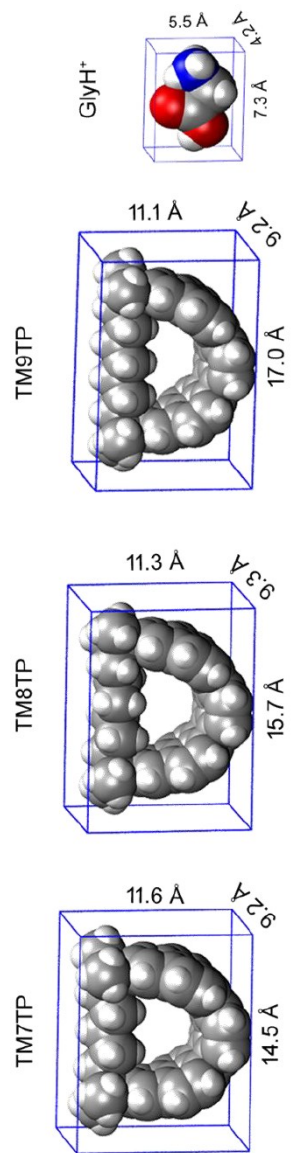


Figure B2. Boxes that enclose the Van de Waals surfaces ($\rho = 0.001$ a.u.) of TMnTP (n=7, 8, 9), and protonated glycine.

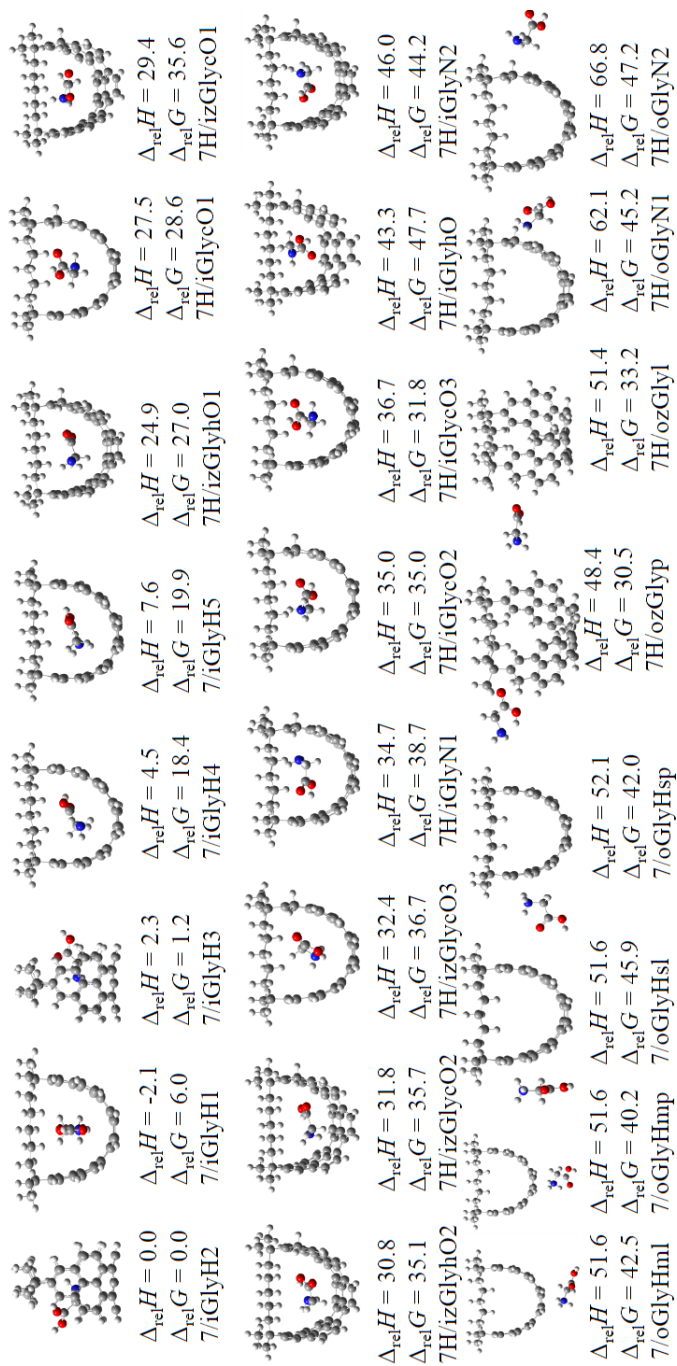


Figure B3. Computed structures and relative energies to the global minimum structure of [(TM7TP)(Gly)]H⁺ at the level of B3LYP-D3/6-31+G(d,p). Energies are listed in kJ mol⁻¹ at 298 K and 1 atm.

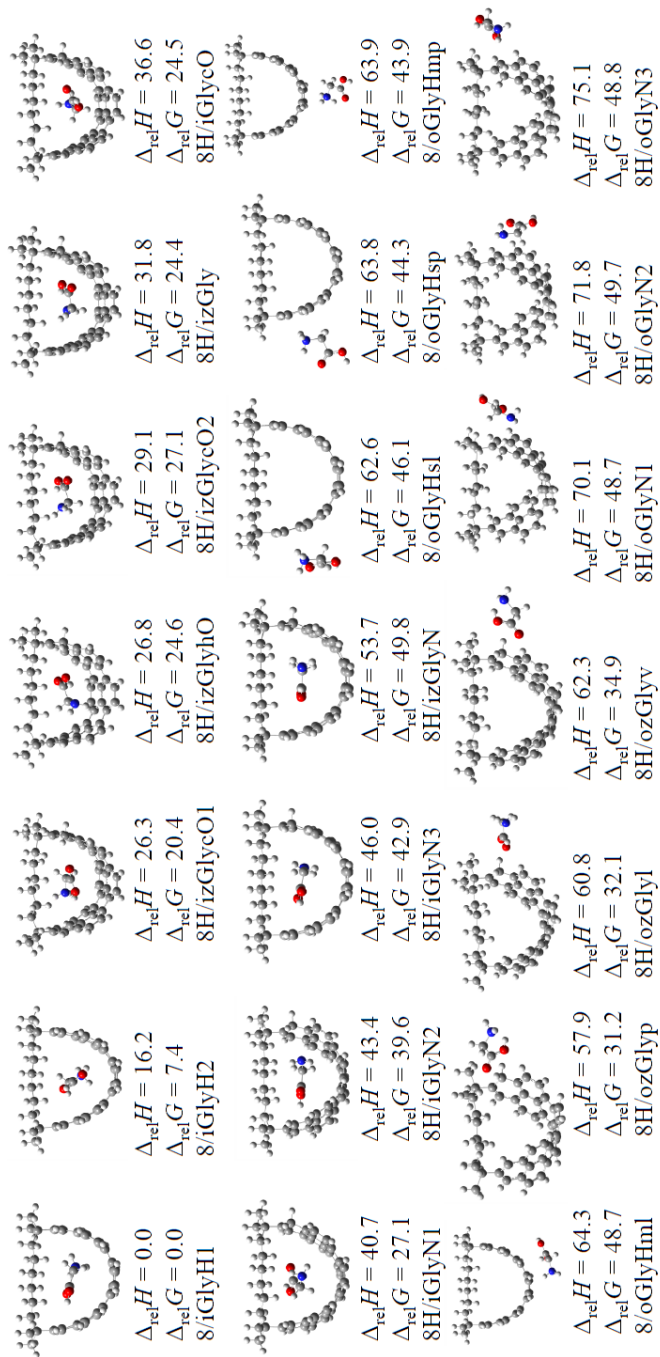


Figure B4. Computed structures and relative energies to the global minimum structure of [(TM8TP)(Gly)]H⁺ at the level of B3LYP-D3/6-31+G(d,p). Energies are listed in kJ mol⁻¹ at 298 K and 1 atm.

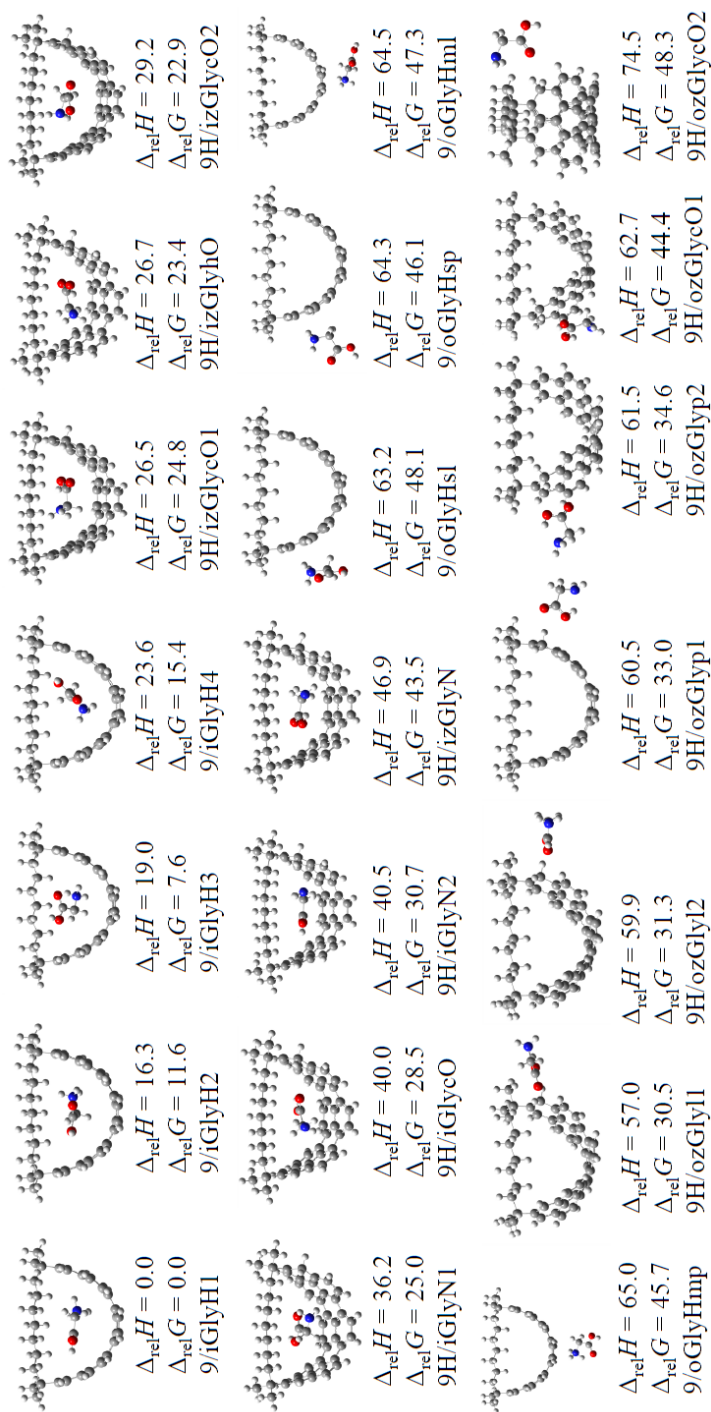


Figure B5. Computed structures and relative energies to the global minimum structure of [(TM9TP)(Gly)]H⁺ at the level of B3LYP-D3/6-31+G(d,p). Energies are listed in kJ mol⁻¹ at 298 K and 1 atm.

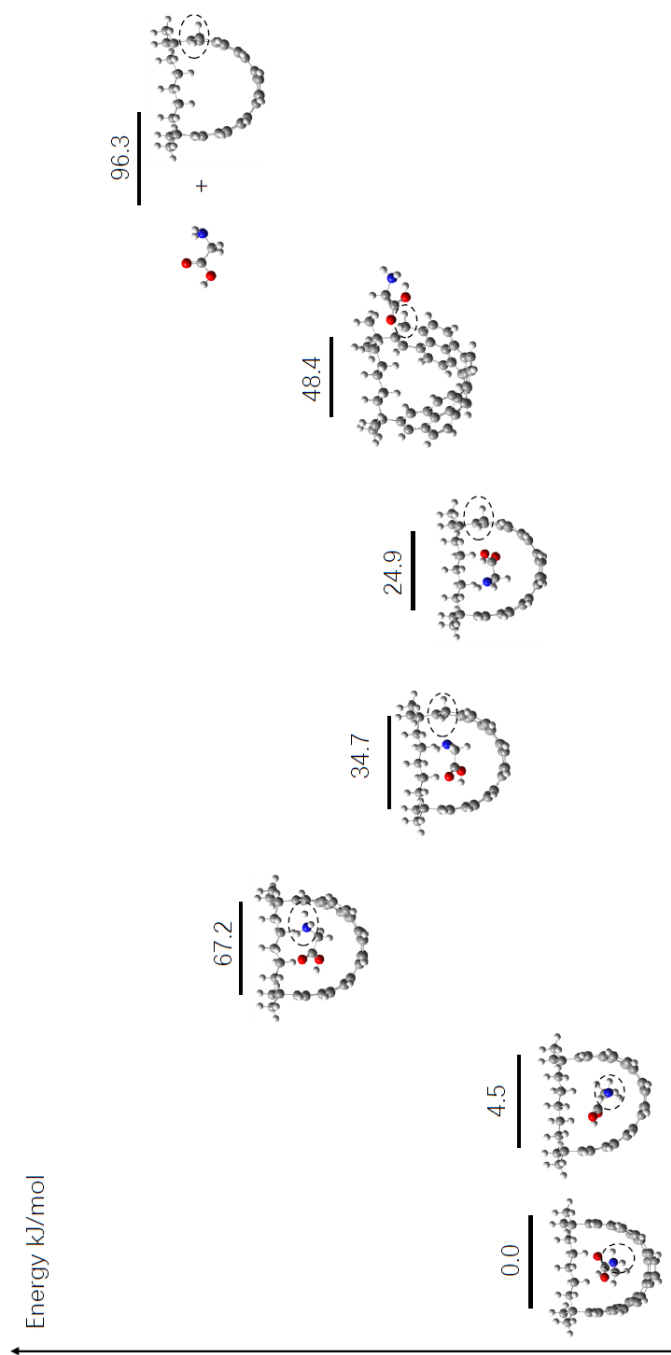


Figure B6. A possible dissociation pathway for *endo*-(TM7TP)(GlyH⁺) at the level of B3LYP-D3/6-31+G(d,p) at 298K 1 atm. Black dashed line circles the protonation site.

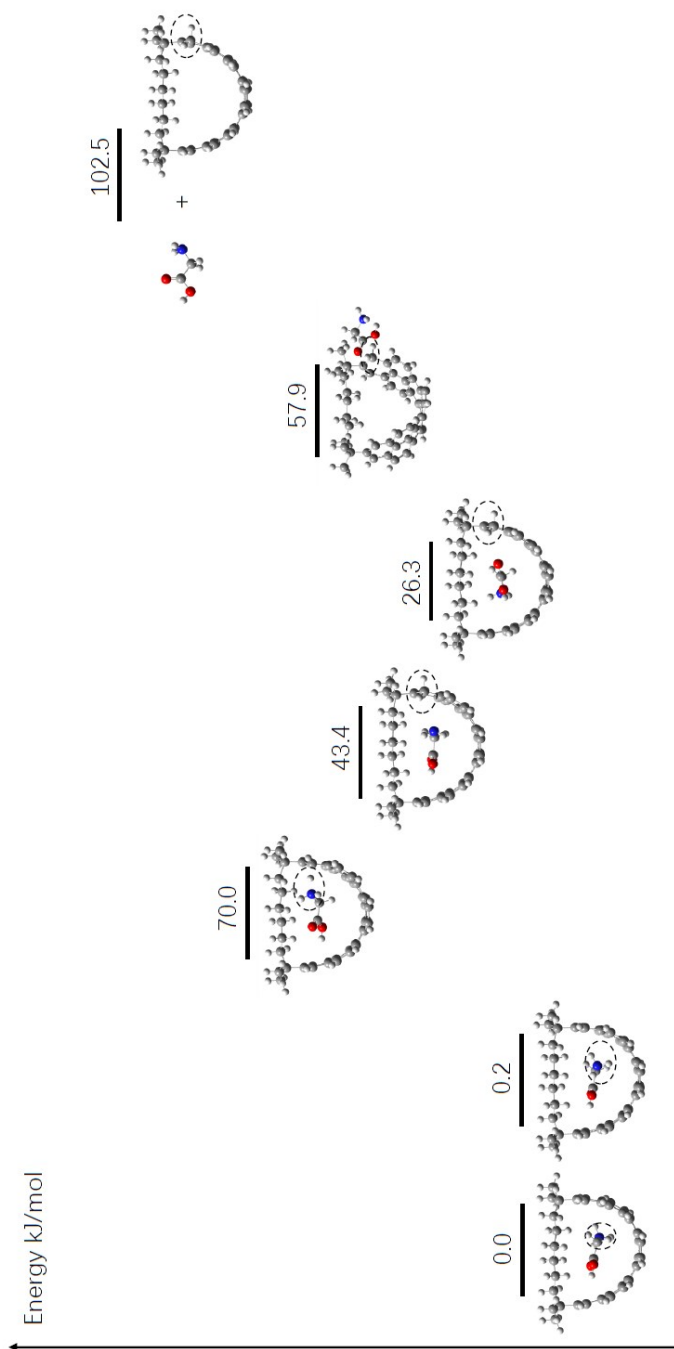


Figure B7. A possible dissociation pathway for *endo*-(TM8TP)(GlyH⁺) at the level of B3LYP-D3/6-31+G(d,p) at 298K 1 atm. Black dashed line circles the protonation site.

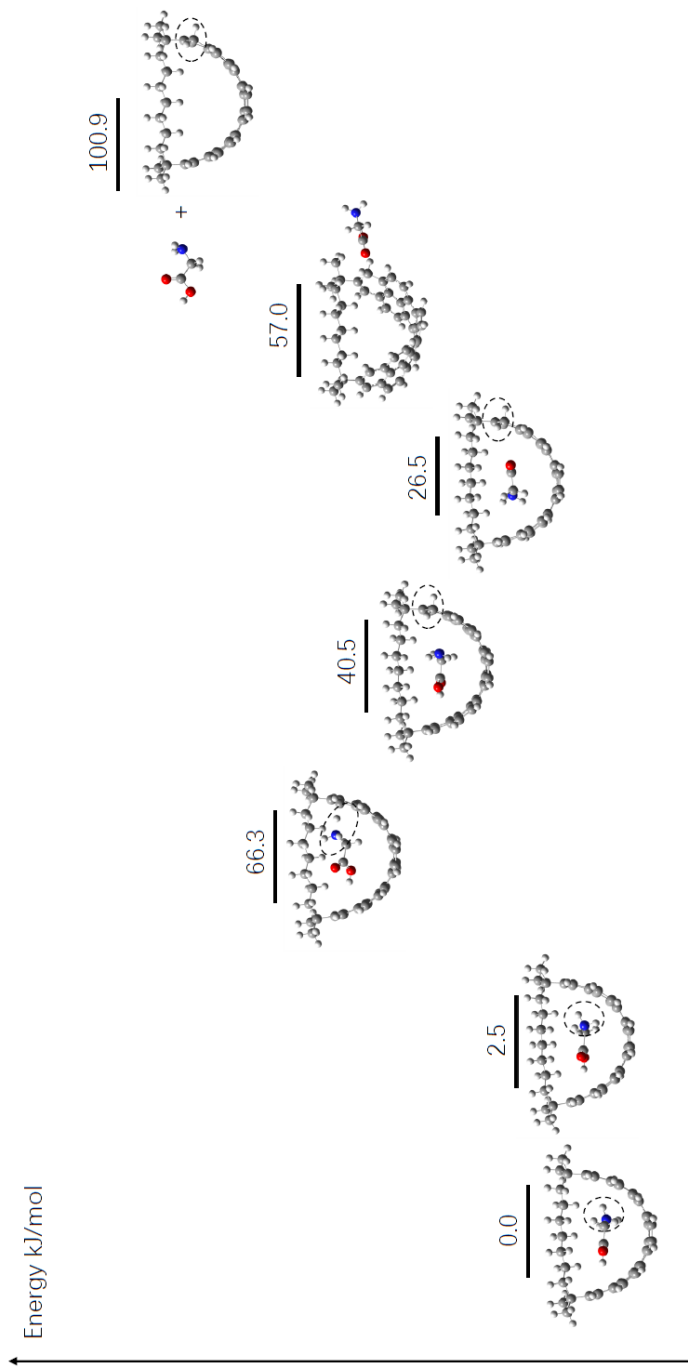
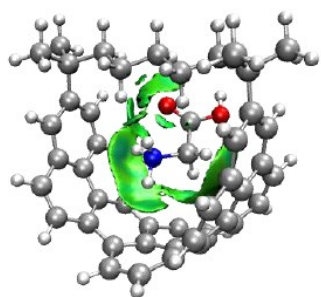
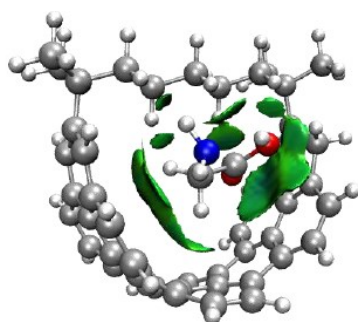
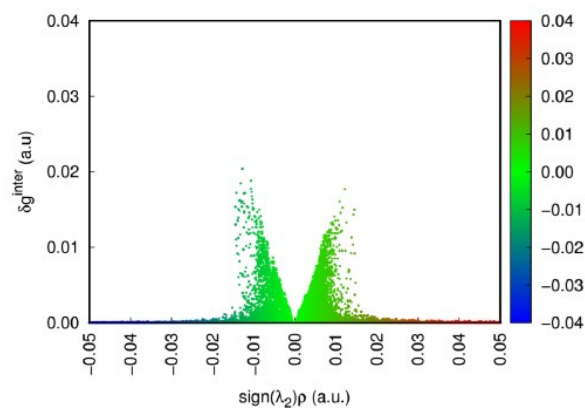


Figure B8. A possible dissociation pathway for *endo*-(TM9TP)(GlyH⁺) at the level of B3LYP-D3/6-31+G(d,p) at 298K 1 atm. Black dashed line circles the protonation site.



endo-(GlyH⁺)(TM7TP)



endo-(Gly)[(TM7TP)H⁺]

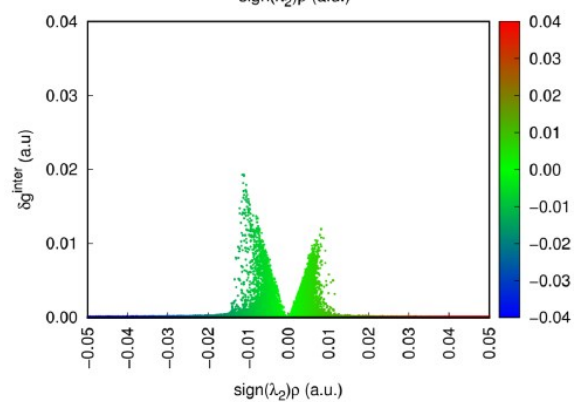
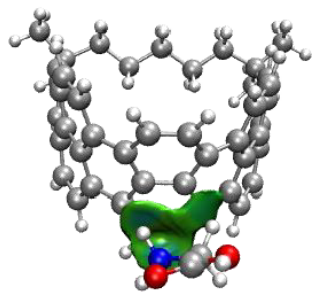
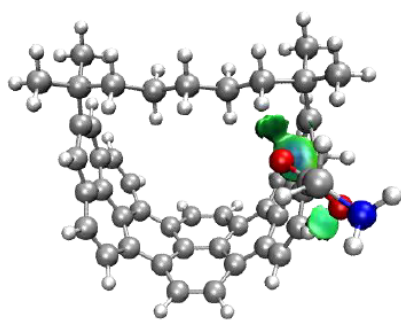
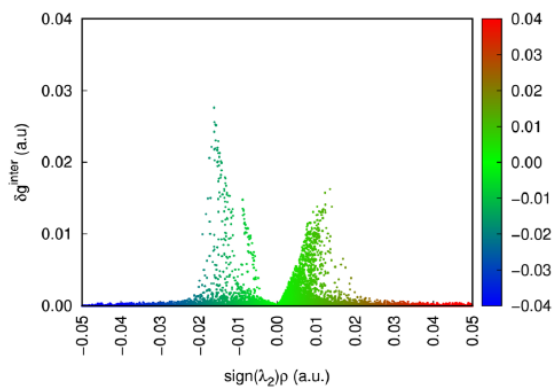


Figure B9. IGMH analysis of the lowest energy structures of each type of [(TM7TP)(Gly)]H⁺ complexes. Upper figures are three dimensional isosurfaces (isovalue = 0.005 a.u.), lower figures are IGMH scatter plots. Both are colored according BGR scheme over the range of $-0.04 < \text{sign}(\lambda_2)\rho < 0.04$ a.u., where the color blue, green and red correspond to strong attraction, weak attraction, and strong repulsion respectively.



exo-(GlyH⁺)(TM7TP)



exo-(Gly)((TM7TP)H⁺)

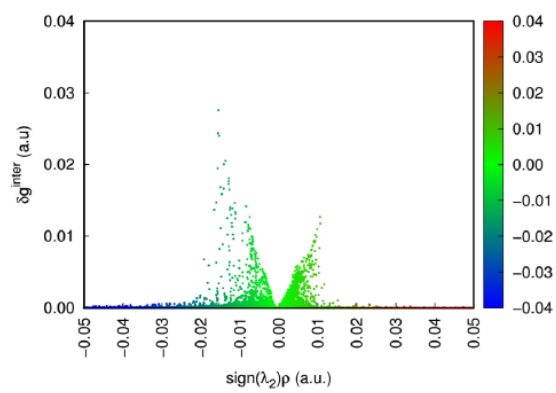
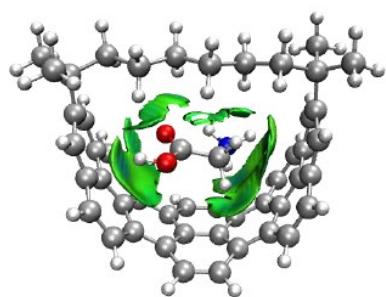
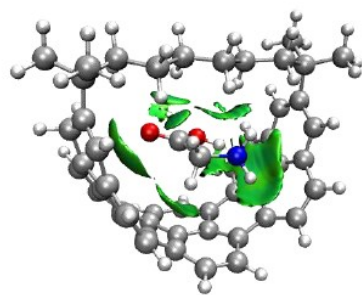
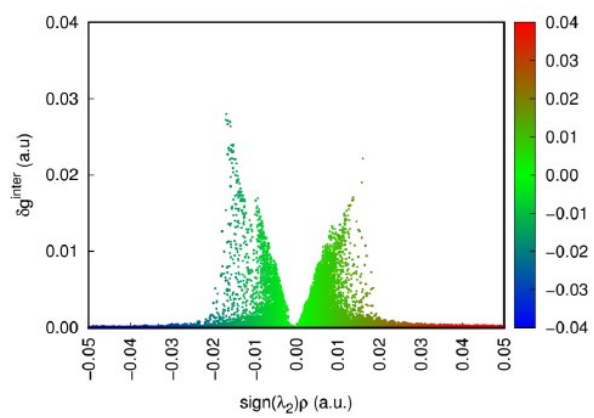


Figure B9 continuous.



endo-(GlyH⁺)(TM8TP)



endo-(Gly)((TM8TP)H⁺)

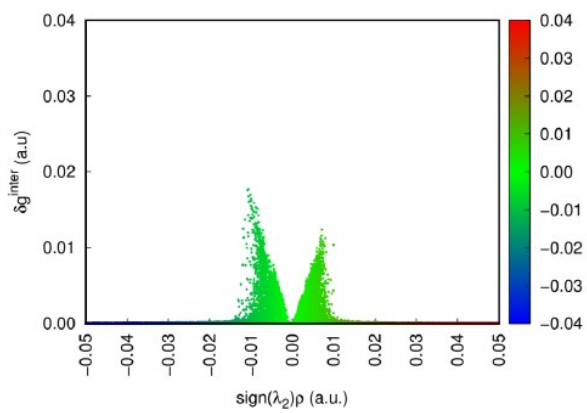


Figure B9 continuous.

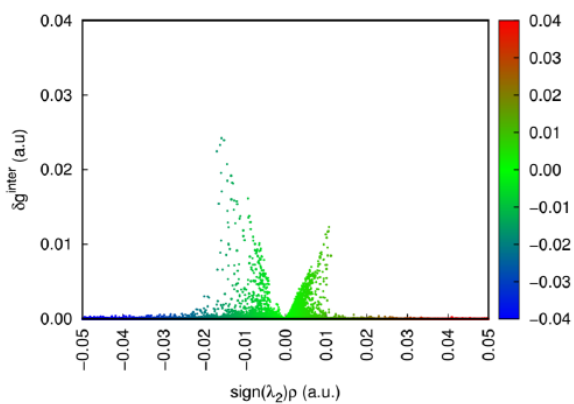
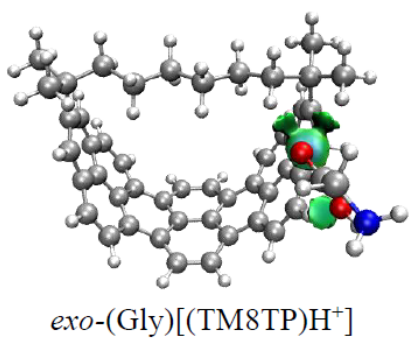
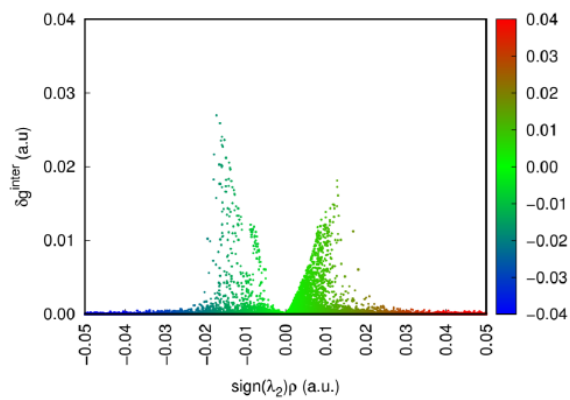
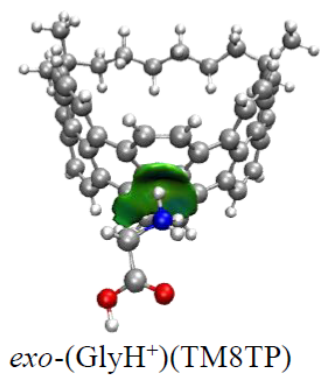


Figure B9 continuous.

Table B1. Experimental PAs of benzene, toluene, naphthalene and 1-methylnaphthalene. All values of energy are listed in kJ mol⁻¹ at 298 K and 1 atm.

| | experimental ^a | B3LYP-D3 / 6-311++g(d,p) | B3LYP-D3 / 6-31+g(d,p) |
|---------------------|---------------------------|-----------------------------|---------------------------|
| benzene | 750.4 | 762.3 ^b | 773.2 |
| toluene | 784.0 | 802.8 ^c | 803.0 |
| naphthalene | 802.9 | 820.9 ^b | 825.5 |
| 1-methylnaphthalene | 834.8 | 832.3 | 835.9 |

^a Experimental PA values from ref. 64.

^b Computed PA values from ref. 65.

^c Computed PA values from ref. 66.

Table B2. Computational proton affinities (kJ mol⁻¹) of TMnTP (n=7-9) at aromatic carbons under B3LYP-D3/6-31+G(d,p)

| Protonation Position | | TM7TP | TM8TP | TM9TP |
|----------------------|------|-------|-------|-------|
| 1 | - | 971.5 | 975.7 | 979.1 |
| 2 | exo | 888.6 | 897.6 | 898.1 |
| | endo | 843.1 | 839.7 | 833.3 |
| 3 | - | 963.9 | 967.5 | 971.6 |
| 3a | exo | 855.9 | 854.4 | 851.7 |
| | endo | 823.6 | 822.5 | 822.2 |
| 4 | - | 950.1 | 952.3 | 954.7 |
| 5 | - | 905.8 | 904.2 | 901.5 |
| 5a | exo | 947.0 | 943.6 | 941.6 |
| | endo | 861.9 | 867.8 | 874.2 |
| 5b | exo | 946.0 | 937.9 | 927.4 |
| | endo | 859.3 | 862.9 | 864.7 |
| 6 | - | 945.0 | 941.3 | 939.7 |
| 16 | - | 945.0 | 943.4 | 939.6 |
| 16a | exo | 946.4 | 935.9 | 927.8 |
| | endo | 859.3 | 861.1 | 864.6 |
| 16b | exo | 899.2 | 889.7 | 854.5 |
| | endo | 809.9 | 815.2 | 820.1 |
| 17 | - | 902.4 | 900.0 | 898.4 |
| 18 | - | 951.5 | 954.8 | 956.1 |
| 18a | exo | 849.4 | 848.0 | 845.7 |
| | endo | 820.1 | 819.3 | 819.5 |
| 18b | exo | 860.7 | 861.1 | 861.2 |
| | endo | 819.6 | 821.7 | 825.9 |
| 18c | exo | 884.6 | 877.8 | 871.3 |
| | endo | 821.3 | 822.1 | 823.6 |
| 18d | exo | 947.7 | 946.9 | 942.9 |
| | endo | 863.3 | 870.1 | 875.6 |

Table B3. Rate constants of [(TMnTP)(Gly)]H⁺ (n=7, 8, 9), at the temperature (T) ranging from 329 K to 371K, the unit of all rate constant values is s⁻¹ and all temperature listed are in K.

| [(TM7TP)(Gly)]H ⁺ | | | [(TM8TP)(Gly)]H ⁺ | | | [(TM9TP)(Gly)]H ⁺ | | |
|------------------------------|-------------|--------------------------|------------------------------|-------------|--------------------------|------------------------------|-------------|--------------------------|
| T | | | T | | | T | | |
| / K | FD | SD × 10 ⁻² | / K | FD | SD × 10 ⁻² | / K | FD | SD × 10 ⁻² |
| 334.8 | 0.37 ± 0.03 | 0.12 ± 0.006 | 330.0 | 0.23 ± 0.01 | 0.25 ± 0.004 | 328.9 | 0.36 ± 0.03 | 0.97 ± 0.02 |
| 341.6 | 0.47 ± 0.02 | 0.18 ± 0.004 | 335.3 | 0.44 ± 0.05 | 0.35 ± 0.03 | 342.2 | 0.75 ± 0.08 | 2.83 ± 0.23 |
| 353.3 | 0.79 ± 0.04 | 0.72 ± 0.03 | 354.1 | 0.71 ± 0.02 | 1.74 ± 0.03 | 350.9 | 1.02 ± 0.07 | 3.71 ± 0.14 |
| 356.7 | 0.83 ± 0.02 | 0.65 ± 0.02 | 356.7 | 1.02 ± 0.10 | 2.95 ± 0.20 | 357.0 | 1.47 ± 0.13 | 9.02 ± 0.55 |
| 363.9 | 1.30 ± 0.07 | 1.52 ± 0.03 | 364.9 | 1.22 ± 0.04 | 3.31 ± 0.08 | 370.6 | 3.20 ± 0.35 | 14.18 ± 0.65 |

Table B4. Natural energy decomposition analysis (NEDA) components in kJ mol⁻¹ under B3LYP-D3/6-31+G(d,p).

| complex | <i>endo</i> -(TMnTP)(GlyH ⁺) | | | <i>endo</i> -(TMnTPH ⁺)(Gly) | | | <i>exo</i> -(TMnTP)(GlyH ⁺) | | | <i>exo</i> -(TMnTPH ⁺)(Gly) | | | |
|----------------------|---|--------|--------|--|--------|--------|--|--------|--------|---|-------|-------|---|
| | n | 7 | 8 | 9 | 7 | 8 | 9 | 7 | 8 | 9 | 7 | 8 | 9 |
| E _{tot} | - | - | - | - | - | - | - | - | - | - | - | - | - |
| ES | 183.97 | 197.97 | 199.30 | -77.40 | -82.62 | -84.78 | 131.48 | 135.41 | 136.58 | 53.09 | 51.89 | 51.40 | - |
| POL | -70.68 | -94.50 | -85.84 | -61.69 | -56.04 | -56.87 | -66.63 | -67.09 | -67.28 | - | - | - | - |
| XC | 460.20 | 598.47 | 571.57 | 215.13 | 235.44 | 237.59 | 386.44 | 385.78 | 389.49 | 87.66 | 88.96 | 76.71 | - |
| CT | 241.25 | 316.68 | 296.20 | 197.72 | 231.76 | 225.10 | 148.16 | 138.00 | 138.54 | 56.77 | 56.32 | 52.06 | - |
| DEF _{host} | -2.00 | -1.69 | -1.54 | -1.57 | -1.75 | -1.35 | -2.22 | -1.67 | -1.31 | -1.16 | -1.10 | -1.21 | - |
| DEF _{guest} | 418.58 | 559.25 | 528.60 | 176.76 | 204.89 | 206.46 | 368.49 | 365.92 | 367.10 | 45.84 | 46.74 | 36.21 | - |
| SE _{host} | 171.85 | 254.11 | 227.25 | 221.97 | 237.48 | 229.66 | 103.47 | 91.20 | 92.94 | 98.36 | 99.37 | 92.28 | - |
| SE _{guest} | 194.20 | 247.01 | 238.11 | 56.87 | 65.76 | 68.16 | 173.54 | 175.82 | 177.29 | 14.98 | 15.46 | 12.04 | - |
| EL | 40.63 | 56.79 | 52.01 | 52.81 | 53.56 | 52.92 | 25.71 | 22.87 | 23.37 | 29.84 | 30.02 | 27.11 | - |
| CT | 296.06 | 389.15 | 367.28 | 167.15 | 172.17 | 173.39 | 253.81 | 254.18 | 256.11 | 94.54 | 95.11 | 87.46 | - |
| CORE | -2.00 | -1.69 | -1.54 | -1.57 | -1.75 | -1.35 | -2.22 | -1.67 | -1.31 | -1.16 | -1.10 | -1.21 | - |
| | 114.08 | 192.87 | 169.52 | 91.33 | 91.29 | 89.96 | 124.55 | 120.44 | 120.83 | 42.61 | 44.31 | 37.28 | - |

Table B5. Relative enthalpies and Gibbs energies (in parentheses) of the lowest energy *endo*-(TMnTP)(GlyH⁺), *endo*-(TMnTPH⁺)(Gly), *exo*-(TMnTP)(GlyH⁺), and *exo*-(TMnTPH⁺)(Gly) structures at the B3LYP-D3/6-31+G(d,p) and wB97xD/6-31+G(d,p) levels and basis set.

| Species | B3LYP/6-31+G(d,p) | wB97xD/6-31+G(d,p) |
|--|-------------------|--------------------|
| <i>endo</i> -(TM7TP)(GlyH ⁺) | 0.0 (0.0) | 0.0 (0.0) |
| <i>endo</i> -(TM7TPH ⁺)(Gly) | 24.9 (27.0) | 44.9 (47.3) |
| <i>exo</i> -(TM7TPH ⁺)(Gly) | 48.4 (30.5) | 72.8 (53.6) |
| <i>exo</i> -(TM7TP)(GlyH ⁺) | 51.6 (45.9) | 59.5 (51.0) |
| <i>endo</i> -(TM8TP)(GlyH ⁺) | 0.0 (0.0) | 0.0 (0.0) |
| <i>endo</i> -(TM8TPH ⁺)(Gly) | 26.3 (20.4) | 41.9 (36.5) |
| <i>exo</i> -(TM8TPH ⁺)(Gly) | 57.9 (31.2) | 80.4 (50.6) |
| <i>exo</i> -(TM8TP)(GlyH ⁺) | 63.5 (48.3) | 69.5 (46.6) |
| <i>endo</i> -(TM9TP)(GlyH ⁺) | 0.0 (0.0) | 0.0 (0.0) |
| <i>endo</i> -(TM9TPH ⁺)(Gly) | 26.5 (24.8) | 40.6 (35.6) |
| <i>exo</i> -(TM9TPH ⁺)(Gly) | 57.0 (30.5) | 78.5 (49.7) |
| <i>exo</i> -(TM9TP)(GlyH ⁺) | 64.3 (46.1) | 70.9 (52.3) |

Coordinates of the lowest-energy TMnTP/Glycine/H⁺ complex types

endo-(TM7TP)(GlyH⁺)

| | | | |
|---|-------------|-------------|-------------|
| C | -4.17939534 | 1.70117786 | 0.32294321 |
| C | -4.05817810 | 1.06605434 | -0.92421518 |
| H | -4.09146754 | 1.65129279 | -1.83702614 |
| C | -3.77565667 | -0.30392687 | -1.03827103 |
| C | -3.59266616 | -1.07869338 | 0.14699166 |
| C | -3.90868294 | -0.48776848 | 1.40354926 |
| C | -4.19810849 | 0.88720189 | 1.46423205 |
| H | -4.35986880 | 1.32228518 | 2.44374432 |
| C | -3.50085326 | -0.93623799 | -2.30530754 |
| H | -3.77601501 | -0.41709587 | -3.21867107 |
| C | -2.82441203 | -2.11903504 | -2.36244041 |
| H | -2.56450332 | -2.53500624 | -3.32937701 |
| C | -2.33298360 | -2.75289541 | -1.16053738 |
| C | -2.86604280 | -2.31426490 | 0.09298240 |
| C | -2.43073063 | -2.90591396 | 1.31960328 |
| C | -3.05635100 | -2.46411023 | 2.54219008 |
| H | -2.88172777 | -3.01328894 | 3.46025542 |
| C | -3.76110013 | -1.29790074 | 2.58438014 |
| H | -4.15041028 | -0.92658388 | 3.52811401 |
| C | -1.12429744 | -3.50130420 | -1.15618542 |
| C | -0.47039911 | -3.71061690 | 0.09569227 |
| C | -1.20247533 | -3.62327888 | 1.31803034 |
| C | -0.34869732 | -3.75231589 | -2.34966629 |
| H | -0.85021425 | -3.90225507 | -3.29963859 |
| C | 1.01309681 | -3.69797838 | -2.30449445 |
| H | 1.58521989 | -3.80222281 | -3.22000746 |
| C | 1.68243639 | -3.37038958 | -1.06620057 |
| C | 0.96899152 | -3.62993705 | 0.14170176 |
| C | 1.59403232 | -3.43290550 | 1.40818302 |
| C | 0.86145189 | -3.85993742 | 2.57563396 |
| H | 1.37998363 | -4.00541209 | 3.51685473 |
| C | -0.49613981 | -3.95861047 | 2.53137616 |
| H | -1.04847638 | -4.18272183 | 3.43688281 |
| C | 2.80575116 | -2.50211377 | -1.00931592 |
| C | 3.15245054 | -1.94070532 | 0.25882189 |
| C | 2.69755575 | -2.53987227 | 1.47407318 |
| C | 3.36462189 | -1.89021440 | -2.19157729 |
| H | 3.27035065 | -2.39115889 | -3.14874275 |
| C | 3.89852497 | -0.63573689 | -2.14364856 |
| H | 4.22693267 | -0.14507566 | -3.05540193 |
| C | 3.94071127 | 0.09841110 | -0.90355162 |
| C | 3.71574808 | -0.62638492 | 0.30404492 |
| C | 3.83214806 | 0.05753810 | 1.54648106 |
| C | 3.67289952 | -0.70723229 | 2.75479608 |
| H | 3.91331256 | -0.24147172 | 3.70641092 |

| | | | |
|---|-------------|-------------|-------------|
| C | 3.13825412 | -1.96149871 | 2.71892305 |
| H | 2.94792555 | -2.48472642 | 3.64906532 |
| C | 4.03806733 | 1.49731536 | -0.84971032 |
| H | 4.11318527 | 2.03628183 | -1.78893702 |
| C | 3.94421738 | 2.20388349 | 0.36254965 |
| C | 3.94478653 | 1.45880164 | 1.54931379 |
| H | 3.95163776 | 1.95985719 | 2.51038416 |
| C | 3.72063635 | 3.72518658 | 0.35050428 |
| C | 3.83800413 | 4.35027773 | 1.75494531 |
| H | 3.09726268 | 3.96192908 | 2.45936612 |
| H | 3.68770610 | 5.43220948 | 1.68795412 |
| H | 4.83191014 | 4.17951900 | 2.18106221 |
| C | 4.76409120 | 4.42068315 | -0.55538737 |
| H | 5.77931378 | 4.22381088 | -0.19702757 |
| H | 4.60614890 | 5.50417449 | -0.55035557 |
| H | 4.70308726 | 4.08758719 | -1.59550473 |
| C | 2.29695653 | 4.01789033 | -0.23626192 |
| H | 2.28801833 | 3.71191964 | -1.29133392 |
| H | 2.16609428 | 5.10823221 | -0.23561860 |
| C | 1.07907832 | 3.38234749 | 0.46356476 |
| H | 1.14489769 | 2.28498219 | 0.36709253 |
| H | 1.10565595 | 3.58749723 | 1.54049167 |
| C | -0.25656501 | 3.88824293 | -0.11494809 |
| H | -0.28738455 | 3.68342177 | -1.19249276 |
| H | -0.28722192 | 4.98120217 | -0.01483885 |
| C | -1.52156275 | 3.30358881 | 0.54100740 |
| H | -1.48855074 | 2.20451714 | 0.50971807 |
| H | -1.53625977 | 3.57459572 | 1.60356964 |
| C | -2.81161702 | 3.77059871 | -0.15838247 |
| H | -2.73772321 | 3.50162395 | -1.21879380 |
| H | -2.85117861 | 4.86740862 | -0.12145404 |
| C | -4.17548046 | 3.23812687 | 0.39887990 |
| C | -5.31079548 | 3.81298308 | -0.48162889 |
| H | -5.19810607 | 3.53771751 | -1.53434807 |
| H | -5.31527573 | 4.90661904 | -0.42636529 |
| H | -6.28597029 | 3.45139609 | -0.14048905 |
| C | -4.38626680 | 3.75743429 | 1.83422020 |
| H | -5.35799120 | 3.44649318 | 2.23161777 |
| H | -4.36630637 | 4.85163769 | 1.83320939 |
| H | -3.61158241 | 3.41656103 | 2.52724006 |
| N | -0.49106714 | -0.23951178 | -0.31458052 |
| H | -1.46970133 | -0.14715386 | -0.63641613 |
| C | 0.45990152 | -0.14496000 | -1.46508374 |
| C | -0.00171602 | 0.96106130 | -2.39129907 |
| H | 1.46641805 | 0.04249583 | -1.09114966 |
| H | 0.45468104 | -1.10039929 | -1.99365546 |
| O | -1.06928051 | 1.52204778 | -2.27903547 |
| O | 0.91269816 | 1.20360606 | -3.33392405 |
| H | 0.57438733 | 1.89315028 | -3.93297346 |
| H | -0.33785960 | 0.51803754 | 0.36001130 |
| H | -0.39649376 | -1.14265868 | 0.16723086 |

endo-(TM7TPH⁺)(Gly)

| | | | |
|---|-------------|-------------|-------------|
| C | -4.19131100 | 1.82992600 | 0.38949100 |
| C | -4.35001000 | 1.16462000 | -0.95201500 |
| H | -3.77209400 | 1.68887800 | -1.71948700 |
| C | -3.97860800 | -0.28711600 | -1.01855200 |
| C | -3.70055700 | -1.00068800 | 0.16415000 |
| C | -3.94901100 | -0.37688500 | 1.42726700 |
| C | -4.17454500 | 1.04285300 | 1.49886200 |
| H | -4.16595700 | 1.48219800 | 2.48961800 |
| C | -3.77658600 | -0.91896100 | -2.25300500 |
| H | -4.06611900 | -0.41510100 | -3.17000500 |
| C | -3.03866100 | -2.09077000 | -2.32021900 |
| H | -2.77542700 | -2.47833800 | -3.29821300 |
| C | -2.49537500 | -2.68268200 | -1.15453100 |
| C | -2.97104900 | -2.22302600 | 0.10696400 |
| C | -2.51077300 | -2.81472700 | 1.32027200 |
| C | -3.05078000 | -2.33055100 | 2.54199500 |
| H | -2.80884400 | -2.82992300 | 3.47359100 |
| C | -3.75334600 | -1.14114400 | 2.59730600 |
| H | -4.04116500 | -0.72887100 | 3.55955600 |
| C | -1.25428000 | -3.41519100 | -1.18121900 |
| C | -0.57826500 | -3.63498900 | 0.05249300 |
| C | -1.29284200 | -3.56653400 | 1.28884100 |
| C | -0.50836600 | -3.63593700 | -2.38142400 |
| H | -1.01748400 | -3.70393700 | -3.33613900 |
| C | 0.86277500 | -3.60181800 | -2.35515700 |
| H | 1.40690800 | -3.64778200 | -3.29257200 |
| C | 1.56524100 | -3.36035600 | -1.13036300 |
| C | 0.85505600 | -3.61131300 | 0.07932100 |
| C | 1.50924800 | -3.49408900 | 1.33927000 |
| C | 0.77496600 | -3.91576700 | 2.49681200 |
| H | 1.29377700 | -4.09408900 | 3.43246600 |
| C | -0.59188100 | -3.96720100 | 2.47129800 |
| H | -1.13542900 | -4.18022300 | 3.38475000 |
| C | 2.75504500 | -2.57447700 | -1.06434000 |
| C | 3.14277000 | -2.06472500 | 0.21141500 |
| C | 2.66225200 | -2.66369100 | 1.41726100 |
| C | 3.37283500 | -1.99545500 | -2.23029000 |
| H | 3.25850900 | -2.47980400 | -3.19429600 |
| C | 4.00116500 | -0.78395900 | -2.15722300 |
| H | 4.39299400 | -0.31545100 | -3.05647600 |
| C | 4.06785300 | -0.06631500 | -0.91175400 |
| C | 3.78742400 | -0.79231000 | 0.27958400 |
| C | 3.92668700 | -0.13381600 | 1.53147000 |
| C | 3.73190500 | -0.91007300 | 2.72515300 |
| H | 3.98858900 | -0.47112700 | 3.68522200 |
| C | 3.14034000 | -2.13893000 | 2.66872000 |
| H | 2.92280700 | -2.66547100 | 3.59089700 |
| C | 4.22243800 | 1.32728700 | -0.83770500 |
| H | 4.34438700 | 1.87471300 | -1.76738800 |

| | | | |
|---|-------------|-------------|-------------|
| C | 4.11211700 | 2.02419100 | 0.37913000 |
| C | 4.08084600 | 1.26257400 | 1.55580600 |
| H | 4.08705000 | 1.75095000 | 2.52325600 |
| C | 3.90663100 | 3.54929500 | 0.38496500 |
| C | 4.05797300 | 4.15850500 | 1.79268500 |
| H | 3.33248300 | 3.76257400 | 2.50795800 |
| H | 3.90487000 | 5.24100300 | 1.74109400 |
| H | 5.06205500 | 3.98273500 | 2.19264800 |
| C | 4.94251200 | 4.23780500 | -0.53517400 |
| H | 5.96267300 | 3.99848400 | -0.21881500 |
| H | 4.81989600 | 5.32483300 | -0.49376200 |
| H | 4.83494700 | 3.94040000 | -1.58272700 |
| C | 2.47552800 | 3.86645700 | -0.17515800 |
| H | 2.42503200 | 3.47715000 | -1.20269500 |
| H | 2.40206600 | 4.95842600 | -0.26874500 |
| C | 1.24536000 | 3.36129600 | 0.60672600 |
| H | 1.29778600 | 2.27260400 | 0.73930300 |
| H | 1.24434500 | 3.79150000 | 1.61552300 |
| C | -0.07526300 | 3.73804300 | -0.09645600 |
| H | -0.08964900 | 3.28817000 | -1.09944500 |
| H | -0.08752800 | 4.82446000 | -0.26385500 |
| C | -1.36530500 | 3.33543300 | 0.65024800 |
| H | -1.36683100 | 2.25526100 | 0.82827500 |
| H | -1.36896800 | 3.82383500 | 1.63251300 |
| C | -2.62154200 | 3.73876700 | -0.14805700 |
| H | -2.53105800 | 3.33293800 | -1.16229800 |
| H | -2.63188100 | 4.83138700 | -0.25914300 |
| C | -4.03547700 | 3.34797500 | 0.42503200 |
| C | -5.10704400 | 4.00247900 | -0.48443800 |
| H | -4.98325200 | 3.72857600 | -1.53635100 |
| H | -5.03187400 | 5.09214500 | -0.42078100 |
| H | -6.11643700 | 3.71659100 | -0.16955000 |
| C | -4.19859900 | 3.92277400 | 1.84446200 |
| H | -5.19632400 | 3.71361300 | 2.24424900 |
| H | -4.07197100 | 5.00926800 | 1.81371600 |
| H | -3.45863500 | 3.52963600 | 2.54613200 |
| H | -5.40454900 | 1.28633500 | -1.25315100 |
| N | 1.19558700 | 1.13298400 | -3.04186900 |
| H | -0.67699200 | 1.45101300 | -3.12911400 |
| C | 0.84014000 | 0.38395100 | -1.83273400 |
| C | -0.62087800 | 0.61108300 | -1.46957500 |
| H | 0.95415100 | -0.68948000 | -2.00172700 |
| H | 1.44819700 | 0.62943100 | -0.95849800 |
| O | -1.33302600 | 1.24677700 | -2.41435500 |
| O | -1.10715500 | 0.23696000 | -0.42382000 |
| H | 1.77034000 | 0.58543400 | -3.67283500 |
| H | 1.70443700 | 1.98336600 | -2.81988000 |

exo-(TM7TPH⁺)(Gly)

| | | | |
|---|-------------|-------------|-------------|
| C | -4.42884402 | 1.68410393 | 0.63282052 |
| C | -4.65866558 | 0.96948308 | -0.66981287 |
| H | -4.26169369 | 1.53776639 | -1.51721529 |
| C | -4.13366896 | -0.43241749 | -0.75083996 |
| C | -3.67686195 | -1.08584101 | 0.41456028 |
| C | -3.86173087 | -0.45443650 | 1.68809105 |
| C | -4.21186017 | 0.94189238 | 1.75217592 |
| H | -4.13547525 | 1.41354078 | 2.72526583 |
| C | -4.00245109 | -1.07744990 | -1.98790385 |
| H | -4.42152265 | -0.61421351 | -2.87546182 |
| C | -3.21140524 | -2.21358483 | -2.09839765 |
| H | -3.02073057 | -2.61218437 | -3.08861442 |
| C | -2.53595642 | -2.75492348 | -0.98006609 |
| C | -2.88735536 | -2.26817135 | 0.31264515 |
| C | -2.28184385 | -2.80800701 | 1.48862473 |
| C | -2.72040663 | -2.31617041 | 2.74313348 |
| H | -2.35277092 | -2.76959580 | 3.65707488 |
| C | -3.49393779 | -1.17084816 | 2.84378847 |
| H | -3.71248044 | -0.75396966 | 3.82222218 |
| C | -1.28437772 | -3.46081511 | -1.11706227 |
| C | -0.46579487 | -3.60048375 | 0.04106985 |
| C | -1.04037145 | -3.51578960 | 1.34673338 |
| C | -0.67131784 | -3.71259042 | -2.38112840 |
| H | -1.27923052 | -3.85349763 | -3.26750471 |
| C | 0.68916378 | -3.58698507 | -2.51236203 |
| H | 1.12784025 | -3.63599501 | -3.50314954 |
| C | 1.49921788 | -3.23747792 | -1.38682635 |
| C | 0.95722764 | -3.50384036 | -0.09644116 |
| C | 1.74408256 | -3.30778071 | 1.07431203 |
| C | 1.16715341 | -3.72058335 | 2.31801092 |
| H | 1.79260359 | -3.82759030 | 3.19769749 |
| C | -0.19264383 | -3.83707064 | 2.45159891 |
| H | -0.61622087 | -4.02791342 | 3.43113642 |
| C | 2.59549181 | -2.32770381 | -1.47617350 |
| C | 3.10554894 | -1.77568354 | -0.26101558 |
| C | 2.84565049 | -2.40439652 | 0.99688742 |
| C | 2.95701112 | -1.68762926 | -2.71199241 |
| H | 2.72270042 | -2.16823767 | -3.65514314 |
| C | 3.45800343 | -0.41683102 | -2.71574137 |
| H | 3.62807879 | 0.09941134 | -3.65659607 |
| C | 3.66698552 | 0.29408430 | -1.48478964 |
| C | 3.64364128 | -0.45375988 | -0.27400757 |
| C | 3.92698815 | 0.21314453 | 0.94829958 |
| C | 3.96748978 | -0.57485139 | 2.14816873 |
| H | 4.33280668 | -0.11933112 | 3.06452329 |
| C | 3.45886516 | -1.84312783 | 2.16935494 |
| H | 3.41534403 | -2.38142709 | 3.10945078 |
| C | 3.73054168 | 1.69353410 | -1.41873095 |
| H | 3.64551681 | 2.24959795 | -2.34728513 |

| | | | |
|---|-------------|------------|-------------|
| C | 3.77662292 | 2.37936079 | -0.19280593 |
| C | 3.98823826 | 1.61830622 | 0.96455874 |
| H | 4.11399380 | 2.10529892 | 1.92479201 |
| C | 3.47030564 | 3.88518821 | -0.14952848 |
| C | 3.66540530 | 4.48498669 | 1.25651490 |
| H | 3.01552667 | 4.02545581 | 2.00639001 |
| H | 3.43218751 | 5.55411507 | 1.23284770 |
| H | 4.70223586 | 4.38035917 | 1.59352662 |
| C | 4.40226361 | 4.65069995 | -1.11865035 |
| H | 5.45169430 | 4.50847018 | -0.84095783 |
| H | 4.18358201 | 5.72324944 | -1.08457820 |
| H | 4.28060268 | 4.32547402 | -2.15607347 |
| C | 1.98927089 | 4.10909850 | -0.61522013 |
| H | 1.91024237 | 3.81112685 | -1.66909344 |
| H | 1.80864736 | 5.19273198 | -0.59391429 |
| C | 0.86619032 | 3.40512939 | 0.17298954 |
| H | 1.00191051 | 2.31662212 | 0.12029385 |
| H | 0.92591291 | 3.67407347 | 1.23543750 |
| C | -0.53178186 | 3.78195404 | -0.35829736 |
| H | -0.60587997 | 3.49722074 | -1.41731098 |
| H | -0.63306321 | 4.87641872 | -0.33241126 |
| C | -1.71586961 | 3.16125576 | 0.41162775 |
| H | -1.66043539 | 2.06572742 | 0.34933184 |
| H | -1.62171128 | 3.41374610 | 1.47574118 |
| C | -3.06951857 | 3.65311900 | -0.13804862 |
| H | -3.14622553 | 3.36876092 | -1.19305522 |
| H | -3.07663688 | 4.75136152 | -0.12224231 |
| C | -4.38467932 | 3.20586101 | 0.60603182 |
| C | -5.58904849 | 3.76066208 | -0.19578354 |
| H | -5.58044007 | 3.42302266 | -1.23561893 |
| H | -5.55263567 | 4.85453103 | -0.20584921 |
| H | -6.53697919 | 3.45911353 | 0.26320646 |
| C | -4.42135908 | 3.82189149 | 2.01722441 |
| H | -5.33384282 | 3.53698509 | 2.55168407 |
| H | -4.40808237 | 4.91316396 | 1.93898180 |
| H | -3.56246443 | 3.52974368 | 2.62720875 |
| H | -5.74734814 | 0.95741417 | -0.85133930 |
| N | -6.33565127 | 2.52115925 | -6.17754493 |
| H | -6.26798508 | 1.25333643 | -4.80478211 |
| C | -5.18602437 | 3.11371028 | -5.48166900 |
| C | -4.84138787 | 2.29686345 | -4.22963237 |
| H | -4.28821098 | 3.14104552 | -6.10698410 |
| H | -5.37269859 | 4.14212242 | -5.15683775 |
| O | -5.62995421 | 1.22989461 | -4.04203252 |
| O | -3.93848314 | 2.58639804 | -3.47119337 |
| H | -6.12010270 | 2.23408821 | -7.12588951 |
| H | -7.14023202 | 3.13782052 | -6.20841401 |

exo-(TM7TP)(GlyH⁺)

| | | | |
|---|-------------|-------------|-------------|
| C | 2.43715506 | 4.33111151 | 0.01811103 |
| C | 1.68269541 | 4.24362073 | -1.16495443 |
| H | 2.17007400 | 4.36413946 | -2.12743616 |
| C | 0.32919093 | 3.88241455 | -1.15714066 |
| C | -0.30188085 | 3.59295994 | 0.08655913 |
| C | 0.38666167 | 3.89999213 | 1.29208906 |
| C | 1.74371709 | 4.26375997 | 1.23337575 |
| H | 2.26842813 | 4.40297979 | 2.17157888 |
| C | -0.41413560 | 3.63474681 | -2.36366734 |
| H | -0.01211637 | 3.98809206 | -3.30922353 |
| C | -1.55167555 | 2.88288443 | -2.34059127 |
| H | -2.04192241 | 2.63344011 | -3.27480774 |
| C | -2.01645487 | 2.29270162 | -1.11066445 |
| C | -1.48434401 | 2.79343095 | 0.11928029 |
| C | -1.95239757 | 2.30189765 | 1.37772379 |
| C | -1.42769838 | 2.90222411 | 2.57667346 |
| H | -1.86635537 | 2.65888175 | 3.53809730 |
| C | -0.29377492 | 3.66117872 | 2.53523097 |
| H | 0.15363917 | 4.02374803 | 3.45660656 |
| C | -2.69509268 | 1.04497894 | -1.08762974 |
| C | -2.76105014 | 0.34570538 | 0.15480668 |
| C | -2.62379297 | 1.04791233 | 1.39038147 |
| C | -3.00160336 | 0.28950109 | -2.28022453 |
| H | -3.23165974 | 0.80702018 | -3.20531224 |
| C | -2.86183372 | -1.06699847 | -2.28575960 |
| H | -2.98311870 | -1.61435611 | -3.21415204 |
| C | -2.39952438 | -1.75085237 | -1.09955430 |
| C | -2.61001658 | -1.09125723 | 0.14878968 |
| C | -2.30869204 | -1.75450622 | 1.38014055 |
| C | -2.68675377 | -1.07313147 | 2.59502417 |
| H | -2.71889853 | -1.61348411 | 3.53537972 |
| C | -2.84767377 | 0.28903841 | 2.59898820 |
| H | -2.99952138 | 0.80124024 | 3.54341817 |
| C | -1.45905505 | -2.81508004 | -1.13583695 |
| C | -0.81815616 | -3.19070743 | 0.08674319 |
| C | -1.37481932 | -2.82614194 | 1.35249406 |
| C | -0.88207375 | -3.27684793 | -2.37298467 |
| H | -1.42378697 | -3.14011946 | -3.30199587 |
| C | 0.39595140 | -3.75178356 | -2.40863457 |
| H | 0.86011881 | -3.99921807 | -3.35934845 |
| C | 1.18452255 | -3.83465733 | -1.20840856 |
| C | 0.51297153 | -3.70447562 | 0.04090548 |
| C | 1.26054604 | -3.86033382 | 1.24031513 |
| C | 0.55215154 | -3.79118223 | 2.48897669 |
| H | 1.07508626 | -4.05384769 | 3.40444804 |
| C | -0.72207864 | -3.30498528 | 2.54318321 |
| H | -1.19852418 | -3.17488567 | 3.50860020 |
| C | 2.58467086 | -3.88347402 | -1.22584863 |
| H | 3.08020564 | -3.88364287 | -2.19169717 |

| | | | |
|---|-------------|-------------|-------------|
| C | 3.34718422 | -3.81144213 | -0.04698573 |
| C | 2.66385767 | -3.91159681 | 1.17197397 |
| H | 3.21243511 | -3.93940553 | 2.10640747 |
| C | 4.85009743 | -3.49961105 | -0.13036895 |
| C | 5.54269776 | -3.56619859 | 1.24461463 |
| H | 5.12817063 | -2.85268477 | 1.96202454 |
| H | 6.60580257 | -3.33286949 | 1.12914514 |
| H | 5.46923134 | -4.56902395 | 1.67899367 |
| C | 5.55818334 | -4.51282607 | -1.06081447 |
| H | 5.44170449 | -5.53389384 | -0.68307032 |
| H | 6.62902848 | -4.29010916 | -1.11521530 |
| H | 5.16677510 | -4.48366663 | -2.08192112 |
| C | 5.02808228 | -2.06567314 | -0.74027493 |
| H | 4.65274718 | -2.08127155 | -1.77206778 |
| H | 6.10862229 | -1.88095816 | -0.81497710 |
| C | 4.37285624 | -0.88146203 | -0.00246446 |
| H | 3.28778792 | -1.03802751 | 0.06190319 |
| H | 4.74060665 | -0.83223180 | 1.03048123 |
| C | 4.66047448 | 0.46464228 | -0.69727678 |
| H | 4.26763577 | 0.43054110 | -1.72376818 |
| H | 5.74884230 | 0.58647023 | -0.79446724 |
| C | 4.08569454 | 1.70180294 | 0.02142632 |
| H | 2.99266119 | 1.61609584 | 0.08440881 |
| H | 4.45553056 | 1.71462804 | 1.05472452 |
| C | 4.46593786 | 3.01443041 | -0.69162482 |
| H | 4.10104237 | 2.96479263 | -1.72607899 |
| H | 5.56086267 | 3.07462612 | -0.76061945 |
| C | 3.97200726 | 4.36227861 | -0.05989055 |
| C | 4.43986658 | 5.52339718 | -0.96909368 |
| H | 4.06584085 | 5.42651610 | -1.99258560 |
| H | 5.53353828 | 5.54411278 | -1.02156495 |
| H | 4.09975188 | 6.48652401 | -0.57466559 |
| C | 4.62806565 | 4.55697294 | 1.32080319 |
| H | 4.33352414 | 5.51134893 | 1.77042889 |
| H | 5.71685047 | 4.56616866 | 1.20928363 |
| H | 4.37869606 | 3.75743971 | 2.02385541 |
| N | -5.50452656 | -0.82653622 | 1.01600375 |
| H | -4.88010882 | -1.33832174 | 0.37413496 |
| C | -6.12231412 | 0.34982439 | 0.33171993 |
| C | -7.24683488 | -0.16109260 | -0.55462719 |
| H | -6.51568565 | 1.03777110 | 1.08444000 |
| H | -5.34883997 | 0.86349001 | -0.24276904 |
| O | -7.63087256 | -1.31043855 | -0.52212656 |
| O | -7.73107011 | 0.81239212 | -1.32268257 |
| H | -8.46657399 | 0.46796513 | -1.86153295 |
| H | -6.22904658 | -1.48142527 | 1.33254276 |
| H | -4.89092889 | -0.54700770 | 1.80476791 |

endo-(TM8TP)(GlyH⁺)

| | | | |
|---|-------------|-------------|-------------|
| C | 4.29666698 | 2.21985121 | 0.02556910 |
| C | 4.28619556 | 1.51188918 | 1.24049474 |
| H | 4.26710801 | 2.05343802 | 2.18105821 |
| C | 4.19062389 | 0.11326247 | 1.29284288 |
| C | 4.09352701 | -0.62055469 | 0.07480750 |
| C | 4.33713671 | 0.06089887 | -1.15383985 |
| C | 4.42315085 | 1.46945897 | -1.15539274 |
| H | 4.53398883 | 1.96780257 | -2.11224705 |
| C | 4.00889276 | -0.60635077 | 2.52743534 |
| H | 4.24867620 | -0.11206106 | 3.46447284 |
| C | 3.44737544 | -1.84856397 | 2.52783938 |
| H | 3.23840536 | -2.33421413 | 3.47394269 |
| C | 2.99373486 | -2.45646554 | 1.29976181 |
| C | 3.48602064 | -1.91961903 | 0.07107629 |
| C | 3.09328661 | -2.48789821 | -1.18137312 |
| C | 3.69275788 | -1.94524589 | -2.37951625 |
| H | 3.58850549 | -2.47749921 | -3.31848524 |
| C | 4.28775762 | -0.71632093 | -2.36982469 |
| H | 4.65738060 | -0.27707091 | -3.29222739 |
| C | 1.83522393 | -3.28416695 | 1.26155459 |
| C | 1.18219924 | -3.47119778 | 0.00487306 |
| C | 1.89959290 | -3.26733569 | -1.21534587 |
| C | 1.10046990 | -3.64722723 | 2.44549261 |
| H | 1.61894208 | -3.75796483 | 3.39099902 |
| C | -0.25977791 | -3.73454416 | 2.41110117 |
| H | -0.80057210 | -3.91790209 | 3.33256206 |
| C | -0.98367191 | -3.46909197 | 1.19584814 |
| C | -0.25544107 | -3.55115562 | -0.02851604 |
| C | -0.92681428 | -3.41063480 | -1.28071914 |
| C | -0.15155516 | -3.63720733 | -2.47291392 |
| H | -0.65371793 | -3.78216923 | -3.42278229 |
| C | 1.21155893 | -3.57826967 | -2.44468336 |
| H | 1.76958810 | -3.67299212 | -3.36939263 |
| C | -2.27656489 | -2.87526232 | 1.18284619 |
| C | -2.79094974 | -2.39392690 | -0.06035541 |
| C | -2.21255607 | -2.80396935 | -1.30139179 |
| C | -2.95778581 | -2.48078468 | 2.39000119 |
| H | -2.70091754 | -2.95464762 | 3.33031196 |
| C | -3.84147160 | -1.44084824 | 2.39122692 |
| H | -4.28008656 | -1.09589141 | 3.32356369 |
| C | -4.12595555 | -0.71828553 | 1.17670778 |
| C | -3.72604927 | -1.31208423 | -0.05469646 |
| C | -4.07429463 | -0.66071093 | -1.27005881 |
| C | -3.71205179 | -1.30089403 | -2.50542909 |
| H | -4.09884256 | -0.89917409 | -3.43782839 |
| C | -2.82345533 | -2.33468668 | -2.51903943 |
| H | -2.50919133 | -2.74808559 | -3.47060641 |
| C | -4.62943340 | 0.60034844 | 1.17228278 |
| H | -4.85422022 | 1.05902691 | 2.12931110 |

| | | | |
|---|-------------|-------------|-------------|
| C | -4.77079564 | 1.33326195 | -0.01694462 |
| C | -4.59322311 | 0.63957021 | -1.22488465 |
| H | -4.75988744 | 1.14808721 | -2.16907429 |
| C | -4.99689383 | 2.85704355 | -0.04244955 |
| C | -6.17853605 | 3.20133308 | -0.97996631 |
| H | -5.97898622 | 2.92382332 | -2.01908543 |
| H | -6.37158499 | 4.27884626 | -0.96183567 |
| H | -7.09065228 | 2.68672998 | -0.66139851 |
| C | -5.31807317 | 3.42852316 | 1.35117755 |
| H | -6.24757317 | 3.00699543 | 1.74821614 |
| H | -5.44883332 | 4.51300137 | 1.28121192 |
| H | -4.52208952 | 3.24355123 | 2.07817702 |
| C | -3.70273878 | 3.54046628 | -0.61018487 |
| H | -3.46758293 | 3.07628231 | -1.57592565 |
| H | -3.94769707 | 4.58846100 | -0.82683756 |
| C | -2.44882238 | 3.49658596 | 0.28481445 |
| H | -2.38519766 | 2.51722419 | 0.77155969 |
| H | -2.54357775 | 4.23106516 | 1.09428578 |
| C | -1.13566877 | 3.75042642 | -0.48072894 |
| H | -1.01583129 | 2.95997446 | -1.23346614 |
| H | -1.20813990 | 4.69407902 | -1.03786347 |
| C | 0.10908516 | 3.80149417 | 0.42814454 |
| H | 0.06947051 | 2.97817183 | 1.15762050 |
| H | 0.07223881 | 4.71835496 | 1.03126678 |
| C | 1.45603430 | 3.74986222 | -0.32230258 |
| H | 1.58399694 | 2.75639595 | -0.78111919 |
| H | 1.42626591 | 4.45372507 | -1.16244696 |
| C | 2.66191559 | 4.07275237 | 0.58242440 |
| H | 2.53607808 | 3.56095653 | 1.54553351 |
| H | 2.63310896 | 5.14591705 | 0.81054171 |
| C | 4.09464531 | 3.74736291 | 0.03257957 |
| C | 5.13182448 | 4.40293650 | 0.97702070 |
| H | 4.99571104 | 4.09787861 | 2.01863478 |
| H | 5.03727248 | 5.49289755 | 0.94102458 |
| H | 6.15108037 | 4.13966749 | 0.67752694 |
| C | 4.26934607 | 4.37073595 | -1.36475420 |
| H | 5.28717136 | 4.22331105 | -1.74041347 |
| H | 4.09014433 | 5.44895516 | -1.30978297 |
| H | 3.57153984 | 3.96280083 | -2.10189223 |
| N | 1.21856940 | -0.00500573 | -1.13264926 |
| H | 0.46142964 | 0.40980370 | -1.70064146 |
| C | 0.81310778 | 0.11767604 | 0.30293445 |
| C | -0.68912263 | 0.32715694 | 0.30734744 |
| H | 1.08879009 | -0.78458603 | 0.84536183 |
| H | 1.32828506 | 0.96765353 | 0.75242218 |
| O | -1.30308423 | 0.51247081 | -0.72522055 |
| O | -1.18859961 | 0.28707617 | 1.52927907 |
| H | -2.16806208 | 0.35530766 | 1.49092151 |
| H | 1.31892081 | -0.99342009 | -1.40354887 |
| H | 2.12221780 | 0.45235503 | -1.31812531 |

endo-(TM8TPH⁺)(Gly)

| | | | |
|---|-------------|-------------|-------------|
| C | -4.67689400 | 1.64347600 | 0.14398000 |
| C | -4.79334000 | 0.84771100 | -1.12835300 |
| H | -4.30544800 | 1.37094300 | -1.95739400 |
| C | -4.25150500 | -0.54949300 | -1.09264300 |
| C | -3.82881600 | -1.11410300 | 0.12930000 |
| C | -4.08628500 | -0.41155400 | 1.34791300 |
| C | -4.49525700 | 0.97085400 | 1.31202600 |
| H | -4.50523700 | 1.49645200 | 2.26017000 |
| C | -4.05200000 | -1.26799600 | -2.27620700 |
| H | -4.44360600 | -0.88397700 | -3.21340300 |
| C | -3.20484500 | -2.36575600 | -2.28860500 |
| H | -2.95689800 | -2.81268700 | -3.24442400 |
| C | -2.55092200 | -2.80099200 | -1.11352800 |
| C | -2.99016700 | -2.26623200 | 0.13216600 |
| C | -2.42890900 | -2.72277000 | 1.36328800 |
| C | -2.93612600 | -2.16819600 | 2.56596900 |
| H | -2.60178300 | -2.55656300 | 3.52165000 |
| C | -3.74093800 | -1.04050700 | 2.56180300 |
| H | -4.01538600 | -0.57242300 | 3.50234700 |
| C | -1.27080500 | -3.46320400 | -1.15211300 |
| C | -0.52113000 | -3.56017000 | 0.05846000 |
| C | -1.17189000 | -3.42056800 | 1.32303700 |
| C | -0.58776300 | -3.75177000 | -2.36877400 |
| H | -1.14279500 | -3.88994900 | -3.28901300 |
| C | 0.78157400 | -3.67840400 | -2.42185300 |
| H | 1.27175900 | -3.76679900 | -3.38490100 |
| C | 1.54490300 | -3.35084600 | -1.26079700 |
| C | 0.91056000 | -3.52538400 | 0.00278300 |
| C | 1.64878000 | -3.36156700 | 1.21094500 |
| C | 0.97189900 | -3.66863200 | 2.43336500 |
| H | 1.53567600 | -3.77375800 | 3.35384900 |
| C | -0.39839000 | -3.70390700 | 2.49013900 |
| H | -0.88537400 | -3.83091200 | 3.45030300 |
| C | 2.74062500 | -2.57066500 | -1.31362700 |
| C | 3.26895900 | -2.06329700 | -0.08681800 |
| C | 2.86273700 | -2.61287700 | 1.16823900 |
| C | 3.22902100 | -2.00834300 | -2.54142800 |
| H | 2.95760700 | -2.46195000 | -3.48730700 |
| C | 3.89968200 | -0.81788400 | -2.54435600 |
| H | 4.16139300 | -0.34356300 | -3.48588700 |
| C | 4.16415700 | -0.12067900 | -1.31775200 |
| C | 3.99114200 | -0.83119400 | -0.09946200 |
| C | 4.31319300 | -0.17850500 | 1.12301100 |
| C | 4.19034500 | -0.93550500 | 2.33833500 |
| H | 4.58713700 | -0.51995100 | 3.26075100 |
| C | 3.49966700 | -2.11476000 | 2.35867200 |
| H | 3.34924000 | -2.62476000 | 3.30362700 |
| C | 4.41614500 | 1.26379000 | -1.27594400 |
| H | 4.45052000 | 1.79654200 | -2.21924800 |

| | | | |
|---|-------------|-------------|-------------|
| C | 4.51085200 | 1.96289500 | -0.06526100 |
| C | 4.56669900 | 1.20060500 | 1.11554400 |
| H | 4.72143800 | 1.69206500 | 2.07101600 |
| C | 4.42920600 | 3.49800400 | 0.01545700 |
| C | 5.52119300 | 4.04614400 | 0.96449900 |
| H | 5.38196300 | 3.71465900 | 1.99780500 |
| H | 5.49763000 | 5.14050900 | 0.97087200 |
| H | 6.51668300 | 3.72951000 | 0.63735200 |
| C | 4.62135600 | 4.16997300 | -1.35760500 |
| H | 5.61132900 | 3.94765600 | -1.76963000 |
| H | 4.54201200 | 5.25610900 | -1.24794500 |
| H | 3.87058300 | 3.86284500 | -2.09027800 |
| C | 3.02806900 | 3.88572400 | 0.60711500 |
| H | 2.91336400 | 3.36996800 | 1.57138100 |
| H | 3.05607600 | 4.95760000 | 0.84437600 |
| C | 1.78866600 | 3.61158300 | -0.26603400 |
| H | 1.82995300 | 2.59444700 | -0.67817900 |
| H | 1.79388400 | 4.28514000 | -1.13144500 |
| C | 0.45969100 | 3.79889900 | 0.49481100 |
| H | 0.37663300 | 3.02778700 | 1.27603600 |
| H | 0.47875400 | 4.75386700 | 1.03723200 |
| C | -0.78888300 | 3.75402200 | -0.40971100 |
| H | -0.69000500 | 2.94404800 | -1.14148600 |
| H | -0.83234000 | 4.68365500 | -0.99330500 |
| C | -2.11309500 | 3.56605600 | 0.35634800 |
| H | -2.10423900 | 2.58675900 | 0.84994500 |
| H | -2.18081600 | 4.31699000 | 1.15358500 |
| C | -3.34785400 | 3.65822000 | -0.55742600 |
| H | -3.14289800 | 3.10332700 | -1.48046200 |
| H | -3.49173200 | 4.70432300 | -0.85684900 |
| C | -4.72222900 | 3.16584600 | 0.03641800 |
| C | -5.84562300 | 3.59651300 | -0.93947000 |
| H | -5.66172100 | 3.25944500 | -1.96369100 |
| H | -5.91316400 | 4.68803800 | -0.96535900 |
| H | -6.81783800 | 3.20821100 | -0.61705000 |
| C | -4.98218000 | 3.84561300 | 1.39362300 |
| H | -5.95263800 | 3.54715500 | 1.80352300 |
| H | -4.99269600 | 4.93178700 | 1.26136300 |
| H | -4.21278900 | 3.61863600 | 2.13571500 |
| H | -5.86171200 | 0.81899100 | -1.40147100 |
| N | 1.13932100 | 0.23226000 | 1.15243400 |
| H | 1.34170100 | -0.01698400 | -0.71946200 |
| C | -0.28509000 | 0.19768600 | 0.83592000 |
| C | -0.49118100 | 0.29216900 | -0.68068200 |
| H | -0.71058800 | -0.75870300 | 1.14857000 |
| H | -0.88400900 | 0.98151800 | 1.30745700 |
| O | 0.62202900 | 0.09165500 | -1.39218000 |
| O | -1.56916400 | 0.51594500 | -1.19220100 |
| H | 1.40732800 | -0.40440700 | 1.89319300 |
| H | 1.47286800 | 1.16164000 | 1.38575600 |

exo-(TM8TPH⁺)(Gly)

| | | | |
|---|-------------|-------------|-------------|
| C | -4.85893518 | 1.70167294 | 0.60803993 |
| C | -5.09867674 | 0.91970059 | -0.65526096 |
| H | -4.78102784 | 1.47270578 | -1.54399188 |
| C | -4.48570841 | -0.44815172 | -0.69903878 |
| C | -3.98103879 | -1.03412679 | 0.48218491 |
| C | -4.18403286 | -0.36729014 | 1.73521178 |
| C | -4.59502514 | 1.01428508 | 1.75237215 |
| H | -4.51654513 | 1.52910995 | 2.70332567 |
| C | -4.32645343 | -1.12228018 | -1.91609208 |
| H | -4.77033325 | -0.70942823 | -2.81648591 |
| C | -3.48096839 | -2.22180364 | -1.99598537 |
| H | -3.27941863 | -2.64262083 | -2.97467684 |
| C | -2.77830116 | -2.69839390 | -0.86660049 |
| C | -3.13484498 | -2.17880681 | 0.41180576 |
| C | -2.50561025 | -2.65946039 | 1.60087037 |
| C | -2.94793975 | -2.13734950 | 2.84094851 |
| H | -2.55426120 | -2.54212649 | 3.76665985 |
| C | -3.76770424 | -1.02182344 | 2.91028873 |
| H | -3.99172913 | -0.57859709 | 3.87583474 |
| C | -1.51791880 | -3.39373543 | -0.98835293 |
| C | -0.69494372 | -3.50638043 | 0.17001550 |
| C | -1.26012073 | -3.36427651 | 1.47551556 |
| C | -0.92101178 | -3.69979428 | -2.24497224 |
| H | -1.53783033 | -3.83623714 | -3.12562788 |
| C | 0.44471117 | -3.65123184 | -2.38667886 |
| H | 0.87085257 | -3.75460748 | -3.37857654 |
| C | 1.28448646 | -3.32712118 | -1.27954116 |
| C | 0.72944931 | -3.48863118 | 0.02241841 |
| C | 1.54069475 | -3.31990454 | 1.18184427 |
| C | 0.94513629 | -3.63350857 | 2.44299492 |
| H | 1.56720880 | -3.74011059 | 3.32486888 |
| C | -0.41866610 | -3.66830217 | 2.58723204 |
| H | -0.84304423 | -3.79641383 | 3.57639761 |
| C | 2.48310074 | -2.55866418 | -1.41234274 |
| C | 3.07512528 | -2.02946662 | -0.22494332 |
| C | 2.73989465 | -2.55701542 | 1.06154698 |
| C | 2.92256814 | -2.03538964 | -2.67460590 |
| H | 2.60283591 | -2.51049727 | -3.59500301 |
| C | 3.62494652 | -0.86346281 | -2.73941552 |
| H | 3.86308313 | -0.42488794 | -3.70463106 |
| C | 3.96327569 | -0.14234812 | -1.54661481 |
| C | 3.81701712 | -0.81326904 | -0.30265276 |
| C | 4.21325651 | -0.14225819 | 0.88790483 |
| C | 4.13436226 | -0.86644636 | 2.12562285 |
| H | 4.57192038 | -0.42977918 | 3.01918353 |
| C | 3.43621748 | -2.03774572 | 2.20648721 |
| H | 3.31910976 | -2.51817560 | 3.17109162 |
| C | 4.26268827 | 1.23338389 | -1.55354728 |
| H | 4.27511719 | 1.74183116 | -2.51100117 |

| | | | |
|---|-------------|------------|-------------|
| C | 4.41690166 | 1.95943098 | -0.36577231 |
| C | 4.50420116 | 1.22761582 | 0.83165447 |
| H | 4.70428051 | 1.74119627 | 1.76662312 |
| C | 4.32527470 | 3.49355080 | -0.31203933 |
| C | 5.46951342 | 4.07948018 | 0.54716078 |
| H | 5.42256690 | 3.74639457 | 1.58811609 |
| H | 5.41174845 | 5.17279314 | 0.55448366 |
| H | 6.44594762 | 3.79313281 | 0.14300692 |
| C | 4.40580055 | 4.13967877 | -1.70793839 |
| H | 5.36381431 | 3.92014135 | -2.19152942 |
| H | 4.32213471 | 5.22694298 | -1.61267667 |
| H | 3.60356665 | 3.80973735 | -2.37349716 |
| C | 2.95784136 | 3.85909991 | 0.36605552 |
| H | 2.93691280 | 3.39328708 | 1.36006613 |
| H | 2.95342226 | 4.94376751 | 0.53984733 |
| C | 1.67135201 | 3.47496021 | -0.39191241 |
| H | 1.75835377 | 2.45512573 | -0.78996104 |
| H | 1.54820740 | 4.13423466 | -1.26081519 |
| C | 0.40787377 | 3.56048319 | 0.48838338 |
| H | 0.43926125 | 2.75283637 | 1.23418329 |
| H | 0.42226706 | 4.50001863 | 1.05913123 |
| C | -0.91162003 | 3.48524157 | -0.30252781 |
| H | -0.88124543 | 2.63181411 | -0.99511662 |
| H | -0.99535183 | 4.38176433 | -0.93297998 |
| C | -2.16774793 | 3.36425545 | 0.58517264 |
| H | -2.18151148 | 2.36779108 | 1.04688222 |
| H | -2.09308137 | 4.08328911 | 1.41097106 |
| C | -3.47211111 | 3.60935075 | -0.19817823 |
| H | -3.42038550 | 3.09751182 | -1.16546641 |
| H | -3.54235342 | 4.67898938 | -0.43613883 |
| C | -4.82845384 | 3.22071224 | 0.50708728 |
| C | -5.99126176 | 3.72816204 | -0.38111027 |
| H | -5.90570789 | 3.37562570 | -1.41200086 |
| H | -5.98120903 | 4.82220322 | -0.40813704 |
| H | -6.95923170 | 3.41124655 | 0.02283781 |
| C | -4.92808882 | 3.91095081 | 1.87936083 |
| H | -5.87461193 | 3.66889757 | 2.37433087 |
| H | -4.88695252 | 4.99630157 | 1.74535801 |
| H | -4.11082447 | 3.63765919 | 2.55147605 |
| H | -6.19276997 | 0.82872121 | -0.77519811 |
| N | -6.43826333 | 2.13578455 | -6.52748188 |
| H | -6.33191572 | 0.84414621 | -5.17863631 |
| C | -5.52996311 | 2.89697084 | -5.65988558 |
| C | -5.22895352 | 2.10813593 | -4.37881805 |
| H | -4.57043503 | 3.10480939 | -6.14352423 |
| H | -5.94368496 | 3.86379710 | -5.35641525 |
| O | -5.82106443 | 0.90789077 | -4.32769340 |
| O | -4.52035099 | 2.53017784 | -3.48769656 |
| H | -6.04373773 | 1.94110064 | -7.44101905 |
| H | -7.33398898 | 2.59274616 | -6.65985127 |

exo-(TM8TP)(GlyH⁺)

| | | | |
|---|-------------|-------------|-------------|
| C | 1.37468505 | 5.08236271 | 0.00475711 |
| C | 0.64796889 | 4.82200899 | -1.17000706 |
| H | 1.07117652 | 5.07759111 | -2.13613765 |
| C | -0.56374995 | 4.11961744 | -1.15340490 |
| C | -1.07719008 | 3.65641886 | 0.09134463 |
| C | -0.47430260 | 4.11672081 | 1.29418771 |
| C | 0.74024701 | 4.82298761 | 1.22668661 |
| H | 1.22631507 | 5.08098739 | 2.16074954 |
| C | -1.23227470 | 3.70347517 | -2.35628223 |
| H | -0.94624972 | 4.15964869 | -3.30000725 |
| C | -2.13799401 | 2.68382316 | -2.33423487 |
| H | -2.55961297 | 2.33044737 | -3.26826177 |
| C | -2.42696009 | 1.98256087 | -1.11000422 |
| C | -2.01530844 | 2.58082400 | 0.12236749 |
| C | -2.33725582 | 1.97727672 | 1.37804085 |
| C | -1.95474755 | 2.66993003 | 2.58033807 |
| H | -2.30079158 | 2.31047989 | 3.54302110 |
| C | -1.04917795 | 3.69103277 | 2.54001571 |
| H | -0.69202611 | 4.13930426 | 3.46309659 |
| C | -2.80894396 | 0.61300796 | -1.09850822 |
| C | -2.72687690 | -0.09721751 | 0.13711154 |
| C | -2.72173199 | 0.60769542 | 1.37994707 |
| C | -2.97183139 | -0.17251955 | -2.29659476 |
| H | -3.27628524 | 0.30708221 | -3.22033336 |
| C | -2.61580911 | -1.48999779 | -2.31375313 |
| H | -2.64375108 | -2.03660049 | -3.24983323 |
| C | -2.06805243 | -2.11307560 | -1.13410787 |
| C | -2.35206553 | -1.49081670 | 0.11856103 |
| C | -1.97088636 | -2.12205867 | 1.34587061 |
| C | -2.43222413 | -1.50791067 | 2.56568833 |
| H | -2.37634956 | -2.05142571 | 3.50287554 |
| C | -2.80138208 | -0.18648692 | 2.58157675 |
| H | -3.02526199 | 0.28685382 | 3.53177491 |
| C | -1.02843901 | -3.08398809 | -1.17783888 |
| C | -0.35865446 | -3.41329982 | 0.04203575 |
| C | -0.93918667 | -3.09793326 | 1.31067943 |
| C | -0.42054613 | -3.49586078 | -2.41537299 |
| H | -0.96629006 | -3.38445889 | -3.34528203 |
| C | 0.88406706 | -3.89704661 | -2.45331360 |
| H | 1.36132885 | -4.10879838 | -3.40618101 |
| C | 1.67546618 | -3.94440919 | -1.25552274 |
| C | 1.00053935 | -3.84611898 | -0.00781863 |
| C | 1.75842636 | -3.95939759 | 1.19236481 |
| C | 1.04983906 | -3.93506612 | 2.44323597 |
| H | 1.59006557 | -4.16683694 | 3.35697442 |
| C | -0.25202867 | -3.53226162 | 2.49950480 |
| H | -0.73487059 | -3.43864024 | 3.46583134 |
| C | 3.08167118 | -3.91936854 | -1.27883515 |
| H | 3.56976371 | -3.90226106 | -2.24667554 |

| | | | |
|---|-------------|-------------|-------------|
| C | 3.83603311 | -3.79630740 | -0.10472268 |
| C | 3.15680498 | -3.93276788 | 1.11855738 |
| H | 3.71251553 | -3.91965572 | 2.05068169 |
| C | 5.31183905 | -3.36401090 | -0.10746790 |
| C | 6.14626489 | -4.26759860 | 0.82978918 |
| H | 5.82349550 | -4.19800368 | 1.87275923 |
| H | 7.19979599 | -3.97140171 | 0.79658794 |
| H | 6.07789890 | -5.31636119 | 0.52262753 |
| C | 5.94444431 | -3.42798387 | -1.51033282 |
| H | 5.93846635 | -4.45103537 | -1.90181725 |
| H | 6.98664805 | -3.09765558 | -1.45648917 |
| H | 5.43676071 | -2.78266808 | -2.23220273 |
| C | 5.37190347 | -1.89351227 | 0.43650727 |
| H | 4.91638748 | -1.88224455 | 1.43535161 |
| H | 6.42975880 | -1.63648924 | 0.58334815 |
| C | 4.71216359 | -0.79877806 | -0.42553817 |
| H | 3.74476477 | -1.15102981 | -0.80773170 |
| H | 5.33652258 | -0.60143463 | -1.30645886 |
| C | 4.49242707 | 0.51962442 | 0.34327533 |
| H | 3.69911691 | 0.36676811 | 1.08946039 |
| H | 5.39954542 | 0.76818853 | 0.91255976 |
| C | 4.13256739 | 1.71575002 | -0.55743310 |
| H | 3.33221134 | 1.42642418 | -1.25395381 |
| H | 5.00357879 | 1.96033000 | -1.18209238 |
| C | 3.68633211 | 2.97152776 | 0.21801617 |
| H | 2.70049590 | 2.78092557 | 0.66280686 |
| H | 4.37410430 | 3.13963356 | 1.05679946 |
| C | 3.63420373 | 4.23453723 | -0.66453472 |
| H | 3.18971963 | 3.97273029 | -1.63363789 |
| H | 4.66207575 | 4.55652128 | -0.88009287 |
| C | 2.85865549 | 5.47349302 | -0.09397050 |
| C | 3.04605507 | 6.65989513 | -1.06785260 |
| H | 2.73829456 | 6.41452034 | -2.08856198 |
| H | 4.10128569 | 6.94903980 | -1.10852039 |
| H | 2.46753262 | 7.52935679 | -0.73874419 |
| C | 3.45469735 | 5.88147333 | 1.26638436 |
| H | 2.94639230 | 6.76199194 | 1.67417160 |
| H | 4.51200292 | 6.13545105 | 1.14064679 |
| H | 3.39977708 | 5.08054691 | 2.00852443 |
| N | -5.26388301 | -1.64649383 | 0.99558583 |
| H | -5.88557419 | -2.40867897 | 1.29083973 |
| C | -6.05555370 | -0.53255379 | 0.39020604 |
| C | -7.14936022 | -1.14723902 | -0.46847528 |
| H | -6.49576779 | 0.06985129 | 1.18892518 |
| H | -5.38156202 | 0.09817373 | -0.19266898 |
| O | -7.38935215 | -2.33557386 | -0.46549298 |
| O | -7.78318057 | -0.21511219 | -1.17640672 |
| H | -8.49615314 | -0.62848960 | -1.69675632 |
| H | -4.67334835 | -1.32461598 | 1.78657446 |
| H | -4.59506676 | -2.03586276 | 0.31481105 |

endo-(TM9TP)(GlyH⁺)

| | | | |
|---|-------------|-------------|-------------|
| C | -5.07351229 | 1.46286931 | 0.02465855 |
| C | -4.87612216 | 0.79146364 | -1.19410703 |
| H | -5.02071091 | 1.31921362 | -2.13152247 |
| C | -4.39328931 | -0.52423021 | -1.25521856 |
| C | -4.08891198 | -1.21022094 | -0.04268028 |
| C | -4.47767252 | -0.61543977 | 1.19426421 |
| C | -4.95637875 | 0.71082397 | 1.20273466 |
| H | -5.17642459 | 1.16049647 | 2.16446174 |
| C | -4.04993825 | -1.16711554 | -2.49645446 |
| H | -4.40722253 | -0.73579290 | -3.42715987 |
| C | -3.21675398 | -2.24627136 | -2.51351561 |
| H | -2.91286091 | -2.66171648 | -3.46712097 |
| C | -2.63513530 | -2.75909093 | -1.29741257 |
| C | -3.20321590 | -2.33739449 | -0.05628657 |
| C | -2.69406420 | -2.83218902 | 1.18584897 |
| C | -3.36010512 | -2.41828508 | 2.39781421 |
| H | -3.11939607 | -2.90862123 | 3.33420090 |
| C | -4.21112081 | -1.35044675 | 2.40576203 |
| H | -4.64429976 | -1.00097516 | 3.33878720 |
| C | -1.35875036 | -3.38970683 | -1.28243111 |
| C | -0.67154556 | -3.50780067 | -0.03509546 |
| C | -1.39273321 | -3.41740610 | 1.19643615 |
| C | -0.60239869 | -3.64255762 | -2.47968416 |
| H | -1.11610850 | -3.79350242 | -3.42202800 |
| C | 0.75975696 | -3.58836013 | -2.46096439 |
| H | 1.30447563 | -3.69878265 | -3.39158448 |
| C | 1.46893151 | -3.27993369 | -1.24864284 |
| C | 0.76606740 | -3.44568852 | -0.01722468 |
| C | 1.44111489 | -3.27878302 | 1.22884161 |
| C | 0.70423128 | -3.58678878 | 2.42401040 |
| H | 1.22746494 | -3.68943464 | 3.36781354 |
| C | -0.65876650 | -3.66100084 | 2.41152299 |
| H | -1.19024168 | -3.82080441 | 3.34265868 |
| C | 2.70923072 | -2.58681224 | -1.23790388 |
| C | 3.20646805 | -2.09985044 | 0.00985539 |
| C | 2.68142336 | -2.58126572 | 1.24755169 |
| C | 3.33514662 | -2.11218036 | -2.44702015 |
| H | 3.09668532 | -2.58106157 | -3.39451547 |
| C | 4.13597834 | -1.00925662 | -2.43637350 |
| H | 4.53017063 | -0.60735858 | -3.36556709 |
| C | 4.39287385 | -0.30209037 | -1.20631474 |
| C | 4.06109277 | -0.95392833 | 0.01860234 |
| C | 4.39123141 | -0.31345695 | 1.24268940 |
| C | 4.09329462 | -1.00631067 | 2.46499273 |
| H | 4.46506214 | -0.60127909 | 3.40202985 |
| C | 3.27749477 | -2.09960472 | 2.46551403 |
| H | 3.00616748 | -2.55321196 | 3.41182199 |
| C | 4.81806897 | 1.03657816 | -1.17305494 |
| H | 4.98136811 | 1.54012413 | -2.12098083 |
| C | 4.95214967 | 1.74722551 | 0.03433018 |
| C | 4.83772225 | 1.02025485 | 1.22533081 |

| | | | |
|---|-------------|-------------|-------------|
| H | 5.00068058 | 1.50696022 | 2.17997571 |
| C | 5.07708048 | 3.28093482 | 0.00535470 |
| C | 5.36707162 | 3.87512906 | 1.39679623 |
| H | 4.58453170 | 3.64666036 | 2.12554164 |
| H | 5.43509811 | 4.96500679 | 1.32176405 |
| H | 6.31993527 | 3.50920182 | 1.79346771 |
| C | 6.22107031 | 3.71284108 | -0.94138695 |
| H | 7.17468597 | 3.28208394 | -0.61986763 |
| H | 6.32187915 | 4.80305468 | -0.93743911 |
| H | 6.04381022 | 3.40692136 | -1.97667284 |
| C | 1.16613558 | 3.90496434 | -0.47202065 |
| H | 1.12505205 | 3.25864769 | -1.36070654 |
| H | 1.18630140 | 4.93589370 | -0.85042472 |
| C | -0.11693533 | 3.70094178 | 0.35539398 |
| H | -0.08604160 | 2.70209192 | 0.81748436 |
| H | -0.12879074 | 4.40566255 | 1.19732668 |
| C | -1.41426008 | 3.85547817 | -0.45914960 |
| H | -1.34426252 | 3.25105994 | -1.37712460 |
| H | -1.50094193 | 4.89411278 | -0.80380221 |
| C | -2.69289778 | 3.46432702 | 0.30387094 |
| H | -2.62197144 | 2.40963715 | 0.61189424 |
| H | -2.74878321 | 4.03980951 | 1.23572035 |
| C | -3.97920448 | 3.66203464 | -0.51982822 |
| H | -3.80591850 | 3.29402214 | -1.53922800 |
| H | -4.17349166 | 4.73796743 | -0.61598178 |
| C | -5.28271264 | 2.98791507 | 0.02981099 |
| C | -6.45786267 | 3.36866583 | -0.90105770 |
| H | -6.27301177 | 3.08654618 | -1.94158713 |
| H | -6.61972199 | 4.45119678 | -0.87985335 |
| H | -7.38246225 | 2.88028729 | -0.57764253 |
| C | -5.59628554 | 3.53606831 | 1.43493234 |
| H | -6.52757524 | 3.11464536 | 1.82733621 |
| H | -5.72053197 | 4.62215674 | 1.38423592 |
| H | -4.80006018 | 3.33334741 | 2.15717465 |
| C | 2.46699606 | 3.60863625 | 0.29800791 |
| H | 2.49603167 | 4.22510586 | 1.20514946 |
| H | 2.45170590 | 2.56647455 | 0.63981022 |
| C | 3.73068456 | 3.86344707 | -0.54681396 |
| H | 3.86272745 | 4.94562974 | -0.67801174 |
| H | 3.57250406 | 3.45519985 | -1.55412571 |
| N | -1.32127328 | -0.05943237 | 1.04452056 |
| H | -1.21490764 | -1.04590673 | 1.32414252 |
| C | -0.77864502 | 0.15812154 | -0.33264483 |
| C | 0.72615165 | 0.32292387 | -0.19684283 |
| H | -1.03804022 | -0.69539090 | -0.95936319 |
| H | -1.22654140 | 1.05897195 | -0.75430721 |
| O | 1.26711597 | 0.34582001 | 0.88992362 |
| O | 1.30890445 | 0.45778277 | -1.37680880 |
| H | 2.28235850 | 0.53156915 | -1.26792338 |
| H | -2.32628996 | 0.15930118 | 1.10483408 |
| H | -0.78436950 | 0.50702352 | 1.71296699 |

endo-(TM9TPH⁺)(Gly)

| | | | |
|---|-------------|-------------|-------------|
| C | -5.17921975 | 1.49226431 | 0.03391619 |
| C | -5.19247204 | 0.76273612 | -1.28265454 |
| H | -4.75107360 | 1.37529435 | -2.07549808 |
| C | -4.52502618 | -0.58000419 | -1.30499015 |
| C | -4.11514799 | -1.18471712 | -0.10018117 |
| C | -4.47684948 | -0.57792138 | 1.14337089 |
| C | -4.98976923 | 0.76729806 | 1.16867203 |
| H | -5.06559356 | 1.23583603 | 2.14304773 |
| C | -4.22438335 | -1.20864020 | -2.51962865 |
| H | -4.60033152 | -0.79307879 | -3.44985675 |
| C | -3.32423801 | -2.26065804 | -2.55463373 |
| H | -3.01817479 | -2.64284240 | -3.52142130 |
| C | -2.70091173 | -2.73350408 | -1.37583323 |
| C | -3.20143605 | -2.27745887 | -0.12351009 |
| C | -2.65170240 | -2.75526339 | 1.10321789 |
| C | -3.24325115 | -2.30587175 | 2.31236432 |
| H | -2.91981637 | -2.72462505 | 3.25888039 |
| C | -4.13605332 | -1.25006075 | 2.33489304 |
| H | -4.48543690 | -0.86002095 | 3.28596450 |
| C | -1.41480463 | -3.37990586 | -1.40309128 |
| C | -0.69241389 | -3.51162066 | -0.18057942 |
| C | -1.36984402 | -3.39863282 | 1.07355291 |
| C | -0.71209391 | -3.65245602 | -2.61439228 |
| H | -1.25372626 | -3.76750124 | -3.54569550 |
| C | 0.65765155 | -3.62199987 | -2.64061081 |
| H | 1.16498665 | -3.71655245 | -3.59407909 |
| C | 1.40951941 | -3.34620406 | -1.45666095 |
| C | 0.74183127 | -3.51301444 | -0.20750306 |
| C | 1.46351233 | -3.40232460 | 1.01671803 |
| C | 0.75109499 | -3.69609061 | 2.22264622 |
| H | 1.29254348 | -3.82304659 | 3.15344390 |
| C | -0.61904352 | -3.70032003 | 2.25128680 |
| H | -1.12429669 | -3.82768034 | 3.20156460 |
| C | 2.64835612 | -2.63776474 | -1.47469109 |
| C | 3.19432502 | -2.19438468 | -0.23016321 |
| C | 2.72752287 | -2.73664156 | 1.00811226 |
| C | 3.19742136 | -2.09164116 | -2.68585091 |
| H | 2.90399978 | -2.50518705 | -3.64351255 |
| C | 3.97757639 | -0.97136005 | -2.65781406 |
| H | 4.30314008 | -0.51111153 | -3.58651040 |
| C | 4.30076323 | -0.32942803 | -1.41438068 |
| C | 4.03108353 | -1.03661815 | -0.20887536 |
| C | 4.41906231 | -0.45126046 | 1.02701008 |
| C | 4.19694055 | -1.21203625 | 2.22480449 |
| H | 4.61862811 | -0.85560811 | 3.16066170 |
| C | 3.38988616 | -2.31663963 | 2.21497418 |
| H | 3.17460648 | -2.82155016 | 3.14973095 |
| C | 4.73187343 | 1.00281696 | -1.34190746 |
| H | 4.84401359 | 1.54925331 | -2.27309889 |
| C | 4.91430238 | 1.66480019 | -0.11535711 |
| C | 4.85385972 | 0.88788699 | 1.04966934 |

| | | | |
|---|-------------|-------------|-------------|
| H | 5.06798353 | 1.33212059 | 2.01532616 |
| C | 5.04764428 | 3.19832950 | -0.09274550 |
| C | 5.33840610 | 3.74234293 | 1.31865105 |
| H | 4.55647491 | 3.48650092 | 2.03945659 |
| H | 5.40368988 | 4.83423081 | 1.28292921 |
| H | 6.29285210 | 3.36602280 | 1.70183492 |
| C | 6.19967639 | 3.64768835 | -1.02190971 |
| H | 7.14918573 | 3.20332101 | -0.70662263 |
| H | 6.30643369 | 4.73684023 | -0.98949578 |
| H | 6.02543116 | 3.36814354 | -2.06511941 |
| C | 1.13530947 | 3.86648661 | -0.55451983 |
| H | 1.07519950 | 3.23112072 | -1.45039877 |
| H | 1.17640800 | 4.89961873 | -0.92519400 |
| C | -0.14352809 | 3.68084930 | 0.28493790 |
| H | -0.11787209 | 2.70135203 | 0.78103868 |
| H | -0.15574233 | 4.41976633 | 1.09791193 |
| C | -1.44350623 | 3.78860922 | -0.53417010 |
| H | -1.38402880 | 3.09897598 | -1.38663253 |
| H | -1.52042791 | 4.80066280 | -0.95565989 |
| C | -2.71797094 | 3.45989688 | 0.26811535 |
| H | -2.64664605 | 2.43204545 | 0.63846089 |
| H | -2.76849477 | 4.11016668 | 1.15086939 |
| C | -3.99727189 | 3.62262184 | -0.57369552 |
| H | -3.82050821 | 3.19500252 | -1.56848670 |
| H | -4.18975537 | 4.69064709 | -0.73893795 |
| C | -5.32596612 | 3.01060325 | 0.00811393 |
| C | -6.49274431 | 3.41545884 | -0.92694845 |
| H | -6.31528253 | 3.12464190 | -1.96656989 |
| H | -6.61887203 | 4.50212265 | -0.91151961 |
| H | -7.43467946 | 2.96323984 | -0.59809886 |
| C | -5.60088802 | 3.59972374 | 1.40391354 |
| H | -6.53874591 | 3.21517603 | 1.81831261 |
| H | -5.68917126 | 4.68778750 | 1.32869840 |
| H | -4.79825753 | 3.38789956 | 2.11476234 |
| C | 2.43928462 | 3.54056711 | 0.19850366 |
| H | 2.47069648 | 4.11203965 | 1.13449388 |
| H | 2.43000503 | 2.48080886 | 0.48721032 |
| C | 3.70913541 | 3.81411203 | -0.62947017 |
| H | 3.85226088 | 4.89911683 | -0.71581489 |
| H | 3.54841293 | 3.44846893 | -1.65182042 |
| H | -6.24927647 | 0.64400528 | -1.57761627 |
| N | 1.00002946 | 0.18062316 | 1.29656148 |
| H | 1.52968627 | 1.01259345 | 1.53327461 |
| C | 0.60039909 | 0.16134666 | -0.11580317 |
| C | -0.92191063 | 0.28610142 | -0.22619600 |
| H | 1.05262797 | 0.96313302 | -0.70473997 |
| H | 0.87973713 | -0.77753176 | -0.59730922 |
| O | -1.51964200 | 0.37771318 | -1.27840205 |
| O | -1.53815954 | 0.26668118 | 0.96206497 |
| H | -0.78903596 | 0.21145138 | 1.61780464 |
| H | 1.55902803 | -0.62396068 | 1.55293575 |

exo-(TM9TPH⁺)(Gly)

| | | | |
|---|-------------|-------------|-------------|
| C | -5.23228881 | 1.45753429 | 0.54313191 |
| C | -5.28455659 | 0.73403406 | -0.77218601 |
| H | -4.96288147 | 1.36366324 | -1.60572454 |
| C | -4.52781157 | -0.55905634 | -0.83337610 |
| C | -4.05121702 | -1.15622087 | 0.35486585 |
| C | -4.41142761 | -0.58382049 | 1.61872492 |
| C | -4.97989663 | 0.74018997 | 1.67023590 |
| H | -5.02362360 | 1.20738678 | 2.64759906 |
| C | -4.21541228 | -1.14433503 | -2.06579458 |
| H | -4.61665342 | -0.70877113 | -2.97523838 |
| C | -3.27998863 | -2.16901482 | -2.13237519 |
| H | -2.97602349 | -2.51949015 | -3.11208794 |
| C | -2.62591095 | -2.65173896 | -0.97730535 |
| C | -3.09724014 | -2.21405768 | 0.29439497 |
| C | -2.50315253 | -2.69280073 | 1.50221628 |
| C | -3.06663780 | -2.26990807 | 2.72951368 |
| H | -2.69489926 | -2.67841597 | 3.66250376 |
| C | -4.00084704 | -1.24732203 | 2.78984930 |
| H | -4.33179806 | -0.87815873 | 3.75583956 |
| C | -1.33289822 | -3.29163561 | -1.04583857 |
| C | -0.56914702 | -3.40812129 | 0.15283054 |
| C | -1.20730151 | -3.31259832 | 1.42870213 |
| C | -0.67146492 | -3.57011832 | -2.27446840 |
| H | -1.24232471 | -3.69200924 | -3.18745230 |
| C | 0.70006204 | -3.53386487 | -2.34536522 |
| H | 1.17370872 | -3.63134173 | -3.31581398 |
| C | 1.48773881 | -3.24361412 | -1.19337580 |
| C | 0.86071203 | -3.39088015 | 0.07822263 |
| C | 1.61714158 | -3.25546705 | 1.27807728 |
| C | 0.95371056 | -3.55985711 | 2.50395160 |
| H | 1.52735004 | -3.66667499 | 3.41784933 |
| C | -0.41665197 | -3.60255412 | 2.57786722 |
| H | -0.88618147 | -3.73746046 | 3.54521792 |
| C | 2.73554450 | -2.55038779 | -1.26193604 |
| C | 3.30735928 | -2.06788293 | -0.04481070 |
| C | 2.86579012 | -2.56286734 | 1.22181760 |
| C | 3.28069554 | -2.07236044 | -2.50092320 |
| H | 2.96592983 | -2.52042459 | -3.43621736 |
| C | 4.09319299 | -0.97371337 | -2.53138698 |
| H | 4.42034012 | -0.56447778 | -3.48326978 |
| C | 4.44446701 | -0.28574754 | -1.32240200 |
| C | 4.16848032 | -0.93139643 | -0.08464711 |
| C | 4.58058627 | -0.30239951 | 1.12084216 |
| C | 4.35783707 | -1.00190523 | 2.35263056 |
| H | 4.78549713 | -0.60305620 | 3.26841111 |
| C | 3.54089370 | -2.09767931 | 2.39936471 |
| H | 3.32496328 | -2.55237938 | 3.35919979 |
| C | 4.89033008 | 1.04415237 | -1.31249630 |
| H | 4.99045571 | 1.55267745 | -2.26626274 |
| C | 5.06816734 | 1.75796142 | -0.11576066 |
| C | 5.02616766 | 1.03129401 | 1.08108497 |

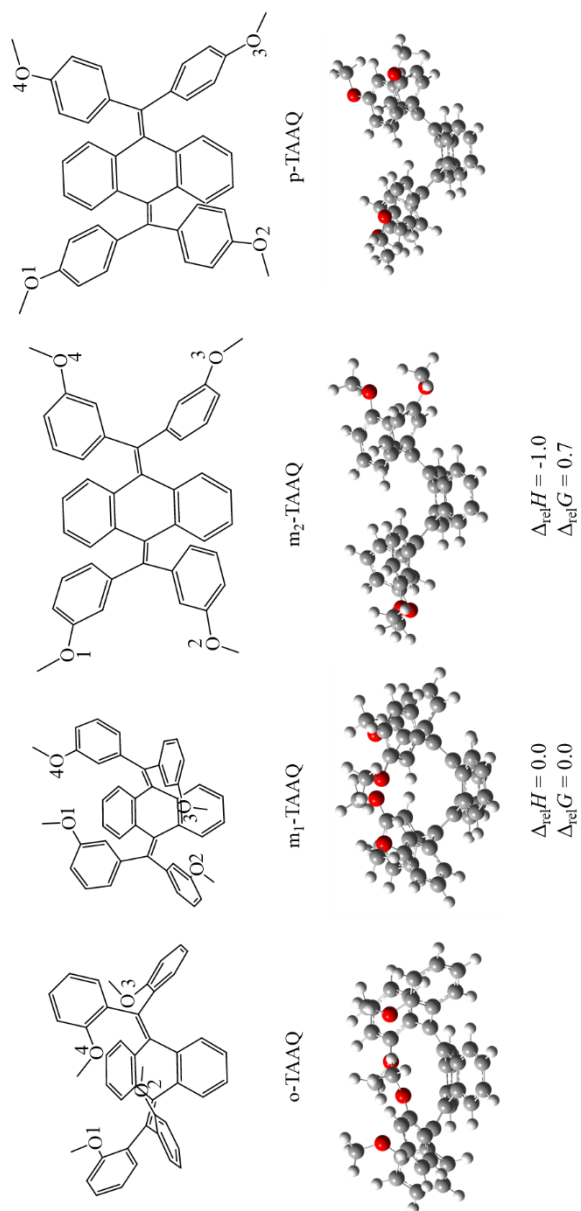
| | | | |
|---|-------------|------------|-------------|
| H | 5.23897234 | 1.51961840 | 2.02519488 |
| C | 5.09300985 | 3.29348312 | -0.14437262 |
| C | 5.39993297 | 3.90493116 | 1.23649563 |
| H | 4.64930407 | 3.64778921 | 1.98909808 |
| H | 5.41932476 | 4.99614712 | 1.15566809 |
| H | 6.37940456 | 3.58274521 | 1.60613283 |
| C | 6.15585598 | 3.81536856 | -1.13715997 |
| H | 7.15984107 | 3.50331877 | -0.83140522 |
| H | 6.13491856 | 4.90979500 | -1.16914331 |
| H | 5.98638260 | 3.45736435 | -2.15683934 |
| C | 1.11426035 | 3.73727578 | -0.42593610 |
| H | 1.06432057 | 3.52716853 | -1.50414695 |
| H | 1.07733601 | 4.83126100 | -0.32646347 |
| C | -0.11808623 | 3.12103383 | 0.26155056 |
| H | -0.08522989 | 2.02791340 | 0.14195547 |
| H | -0.06273922 | 3.31119711 | 1.34319652 |
| C | -1.46207826 | 3.64719810 | -0.27519218 |
| H | -1.50763681 | 3.48156362 | -1.36115658 |
| H | -1.50811524 | 4.73569218 | -0.13004467 |
| C | -2.68859511 | 2.99198811 | 0.38632653 |
| H | -2.63059186 | 1.90531644 | 0.23768467 |
| H | -2.63907406 | 3.15069422 | 1.47145160 |
| C | -4.02750088 | 3.51895178 | -0.16296427 |
| H | -4.07237964 | 3.30947191 | -1.23894389 |
| H | -4.05572805 | 4.61224367 | -0.06710203 |
| C | -5.34253489 | 2.97462360 | 0.51625337 |
| C | -6.55525341 | 3.42493054 | -0.33246674 |
| H | -6.52559132 | 3.02738857 | -1.34996938 |
| H | -6.57307449 | 4.51769141 | -0.39875572 |
| H | -7.49335556 | 3.09914325 | 0.12989137 |
| C | -5.48531860 | 3.58503146 | 1.92331203 |
| H | -6.37428859 | 3.20060427 | 2.43441723 |
| H | -5.59350270 | 4.67064911 | 1.84042713 |
| H | -4.61552511 | 3.39136309 | 2.55694165 |
| C | 2.45423624 | 3.21761967 | 0.12819416 |
| H | 2.52243003 | 3.47285686 | 1.19372970 |
| H | 2.45732770 | 2.12135457 | 0.07532081 |
| C | 3.67685999 | 3.76994749 | -0.62918445 |
| H | 3.66658166 | 4.86762738 | -0.58591265 |
| H | 3.57229789 | 3.50578178 | -1.68993030 |
| H | -6.34611501 | 0.54433503 | -1.00558167 |
| N | -8.68457385 | 2.19345293 | -5.33825293 |
| H | -8.39196710 | 1.59675987 | -3.58712651 |
| C | -7.22919765 | 2.04668478 | -5.46859545 |
| C | -6.62291744 | 1.53800061 | -4.15386711 |
| H | -6.94514409 | 1.33783277 | -6.25269759 |
| H | -6.73366026 | 2.99291070 | -5.70746106 |
| O | -7.52034972 | 1.34797141 | -3.17891110 |
| O | -5.43573641 | 1.32864125 | -4.00402037 |
| H | -9.20170978 | 1.58580019 | -5.96412078 |
| H | -9.00186674 | 3.14517491 | -5.48559759 |

exo-(TM9TP)(GlyH⁺)

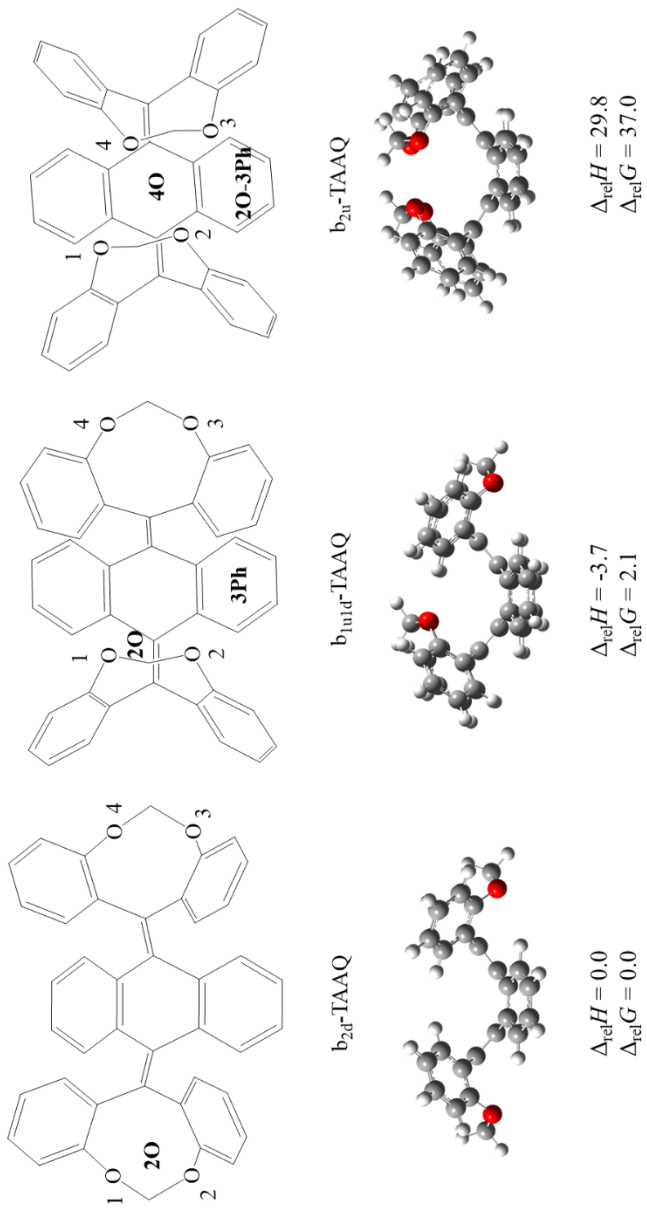
| | | | |
|---|-------------|-------------|-------------|
| C | 3.20890365 | -4.58038869 | 0.03211106 |
| C | 3.43049182 | -3.86410137 | -1.15632714 |
| H | 3.34396984 | -4.36595093 | -2.11487444 |
| C | 3.62690847 | -2.47686371 | -1.15923852 |
| C | 3.60668050 | -1.77233053 | 0.07840386 |
| C | 3.62067649 | -2.51718601 | 1.28958620 |
| C | 3.42504712 | -3.90866219 | 1.24184119 |
| H | 3.34138814 | -4.43812278 | 2.18397871 |
| C | 3.68929898 | -1.70840040 | -2.37199149 |
| H | 3.83991050 | -2.22776783 | -3.31437457 |
| C | 3.46850456 | -0.36224360 | -2.35913839 |
| H | 3.43798799 | 0.17564459 | -3.29960315 |
| C | 3.14193510 | 0.32144230 | -1.13513316 |
| C | 3.35834528 | -0.36684768 | 0.10001347 |
| C | 3.12406215 | 0.27841650 | 1.35428752 |
| C | 3.43680541 | -0.44481271 | 2.55764651 |
| H | 3.39055595 | 0.05835170 | 3.51689030 |
| C | 3.66618307 | -1.79048621 | 2.52706416 |
| H | 3.80766277 | -2.34043044 | 3.45338689 |
| C | 2.36649377 | 1.51351306 | -1.11936497 |
| C | 1.80462889 | 1.93976742 | 0.12269041 |
| C | 2.33939785 | 1.46597015 | 1.36059037 |
| C | 1.89331587 | 2.16512710 | -2.31316967 |
| H | 2.43311679 | 2.04145363 | -3.24533672 |
| C | 0.70683328 | 2.84000345 | -2.31577118 |
| H | 0.32730857 | 3.24010472 | -3.24915092 |
| C | -0.10116438 | 2.90933473 | -1.12523144 |
| C | 0.54957723 | 2.65048192 | 0.11966211 |
| C | -0.14464739 | 2.84899641 | 1.35590159 |
| C | 0.62655999 | 2.72835098 | 2.56477565 |
| H | 0.21138670 | 3.06486419 | 3.50859745 |
| C | 1.82947702 | 2.06657385 | 2.56650328 |
| H | 2.33088896 | 1.89315500 | 3.51255278 |
| C | -1.52301274 | 2.93719155 | -1.14940036 |
| C | -2.22910233 | 2.74807595 | 0.08002918 |
| C | -1.56677883 | 2.88570490 | 1.33989326 |
| C | -2.26784354 | 2.85764201 | -2.37840099 |
| H | -1.79080170 | 3.12523080 | -3.31405417 |
| C | -3.52546916 | 2.32920342 | -2.40216563 |
| H | -4.03977982 | 2.18700726 | -3.34861402 |
| C | -4.15159432 | 1.86258529 | -1.19600248 |
| C | -3.55216952 | 2.21398647 | 0.04717569 |
| C | -4.20006016 | 1.82737983 | 1.25246900 |
| C | -3.61696660 | 2.24698177 | 2.49569438 |
| H | -4.16576590 | 2.07394104 | 3.41731541 |
| C | -2.35432343 | 2.76460489 | 2.53725810 |
| H | -1.91015920 | 2.99033263 | 3.50017020 |
| C | -5.22426521 | 0.96097899 | -1.20392228 |
| H | -5.59745469 | 0.62528973 | -2.16629250 |
| C | -5.72391414 | 0.39079418 | -0.02097623 |
| C | -5.27699606 | 0.92578557 | 1.19391187 |

| | | | |
|---|-------------|-------------|-------------|
| H | -5.68968706 | 0.57235847 | 2.13184281 |
| C | -6.56309760 | -0.89371426 | -0.09406926 |
| C | -7.11944143 | -1.31562802 | 1.27969325 |
| H | -6.33170501 | -1.52958192 | 2.00728734 |
| H | -7.71481563 | -2.22705263 | 1.16736461 |
| H | -7.77232519 | -0.54261865 | 1.69941330 |
| C | -7.76181758 | -0.72011703 | -1.05385909 |
| H | -8.43394481 | 0.06777195 | -0.69817312 |
| H | -8.33276131 | -1.65264047 | -1.11415230 |
| H | -7.44917395 | -0.46451179 | -2.07046954 |
| C | -3.42654928 | -3.34616798 | -0.58258927 |
| H | -3.25019048 | -3.06805742 | -1.63186237 |
| H | -3.97410825 | -4.29887411 | -0.60759007 |
| C | -2.07027225 | -3.55551438 | 0.11500191 |
| H | -1.53523384 | -2.59493360 | 0.15211661 |
| H | -2.24181898 | -3.84924410 | 1.16065589 |
| C | -1.17100714 | -4.60320938 | -0.56579884 |
| H | -1.01601942 | -4.31402647 | -1.61545499 |
| H | -1.69262781 | -5.57038405 | -0.58988737 |
| C | 0.19966700 | -4.77428216 | 0.11503135 |
| H | 0.69604457 | -3.79623915 | 0.15678859 |
| H | 0.04501872 | -5.08439049 | 1.15668795 |
| C | 1.11264138 | -5.78265530 | -0.60736909 |
| H | 1.20051089 | -5.47717593 | -1.65843412 |
| H | 0.62957896 | -6.76927919 | -0.61628572 |
| C | 2.56135184 | -5.97192713 | -0.03196902 |
| C | 3.34927725 | -6.90749409 | -0.97650614 |
| H | 3.40989753 | -6.51628494 | -1.99626130 |
| H | 2.85903214 | -7.88515996 | -1.03179057 |
| H | 4.37024297 | -7.05916899 | -0.61087747 |
| C | 2.48590117 | -6.65296269 | 1.34827879 |
| H | 3.48371454 | -6.79639746 | 1.77697531 |
| H | 2.02576050 | -7.64034203 | 1.24279604 |
| H | 1.88363622 | -6.08842418 | 2.06546527 |
| C | -4.30099324 | -2.26707443 | 0.08251593 |
| H | -4.49526801 | -2.55642240 | 1.12352807 |
| H | -3.73094869 | -1.33015806 | 0.12600091 |
| C | -5.63047048 | -2.02493783 | -0.65647622 |
| H | -6.21324683 | -2.95608848 | -0.67107212 |
| H | -5.40456069 | -1.79043499 | -1.70519580 |
| N | 2.51397696 | 4.82735052 | 0.96328435 |
| H | 2.41495686 | 5.80709651 | 1.25476043 |
| C | 3.85918747 | 4.59897609 | 0.35291839 |
| C | 4.19479969 | 5.80651876 | -0.50772631 |
| H | 4.59925291 | 4.48487011 | 1.14908345 |
| H | 3.82698830 | 3.67616378 | -0.22935443 |
| O | 3.52480271 | 6.81691165 | -0.50209912 |
| O | 5.29878213 | 5.59477637 | -1.22051294 |
| H | 5.50878723 | 6.39095836 | -1.74200652 |
| H | 2.32941533 | 4.18559201 | 1.75830608 |
| H | 1.76289260 | 4.62674104 | 0.28700204 |

Appendix C: Chapter 4 Supplementary Information



Scheme C1. On the top are 3-dimensional structures of the four TAAQs. They provide better perspective of view when doing structural analysis of fragments that are dissociated from alkali metal cationized TAAQs through SORI-CID experiments. Numbering oxygens and naming binding positions for alkali metal cations are shown. Bottoms are side view structures and the energies recorded are computed under B3LYP-D3/6-31+G(d,p) with the unit of kJ mol⁻¹, at 298 K, 1 atm. The relative energies are with respect to the lowest energy structure of a m-TAAQ or b-TAAQ.



Scheme C1 continuous.

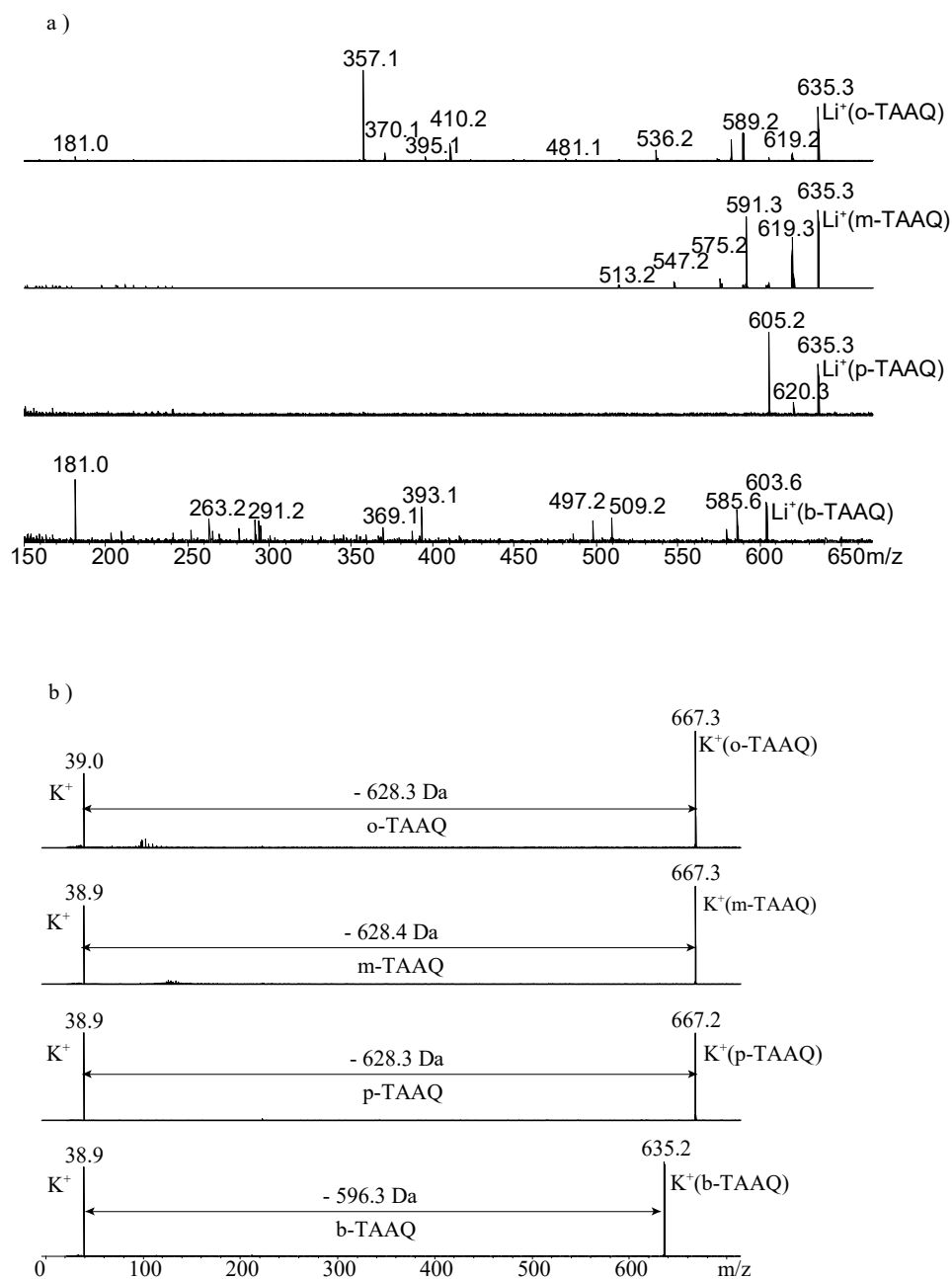


Figure C1. SORI-CID mass spectra of a) Li⁺(o-, m-, p- and b-TAAQ) complexes, b) K⁺(o-, m-, p- and b-TAAQ) complexes, c) Rb⁺(o-, m-, p- and b-TAAQ) and d) Cs⁺(o-, m-, p- and b-TAAQ)

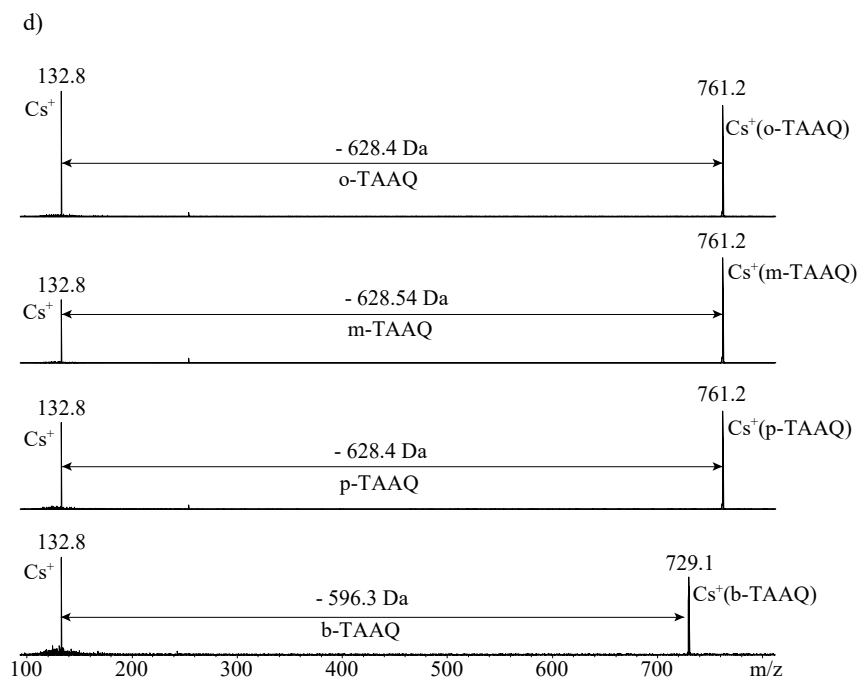
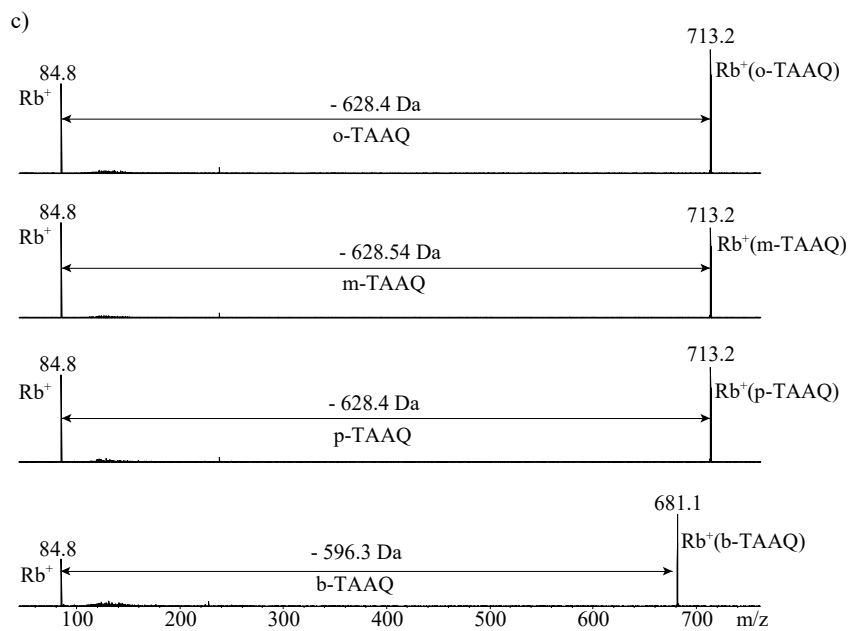


Figure C1 continuous.

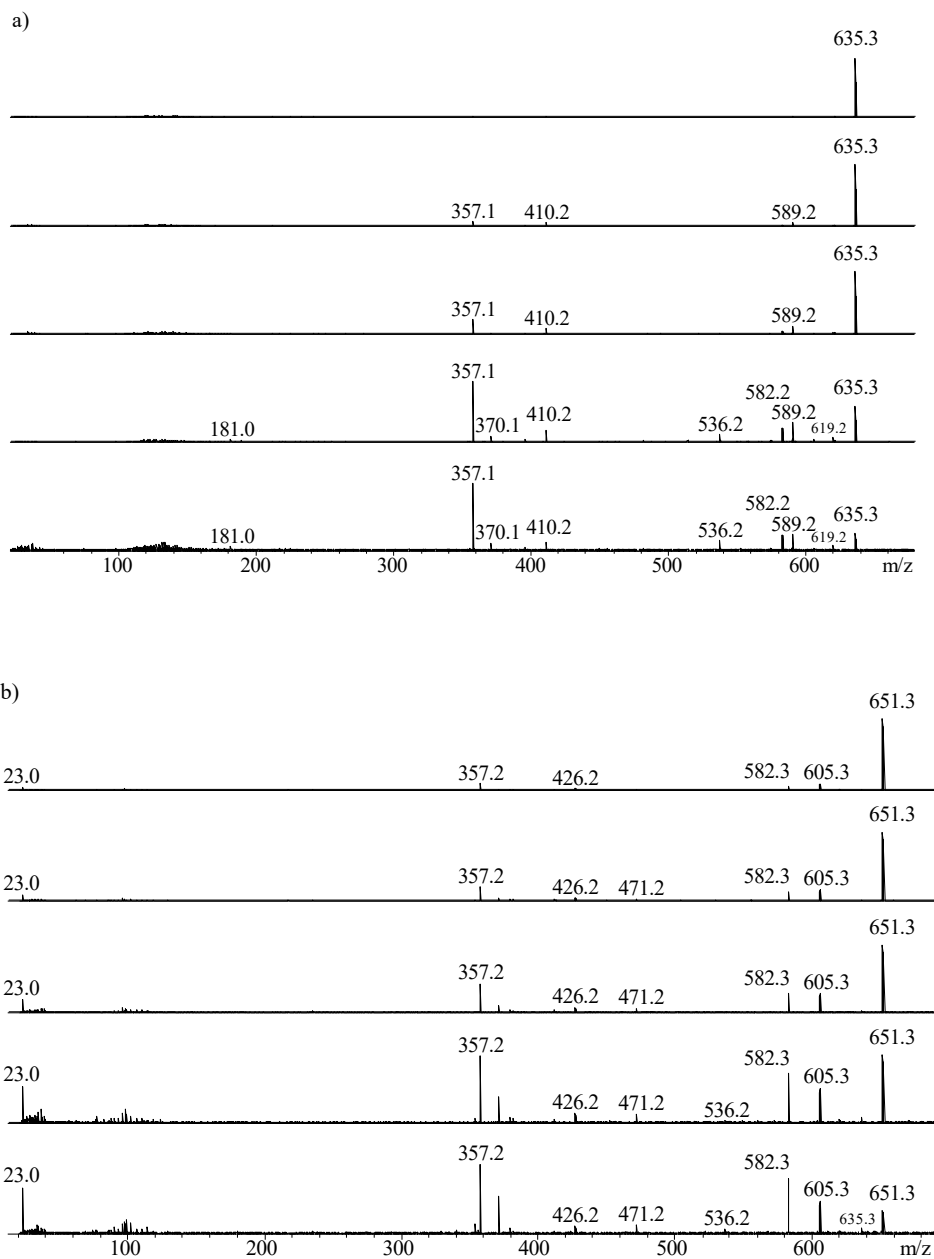


Figure C2. a) SORI-CID spectra of $\text{Li}^+(\text{o-TAAQ})$, the E_{CM} of which from top to bottom are 1.0, 1.1, 1.3, 1.6 and 1.8 eV respectively, b) SORI-CID spectra of $\text{Li}^+(\text{o-TAAQ})$, the E_{CM} of which from top to bottom are 0.6, 0.8, 0.9, 1.1 and 1.3 eV respectively.

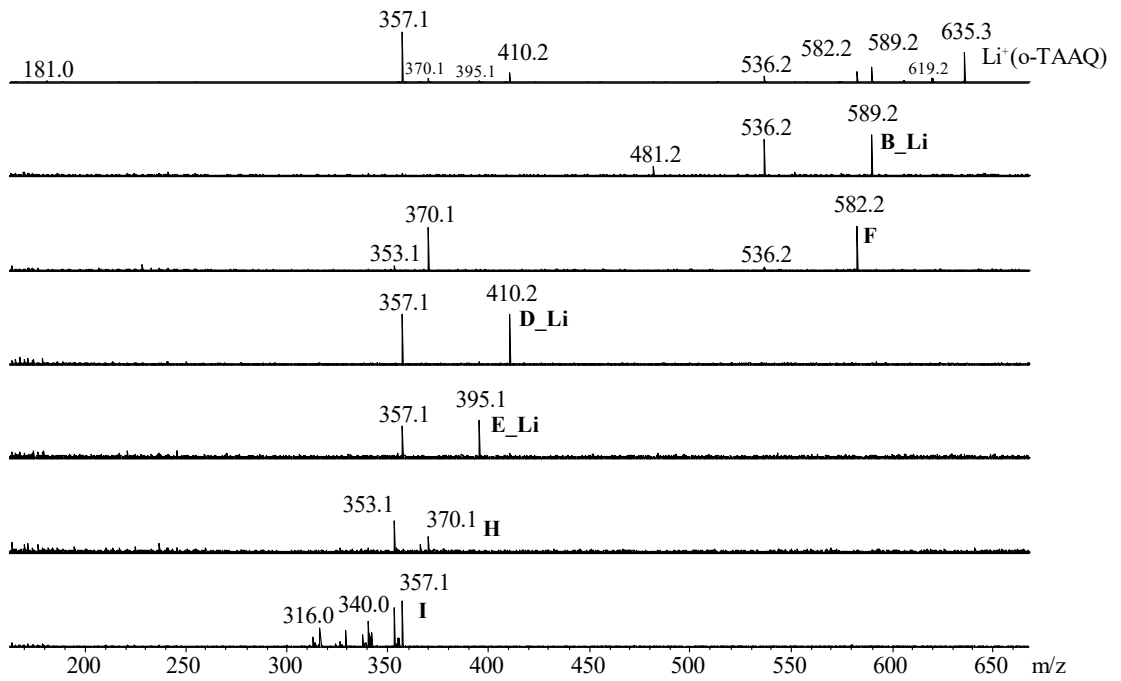


Figure C3. Tandem SORI-CID spectra on fragments of **B_Li** (m/z 589.2), **F** (m/z 582.2), **D_Li** (m/z 410.2), **E_Li** (m/z 395.1), **H** (m/z 370.1) and **I** (m/z 357.1) of $\text{Li}^+(\text{o-TAAQ})$ (m/z 635.3).

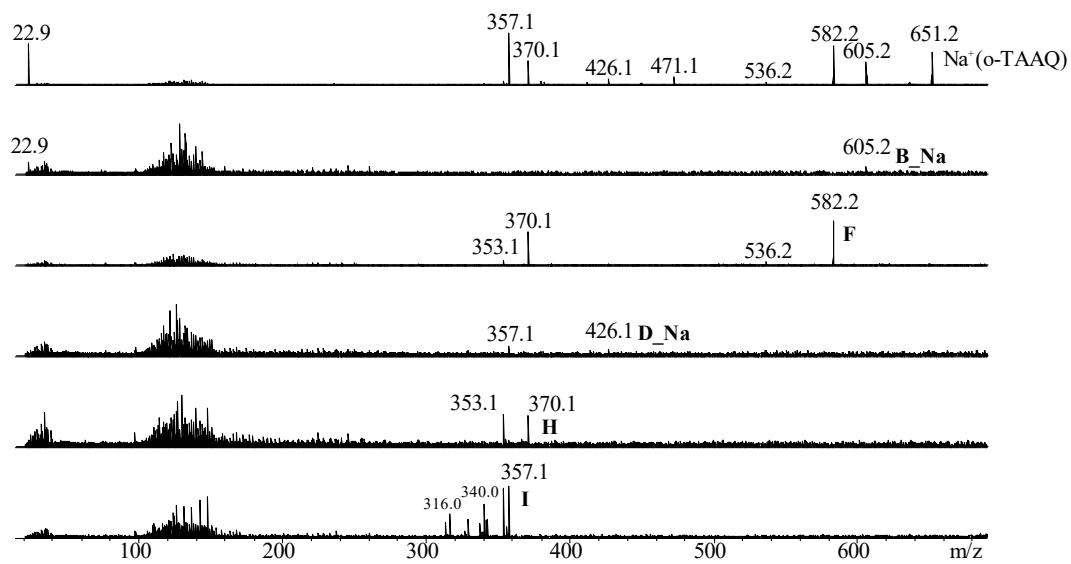


Figure C4. Tandem SORI-CID spectra on fragments of **B_Na** (m/z 605.2), **F** (m/z 582.2), **D_Na** (m/z 426.2), **H** (m/z 370.1) and **I** (m/z 357.1) of Na⁺(o-TAAQ) (m/z 651.2).

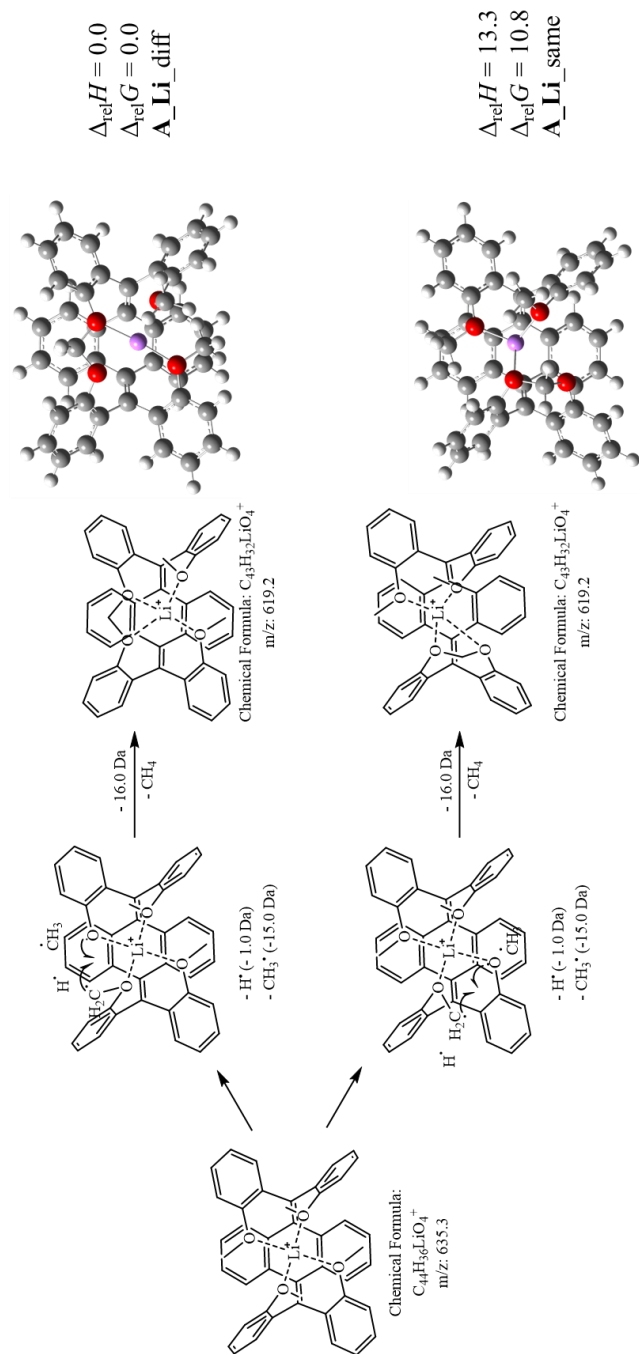


Figure C5. Fragment A_Li (m/z 619.2)

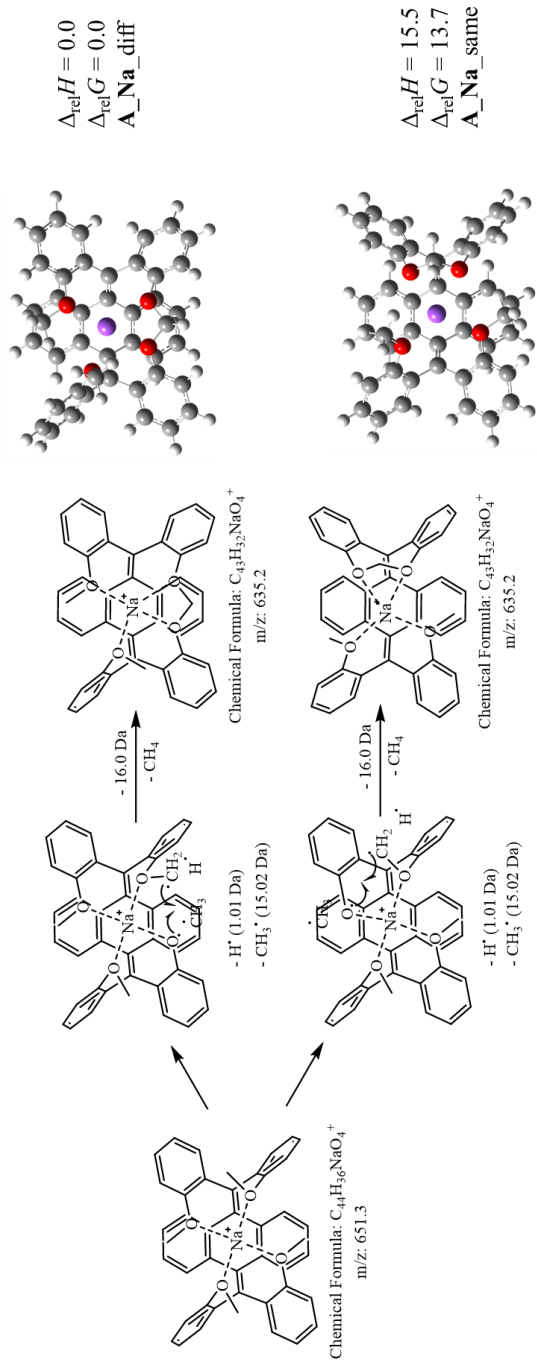


Figure C6. Fragment A_Na (m/z 635.2)

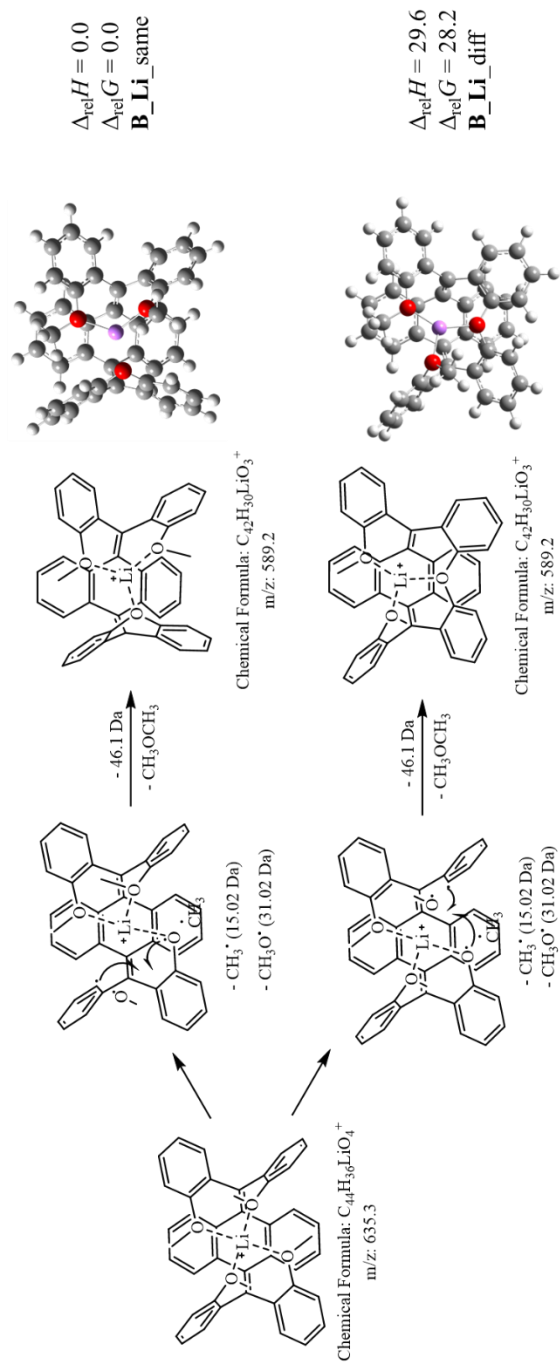


Figure C7. Fragment **B_Li** (m/z 589.2)

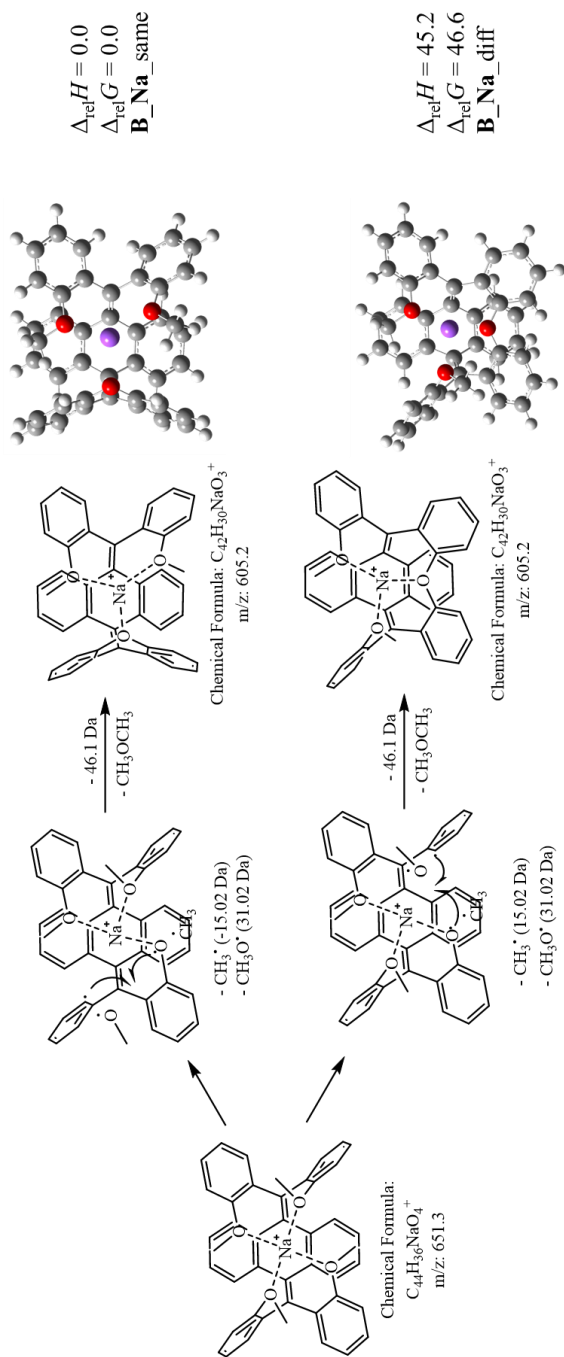


Figure C8. Fragment B_Na (m/z 605.2)

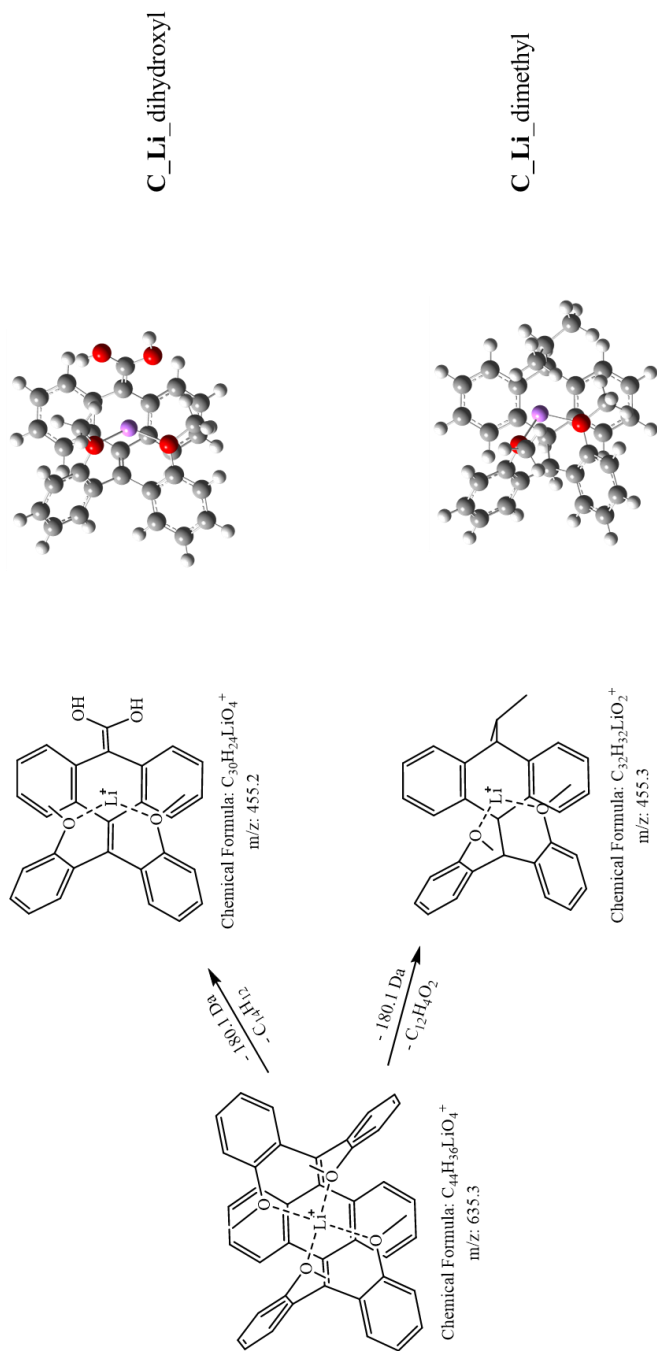


Figure C9. Fragment C_Li (m/z 455.1)

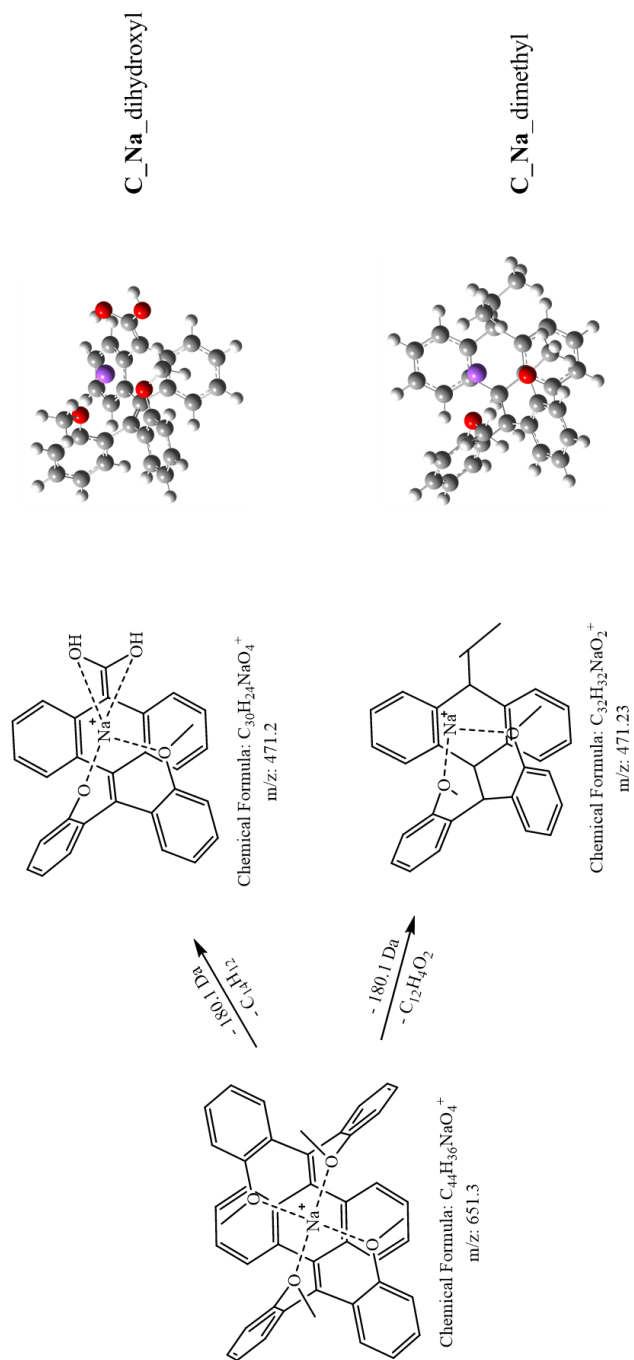


Figure C10. Fragment C_Na (m/z 471.1)

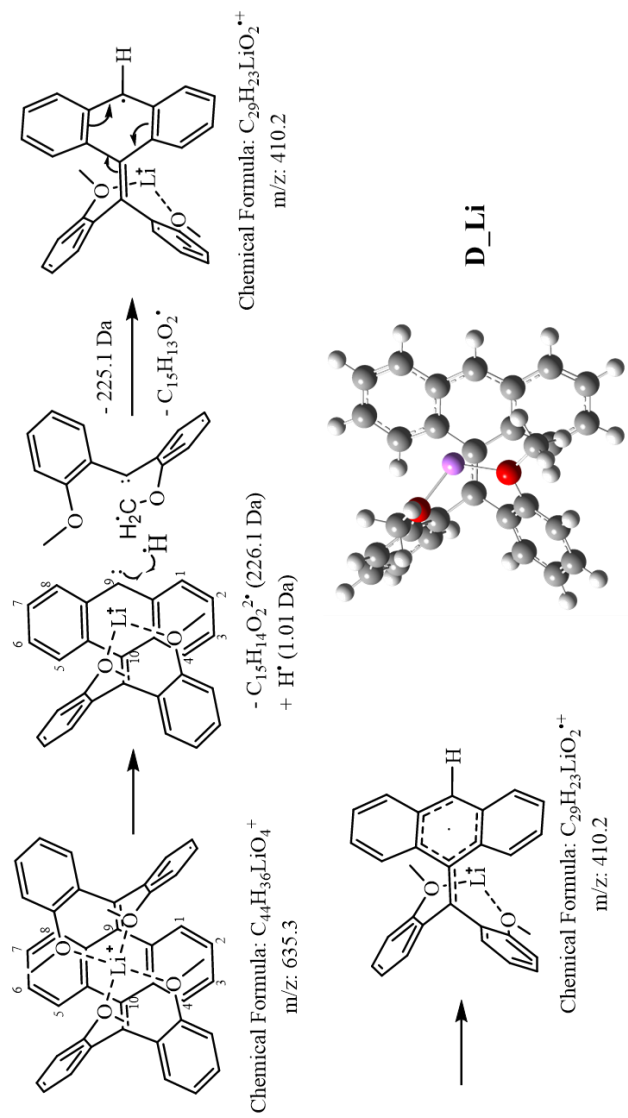


Figure C11. Fragment **D_Li** (m/z 410.2)

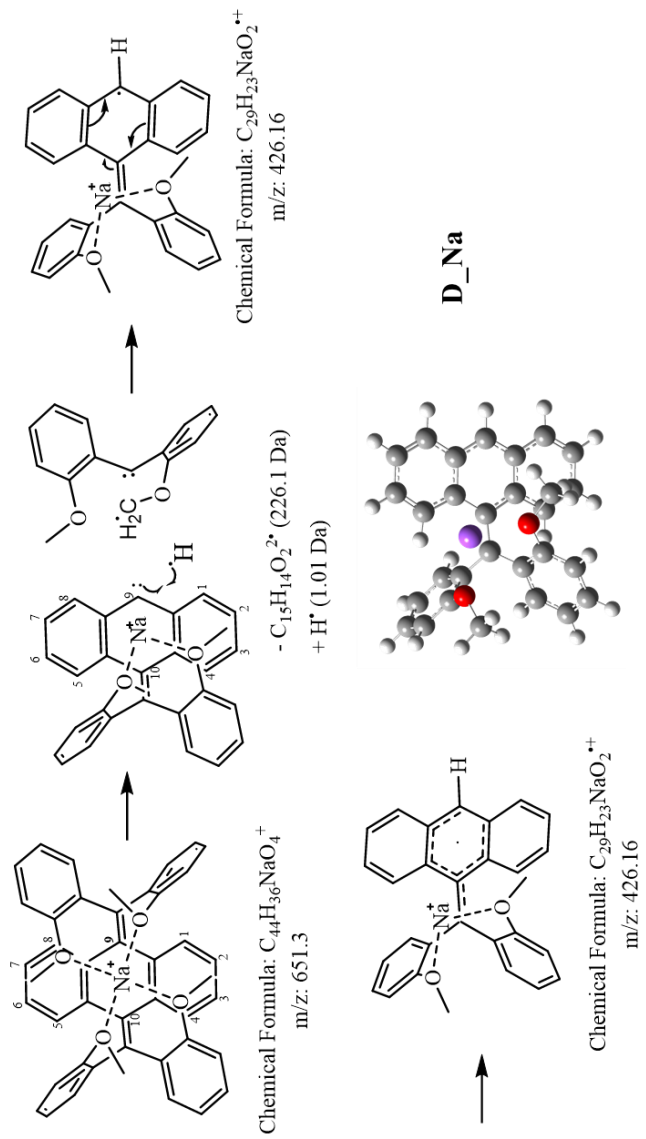


Figure C12. Fragment **D_Na** (m/z 426.1)

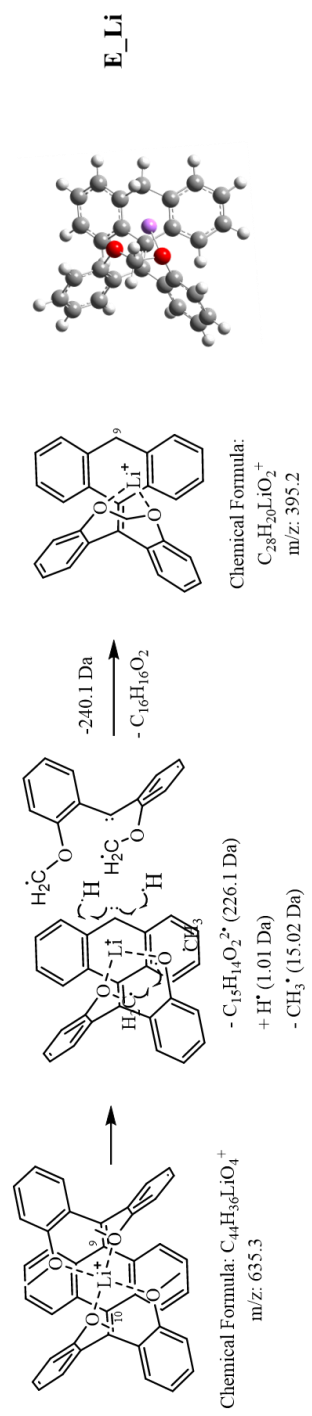


Figure C13. Fragment E_Li (m/z 395.1)

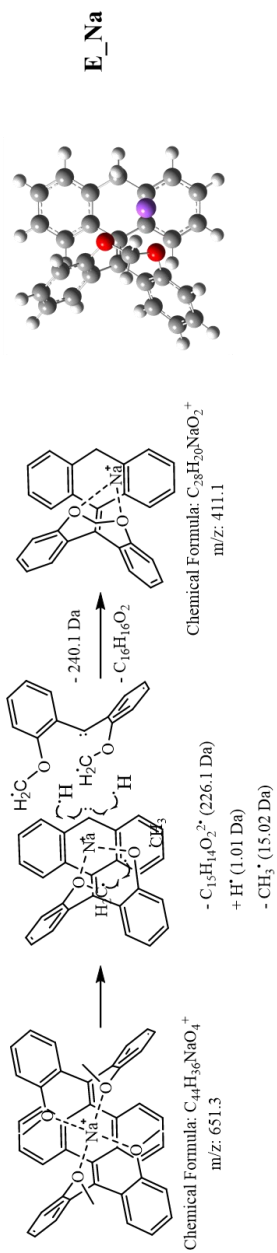


Figure C14. Fragment **E_Na** (m/z 411.1)

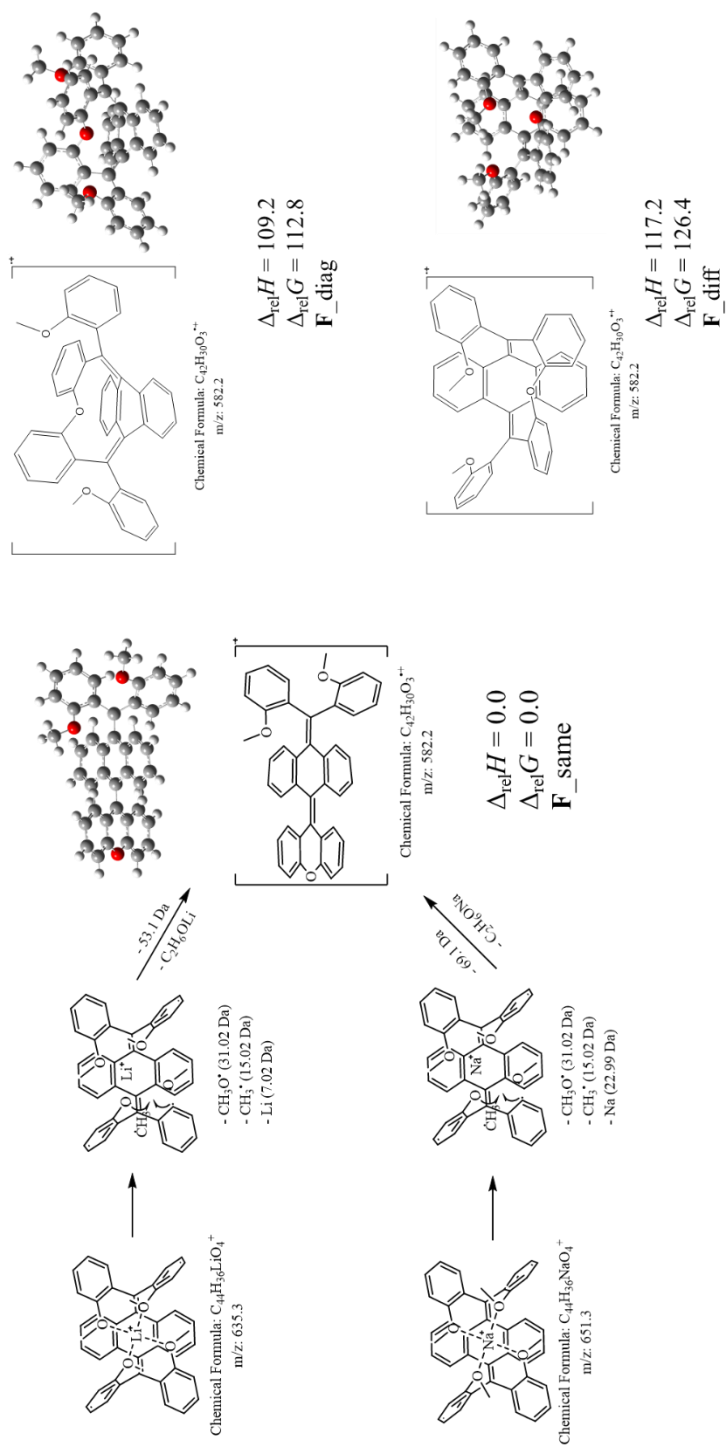


Figure C15. Fragment F (m/z 582.2)

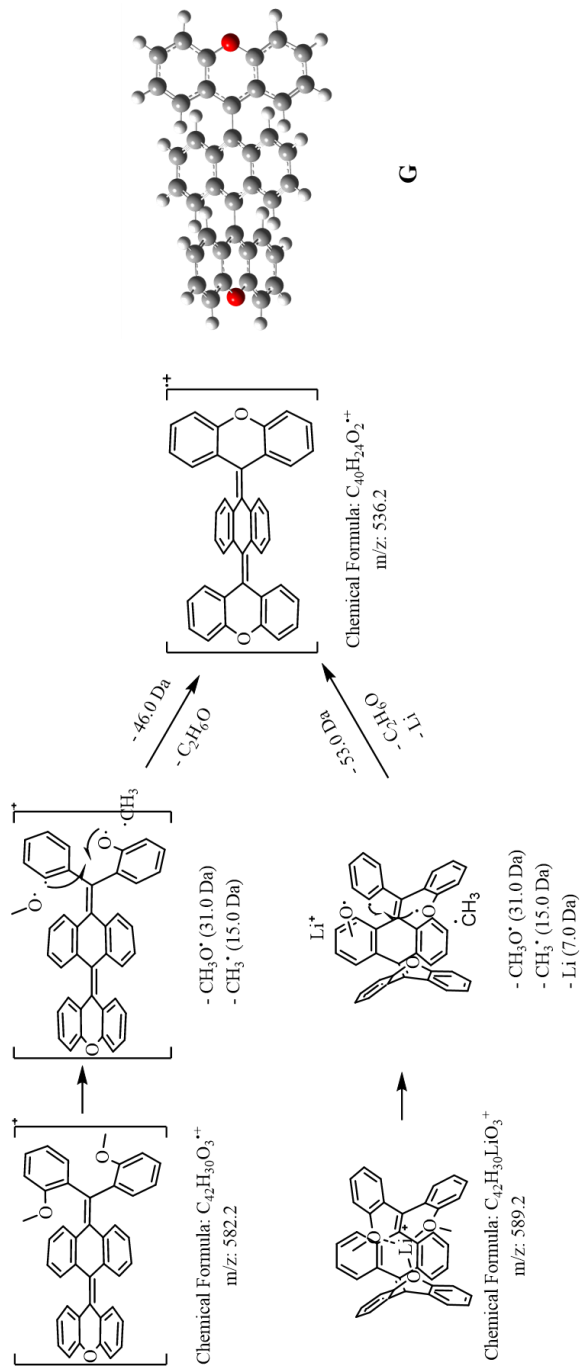


Figure C16. Fragment **G** (m/z 536.2)

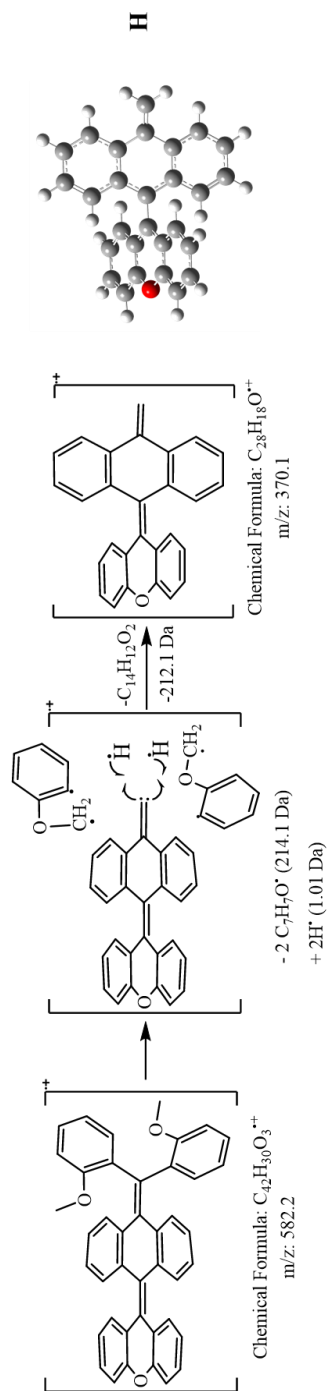


Figure C17. Fragment **H** (m/z 370.1)

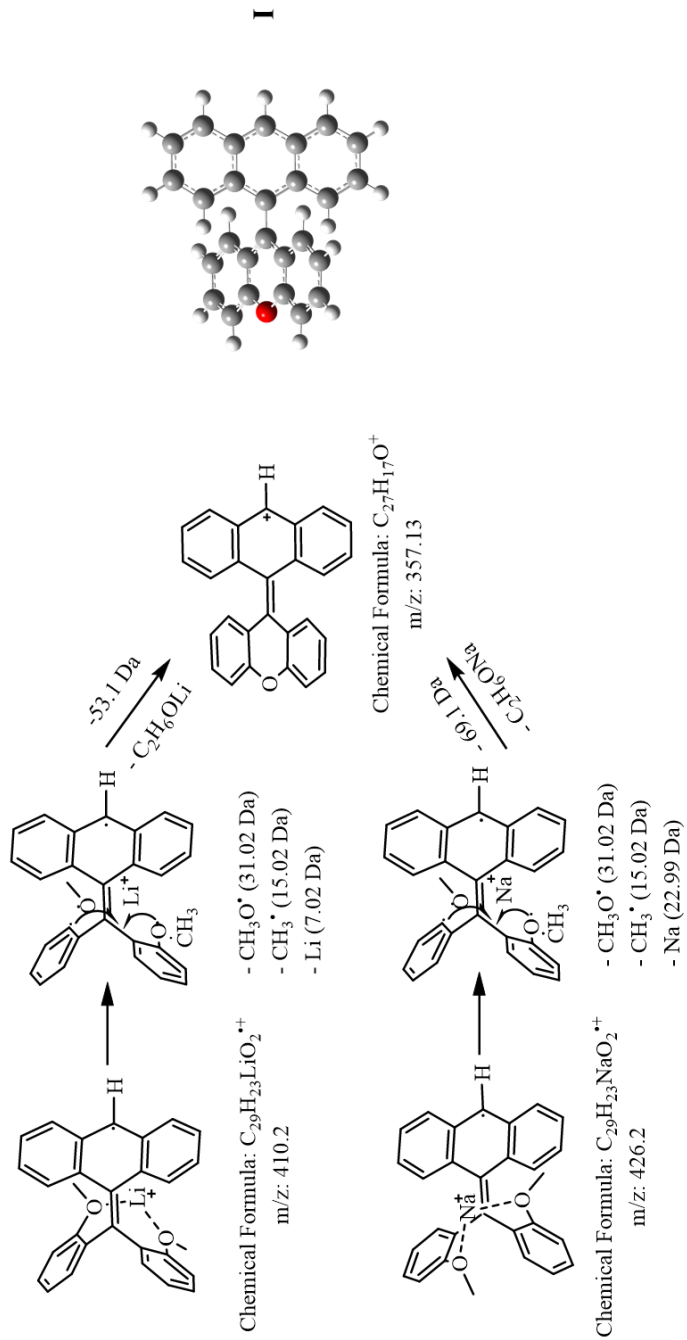


Figure C18. Fragment I (m/z 357.1)

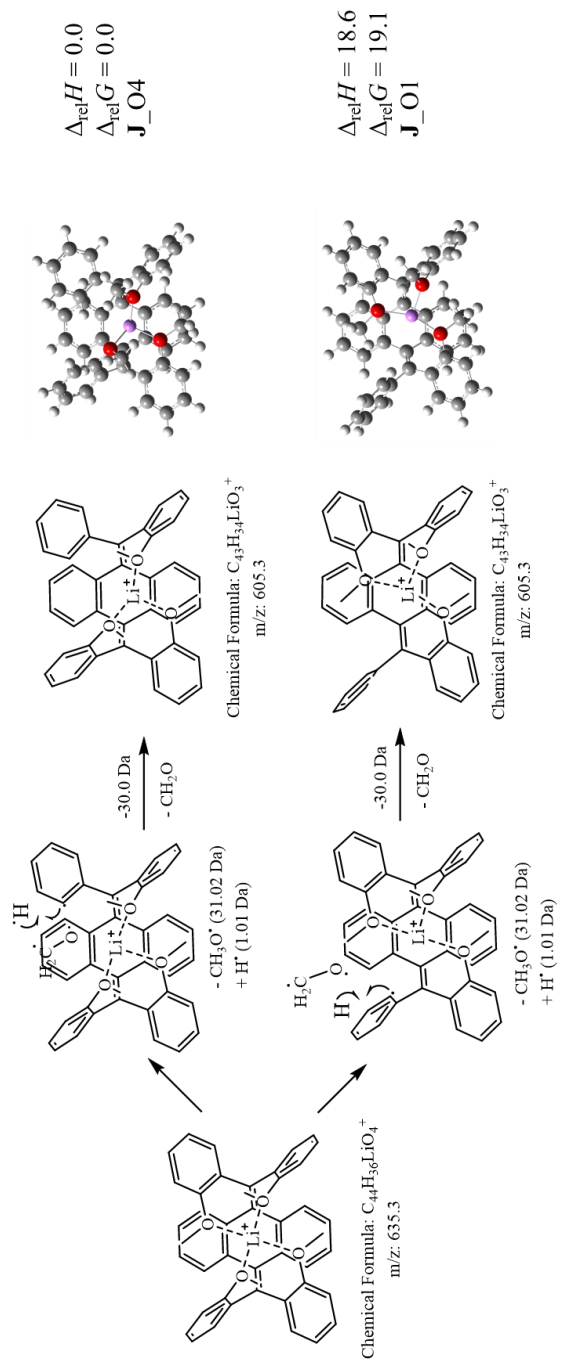


Figure C19. Fragment J (m/z 605.2)

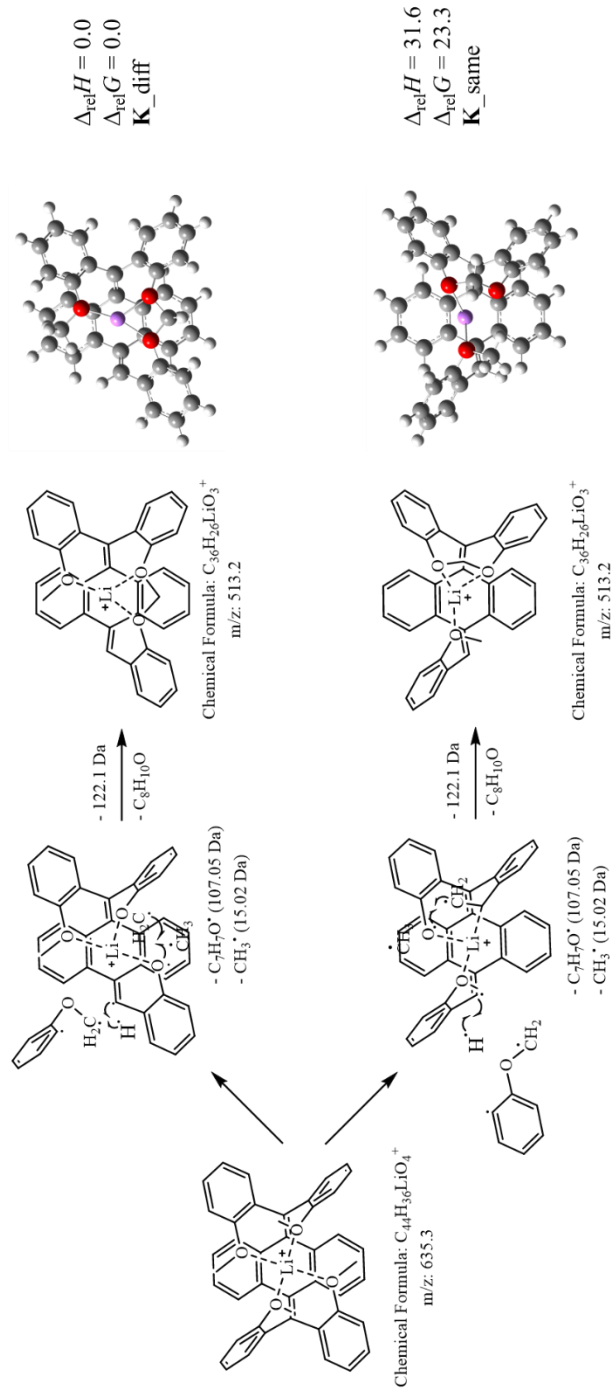


Figure C20. Fragment **K** (m/z 513.2)

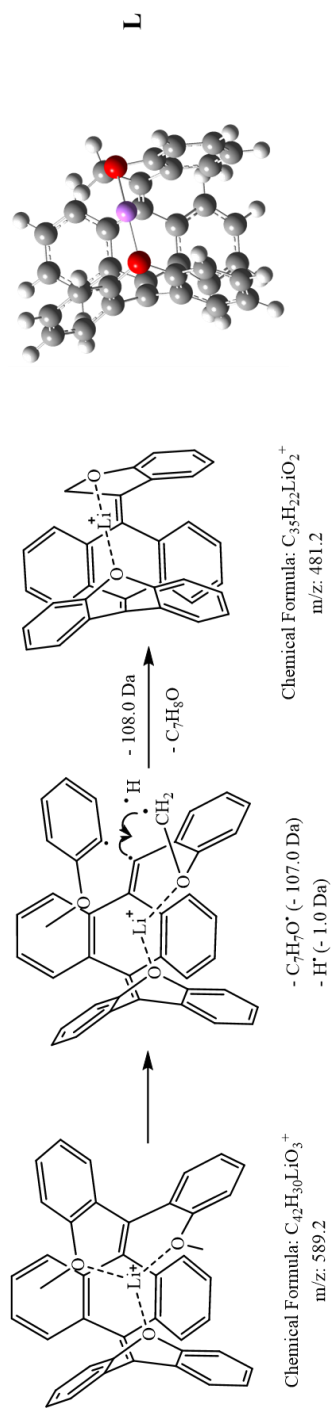


Figure C21. Fragment L (m/z 481.2)

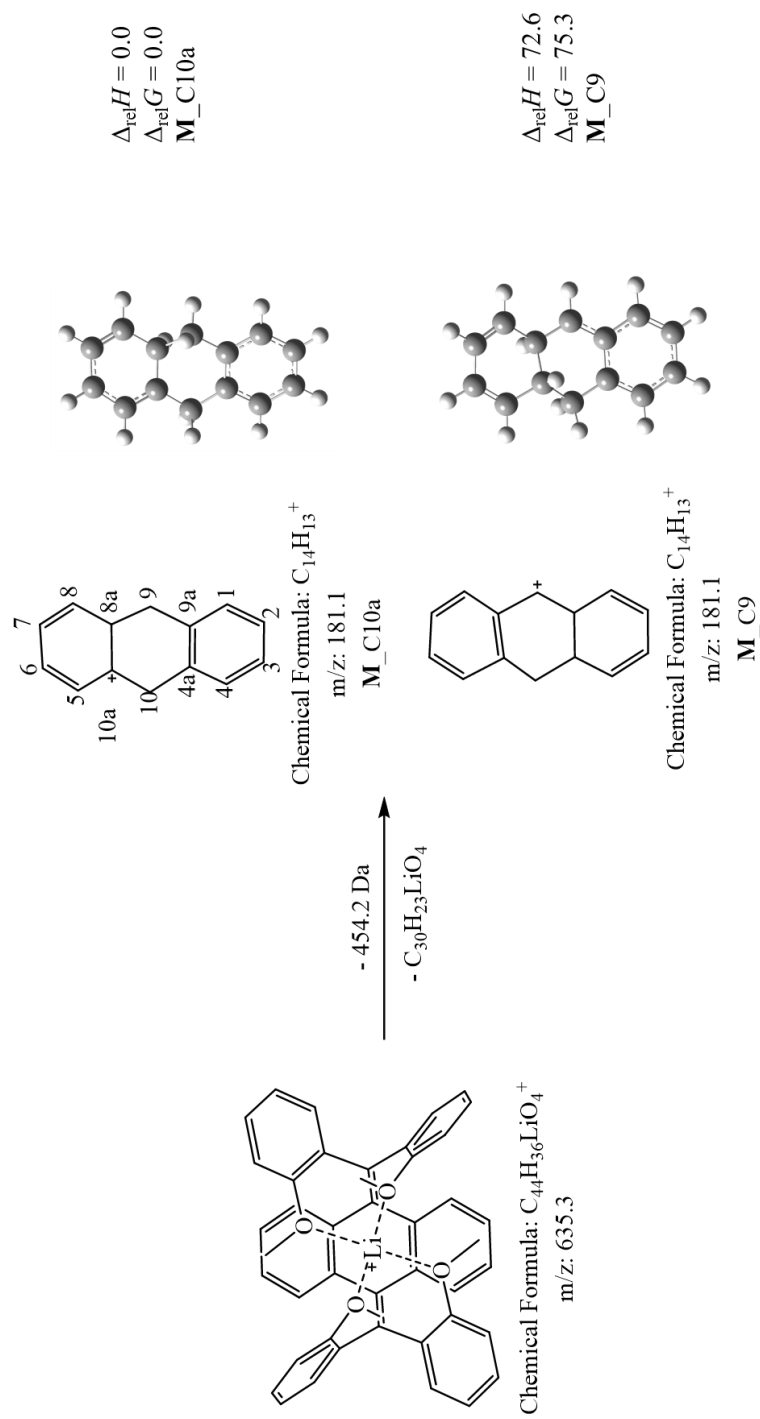


Figure C22. Fragment **M** (m/z 181.0)

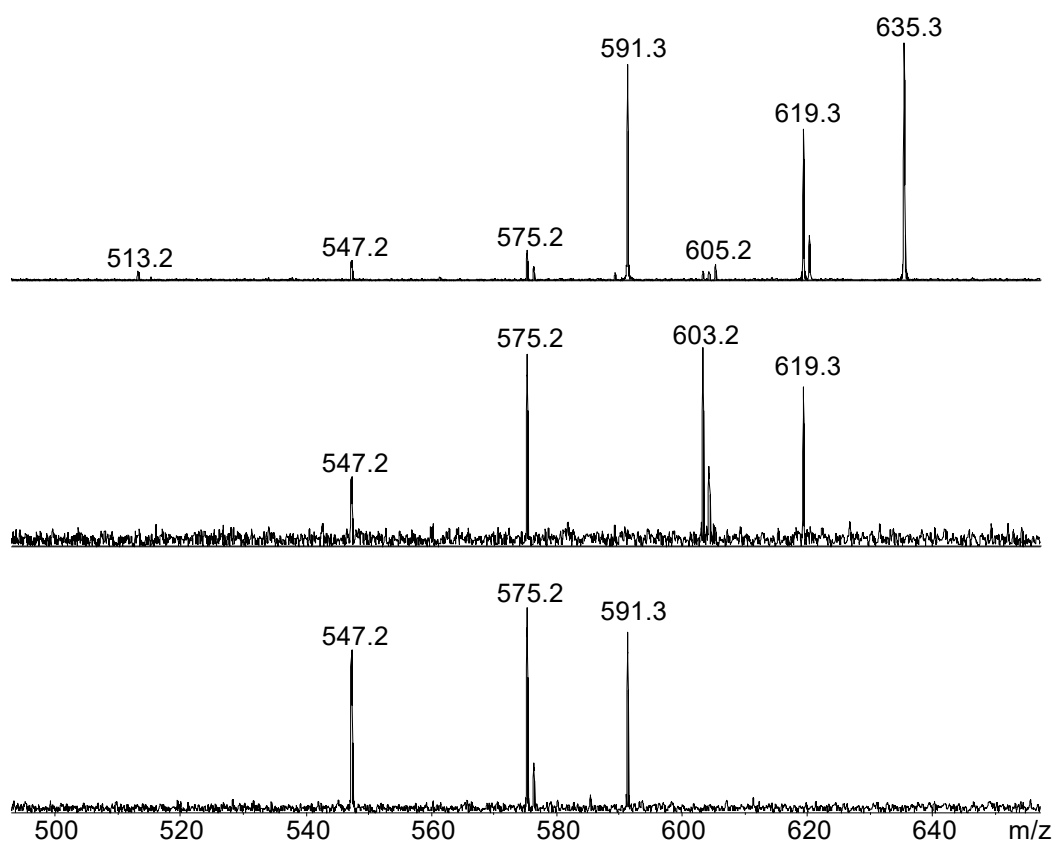


Figure C23. Tandem SORI-CID spectra on fragments of **619** (m/z 619.3) and **519** (m/z 591.3) of $\text{Li}^+(\text{m-TAAQ})$ (m/z 635.3).

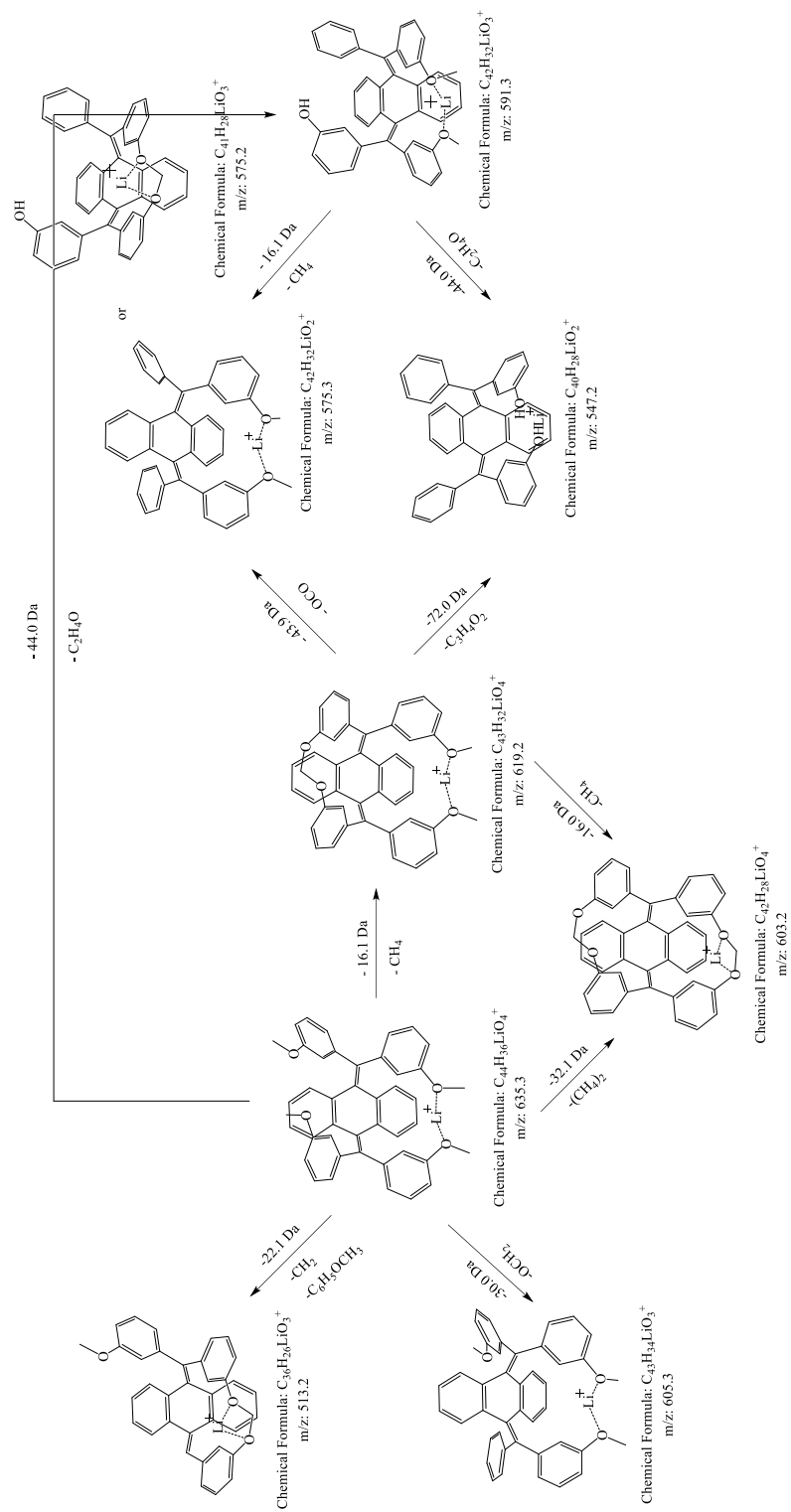


Figure C24. Postulated dissociation pathways of $Li^+(m\text{-TAAQ})$ (m/z 635.3).

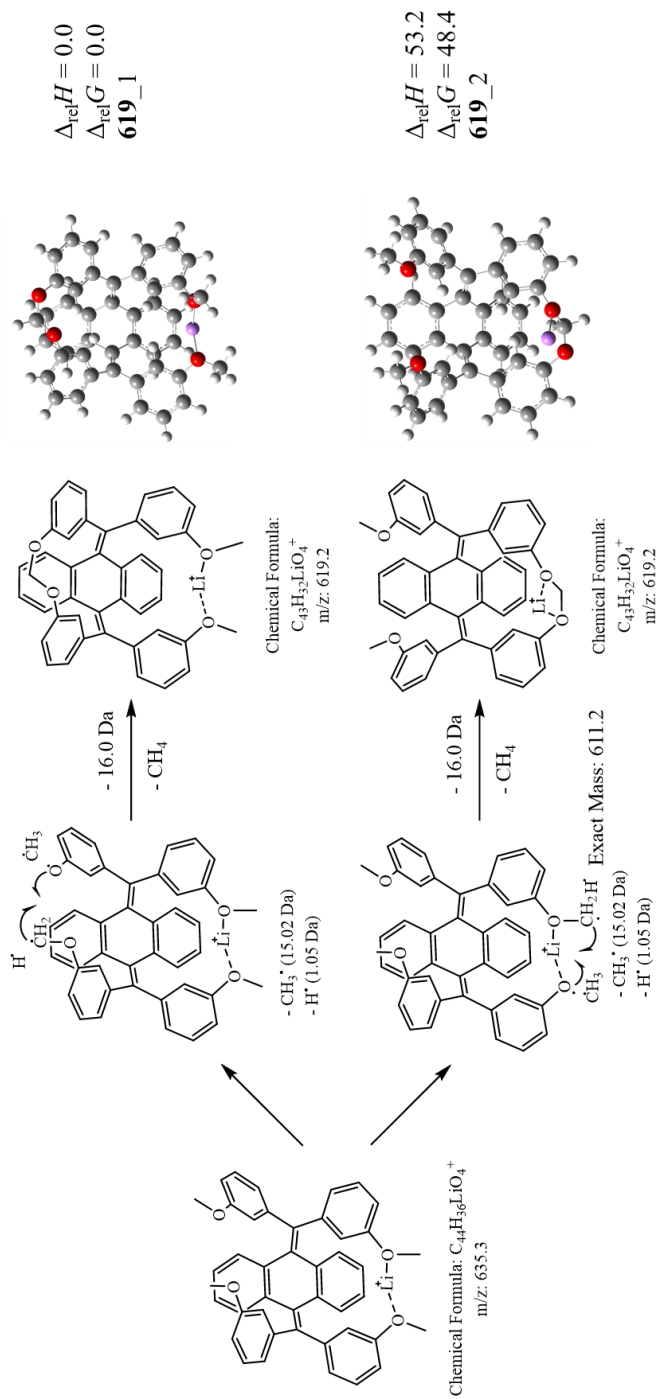


Figure C25. Fragment 619 of Li^+ (m-TAAQ).

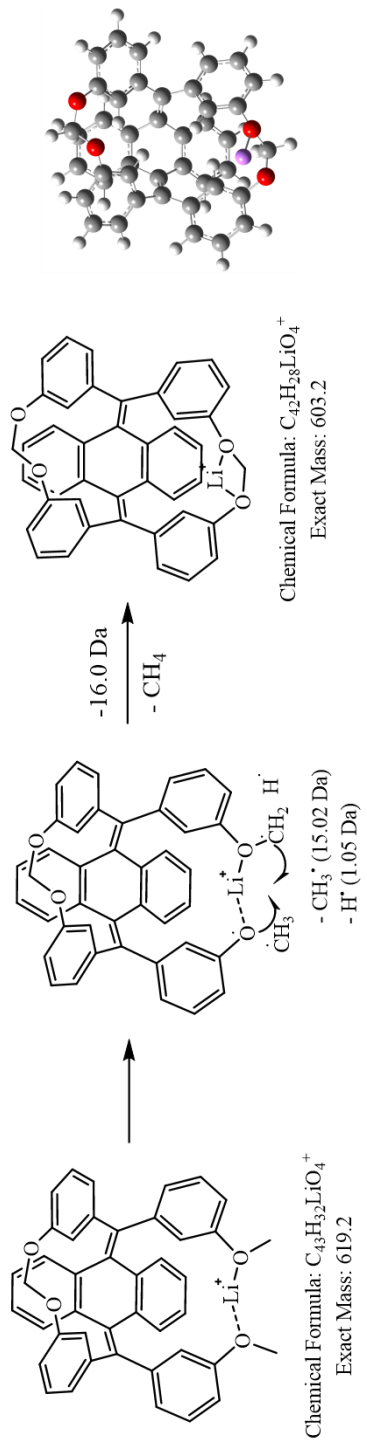


Figure C26. Fragment 603 of Li^+ (m-TAAQ).

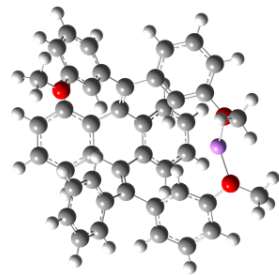
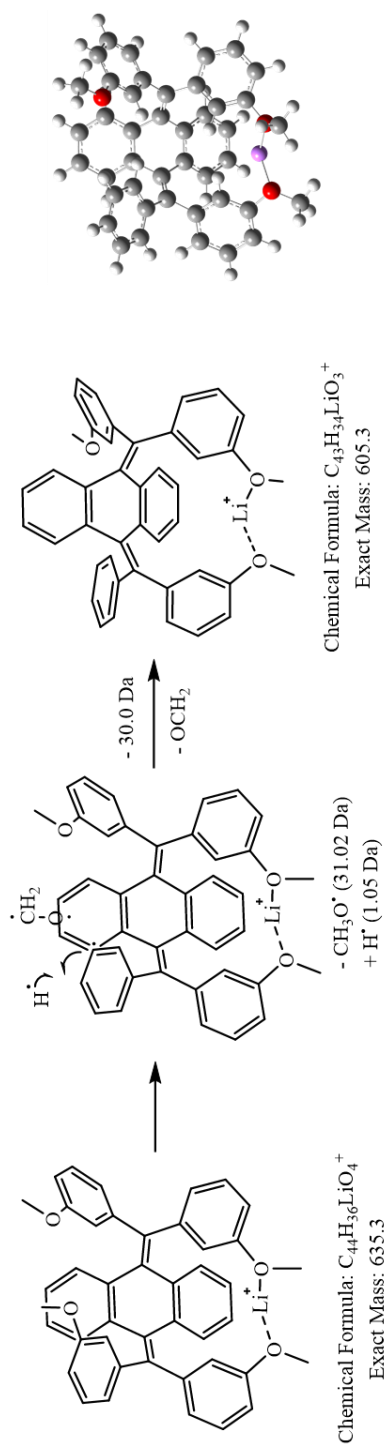


Figure C27. Fragment 605_m of Li^+ (m-TAAQ).

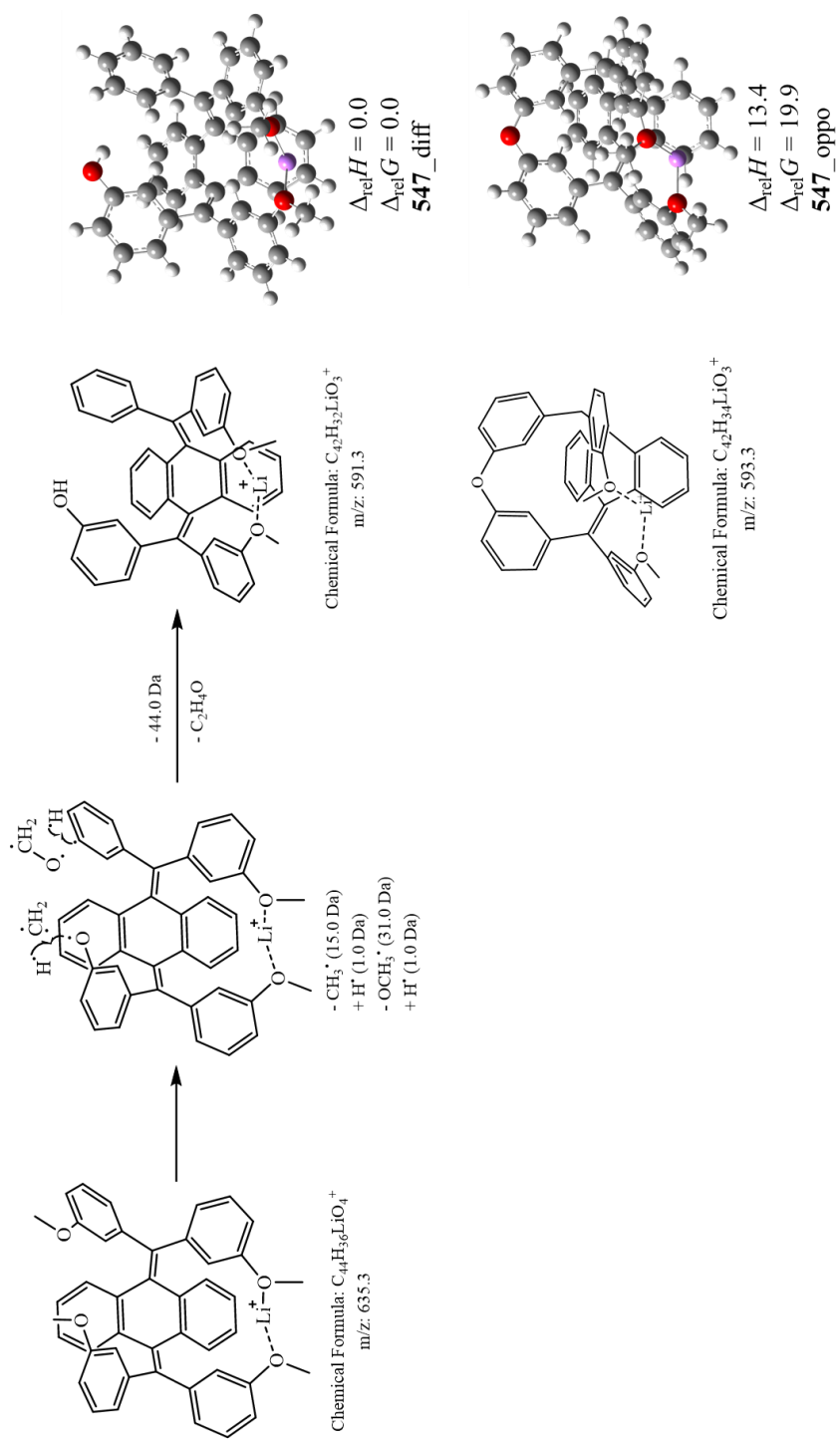


Figure C28. Fragment **591** of Li^+ (m-TAAQ).

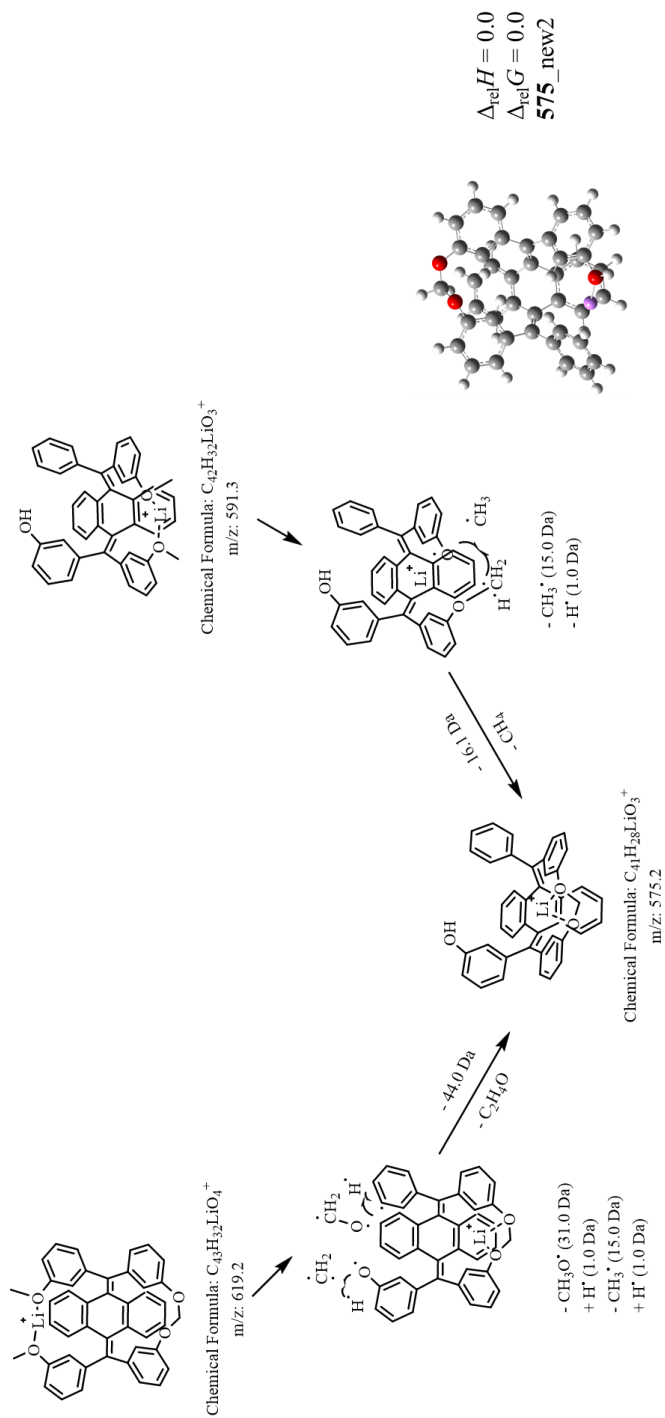


Figure C29. Fragment 575 of Li^+ (m-TAAQ), which is a fragment of 619 and 591.

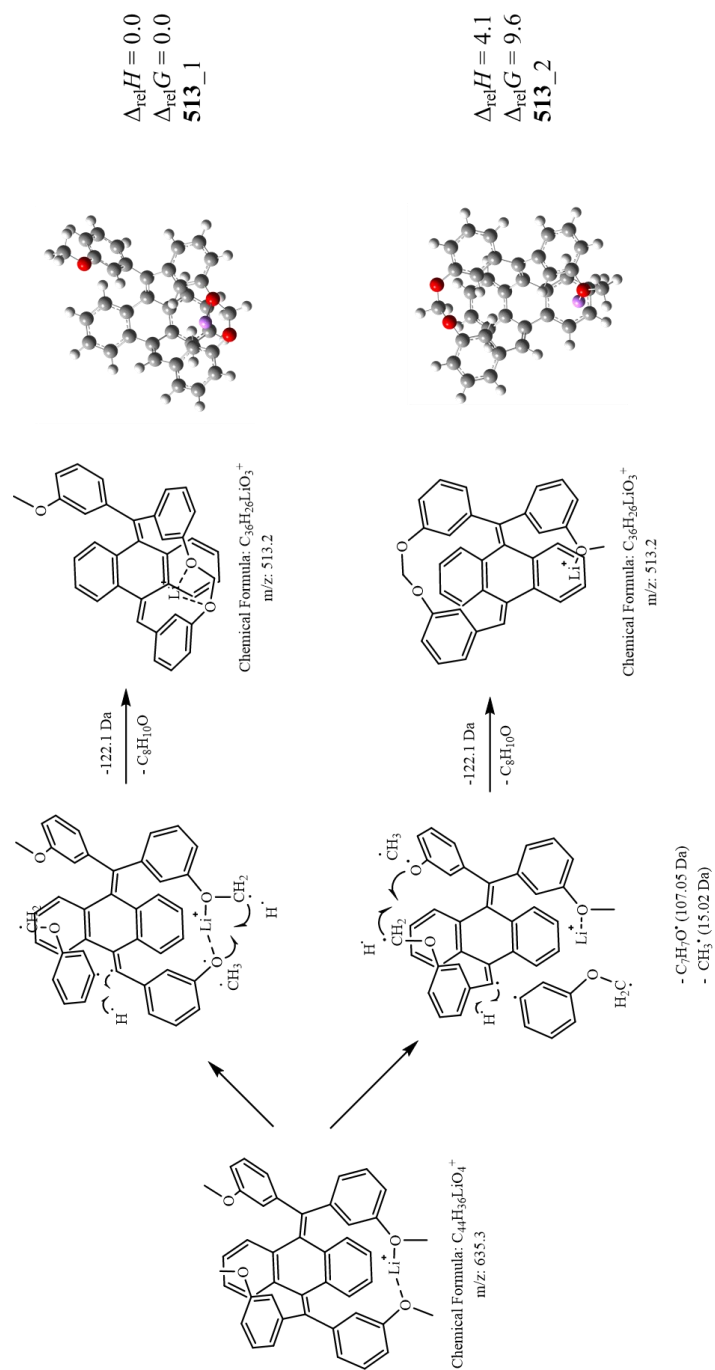


Figure C31. Fragment 513 of Li^+ (m-TAAQ).

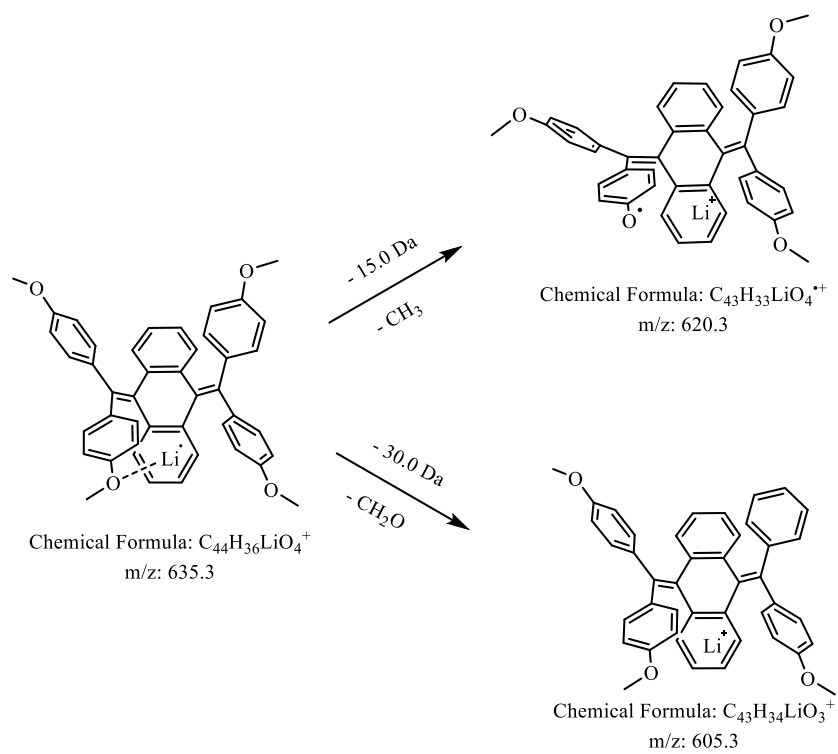


Figure C32. Postulated dissociation pathways of $Li^+(p-TAAQ)$ (m/z 635.3).

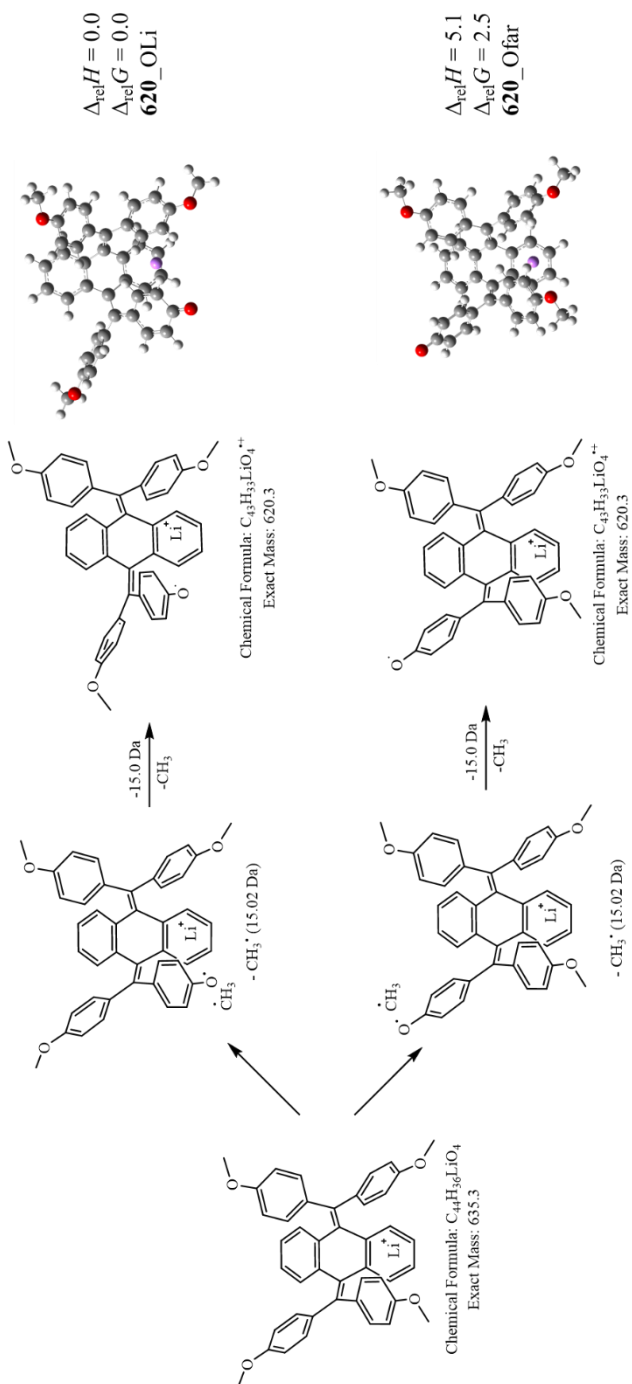


Figure C33. Fragment 620 of Li⁺(p-TAAQ).

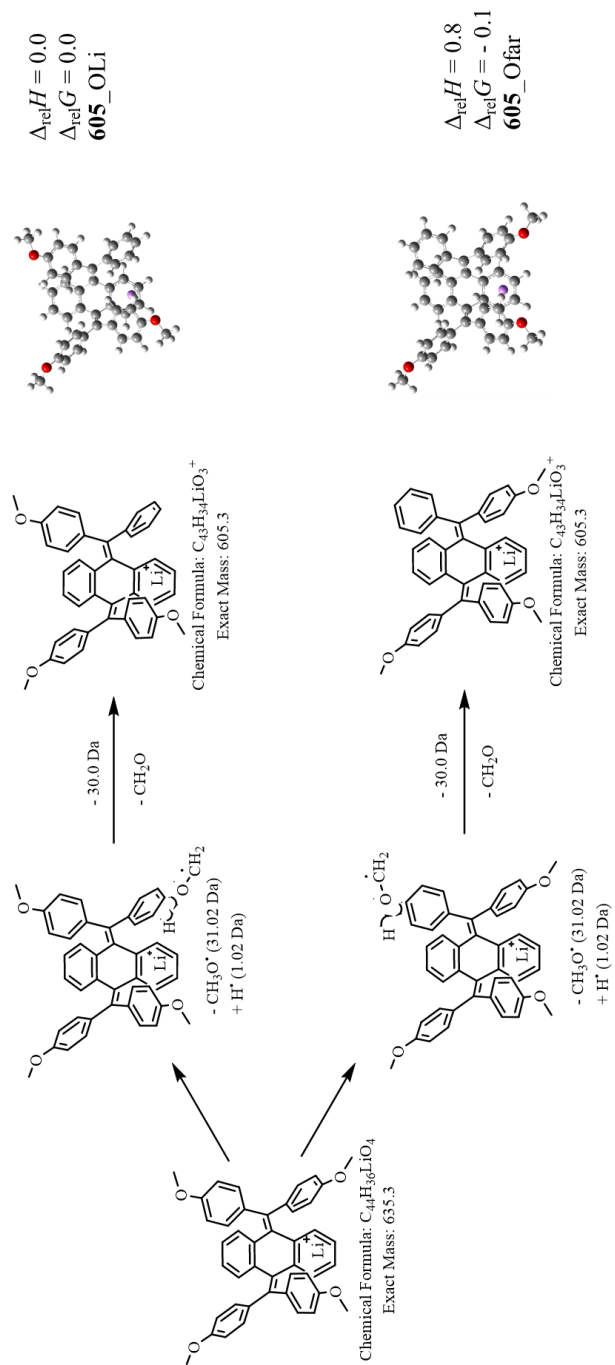


Figure C34. Fragment **605_p** of Li^+ (p-TAAQ).

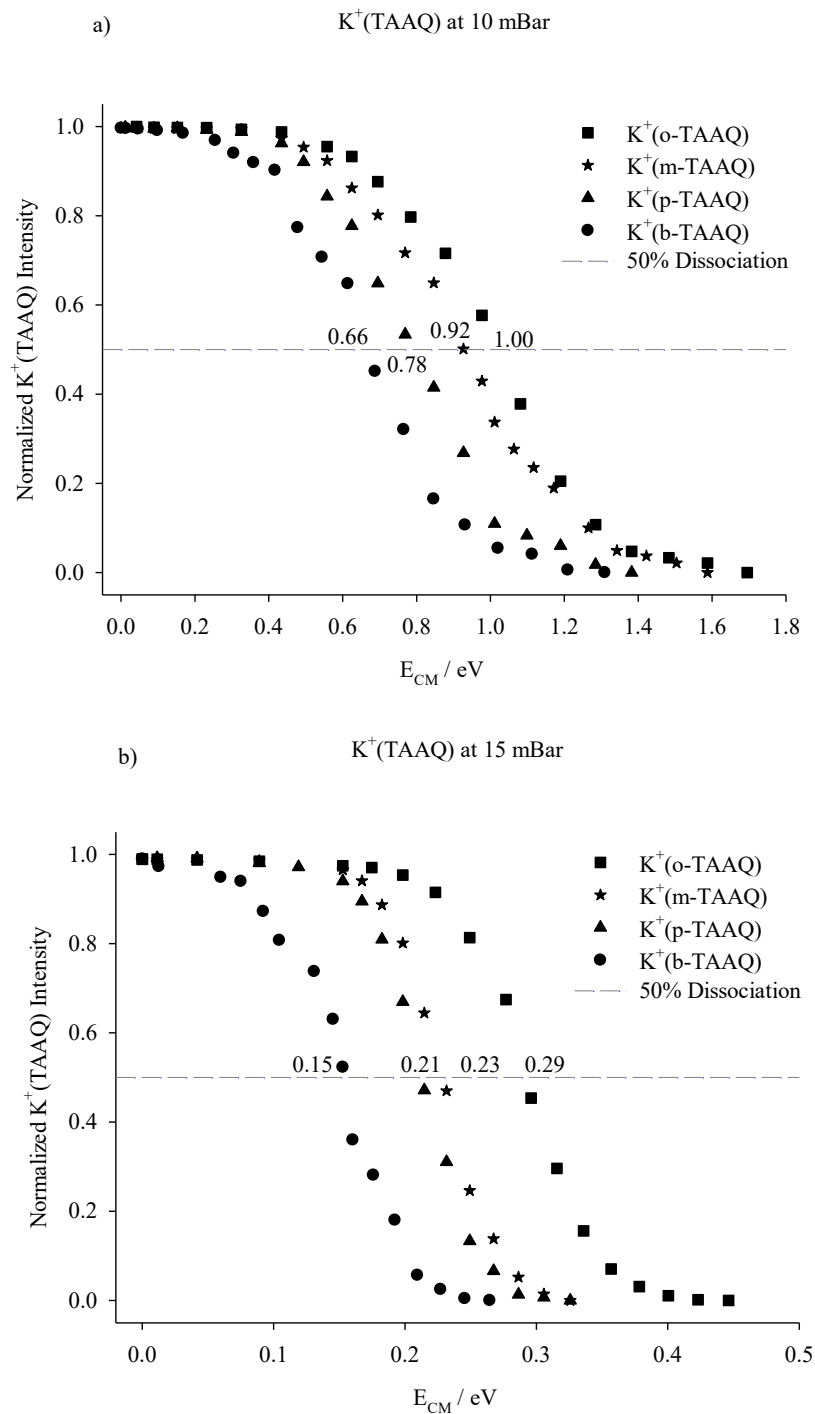


Figure C35. Normalized intensity of $K^+(\text{TAAQs})$ under a) 10 mBar and b) 15 mBar, $Rb^+(\text{TAAQs})$ under b) 10 mBar and c) 15 mBar and $Cs^+(\text{TAAQs})$ under e) 10 mBar and f) 15 mBar vs. center of mass energy decay curves obtained from the ER-SORI-CID experiments. The values in eV of $E_{50\%}$ are also shown in the graphs.

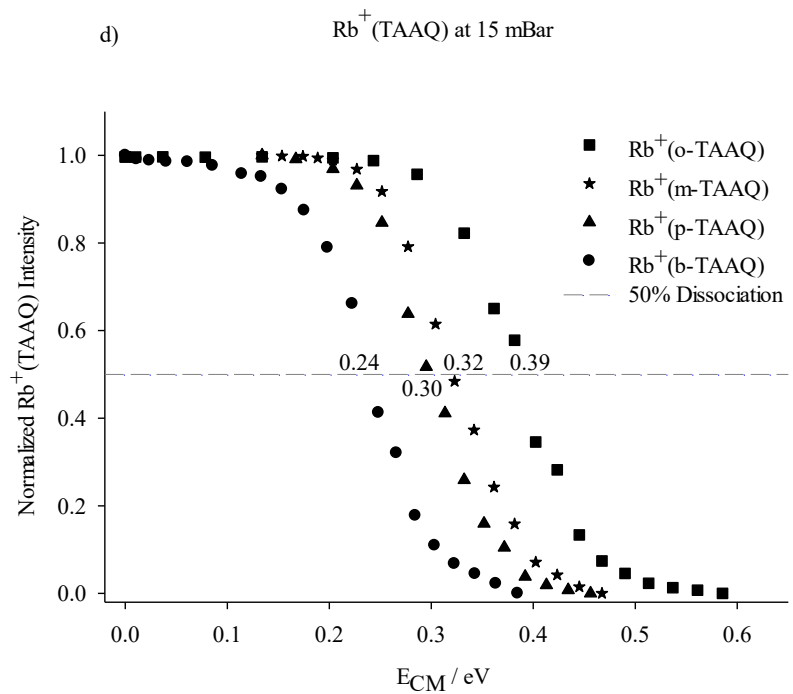
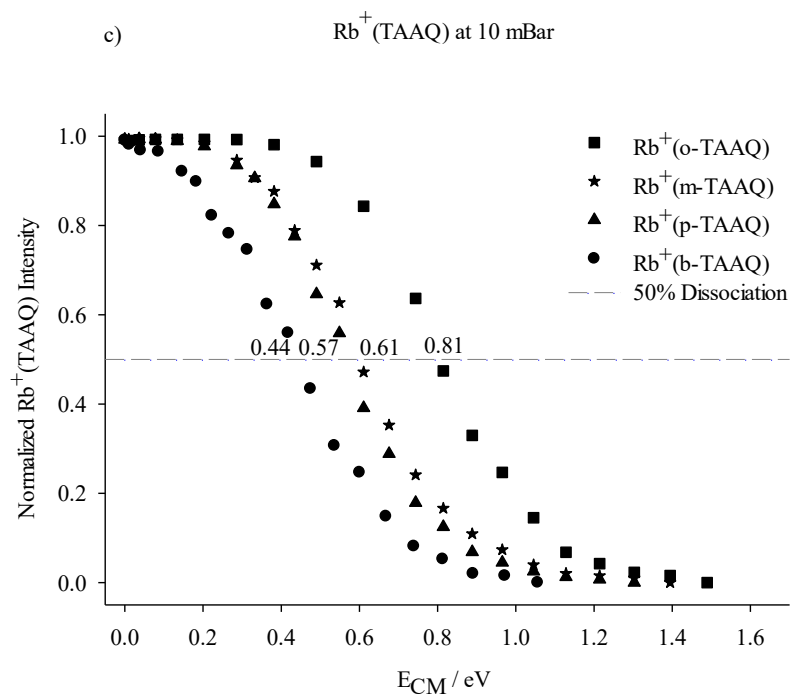


Figure C35 continuous.

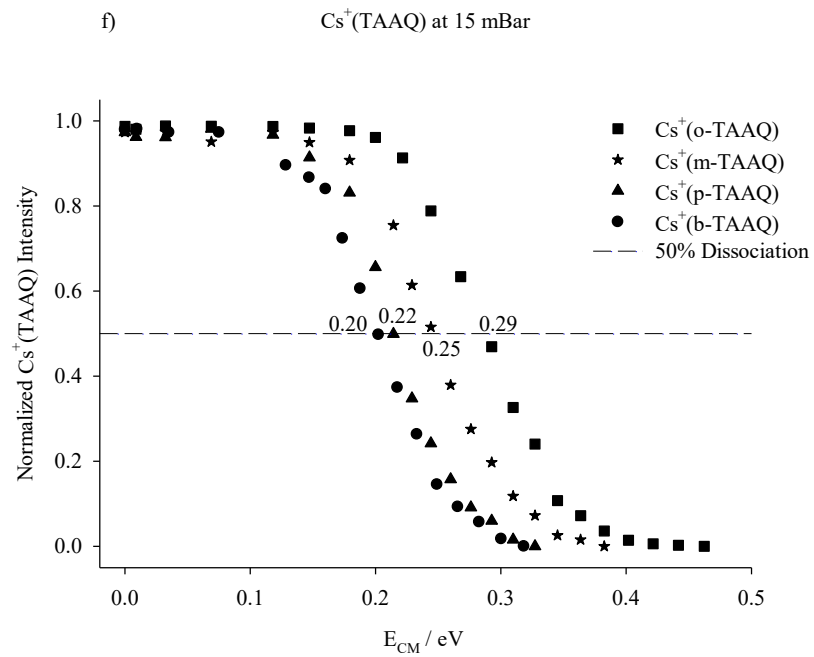
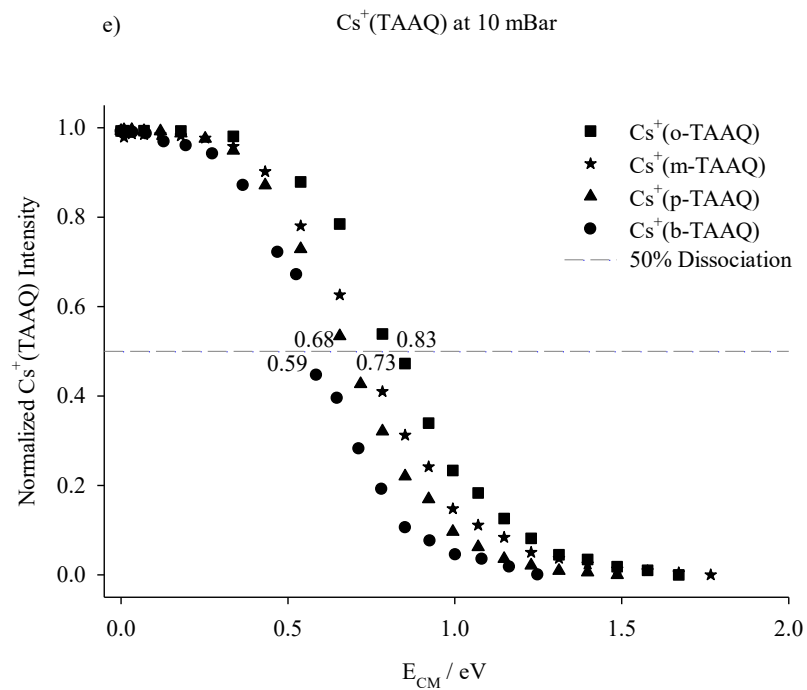


Figure C35 continuous.

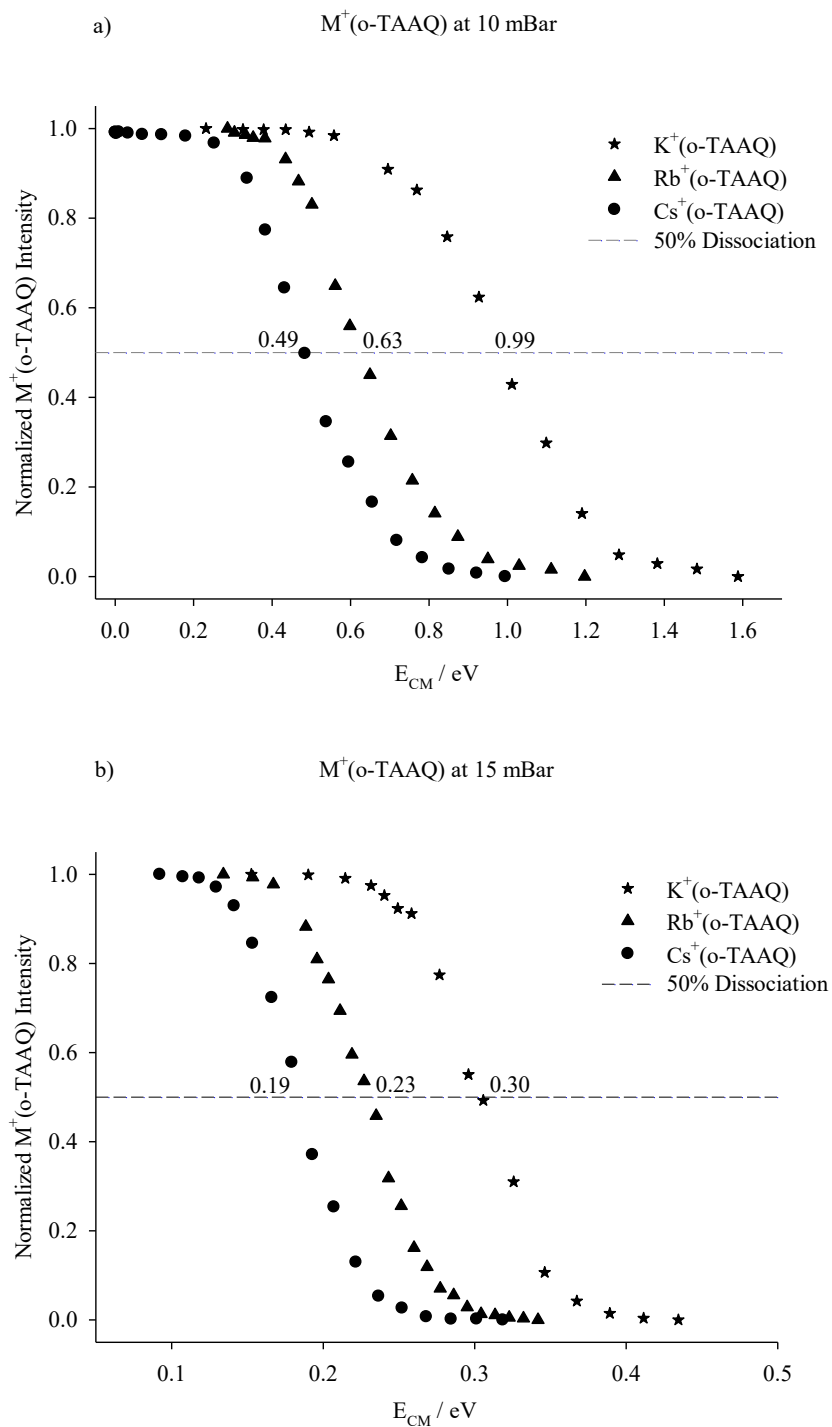


Figure C36. Normalized intensity of $M^+(\text{o-TAAQ})$ vs. center of mass energy decay curves from the ER-SORI-CID experiments under a) 10 mBar and b) 15 mBar. The values of $E_{50\%}$ are also shown in the graphs.

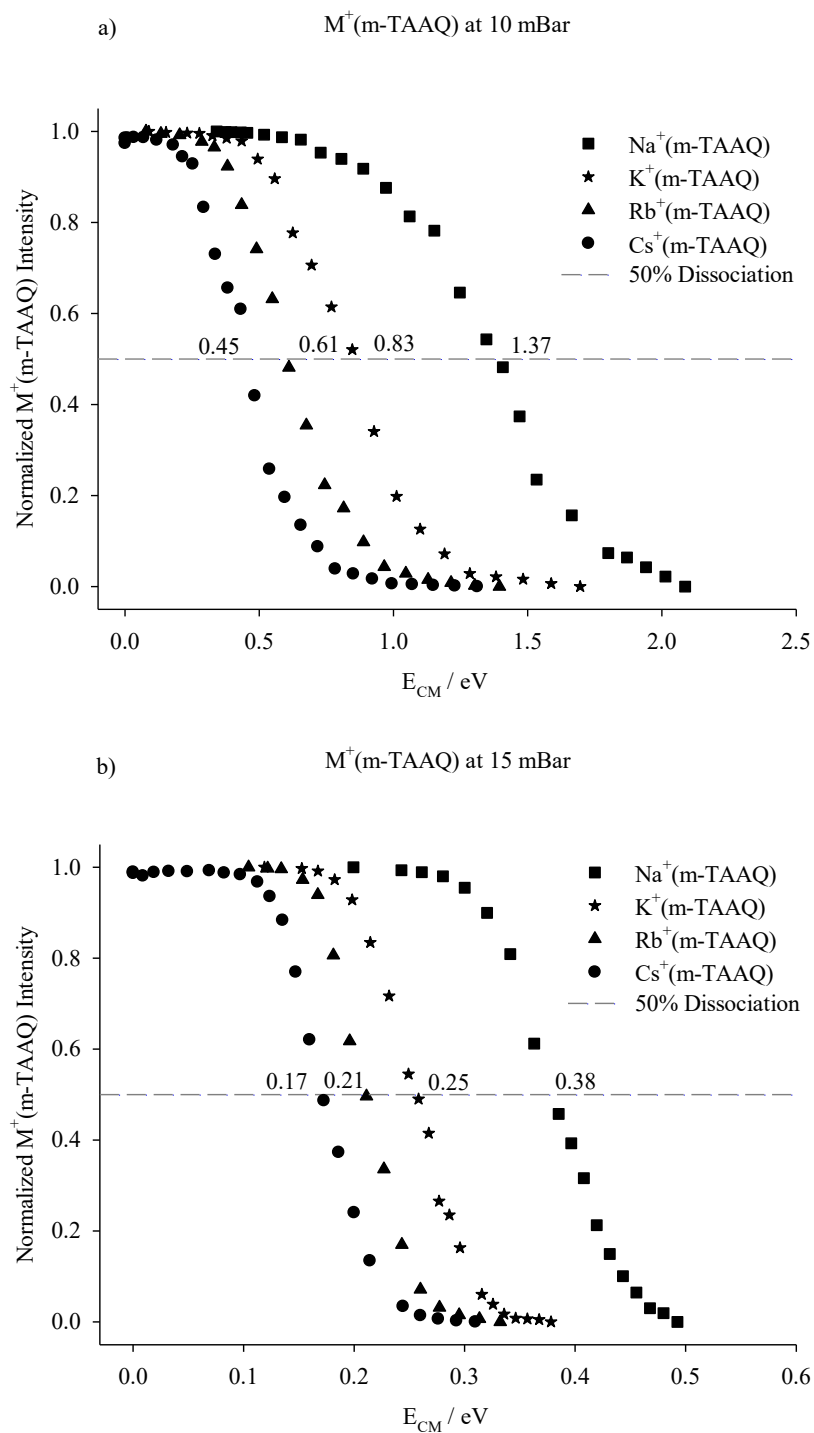


Figure C37. Normalized intensity of $M^+(m\text{-TAAQ})$ vs. center of mass energy decay curves from the ER-SORI-CID experiments under a) 10 mBar and b) 15 mBar. The values of $E_{50\%}$ are also shown in the graphs.

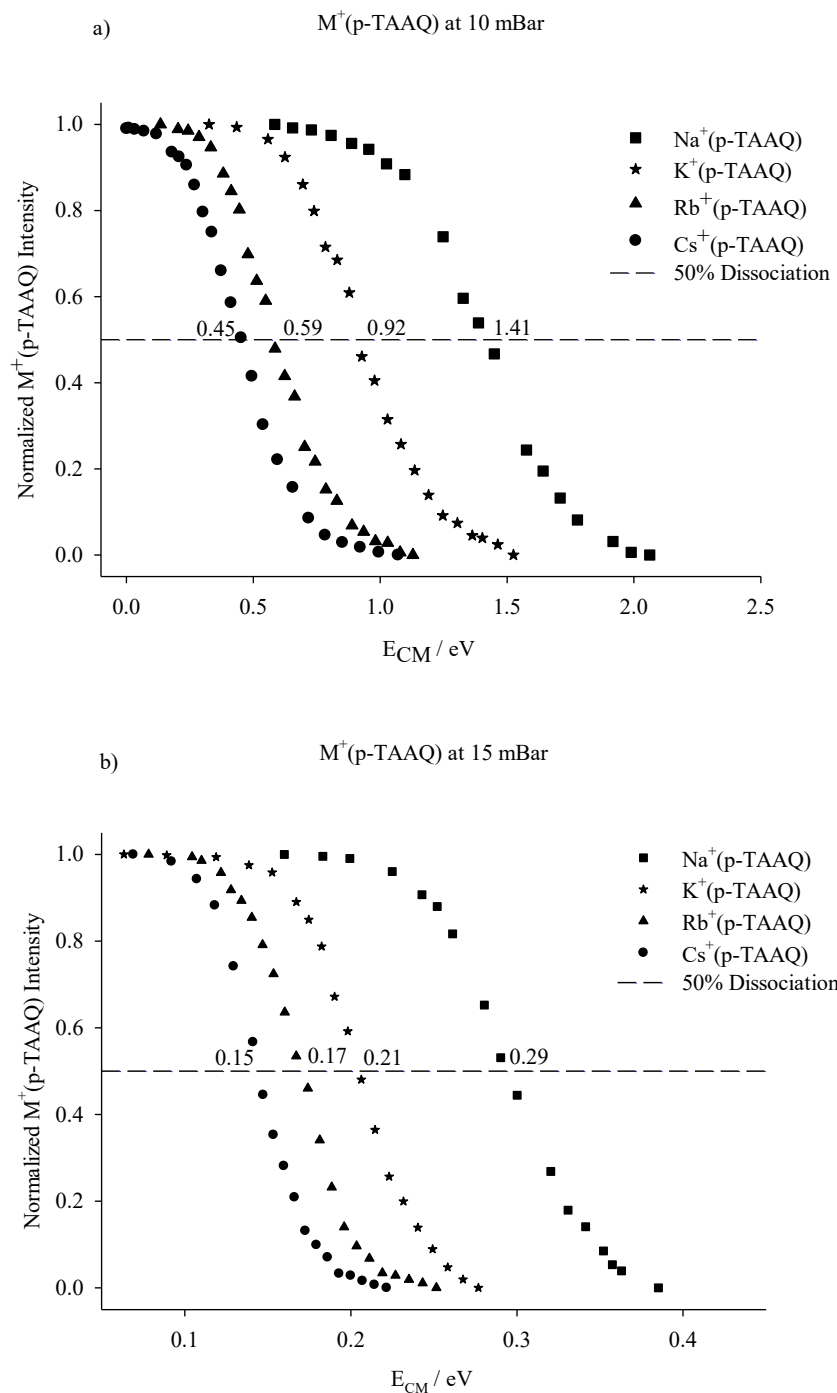


Figure C38. Normalized intensity of $M^+(\text{p-TAAQ})$ vs. center of mass energy decay curves from the ER-SORI-CID experiments under a) 10 mBar and b) 15 mBar. The values of $E_{50\%}$ are also shown in the graphs.

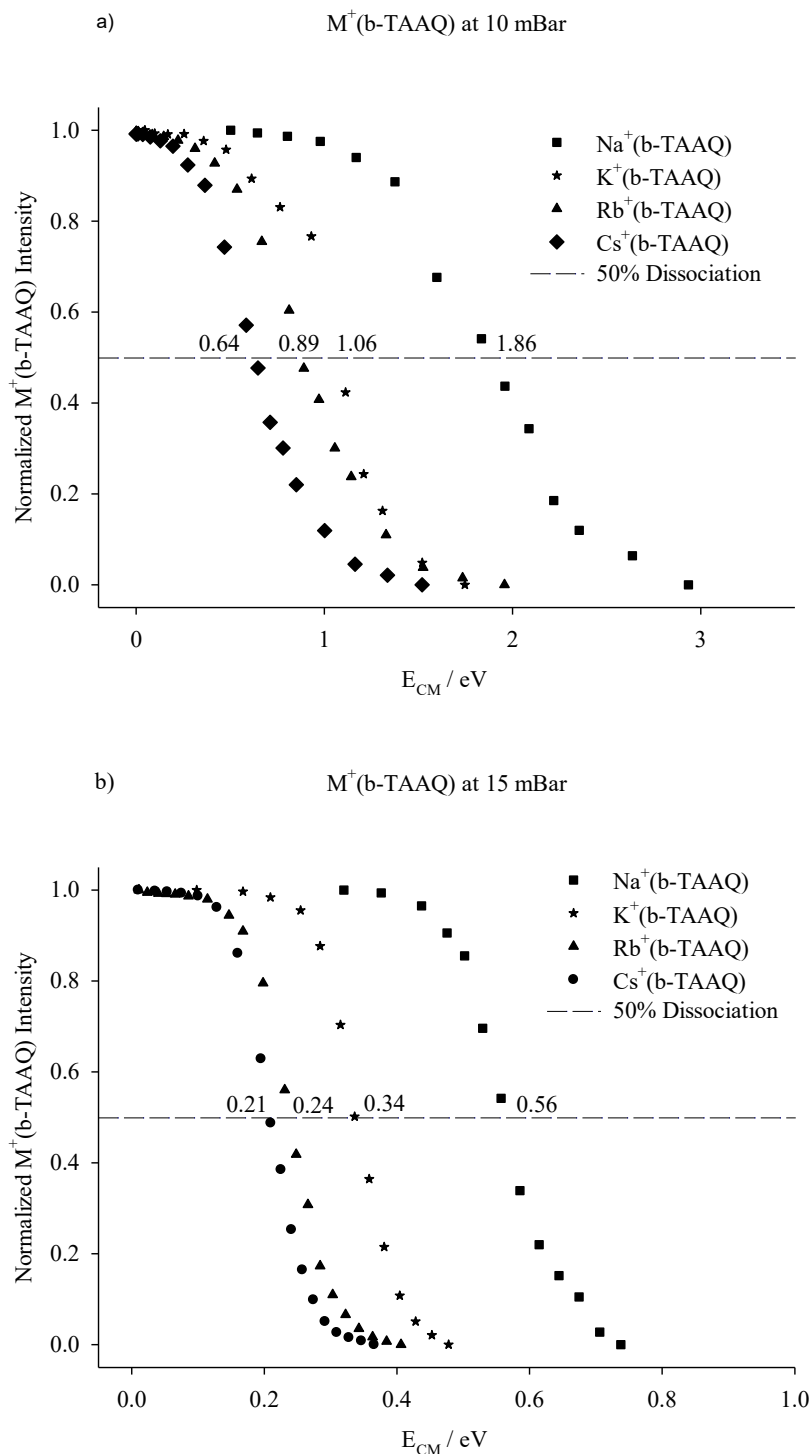


Figure C39. Normalized intensity of $M^+(b\text{-TAAQ})$ vs. center of mass energy decay curves from the ER-SORI-CID experiments under a) 10 mBar and b) 15 mBar. The values of $E_{50\%}$ are also shown in the graphs.

Table C1. Summary of m/z values proposed chemical identities, and chemical formulae of observed fragment ions of lithiated TAAQ complexes. The observed m/z values are primary fragments of parent ions except bolded m/z values the parent of which are specified in the following loss m/z column.

| complexes | Label of fragments | Observed m/z values | Loss m/z | Proposed chemical identity of loss | Chemical formula | Theoretical m/z |
|---|--------------------|---------------------|---|---|--|-----------------|
| Li ⁺ (o-TAAQ) C ₄₄ H ₃₆ LiO ₄ ⁺ m/z 635.3 | A_Li | 619.2 | 16.1 | CH ₄ | C ₄₃ H ₃₂ LiO ₄ ⁺ | 619.3 |
| | B_Li | 589.2 | 46.1 | CH ₃ OCH ₃ | C ₄₂ H ₃₀ LiO ₃ ⁺ | 589.2 |
| | C_Li | 455.1 | 180.1 | C ₁₄ H ₁₂ | C ₃₀ H ₂₄ LiO ₄ ⁺ | 455.3 |
| | | | | C ₁₂ H ₄ O ₂ | C ₃₂ H ₃₂ LiO ₂ ⁺ | 455.3 |
| | D_Li | 410.2 | 225.1 | C ₁₅ H ₁₃ O ₂ ⁺ | C ₂₉ H ₂₃ LiO ₂ ⁺ | 410.2 |
| | E_Li | 395.1 | 240.2 | C ₁₆ H ₁₆ O ₂ | C ₂₈ H ₂₀ LiO ₂ ⁺ | 395.2 |
| | F | 582.2 | 53.1 | CH ₃ OCH ₃ Li | C ₄₂ H ₃₀ O ₃ ⁺⁺ | 582.2 |
| | G | 536.2 | 589.2-53.1 | (CH ₃ OCH ₃) ₂ Li | C ₄₀ H ₂₄ O ₂ ⁺⁺ | 536.2 |
| | | | 582.2-46.1 | CH ₃ OCH ₃ | | |
| | H | 370.1 | 582.2-212.2 | (C ₇ H ₆ O) ₂ | C ₂₈ H ₁₈ O ⁺⁺ | 370.1 |
| | I | 357.1 | 410.2-53.1 | CH ₃ OCH ₃ Li | C ₂₇ H ₁₇ O ⁺ | 357.1 |
| | | | 395.2-38.1 | CH ₃ OLi | | |
| | J | 605.2 | 30.1 | CH ₂ O | C ₄₃ H ₃₄ LiO ₃ ⁺ | 605.2 |
| | K | 513.2 | 122.1 | C ₇ H ₇ OCH ₃ | C ₃₆ H ₂₆ LiO ₃ ⁺ | 513.2 |
| L | 481.1 | 589.2-108.1 | C ₇ H ₈ O | C ₃₅ H ₂₂ LiO ₂ ⁺ | 481.2 | |
| M | 181.0 | 454.3 | C ₃₀ H ₂₃ O ₄ Li | C ₁₄ H ₁₃ ⁺ | 181.1 | |
| Li ⁺ (m-TAAQ) C ₄₄ H ₃₆ LiO ₄ ⁺ m/z 635.3 | 619 | 619.3 | 16.0 | CH ₄ | C ₄₃ H ₃₂ LiO ₄ ⁺ | 619.2 |
| | 605 | 605.2 | 30.1 | CH ₂ O | C ₄₃ H ₃₄ LiO ₃ ⁺ | 605.3 |
| | 603 | 603.2 | 619.3-16.1 | (CH ₄) ₂ | C ₄₂ H ₂₈ LiO ₄ ⁺ | 603.2 |
| | 591 | 591.3 | 44.0 | CH ₂ OCH ₂ | C ₄₂ H ₃₂ LiO ₃ ⁺ | 591.2 |
| | 575 | 575.2 | 619.3-44.1 | CH ₂ OCH ₂ | C ₄₁ H ₂₈ LiO ₃ ⁺ | 575.2 |
| | | | 591.3-16.1 | CH ₄ | | |
| | 547 | 547.2 | 619.3-72.1 | CO+(CH ₂) ₂ | C ₄₀ H ₂₈ LiO ₂ ⁺ | 547.2 |
| 591.3-44.1 | | | CH ₂ OCH ₂ | | | |
| 513 | 513.2 | 122.1 | C ₇ H ₇ OCH ₃ | C ₄₄ H ₃₆ LiO ₄ ⁺ | 513.2 | |
| Li ⁺ (p-TAAQ) C ₄₄ H ₃₆ LiO ₄ ⁺ m/z 635.3 | 620 | 620.3 | 15.0 | CH ₃ | C ₄₃ H ₃₃ LiO ₄ ⁺ | 620.3 |
| | 605 | 605.2 | 30.1 | CH ₂ O | C ₄₃ H ₃₄ LiO ₃ ⁺ | 605.3 |
| Li ⁺ (b-TAAQ) C ₄₂ H ₂₈ LiO ₄ ⁺ m/z 603.6 | 585 | 585.6 | 18.0 | CLi-H | C ₄₁ H ₂₈ O ₄ ⁺ | 585.2 |
| | 579 | 579.2 | 24.4 | C ₂ | C ₄₀ H ₂₈ LiO ₄ ⁺ | 579.2 |
| | 509 | 509.2 | 94.4 | (CO ₂) ₂ Li-H | C ₄₀ H ₂₉ ⁺ | 509.1 |
| | 497 | 497.2 | 106.4 | C ₇ H ₆ O | C ₃₅ H ₂₂ LiO ₃ ⁺ | 497.2 |
| | 393 | 393.1 | 210.5 | C ₁₄ H ₁₀ O ₂ | C ₂₈ H ₁₈ LiO ₂ ⁺⁺ | 393.1 |
| | M | 181.0 | 422.6 | C ₂₈ H ₁₅ LiO ₄ | C ₁₄ H ₁₃ ⁺ | 181.1 |

Table C2. The computed lowest energy structures of $M^+(m\text{-TAAQs})$ which are $M^+(m_1\text{-}2\text{O-}3\text{Ph-TAAQs})$ ($M=\text{Li, Na, K, Rb}$ and Cs) under the B3LYP-D3/6-31+G(d,p) on C, H, O and def2svp on metal atoms. The computed binding enthalpies ($\Delta_{\text{bind}}H$) and Gibbs free energies ($\Delta_{\text{bind}}G$) are in unit kJ mol^{-1} at 298 K, 1 atm.

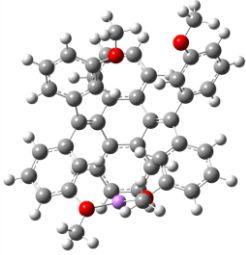
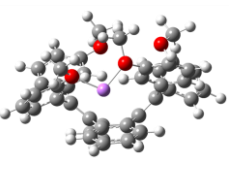
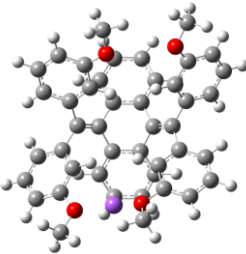
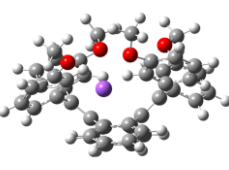
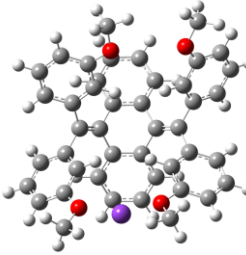
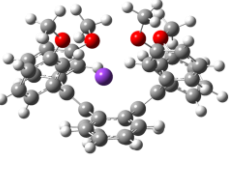
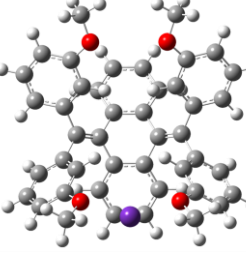
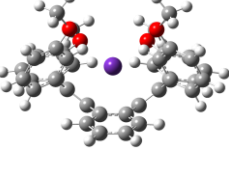
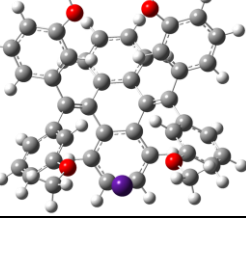
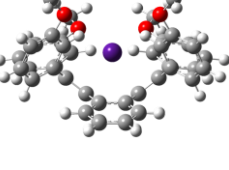
| M^+ (m-TAAQ) | Top view | Side view | Energies |
|-------------------|---|--|--|
| Li^+ |  |  | $\Delta_{\text{bind}}H = 226.8$ $\Delta_{\text{bind}}G = 189.6$ |
| Na^+ |  |  | $\Delta_{\text{bind}}H = 172.7$ $\Delta_{\text{bind}}G = 136.3$ |
| K^+ |  |  | $\Delta_{\text{bind}}H = 117.0$ $\Delta_{\text{bind}}G = 85.0$ |
| Rb^+ |  |  | $\Delta_{\text{bind}}H = 96.7$ $\Delta_{\text{bind}}G = 64.4$ |
| Cs^+ |  |  | $\Delta_{\text{bind}}H = 80.7$ $\Delta_{\text{bind}}G = 48.1$ |

Table C3. The computed lowest energy structures of $M^+(\text{p-TAAQs})$ which are $M^+(\text{p-2O-3Ph-TAAQ})$ ($M=\text{Li, Na, K, Rb and Cs}$) under the B3LYP-D3/6-31+G(d,p) on C, H, O and def2svp on metal atoms. The computed binding enthalpies ($\Delta_{\text{bind}}H$) and Gibbs free energies ($\Delta_{\text{bind}}G$) are in unit kJ mol^{-1} at 298 K, 1 atm.

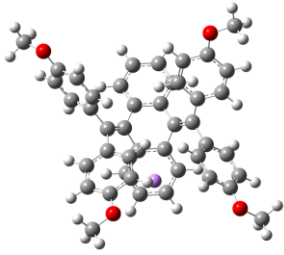
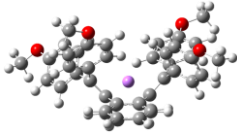
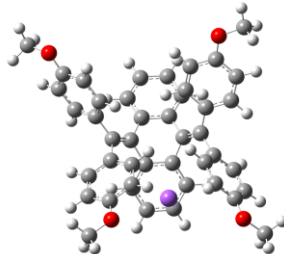
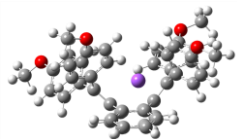
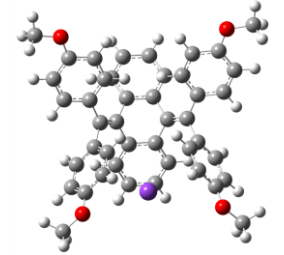
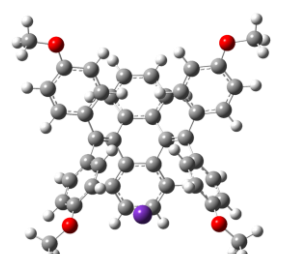
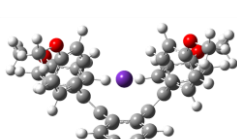
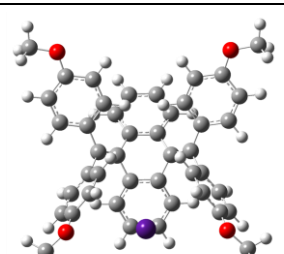
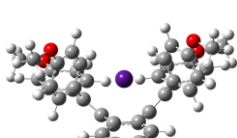
| M^+ (p-TAAQ) | Top view | Side view | Energies |
|-------------------|---|--|--|
| Li^+ |  |  | $\Delta_{\text{bind}}H = 180.0$ $\Delta_{\text{bind}}G = 145.9$ |
| Na^+ |  |  | $\Delta_{\text{bind}}H = 138.5$ $\Delta_{\text{bind}}G = 108.2$ |
| K^+ |  |  | $\Delta_{\text{bind}}H = 92.2$ $\Delta_{\text{bind}}G = 62.0$ |
| Rb^+ |  |  | $\Delta_{\text{bind}}H = 77.5$ $\Delta_{\text{bind}}G = 45.4$ |
| Cs^+ |  |  | $\Delta_{\text{bind}}H = 63.4$ $\Delta_{\text{bind}}G = 31.8$ |

Table C4. The computed lowest energy structures of $M^+(b_{2d}\text{-TAAQs})$ which are $M^+(b_{2d}\text{-2O-TAAQ})$ ($M=\text{Li, Na, K, Rb}$ and Cs) under the B3LYP-D3/6-31+G(d,p) on C, H, O and def2svp on metal atoms. The computed binding enthalpies ($\Delta_{\text{bind}}H$) and Gibbs free energies ($\Delta_{\text{bind}}G$) are in unit kJ mol^{-1} at 298 K, 1 atm.

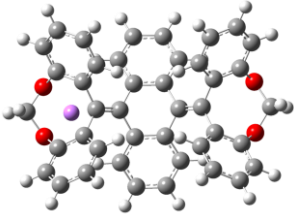
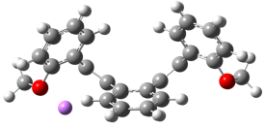
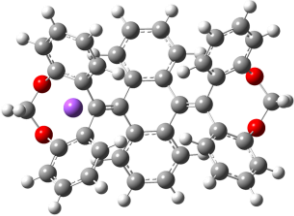
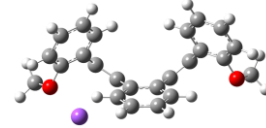
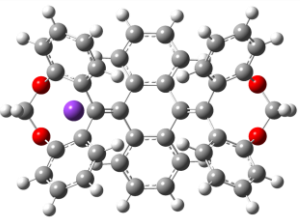
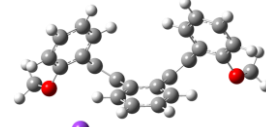
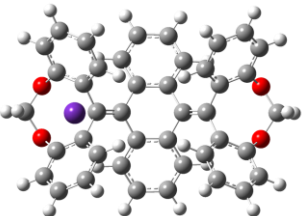
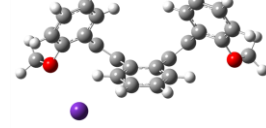
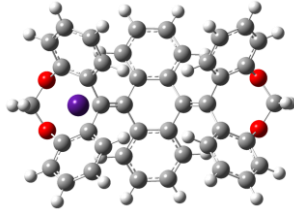
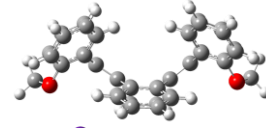
| M^+ ($b_{2d}\text{-TAAQ}$) | Top view | Side view | Energies |
|-----------------------------------|---|--|--|
| Li^+ |  |  | $\Delta_{\text{bind}}H = 176.8$ $\Delta_{\text{bind}}G = 143.3$ |
| Na^+ |  |  | $\Delta_{\text{bind}}H = 125.2$ $\Delta_{\text{bind}}G = 93.3$ |
| K^+ |  |  | $\Delta_{\text{bind}}H = 81.3$ $\Delta_{\text{bind}}G = 49.4$ |
| Rb^+ |  |  | $\Delta_{\text{bind}}H = 66.3$ $\Delta_{\text{bind}}G = 34.3$ |
| Cs^+ |  |  | $\Delta_{\text{bind}}H = 52.3$ $\Delta_{\text{bind}}G = 23.9$ |

Table C5. The computed lowest energy structures of $M^+(\text{b}_{1\text{u}1\text{d}}\text{-TAAQs})$ which are $M^+(\text{b}_{1\text{u}1\text{d}}\text{-3Ph-TAAQ})$ ($M = \text{Li, Na, K, and Rb}$) and $\text{Cs}^+(\text{b}_{1\text{u}1\text{d}}\text{-2O-TAAQ})$ under the B3LYP-D3/6-31+G(d,p) on C, H, O and def2svp on metal atoms. The computed binding enthalpies ($\Delta_{\text{bind}}H$) and Gibbs free energies ($\Delta_{\text{bind}}G$) are in unit kJ mol^{-1} at 298 K, 1 atm.

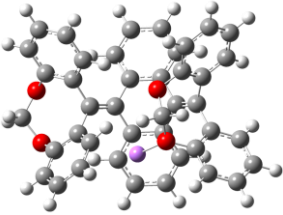
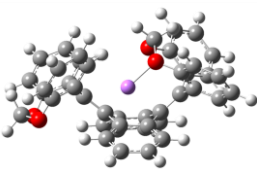
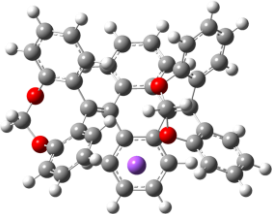
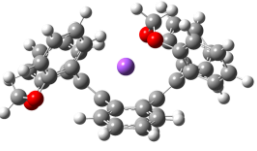
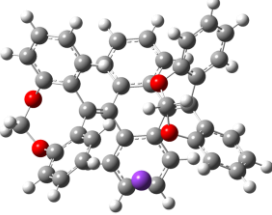
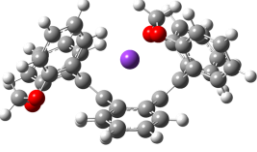
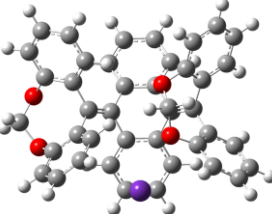
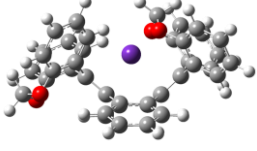
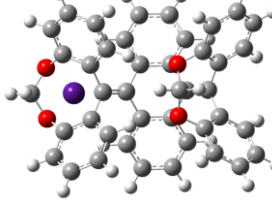
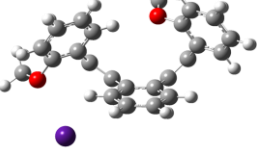
| M^+ ($\text{b}_{1\text{u}1\text{d}}\text{-TAAQ}$) | Top view | Side view | Energies |
|--|---|--|--|
| Li^+ |  |  | $\Delta_{\text{bind}}H = 211.2$ $\Delta_{\text{bind}}G = 171.5$ |
| Na^+ |  |  | $\Delta_{\text{bind}}H = 154.8$ $\Delta_{\text{bind}}G = 115.9$ |
| K^+ |  |  | $\Delta_{\text{bind}}H = 97.3$ $\Delta_{\text{bind}}G = 60.8$ |
| Rb^+ |  |  | $\Delta_{\text{bind}}H = 77.7$ $\Delta_{\text{bind}}G = 41.5$ |
| Cs^+ |  |  | $\Delta_{\text{bind}}H = 63.0$ $\Delta_{\text{bind}}G = 25.4$ |

Table C6. The computed lowest energy structures of $M^+(b_{2u}\text{-TAAQs})$ which are $M^+(b_{2u}\text{-4O-TAAQ})$ ($M = \text{Li, Na}$) and $M^+(b_{2u}\text{-3Ph-TAAQ})$ ($M = \text{K, Rb}$ and Cs) under the B3LYP-D3/6-31+G(d,p) on C, H, O and def2svp on metal atoms. The computed binding enthalpies ($\Delta_{\text{bind}}H$) and Gibbs free energies ($\Delta_{\text{bind}}G$) are in unit kJ mol^{-1} at 298 K, 1 atm.

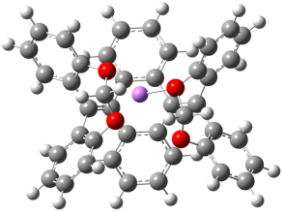
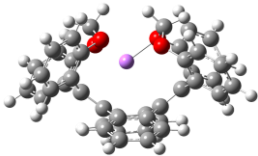
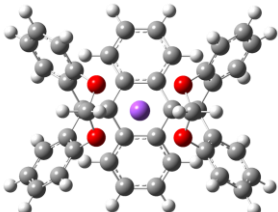
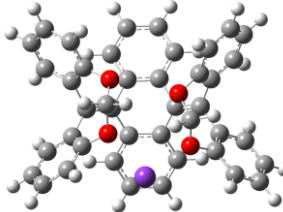
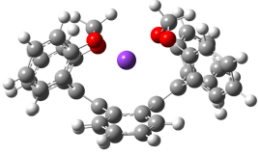
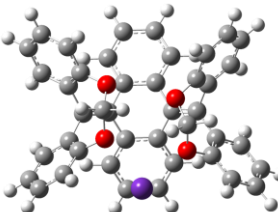
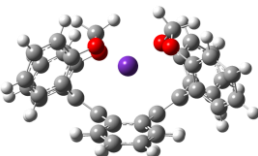
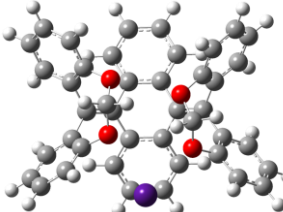
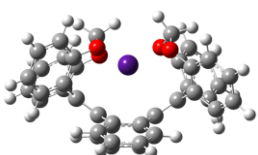
| M^+ ($b_{2u}\text{-TAAQ}$) | Top view | Side view | Energies |
|-----------------------------------|---|--|--|
| Li^+ |  |  | $\Delta_{\text{bind}}H = 264.0$ $\Delta_{\text{bind}}G = 220.5$ |
| Na^+ |  |  | $\Delta_{\text{bind}}H = 190.1$ $\Delta_{\text{bind}}G = 149.2$ |
| K^+ |  |  | $\Delta_{\text{bind}}H = 107.1$ $\Delta_{\text{bind}}G = 65.4$ |
| Rb^+ |  |  | $\Delta_{\text{bind}}H = 83.3$ $\Delta_{\text{bind}}G = 42.6$ |
| Cs^+ |  |  | $\Delta_{\text{bind}}H = 63.0$ $\Delta_{\text{bind}}G = 23.2$ |

Table C7. Natural energy decomposition analysis (NEDA) components in kJ mol⁻¹ under B3LYP-D3/6-31+G(d,p) on C, H, O and def2svp on metal atoms.

| Host | Guest | E _{tot} | ES | POL | XC | CT | DEF _{host} | DEF _{guest} | SE _{host} | SE _{guest} | EL | CT | CORE |
|--------------------------------|-----------------|------------------|-------|-------|-------|-----|---------------------|----------------------|--------------------|---------------------|-------|-----|-------|
| <i>o</i> -TAAQ | Li ⁺ | - | - | - | -85.7 | - | 549.3 | 1.9 | 329.2 | 0.6 | - | - | 135.7 |
| | | 488.4 | 292.3 | 659.3 | | 2.3 | | | | | 621.8 | 2.3 | |
| | Na ⁺ | - | -268 | - | - | - | 882.8 | 5.8 | 431.7 | 1.7 | - | - | 307 |
| | | 395.9 | | 866.2 | 148.1 | 2.2 | | | | | 700.7 | 2.2 | |
| | K ⁺ | - | - | - | - | - | 960.5 | 5.8 | 427.3 | 3.1 | - | - | 352.4 |
| | 304.1 | 225.7 | 858.9 | 183.4 | 2.3 | | | | | 654.1 | 2.3 | | |
| | Rb ⁺ | -280 | - | - | - | - | 417.9 | 7.6 | 165.6 | 5.3 | - | - | 83.4 |
| | | | 193.6 | 338.8 | 171.2 | 1.9 | | | | | 361.6 | 1.9 | |
| | Cs ⁺ | - | - | - | - | - | 396.4 | 13.9 | 142.7 | 9.4 | -322 | - | 77.3 |
| | | 247.4 | 173.9 | 300.3 | 180.9 | 2.7 | | | | | | 2.7 | |
| <i>m</i> -TAAQ | Li ⁺ | - | - | - | -71.6 | - | 484.5 | 1.2 | 277.6 | 0.5 | - | - | 136.1 |
| | | 360.7 | 216.9 | 555.9 | | 2.0 | | | | | 494.7 | 2.0 | |
| | Na ⁺ | - | - | - | -100 | - | 632.5 | 3.3 | 326.5 | 0.9 | - | - | 208.4 |
| | | 280.3 | 159.1 | 654.6 | | 2.5 | | | | | 486.2 | 2.5 | |
| | K ⁺ | - | - | - | - | - | 631.1 | 3 | 300.9 | 1.3 | - | - | 214.4 |
| | 218.9 | 130.3 | 603.4 | 117.4 | 1.9 | | | | | 431.4 | 1.9 | | |
| | Rb ⁺ | - | - | - | - | - | 271.2 | 2.4 | 128.2 | 1.6 | - | - | 32.8 |
| | | 207.6 | 110.1 | 258.2 | 111.1 | 1.8 | | | | | 238.5 | 1.8 | |
| | Cs ⁺ | - | - | -224 | - | - | 253.6 | 4 | 110.3 | 2.6 | - | - | 25.1 |
| | | 190.8 | 101.5 | | 119.5 | 3.2 | | | | | 212.6 | 3.2 | |
| <i>p</i> -TAAQ | Li ⁺ | - | - | - | -65.5 | - | 507.3 | 1.4 | 311.5 | 0.4 | - | - | 131.3 |
| | | 295.7 | 113.3 | 623.4 | | 2.2 | | | | | 424.9 | 2.2 | |
| | Na ⁺ | -248 | - | -660 | -93.4 | - | 623 | 3.4 | 329.2 | 1 | - | - | 202.9 |
| | | | 119.1 | | | 2.1 | | | | | 448.8 | 2.1 | |
| | K ⁺ | - | - | - | -99.9 | - | 522.9 | 2.3 | 260.3 | 0.9 | - | - | 163.9 |
| | 205.4 | 107.3 | 521.4 | | 1.9 | | | | | 367.5 | 1.9 | | |
| | Rb ⁺ | - | -94.8 | - | -97.1 | - | 223.4 | 1.7 | 114.1 | 1.3 | - | - | 12.6 |
| | | 197.7 | | 229.5 | | 1.5 | | | | | 208.9 | 1.5 | |
| | Cs ⁺ | - | -90 | - | - | - | 219.3 | 2.7 | 102.1 | 2 | - | - | 11.6 |
| | | 182.8 | | 206.5 | 106.2 | 2.1 | | | | | 192.3 | 2.1 | |
| <i>b</i> _{2d} -TAAQ | Li ⁺ | - | - | - | -61.9 | - | 482.8 | 1.1 | 277.7 | 0.5 | - | - | 143.7 |
| | | 283.0 | 145.6 | 556.1 | | 3.3 | | | | | 423.4 | 3.3 | |
| | Na ⁺ | - | - | - | -81.3 | - | 539.8 | 2.6 | 279.0 | 0.8 | - | - | 181.2 |
| | | 222.2 | 120.8 | 559.2 | | 3.2 | | | | | 400.2 | 3.2 | |
| | K ⁺ | - | -96.3 | - | -85.7 | - | 457.9 | 3.0 | 225.0 | 1.6 | - | - | 148.6 |
| | 176.0 | | 451.4 | | 3.4 | | | | | 321.1 | 3.4 | | |
| | Rb ⁺ | - | -84.0 | - | -80.7 | - | 201.7 | 2.7 | 100.4 | 2.1 | - | - | 21.3 |
| | | 166.3 | | 202.9 | | 3.2 | | | | | 184.4 | 3.2 | |
| | Cs ⁺ | - | -79.1 | - | -86.6 | - | 195.4 | 3.9 | 89.7 | 2.9 | - | - | 20.1 |
| | | 152.4 | | 182.8 | | 3.3 | | | | | 169.3 | 3.3 | |
| <i>b</i> _{2u} -TAAQ | Li ⁺ | - | - | - | -84.4 | - | 588.3 | 1.9 | 339.5 | 0.7 | - | - | 165.6 |
| | | 403.9 | 227.4 | 680.0 | | 2.3 | | | | | 567.2 | 2.3 | |
| | Na ⁺ | - | - | - | - | - | 848.5 | 5.2 | 419.4 | 1.6 | - | - | 301.4 |
| | | 332.6 | 210.3 | 841.3 | 131.3 | 3.4 | | | | | 630.7 | 3.4 | |
| | K ⁺ | - | - | - | - | - | 726.8 | 5.1 | 335.9 | 2.8 | - | - | 256.1 |
| | 235.3 | 151.8 | 675.5 | 137.1 | 2.8 | | | | | 488.5 | 2.8 | | |
| | Rb ⁺ | - | - | - | - | - | 311.2 | 5.4 | 136.9 | 3.9 | - | - | 50.7 |
| | | 219.8 | 129.6 | 279.2 | 125.1 | 2.4 | | | | | 268.0 | 2.4 | |
| | Cs ⁺ | - | - | - | - | - | 288.1 | 7.9 | 118.0 | 5.5 | - | - | 41.4 |
| | | 199.0 | 117.3 | 243.9 | 131.2 | 2.7 | | | | | 237.8 | 2.7 | |
| <i>b</i> _{1u1d} -TAAQ | Li ⁺ | - | - | - | -74.1 | - | 534.9 | 1.4 | 314.5 | 0.5 | - | - | 147.2 |
| | | 324.1 | 154.3 | 629.8 | | 2.2 | | | | | 469.1 | 2.2 | |
| | Na ⁺ | - | - | - | - | - | 678.2 | 3.7 | 346.1 | 1.1 | - | - | 229.5 |
| | | 257.7 | 138.2 | 693.9 | 105.1 | 2.4 | | | | | 484.8 | 2.4 | |
| | K ⁺ | - | - | - | - | - | 646.3 | 3.4 | 308.2 | 1.7 | - | - | 224.4 |
| | 198.1 | 111.8 | 618.2 | 115.4 | 2.4 | | | | | 420.1 | 2.4 | | |
| | Rb ⁺ | - | -94.7 | - | - | - | 265.6 | 3.1 | 125.5 | 2.3 | - | - | 36.4 |
| | | 186.7 | | 253.6 | 104.5 | 2.6 | | | | | 220.5 | 2.6 | |
| | Cs ⁺ | - | -84.9 | - | -85.5 | - | 191.0 | 4.2 | 87.6 | 3.2 | - | - | 18.9 |
| | | 157.1 | | 179.0 | | 2.9 | | | | | 173.1 | 2.9 | |

